UNIVERSITE PARIS-SUD

ECOLE DOCTORALE : Sciences et Technologies de l'Information des Télécommunications et des Systèmes
Laboratoire : Institut d'Electronique Fondamentale

DISCIPLINE : Physique

THESE DE DOCTORAT
Soutenue le 7/3/2013

par
Daniele COSTANTINI

Generation and amplification of surface plasmon polaritons at telecom wavelength with compact semiconductor-based devices

Directeur de thèse	COLOMBELLI Raffaele
Co-encadrant	BOUSSEKSOU Adel
Rapporteur	BOUHELIER Alexandre
Rapporteur	LETARTRE Xavier
Examinateur	GREFFET Jean-Jacques
Examinateur	GAUTHIER LAFAYE Olivier
Membres invité	DE WILDE Yannick

Alla nostra felicità

Contents

Introduction

The field of plasmonics is experiencing a rapid development, due to the interest in studying the behavior of light at the nanometer scale. Key ingredients of plasmonics are the Surface Plasmons (SPs), electromagnetic modes localized at the interface between a metal and a dielectric. SPs rely on the interaction between electromagnetic radiation and conduction electrons at metallic interfaces or in "small" metallic nanostructures. The recent intense activity on plasmonics has been also enabled by state-of-the-art nano-fabrication techniques [1] and by high-sensitivity optical characterization techniques. Among others, electromagnetic near-field microscopy has been playing a major role [2]. These tools pave the way to promising applications, which exploit the SP peculiarity of confining optical fields over sub-wavelength mode volumes [3]. Stimulated emission below the diffraction limit can be obtained with SPs realizing an ultra fast non-radiating laser, called SPASER [4]. The number of publications concerning plasmonics has been continuously increasing over the last twenty years [5] giving rise to a dynamic research context.

General context

The sub-wavelength confinement properties of SPs make them attractive for applications. Several concepts for sensing and opto-electronic integration based on SPs have been proposed.

A well known application is Surface Enhanced Raman Scattering (SERS), which exploits high local field intensities to increase the Raman signal, typically of molecules. Raman lines can be increased by 10^{10} times, with benefit for single-molecule detection [6, 7].

Another application of SPs is the determination of refractive index variations, *via* the resonance frequency shift. Systems based on this principle are

already commercial [8].

Planar plasmonic structures can also be employed as light collectors and plasmonic antennas are a tool which can increase light harvesting in photovoltaic devices [9].

Intense activity is also devoted to the development of SP component devices, such as couplers and modulators [10], with the initial goal of developing a technology for intra-chip optical interconnections [11]. We speak in this case of surface plasmon polaritons (SPPs), which propagate along the interface. However, the generation of SPPs with a compact device is challenging. SPPs cannot be optically excited unless the missing momentum between free photons and SPs of the same frequency is provided. Three main techniques are available to overcome this problem: prism-coupling, periodic gratings, and sub-λ scatterers in the near-field [12]. Recently the generation of SPs was also demonstrated exploiting non-linear four-wave mixing [13]. These techniques require an alignment and an external photon source, leading to somewhat bulky devices. A compact device capable of generating SPPs would represent an advantage, simplifying SP manipulation and allowing the integration in chip-size devices.

An additional issue hinders the development of many potential applications of surface plasmons: the ohmic losses. Losses can in principle be overcome by developing schemes exploiting optical gain. A first demonstration of SP loss compensation *via* optical gain has been reported by the Eng's group [14] in 2005. This result is based on optical pumping.

Krenn's group proposed an electrical generation of SPs using organic light-emitting diodes (OLEDs, $\lambda \approx 500$ nm) [15]. This system is interesting for several aspects (e.g. low cost), but it also presents a few disadvantages: standard lithographic processes cannot be applied (damage to the organic materials) and encapsulation is mandatory to avoid device degradation.

Devices exploiting metal-insulator-metal waveguides exist with quantum dots [16] and semiconductors ($\lambda \approx 800$ nm) [17] as gain media. In these architectures though the SPPs are not directly accessible (at least from the top of the device).

A beautiful approach for SPP generation and circuitry is presented in Ref. [18]: a GaAs nanowire is used as photon source. The photons are then coupled into silver plasmonic waveguides. This design depends on the random nanowire orientation on the substrate, which hinders the use of top-

down approaches.

The aforementioned schemes are excellent achievements, nevertheless they provide low efficiency and low amplification, making the laser regime hardly achievable. Our approach aims at providing a relevant SPP power at room temperature, with a reproducible fabrication process.

A semiconductor-based approach

In the present thesis work we propose and develop a semiconductor-based approach suitable to implement compact devices and to obtain optical gain by electrical injection. We adopt state-of-the art active regions (ARs), based on semiconductor quantum wells, which provide optical gains of several hundreds cm^{-1} at room temperature. We demonstrate the generation and the amplification of SPPs with electrically pumped devices at telecom wavelengths (1.3 μm $< \lambda <$ 1.55 μm), in particular at $\lambda = 1.3$ μm.

I performed the device design and the data analysis. I personally fabricated the devices in the CTU-Minerve clean-room at the IEF. I characterized the devices electrically and optically. The near-field characterizations were performed in collaboration with of the Institut Langevin (ESPCI, Paris), in the team led by Y. De Wilde.

In the first chapter SPPs are introduced solving Maxwell equations at the interface between two media. The optical response of metals in the telecom frequency range is discussed. Subsequently the main properties of SPPs are described, focusing on the confinement as a function of λ. We conclude by quantitatively justifying, through a figure of merit, the advantages of using telecom wavelengths in plasmonics.

Chapter 2 is devoted to SPP generation in general. Since SPPs arise from the strong coupling of photons and charge oscillations, they can be generated both by optical (eg. laser) or electronic (eg. electron-beam) means. The standard generation techniques are reviewed, then we introduce the concept of electrical injection. We discuss two schemes to implement the electrical injection, which is extremely interesting for the integration of plasmonic devices. We conclude by presenting the results obtained by our group at mid-infrared wavelengths ($\lambda = 7.5$ μm).

Chapter 3 presents the semiconductor AR necessary to transpose the electrical injection concept from mid-infrared wavelengths to telecom wave-

lengths. Our choice of the material system fell on tensile strained quantum wells, which represent one of the best semiconductor gain media at telecom wavelength. I studied the effects of the metal proximity to the AR by thinning down the top cladding. This reduces the laser performances, but the gain medium, closer to the metal, provides gain to the SPPs. We demonstrate "thin cladding" lasers operating at room temperature, in which the metal is extremely close to the AR compared to standard lasers. Passive and active device measurements allowed us to tune our finite element model, which is used in the rest of the thesis.

Chapter 4 is dedicated to the generation of SPPs at telecom wavelengths with semiconductor-based devices. I demonstrated the in-situ generation of SPPs with an integrated coupler approach, using the thin cladding structure previously demonstrated. Thanks to the near-field microscopy we could directly prove the SPPs generation and provide the original measurement of their evanescent extension in the vertical direction. The near-field measurements were performed by L. Greusard and Y. De Wilde (Institut Langevin). I also obtained an end fire coupling device, which is demonstrated by probing the SPP in far-field.

Chapter 5 opens with a review on SPP amplification, including recent advances in SPASERs and nanolasers. The concept of hybrid plasmonic mode is introduced. The interest in hybrid modes arises from the possibility of tailoring the plasmonic mode component and the related losses. Our results on the amplification of hybrid SPP modes are then reported. By further approaching the metal to the AR we achieved a hybrid SPP laser, electrically pumped and operating at room temperature. The strength of the demonstration is also based on the direct near-field imaging of the plasmonic mode.

Chapter 6 is dedicated to device applications which aim at reducing the mode losses through patterning of the top metal. We first discuss the concept of low-loss mode in presence of a first order metallic grating. We then characterize the device, demonstrating its correct operation. Initial evidence of loss reduction is experimentally observed.

The experimental techniques of fabrication and measurements constitute a relevant part of the thesis work. They are detailed in the Appendix.

Chapter 1

Surface plasmons: theory and applications

Two key ingredients of plasmonics are *surface plasmon polaritons* and *localized surface plasmons*. They are particular solutions of the electromagnetic equations and have been both described as early as 1900. Nevertheless a global picture of all the related phenomena and applications was built along all the 20^{th} century, due to the rediscovery of surface plasmon polaritons in a variety of different contexts.

Surface Plasmon Polaritons (SPPs) are electromagnetic excitations propagating at the interface between a dielectric and a conductor, evanescently decaying in the perpendicular direction. These electromagnetic surface waves arise *via* the coupling of the electromagnetic fields to oscillations of the conductor electron's plasma [19]. SPPs were considered for the first time around the turn of the 20^{th} century in the context of radio waves propagation. Sommerfeld in 1899 [20] and then Zenneck [21] in 1907 described mathematically the propagation of SPPs along a surface of finite conductivity. At the same time Wood in 1902 observed the production of *anomalous* intensity drops when visible light reflects at metallic gratings [22]. The connection of the above mentioned phenomena was established by Fano in the mid-century (1941) [23]. Other experimental observations in the 1960s of Ritchie [24], Kretschmann and Raether [25] finally brought to a unified description of all these phenomena in the form of SPPs. [1]

Localized surface plasmons (LSPs), as SPPs, are electromagnetic exci-

1. More historical details can be found in ref. [26]

tations at the interface between a dielectric and a finite size conductor, in general a metallic nanoparticle. The history of LSPs is less turbulent and the mathematical foundation was also established at the beginning of the 20th century by Mie (1908). The Mie theory [27] applies to metallic nanoparticles and allows, for instance, to explain the emblematic and charming phenomenon of the Lycurgus cup. This ancient roman cup shown in Fig. 1.1 normally appears of a green opaque color, but when illuminated from within it becomes red colored. In fact the transmitted light is filtered by metallic particles which are embedded in the glass of the cup. Due to their size, the particles absorb green light transmitting only frequencies around the red color.

Figure 1.1: The Lycurgus glass cup, demonstrating the bright red color of transmitted light though gold nanocrystals [28].

From now on we will only consider SPPs, which are the object of discussion of the present manuscript.

A classical framework - based on standard electromagnetic equations - is a suitable approach to precisely describe plasmonic phenomena. Even metallic nanostructures down to sizes of the order of a few nanometers can be described without resorting to quantum mechanics [29]. This chapter presents the theory of SPPs, starting from the Maxwell equations, in the simple case of a single interface. The simplest metal/insulator geometry allows one to highlight the main properties of SPPs with a significant mathematical simplicity. We will discuss the existence condition of surface waves at a generic interface and then supply a physical interpretation of SPPs describing the

electromagnetic response of metals. The last section is dedicated to the main properties of SPPs, their dispersion relation, their typical length scales and an adequate figure of merit, which is an indicator of the trade-off between losses and confinement as a function of the frequency.

1.1 Surface modes

SPPs are surface waves. We will investigate surface waves starting from Maxwell's equations:

$$\nabla \cdot \mathbf{D} = \rho_{ext} \tag{1.1}$$

$$\nabla \cdot \mathbf{B} = 0 \tag{1.2}$$

$$\nabla \wedge \mathbf{E} = -\frac{\partial \mathbf{B}}{\partial t} \tag{1.3}$$

$$\nabla \wedge \mathbf{H} = \mathbf{J}_{ext} + \frac{\partial \mathbf{D}}{\partial t} \tag{1.4}$$

The equations link the four macroscopic fields $\mathbf{D}$ (the electric displacement), $\mathbf{E}$ (the electric field), $\mathbf{H}$ (the magnetic field), and $\mathbf{B}$ (the magnetic induction or magnetic flux density) with the external charge and current densities ρ_{ext} and $\mathbf{J}_{ext}$. The four macroscopic field are further linked via the polarization $\mathbf{P}$ and the magnetization $\mathbf{M}$ by:

$$\mathbf{D} = \varepsilon_0 \mathbf{E} + \mathbf{P} \tag{1.5}$$

$$\mathbf{H} = \frac{1}{\mu_0}\mathbf{B} - \mathbf{M} \tag{1.6}$$

where ε_0 and μ_0 are, respectively, the electric permittivity and the magnetic permeability [2] of vacuum. Since in the present manuscript we will only consider non magnetic media ($\mu = 1$), the term $\mathbf{M}$ can be set to zero. The description will be limited to the polarization effects.

It is advantageous to cast the equations in a form applicable to the electromagnetic guiding, the wave equation. Hereinafter we will obtain the specific

2. ϵ_0 and μ_0 satisfy the ralation $\epsilon_0 \mu_0 = 1/c^2$

wave equation for the electric field, but a similar procedure is also valid for the magnetic field.

In absence of external charge and current densities the curl equations 1.3 and 1.4 can be combined to yield:

$$\nabla \wedge \nabla \wedge \mathbf{E} = -\mu_0 \frac{\partial^2 \mathbf{D}}{\partial t^2.} \tag{1.7}$$

Due to the absence of external charge and current densities we have $\nabla \cdot \mathbf{D} = 0$ and Eq. 1.7 can be rewritten as:

$$\nabla \left(-\frac{1}{\varepsilon} \mathbf{E} \cdot \nabla \varepsilon - \nabla^2 \mathbf{E} \right) = -\mu_0 \varepsilon_0 \varepsilon \frac{\partial^2 \mathbf{E}}{\partial t^2.} \tag{1.8}$$

For negligible variation of the dielectric profile $\varepsilon = \varepsilon(\mathbf{r})$ over distances of the order of one optical wavelength, Eq. 1.8 simplifies to the homogeneous wave equation,

$$\nabla^2 \mathbf{E} - \frac{\varepsilon}{c^2} \frac{\partial^2 \mathbf{E}}{\partial t^2} = 0. \tag{1.9}$$

This equation has to be solved separately in regions of constant ε and the solutions must be matched using appropriate boundary conditions.

As mentioned above, a similar manipulation of the Maxwell Eq. 1.3 and Eq. 1.4, with the same conditions of absence of external charge and current densities, allows to obtain the wave equation for the magnetic field. The Eq. 1.9 can be written as:

$$\nabla^2 \mathbf{F} - \frac{\varepsilon}{c^2} \frac{\partial^2 \mathbf{F}}{\partial t^2} = 0, \tag{1.10}$$

valid for the polar vector electric field ($\mathbf{F} = \mathbf{E}$) and the axial vector magnetic field ($\mathbf{F} = \mathbf{H}$).

In order to adapt Eq. 1.10 to the description of confined propagating waves we first assume a general harmonic time dependence $\mathbf{F}(\mathbf{r}, t) = \mathbf{F}(\mathbf{r}) e^{-i\omega t}$ of the electric field. Inserted into Eq. 1.10, this yields:

$$\nabla^2 \mathbf{F} + k_0^2 \varepsilon \mathbf{F} = 0, \tag{1.11}$$

where $k_0 = \omega / c$ is the wavevector of the propagating wave in vacuum. Equation 1.11 is known as the *Helmholtz equation.*

The simplest geometry of surface waves is a plane interface that separates two homogeneous media. As shown in Fig. 1.2, medium 1, characterized by a complex dielectric constant ε_1 (or refractive index $n_1 = \sqrt{\varepsilon_1}$), previously with z < 0, and medium 2, characterized by a real dielectric constant ε_2 (or refractive index $n_2 = \sqrt{\varepsilon_2}$), fills the part of space with z > 0.

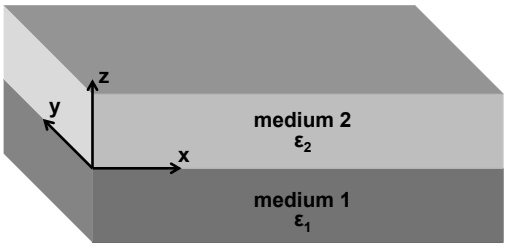

Figure 1.2: Geometry for the propagation of surface waves on a plane interface separating two homogeneous materials.

Following the definition, surface waves, or surface modes, are waves propagating along the interface plane and presenting a confinement in the direction perpendicular to the interface. If we consider a wave propagating along the x direction and independent of y ($\partial/\partial y = 0$), the electric and the magnetic fields can be written in the form $\mathbf{F}(x, y, z) = \mathbf{F}(z)e^{i\beta x}$, where β is the wavevector. The Eq. 1.11 becomes:

$$\frac{\partial^2 \mathbf{F}(z)}{\partial z^2} + (\varepsilon(z)k_0^2 - \beta^2)\mathbf{F}(z) = 0, \tag{1.12}$$

where $\varepsilon(z)$ is ε_1 for z < 0 and ε_2 for z > 0.

Solutions of Eq. 1.12 are complex exponential functions. Surface waves correspond to the particular case in which electromagnetic fields decay exponentially away from the interface, i.e. with the form $\mathbf{F}_1(z) = \mathbf{F}_1 e^{+k_1 z}$ for z < 0 and $\mathbf{F}_2(z) = \mathbf{F}_2 e^{-k_2 z}$ for z > 0 with Re$[k_1] > 0$ and Re$[k_2] > 0$, as shown in Fig. 1.3. The constants k_1 and k_2 represent the exponential fall-off of the fields in the the media and a penetration depth can be easily deduced (see section 1.4).

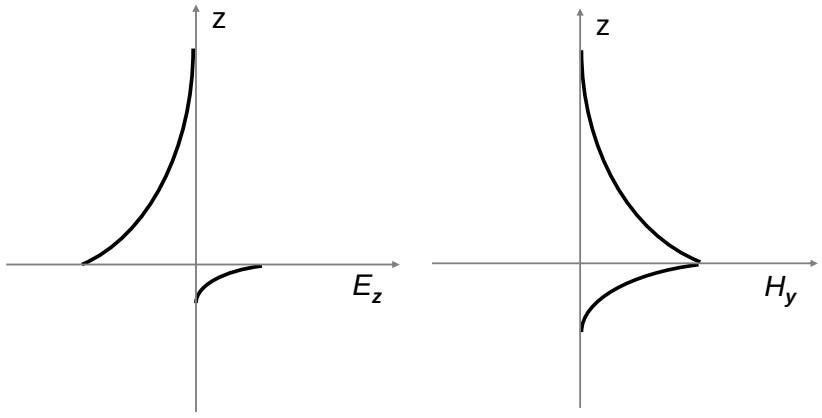

(a) (b)

Figure 1.3: Schematic decay at a metal/insulator interface of the: (a) electric field in the z direction (b) magnetic field in the y direction.

1.2 Dispersion relation

In order to obtain the dispersion relation of surface waves, i.e. the relation $\omega - \beta$, we consider Maxwell-Faraday Eq. 1.3 for the component E_x, E_y, E_z and Maxwell-Ampére for the components H_x, H_y, H_z. Furthermore it is convenient to distinguish between the TM ($H_z = 0$) and TE ($E_z = 0$) polarizations.

For TM polarization, the non zero field components are H_y, E_x, E_z and satisfy:

$$\begin{aligned} \frac{\partial^2 H_y}{\partial z^2} + (\varepsilon k_0^2 - \beta^2) H_y &= 0 \\ E_x &= -\frac{i}{\omega \varepsilon_0 \varepsilon} \frac{\partial H_y}{\partial z} \\ E_z &= -\frac{\beta}{\omega \varepsilon_0 \varepsilon} H_y. \end{aligned} \tag{1.13}$$

Evanescent solutions along z have the following form:

$$\begin{aligned} H_y(z) &= A_1 e^{k_1 z} \\ E_x(z) &= -A_1 \frac{i k_1}{\omega \varepsilon_0 \varepsilon_1} e^{k_1 z} \\ E_z(z) &= -A_1 \frac{\beta}{\omega \varepsilon_0 \varepsilon_1} e^{k_1 z} \end{aligned} \tag{1.14}$$

for $z < 0$ and

$$\begin{aligned} H_y(z) &= A_2 e^{-k_2 z} \\ E_x(z) &= A_2 \frac{ik_2}{\omega\varepsilon_0\varepsilon_2} e^{-k_2 z} \\ E_z(z) &= -A_2 \frac{\beta}{\omega\varepsilon_0\varepsilon_2} e^{-k_2 z} \end{aligned} \tag{1.15}$$

for $z > 0$. The wave equation applied in Eq. 1.13 imposes the conditions on the constants k_i:

$$\begin{aligned} k_1^2 &= \beta^2 - k_0^2\varepsilon_1 \\ k_2^2 &= \beta^2 - k_0^2\varepsilon_2. \end{aligned} \tag{1.16}$$

The continuity conditions at the interface, impose: i) $H_y(z = 0^+) = H_y(z = 0^-)$ that entails $A_1 = A_2$, and ii) $E_x(z = 0^+) = E_x(z = 0^-)$, which implies:

$$\frac{k_1}{k_2} = -\frac{\varepsilon_1}{\varepsilon_2}. \tag{1.17}$$

The third continuity condition $D_z = \varepsilon E_z$ entails the same consequence as the first one ($A_1 = A_2$).

We previously saw that a surface wave decays exponentially away from the surface, implying $k_1 > 0$ and $k_2 > 0$. When the dielectric constants are both real, ε_1 and ε_2 in Eq. 1.17 must be opposite in sign. If medium one has a metallic character ($\varepsilon_1 < 0$), medium two must have a dielectric character ($\varepsilon_2 > 0$). The general case will be detailed in the next paragraph.

For TE modes, the continuity conditions on E_y and H_x lead to $\mathbf{A}_1(k_1 + k_2) = 0$, which cannot be satisfied for surface modes. No surface modes exist for TE polarization: surface waves only exist for TM polarization.

Combining Eq. 1.17 and Eq. 1.16 leads to the dispersion relation of SPP at the interface between two half spaces:

$$\beta = k_0 \sqrt{\frac{\varepsilon_1\varepsilon_2}{\varepsilon_1 + \varepsilon_2}}. \tag{1.18}$$

An effective index can be defined,

$$n_{eff} = \beta/k_0 = \sqrt{\frac{\varepsilon_1\varepsilon_2}{\varepsilon_1 + \varepsilon_2}}, \tag{1.19}$$

and also a wavelength for the surface wave,

$$\lambda_{sw} = \frac{2\pi}{\mathrm{Re}[\beta]} = \frac{\lambda_0}{\mathrm{Re}[n_{eff}]}. \tag{1.20}$$

1.2.1 Existence conditions

We now discuss the physical existence conditions of the surface modes as a function of the material optical properties [30]. At the end of section 1.1 we imposed a requirement on the confinement of the surface mode at the interface, namely $\mathrm{Re}[k_i]>0$, for $i = 1, 2$. It follows that surface waves have a TM polarization and, taking into account equations 1.16, that $\mathrm{Re}[\sqrt{n_{eff}^2 - n_i^2}]>0$, for $i = 1, 2$. In the simplest case where the dielectric constants are real we obtain the existence condition $\varepsilon_1\varepsilon_2 < 0$. Nevertheless if complex values of ε are introduced the problem is more delicate and an implicit relation has to be satisfied.

Substituting β with the expression 1.18, the equations 1.16 can be written as,

$$\begin{aligned} k_1^2 &= -\frac{{\varepsilon_1}^2}{\varepsilon_1 + \varepsilon_2} k_0^2 \\ k_2^2 &= -\frac{{\varepsilon_2}^2}{\varepsilon_1 + \varepsilon_2} k_0^2. \end{aligned} \tag{1.21}$$

We now consider ε_1 and ε_2 complex numbers in the polar coordinates representation: $\varepsilon_1 = |\varepsilon_1|e^{i\theta_1}$ et $\varepsilon_2 = |\varepsilon_2|e^{i\theta_2}$. Excluding the meta-materials case and taking into account the fields time dependence ($e^{-i\omega t}$) we have $\theta_1, \theta_2 \in [0, \pi]$ [31]. We then define $\varepsilon_{12} = \varepsilon_1 + \varepsilon_2 = |\varepsilon_{12}|e^{i\theta_{12}}$, also with $\theta_{12} \in [0, \pi]$.

The equations 1.21 allow for two solutions for k_1 and two solutions for k_2, that differ only in sign, that is $e^{i\pi}$:

$$\begin{aligned} k_1 &= \pm\frac{|\varepsilon_1|}{\sqrt{|\varepsilon_{12}|}} e^{i(\theta_1 - \theta_{12}/2 + \pi/2)} k_0 \\ k_2 &= \pm\frac{|\varepsilon_2|}{\sqrt{|\varepsilon_{12}|}} e^{i(\theta_2 - \theta_{12}/2 + \pi/2)} k_0. \end{aligned} \tag{1.22}$$

Not all the four possible pairs of solutions (k_1,k_2) are physically allowed because k_1 and k_2 have to satisfy Eq. 1.17, which can be written as follows

in complex notation:

$$\frac{k_1}{k_2} = -\frac{|\varepsilon_1|}{|\varepsilon_2|} e^{i(\theta_1 - \theta_2)}. \tag{1.23}$$

The direct comparison between the two previous equations shows that Eq. 1.23 is satisfied only if the signs of k_1 and k_2 in Eq. 1.22 are different. This requirement and the confinement one are fulfilled in Eq. 1.22 if:

$$\begin{cases} \cos(\theta_1 - \frac{\theta_{12}}{2} + \frac{\pi}{2}) & > & 0 \\ \cos(\theta_2 - \frac{\theta_{12}}{2} + \frac{\pi}{2}) & < & 0 \end{cases} \tag{1.24}$$

for the sign combination $(+,-)$, or

$$\begin{cases} \cos(\theta_1 - \frac{\theta_{12}}{2} + \frac{\pi}{2}) & < & 0 \\ \cos(\theta_2 - \frac{\theta_{12}}{2} + \frac{\pi}{2}) & > & 0 \end{cases} \tag{1.25}$$

for the sign combination $(-,+)$. In both cases the signs of the terms are opposite. Therefore a unique inequality can be written

$$\cos\left(\theta_1 - \frac{\theta_{12}}{2} + \frac{\pi}{2}\right) \cos\left(\theta_2 - \frac{\theta_{12}}{2} + \frac{\pi}{2}\right) < 0 \tag{1.26}$$

$$\sin\left(\theta_1 - \frac{\theta_{12}}{2}\right) \sin\left(\theta_2 - \frac{\theta_{12}}{2}\right) < 0 \quad . \tag{1.27}$$

Eq. 1.26 is a necessary and sufficient condition for the existence of a surface mode at the interface between two materials of dielectric constant ε_1 and ε_2. Using a trigonometric equivalence of Werner the condition 1.26 can be expressed as:

$$\cos(\theta_1 - \theta_2) < \cos(\theta_1 + \theta_2 - \theta_{12}) \tag{1.28}$$

more clearly:

$$\cos\left(\arg\left(\frac{\varepsilon_1}{\varepsilon_2}\right)\right) < \cos\left(\arg\left(\frac{\varepsilon_1\varepsilon_2}{\varepsilon_1 + \varepsilon_2}\right)\right) \tag{1.29}$$

where $\arg(z)$ is the complex argument.

Before discussing some specific cases of the inequality 1.26 a short recall of the ε frequency dependence of typical materials is needed. In the solid state

physics literature [32] we find that there is an intimate relation between the dielectric function $\varepsilon(\omega)$ and the material conductivity $\sigma(\omega)$:

$$\varepsilon(\omega) = 1 + \frac{4\pi i\sigma(\omega)}{\omega}, \tag{1.30}$$

the real part of $\varepsilon(\omega)$ is

$$Re[\varepsilon(\omega)] = 1 - \frac{4\pi Im[\sigma(\omega)]}{\omega} \tag{1.31}$$

Eq. 1.31 allows us to state that materials with:

– high conductivity (conductors, i.e. metals) have a negative Re[ε]

– low conductivity (insulators, i.e. dielectrics) have a positive Re[ε]

Therefore referring to Eq. 1.28 we can have the following combinations:

Interface **Metal / Metal**, Re[ε_1] < 0 and Re[ε_2] <0, that is $\theta_1, \theta_2 \in [\pi/2, \pi]$. Assuming without loss of generality that $\theta_1 \leq \theta_{12} \leq \theta_2$, after some manipulation we have $0 \leq \theta_1 - \theta_{12}/2 \leq \pi/2$ and $\pi/4 \leq \theta_2 - \theta_{12}/2 \leq 3\pi/4$. It follows that the inequality 1.26 cannot be verified and, in the case of an interface between two metals, no surface modes are permitted.

Interface **Any material / no-loss dielectric**, Re[ε_2] > 0 and Im[ε_2] $=0$ that corresponds to the case of a dielectric material without losses. We have $\theta_2 = 0 \leq \theta_{12} \leq \theta_1$, consequently $-\pi \leq \theta_2 - \theta_{12}/2 \leq 0$ and $0 \leq \theta_1 - \theta_{12}/2 \leq \pi$. The inequality 1.26 is always satisfied, unless when $\theta_1 = 0$ and, in some cases, when $\theta_1 = \pi$. In the specific case where $\theta_1 = \pi$ we have to distinguish the cases in which:

– $|\varepsilon_1| \leq |\varepsilon_2|$, then θ_{12}=0 and the inequality 1.26 is not satisfied.

– $|\varepsilon_1| > |\varepsilon_2|$, then θ_{12}=π and the surface mode exists.

We conclude that a surface mode can exist at the interface between a metal and a dielectric (Re[ε_1] < 0 and Re[ε_2] > 0) or between two dielectrics such that Re[ε_1] > 0 and Re[ε_2] > 0, but can not between two metals. In the specific case in which the dielectric material is without losses (ε_2 real and positive) the surface mode can exists unless the other material is a dielectric without losses or unless the other material is a metal without losses and $0 > \varepsilon_1 \geq -\varepsilon_2$.

In order to illustrate typical behaviors of surface waves we propose two different specific cases. We plot the cross-section of Re[H_y], at a given frequency of 230 THz (λ=1.3 μm), for an interface between air and doped

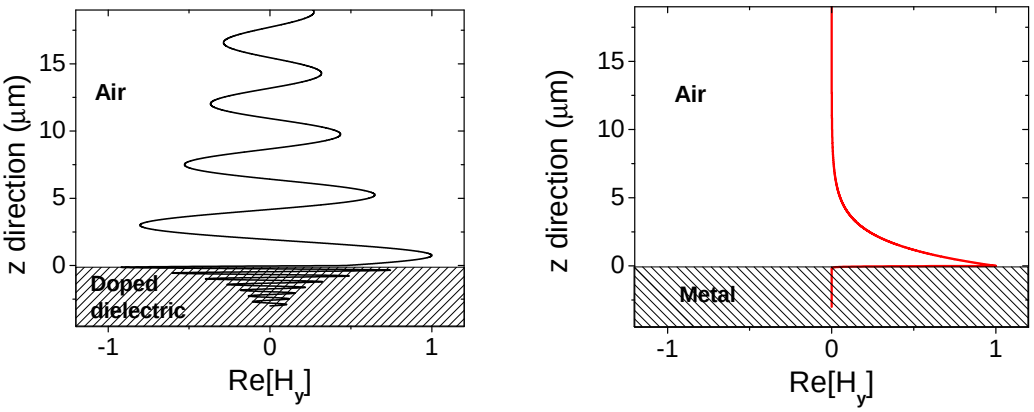

(a) (b)

Figure 1.4: Cross-section of Re$[H_y]$ for surface waves at a plane interface, as a function of the distance from the interface, at the frequency of 230 THz corresponding to a wavelength λ=1.3 μm. (a) Air ($n = 1$)/doped semiconductor interface (n=3.2 - i· 0.2 or ε=10.2 - i·1.28) (b) Air ($n = 1$)/metal interface (n=0.403 - i·8.25 or ε=-67.9 - i·6.65). The 1D simulation is performed with a finite element software [33].

semiconductor (Fig. 1.4a) and for an interface between air and metal (Fig. 1.4b).

In the case of the interface with the doped semiconductor we observe a rapid oscillation of the field convoluted with an exponential decay. The oscillations are due to the imaginary part of k_1 and k_2. On the other hand the interface with metal shows a faster decay of the field away from the surface which corresponds to a better confinement. Since the confinement is the most desirable property, surface wave are mainly studied on metal materials.

In the following we will refer to the case of an air/metal interface only and we will consider surface plasmon polaritons (SPPs) to highlight the coupling with the charge oscillations of the electron plasma in the metal.

1.3 Electromagnetic response of metals

After having determined the existence condition for SPPs, we now discuss their nature from a physical point of view. The existence of surface waves requires a metal or a doped dielectric, as demonstrated in the previous section. Free carriers hence play a major role in the optical response. In the case of metal the contribution of free carriers is dominant and their response can be predicted thanks to a simple model, called plasma model or Drude model.

The free charges in metals are considered a gas of free electrons of density n, moving through a background of positive fixed ions. This description is valid for a wide range of frequencies and, in particular, it correctly predicts the behavior of metals in the near-infrared range and larger wavelengths. For alkali metals, the validity range extends up to the ultraviolet, while for noble metals only until visible frequencies, where interband transitions occur. In the plasma model, the details of the lattice potential and electron-electron interactions are not taken into account. Instead, one simply assumes that some aspects of the band structure are incorporated into the effective optical mass m of each electron. The electrons oscillate in response to the applied electromagnetic field, and their motion is damped via collisions occurring with a characteristic collision frequency $\gamma = 1/\tau$. The time constant τ is known as the relaxation time of the free electron gas, which is typically on the order of 10^{-14} s at room temperature, corresponding to $\gamma = 100$ THz.

We consider an electron of the plasma sea, with charge $-e$ and effective mass m, placed in a uniform electric field along the x direction, $\mathbf{E(r,t)} = E(t)\mathbf{e}_x$. The position $x(t)$ satisfies the laws of classical mechanics:

$$m\frac{d^2x}{dt^2} + m\gamma\frac{dx}{dt} = -eE. \tag{1.32}$$

If we assume a harmonic time dependence $E(t) = E_0 e^{-i\omega t}$ of the driving field, a particular solution of this equation describing the oscillation of the electron is $x(t) = x_0 e^{-i\omega t}$. Eq. 1.32 can be rewritten:

$$-m\omega^2 x_0 - im\gamma\omega x_0 = -eE_0, \tag{1.33}$$

which leads to the position of the electron:

$$x_0 = \frac{e}{m(\omega^2 + i\gamma\omega)} E_0. \tag{1.34}$$

The polarization vector $\mathbf{P}$=Pe_x is given by $P = -eNx$ where N=nV is the number of electrons in a volume unit. Inserting the expression for $\mathbf{P}$ into equation 1.5 yields the x component of the electric displacement vector $\mathbf{D}$,

$$D = \varepsilon_0 \left(1 - \frac{Ne^2/\varepsilon_0}{m(\omega^2 + i\gamma\omega)}\right) E_0. \tag{1.35}$$

Therefore the dielectric function of a metal is:

$$\varepsilon(\omega) = 1 - \frac{Ne^2/\varepsilon_0}{m(\omega^2 + i\gamma\omega)}. \tag{1.36}$$

which can be expressed in the well known Drude form:

$$\varepsilon(\omega) = 1 - \frac{\omega_p^2}{\omega^2 + i\gamma\omega}, \tag{1.37}$$

where $\omega_p = (Ne^2/\varepsilon_0 m)^{1/2}$ is the plasma frequency of the metal.

The real and imaginary components of this complex dielectric function $\varepsilon(\omega) = \varepsilon_R(\omega) + i \cdot \varepsilon_I(\omega)$ are:

$$\varepsilon_R(\omega) = 1 - \frac{\omega_p^2 \tau^2}{1 + \omega^2 \tau^2} \tag{1.38}$$

$$\varepsilon_I(\omega) = \frac{\omega_p^2 \tau}{\omega(1 + \omega^2 \tau^2)} \tag{1.39}$$

In Tab.1.3 we report the parameters of the Drude model for different materials [34]. Gold and silver are the most used metals in plasmonics; copper is less suitable although compatible with silicon technology. Aluminum is taken as an example of a *bad* plasmonic material (low τ).

From Eq. 1.37 we observe that for large frequencies $\omega \approx \omega_p$ and $\omega > \omega_p$ (Ultraviolet region) the imaginary part of the dielectric function vanishes, leading to negligible damping. The metal becomes transparent and the dielectric function $\varepsilon(\omega)$ is predominantly real and positive,

$$\varepsilon(\omega) = 1 - \frac{\omega_p^2}{\omega^2} \tag{1.40}$$

Metal	ω_p	$\lambda_p = 2\pi c/\omega_p$	γ	$\tau = 1/\gamma$
Au	$1.37 \cdot 10^{16}$ s^{-1}	138 nm	$4.05 \cdot 10^{13}$ s^{-1}	24.7 fs
Ag	$1.37 \cdot 10^{16}$ s^{-1}	138 nm	$2.73 \cdot 10^{13}$ s^{-1}	36.6 fs
Cu	$1.20 \cdot 10^{16}$ s^{-1}	157 nm	$5.24 \cdot 10^{13}$ s^{-1}	19.1 fs
Al	$2.24 \cdot 10^{16}$ s^{-1}	161 nm	$1.22 \cdot 10^{14}$ s^{-1}	8.2 fs

Table 1.1: Drude parameters for gold, silver, copper and aluminum taken from Ordal et al. [34].

However, a notable exception exist: the behavior of noble metals in this frequency region is altered by interband transitions, as detailed in the following subsection.

For frequencies lower than ω_p the metal absorbs light and, in presence of an interface with a dielectric medium, the large difference of indexes causes light reflection at the metal surface.

1.3.1 Real metals

We anticipated before that the dielectric function, Eq. 1.37, of the Drude model adequately describes the optical response of metals only for photon energies below the threshold of transitions between electronic bands. For some of the noble metals, interband effects already start to occur for energies in excess of 1 eV (corresponding to a wavelength $\lambda \approx 1\mu$m). The validity limit of the free-electron description of Eq. 1.37 is illustrated in Fig. 1.5 in the case of gold, considered one of the best metals for plasmonics. Fig. 1.5 shows the experimentally measured values of the complex dielectric function, real (ε_{real}) and imaginary ($\varepsilon_{imag.}$) components taken from Palik [35], and the values calculated using Eq. 1.38, Eq. 1.39 and data in Tab. 1.3. Clearly, at visible frequencies (400 THz $< f <$ 800 THz) the applicability of the free-electron model breaks down due to the occurrence of interband transitions, leading to an increase in ε_2.

In the rest of the manuscript we will employ the experimental data of [35]. We also plot the experimental components, n_{real} and n_{imag}, of the complex refractive index ($n = \sqrt{\varepsilon}$) in Fig. 1.6. The real part of the index, n_{real}, increases for frequencies f $>$ 400 THz, with a similar behavior to $\varepsilon_{imag.}$

For long wavelengths in the mid-infrared (mid-IR) and far-infrared (FIR)

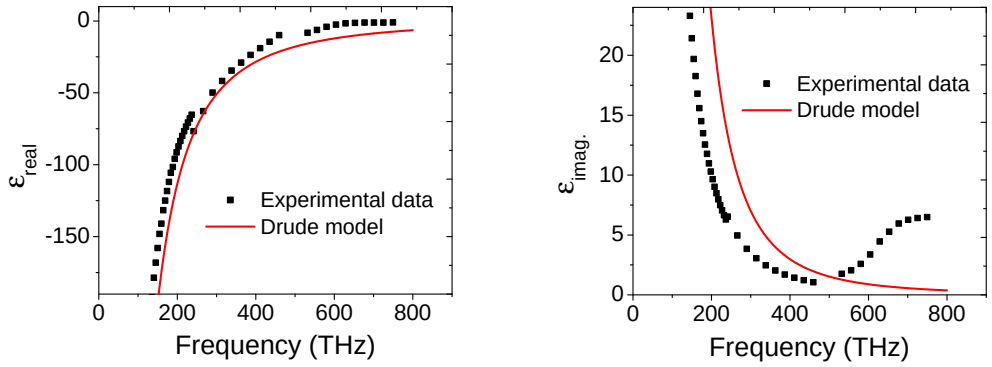

(a) (b)

Figure 1.5: Real part (a) and imaginary part (b) of the dielectric function of gold. Comparison between the experimental data of gold (black square dots), taken from [35], and data obtained with the Drude model and values for gold in Tab.1.3 (red solid line). Note that the Drude model cannot reproduce the trend of the imaginary part of the dielectric function (ε_2) for frequencies in the visible range.

the Drude model perfectly fits the experimental data, much better than in the NIR.

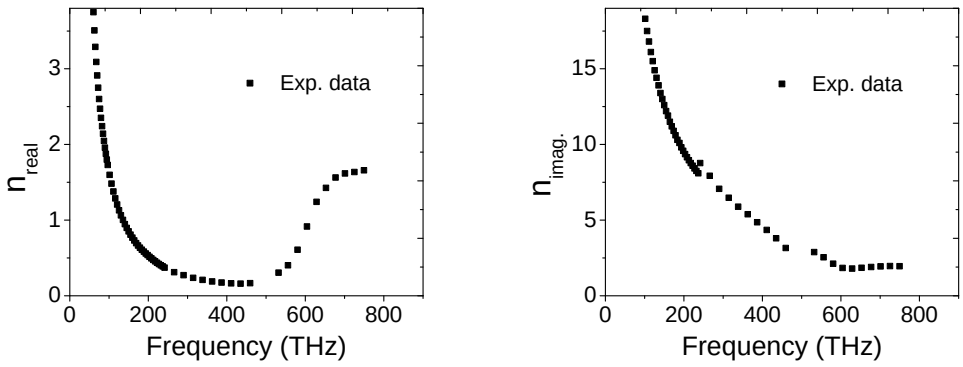

(a) (b)

Figure 1.6: (a) Real and (b) imaginary part of the gold index, experimental values are taken from [35]. The relevant discontinuities are due to different experimental data-set considered in [35].

1.4 SPPs properties and energy confinement

In this section we will plot the dispersion relation of SPPs showing the effects of the damping. Then the four characteristic length scales of SPP are presented and discussed. Finally a figure of merit is introduced to quantify the SPP "benefit-to-cost" and validate their use at telecom wavelengths.

For frequencies smaller then the plasma frequency ($\omega < \omega_p$) light can propagate along the surface of the metal, thanks to the coupling with the electron plasma. The new modes arising from the coupling between two different excitations are called *polaritons*. This explains why the surface wave originating from light (photons) and plasma oscillations (electrons) is called surface plasmon polariton. Fig. 1.7 shows the charge distribution compared to the field lines of the electric field.

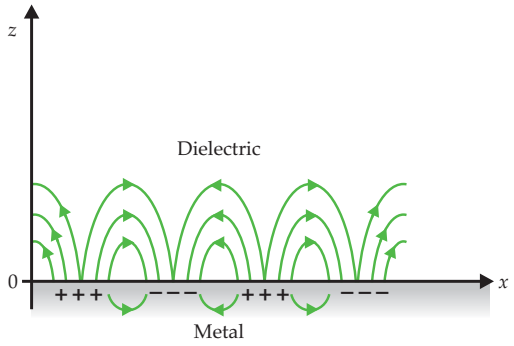

Figure 1.7: Electric field lines and charge distribution for a SPP propagating at the interface between a metal and a dielectric [11].

1.4.1 Dispersion relation with Drude model

Since the dielectric function of metal (Eq. 1.37) strongly depends on the frequency, we expect a similar dependence for the SPP dispersion. The dispersion relation provides information on the SPP properties of propagation and confinement.

We plot in Fig. 1.8 (a) the dispersion relations of a SPP at the interface gold/air and at the interface gold/indium phosphide (InP). The metal is considered without damping ($\gamma = 0$) and the indexes for the dielectrics are $n_{air} = 1$ and $n_{InP} = 3.2$. For the sake of simplicity we assume a constant

and real index for InP. Its absorption will be taken into account later. In the plot the real part (continuous curves) and the imaginary part (broken curves) of the wave vector β are shown. Due to their bound nature, SPP excitations lie to the right of their respective light lines. The modes existing at $\omega > \omega_p$ are radiative modes. Between the bound and the radiative regime a gap with purely imaginary β prohibits any propagation.

For small values of β, corresponding to low frequencies up to the mid-infrared (2.5 μm λ 10 μm), the SPP dispersion relation is close to the light line of the dielectric material and the surface wave is weakly confined. In this regime SPPs are also known as Sommerfeld-Zenneck waves. In the opposite regime, for large β the SPPs frequency approaches the *surface plasmon* frequency:

$$\omega_{sp} = \frac{\omega_p}{\sqrt{1+\varepsilon_2}} \tag{1.41}$$

that follows from Eq. 1.18 and Eq. 1.37. In the case of undamped metal, for frequencies approaching ω_{sp}, the SPP wave-vector $\beta \to \infty$ and the group velocity (corresponding to the derivative of the dispersion relation $\partial\omega/\partial\beta$) $v_g \to 0$. The mode acquires an electrostatic character and it is called *surface plasmon*.

If the damping in the metal is introduced, the dielectric function ε_1 becomes complex and so does β. In this case the damping, experienced by the carriers during their oscillations, is responsible of an attenuation along the propagation direction because the energy is gradually dissipated *via* heating of the metal. Therefore SPPs are characterized by a decay length (L_{SPP}) along their propagation direction.

To obtain the dispersion relation considering the damping in the metal we can use a non-zero collision frequency, $\gamma \neq 0$, in the Drude model. In Fig. 1.8 (b) are plotted the dispersion relation $\omega - Re[\beta]$ of the same two systems of Fig. 1.8 (a), but using the damped Drude model. Compared to the case of completely undamped metal we observe a *back-bending* in the SPP dispersion. This behavior effect was experimentally observed in 1973 by Arakawa et al. [36] in SPPs at the interface between CaF_2/Ag and Sapphire/Ag. In case of *back-bending* the SPP shows a maximum β wavevector at frequency ω_{sp}, putting a lower bound in the surface plasmon wavelength $\lambda_{SPP} = 2\pi/Re[\beta]$. This imposes also a limit in the perpendicular confinement to the interface, since, from Eq. 1.16, the SPP field falls in the dielectric as $e^{|k_2||z|}$ with

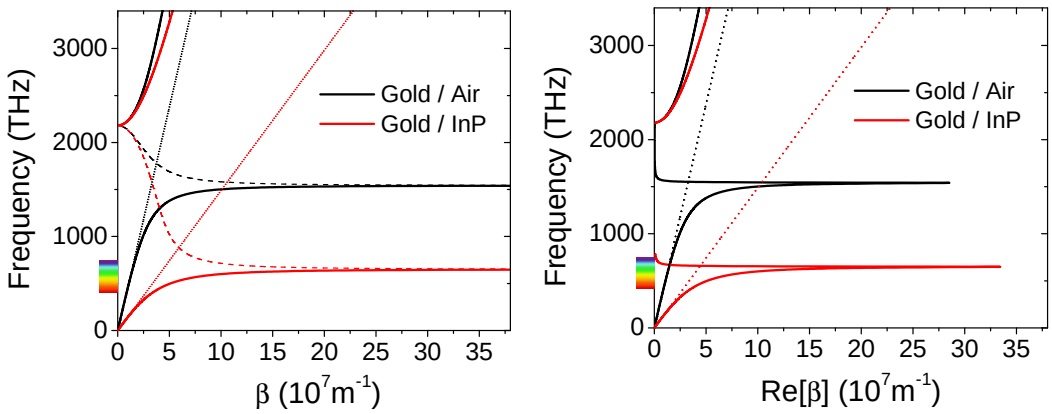

(a) (b)

Figure 1.8: Dispersion relation of SPPs at the interface gold/air (black curve) and gold/InP (red curve). The gold index is computed with the Drude model using $\omega_p = 1.37 \cdot 10^{16} s^{-1}$ (a) without damping and (b) with damping ($\gamma = 4.05 \cdot 10^{13} s$) taken from Tab.1.3. In (a) β is purely imaginary in the gap between bound and radiative modes (imaginary parts plotted in broken lines). Note: the lower branch of the dispersion relation is asymptotic to the surface plasma frequency shown in Eq. 1.41, that depends on the dielectric constant of the dielectric material.

$k_2 = \sqrt{\beta^2 - \varepsilon_2 \left(\frac{\omega}{c}\right)^2}$. Moreover in this case the frequency gap between ω_{sp} and ω_p, forbidden with a perfect conductor, is allowed.

1.4.2 Length scales

We examine now in more detail the 4 characteristic lengths of SPPs introduced until now: the field penetration in the metal (δ_m), the field penetration in the dielectric (δ_d), the wavelength (λ_{SPP}) and the propagation distance (L_{SPP}). Fig. 1.4.2 schematically shows how these 4 lengths span several orders of magnitude, from several nanometers for the penetration depth in the metal (δ_m) to the mm scale for the propagation length of SPP (L_{SPP}) in the mid-IR.

Each length is plotted as a function of the frequency (as for the dispersion relation in Fig. 1.8) using the experimental dielectric function of the metal shown in Fig. 1.6.

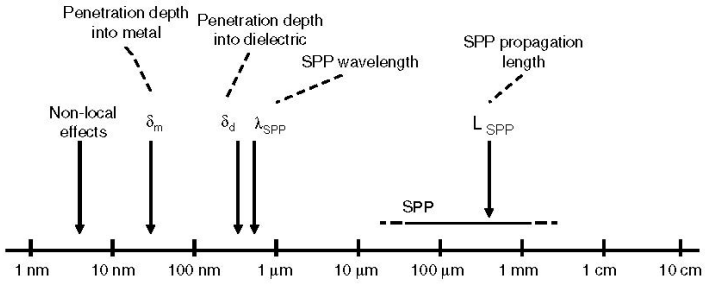

Figure 1.9: The different length scales of importance for SPPs in the visible and near-infrared (on a logarithmic scale). The important length scales span several orders of magnitude [3].

δ_m is the penetration depth of the electric field in the metal. [3] It is linked to k_1 (formula 1.16) as follows,

$$\delta_m = \frac{1}{Re[k_1]} \tag{1.42}$$

The dependence on the frequency is shown with broken lines in Fig. 1.10. At telecom wavelengths the penetration depth in the metal is about 10 nm.

δ_d is the penetration depths of the fields in the dielectric. It is linked to k_2 (formula 1.16) as follows,

$$\delta_d = \frac{1}{Re[k_2]} \tag{1.43}$$

The frequency dependence is shown with solid lines in Fig. 1.10. At telecom wavelengths the penetration depth in the air is $\approx$ 850 nm, while in the InP is $\approx$ 80 nm.

λ_{SPP} is the SPP wavelength introduced in Eq. 1.20,

$$\lambda_{SPP} = \frac{2\pi}{\mathrm{Re}[\beta]} \tag{1.44}$$

The dependence on the frequency is shown in Fig. 1.11. At telecom wavelengths the λ_{SPP} is slightly shorter than the vacuum wavelength. For instance at a gold/air interface λ_{SPP} = 1.29 μm, for λ_0=1.3 μm.

3. In the literature δ is also used to indicate the electromagnetic energy decay.

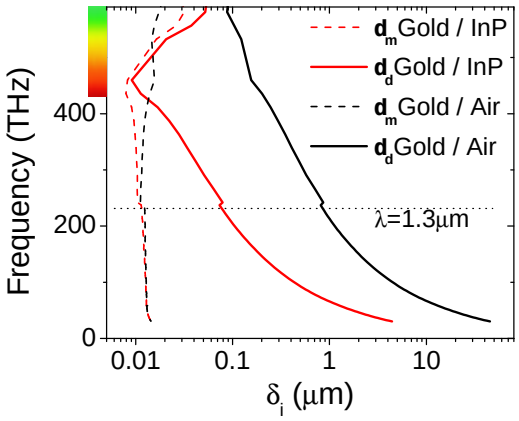

Figure 1.10: Penetration depth (δ) of the fields for a gold/air (black color) and a gold/InP (red color) interface. The penetration depths in the dielectric are plotted with a solid line while the one in the metal is plotted with a broken line. The horizontal dotted line indicates the frequency corresponding to the wavelength 1.3 μm.

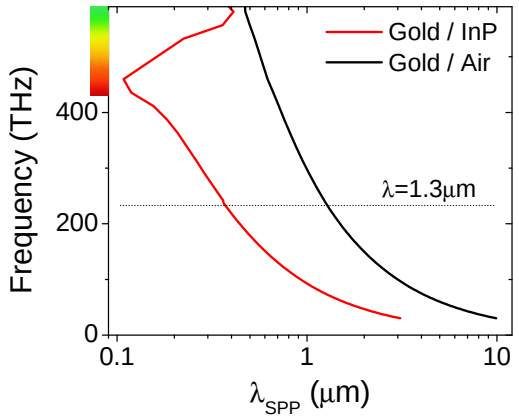

Figure 1.11: SPP wavelength for a gold/air (black line) and a gold/InP (red line) interface. The horizontal dotted line indicates the frequency corresponding to λ= 1.3μm.

L_{SPP} is the SPP propagation length. Physically the energy is dissipated trough the metal heating and L_{SPP} is the propagation distance where the intensity is damped of 1/e. The electronic response contributes to the imaginary part of the dielectric function, hence of the wave-vector β. L_{SPP} is

defined as:

$$L_{SPP} = \frac{1}{2Im[\beta]} \tag{1.45}$$

A SPP at a gold/air interface exhibits a L_{SPP} of $\approx$ 150 μm, while for a gold/InP interface L_{SPP} is $\approx$ 3 μm. This shows the strong dependence of propagation losses with the refractive index of the dielectric. The L_{SPP} roughly scales with the optical index of the dielectric to the 3^{rd} power [19]. Surface roughness can affect the propagation length, increasing the electronic damping and radiation losses. The plotted values represent therefore an upper limit for real plasmonic devices. Note that recent studies propose metal epitaxy growth as a strategy to obtain extremely smooth surfaces [37], hence increasing the propagation length and decreasing the losses.

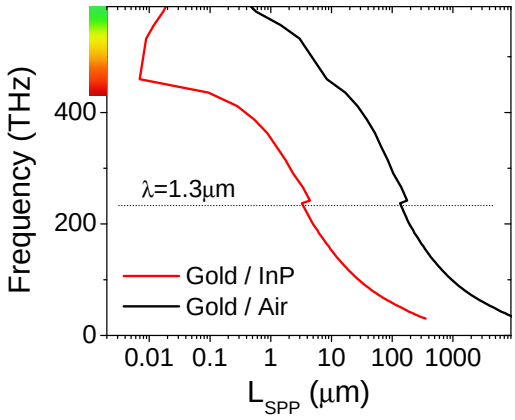

Figure 1.12: SPP propagation length for a gold/air (black line) and a gold/InP (red line) interface. An horizontal dotted line indicates the frequency corresponding to the wavelength 1.3 μm.

In Tab. 1.2 we report the 4 typical plasmonic lengths for a few representative wavelengths. We distinguish two regimes comparing the penetration of the field in the field in the air z_{air} with the vacuum wavelength (λ_0). For wavelengths in the visible and in the near infrared (λ<2 μm) the penetration depth in the air is smaller than the vacuum wavelength $z_{air} < \lambda$, vice-versa for λ>2 μm. Therefore SPPs at telecom wavelengths appear to be a good candidate for plasmonic sub-wavelength circuitry. In order to confirm the appropriate choice of telecom wavelength we will in the next section present a quantitative tool to evaluate the SPP *quality* for applications.

λ_0	n_{gold}	λ_{SPP}	L_{sp}	z_{air}	z_{metal}	
600 nm	$0.240 + 2.90i$	564 nm	4 μm	131 nm	15.5 nm	$(z_{air} \vee \lambda)$
900 nm	$0.212 + 5.90i$	887 nm	67 μm	417 nm	12.0 nm	
1.3 μm	$0.403 + 8.25i$	1.29 μm	142 μm	849 nm	12.4 nm	
1.55μm	$0.560 + 11.50i$	1.54 μm	333 μm	1.42 μm	10.7 nm	
2 μm	$0.85 + 12.6i$	1.99 μm	374 μm	2.01 μm	12.6 nm	$(z_{air} \wedge \lambda)$
5 μm	$3.80 + 31.0i$	5.00 μm	3.21 mm	12.5 μm	12.8 nm	
7.5 μm	$7.66 + 44.1i$	7.50 μm	7.09 mm	27.1 μm	13.5 nm	
10 μm	$12.24 + 55.0i$	10.0 μm	11.91 mm	45.9 μm	14.5 nm	

Table 1.2: The characteristic lengths for SPP at a gold/air interface, using $n_{air} = 1$ and the experimental values from Ordal [35] for the gold refractive index, n_{gold}. The horizontal discontinuity highlights two different regimes: for λ_0<2 μm we have a penetration of the field in the air smaller than the wavelength ($z_{air} < \lambda_0$), while for λ_0>2 μm the penetration of the field is larger ($z_{air} > \lambda_0$).

1.4.3 Figure of merit

SPPs are characterized by a correlation between confinement and attenuation, that sets the propagation length. Since a quantitative criterion to find the confinement-attenuation trade-off is needed, we introduce a function called *figure of merit*.

The figure of merit must have a simple and intuitive definition, and must be easy to compute from modal quantities. The definition is inspired from economics, particularly from the *benefit-to-cost* ratio formed by consumers when comparing similar products from different manufacturers. In the case of SPPs the benefit is the confinement, and the cost is the attenuation. The figure of merit must diverge ($\longrightarrow \infty$) as the attenuation vanishes and, according to the definition, lossless waveguides are *infinitely meritorious*. In order to simplify calculations we will consider a figure of merit useful for a 1D waveguide. This specific restriction does not exclude the 2D waveguides analyzed in this manuscript, since their width is always larger than the operating wavelength. Effects on the mode losses and operating frequency are rather expected as the waveguide width becomes comparable with the wavelength. In reference [38] Berini discusses the plasmonic figures of merit for

waveguides in 1D, 2D and 3D.

In a 1D structure the field penetration depth in the dielectric medium gauges the confinement, while $Im[\beta]$ describes the attenuation. The quantity,

$$M_1 = \frac{1}{\delta_i Im[\beta]}, \tag{1.46}$$

is dimension-less and obeys to the *benefit-to-cost* requirement: it increases when the penetration depth and the propagation losses decrease. Before developing Eq. 1.46 we recall that $\varepsilon = \varepsilon_R - i\varepsilon_I$ is the metal dielectric function (see section 1.3), and ε_2 is the dielectric function of the dielectric medium. Considering the penetration depth in the dielectric ($\delta_i = \delta_d$), in the limit of low-losses ($Im[\beta] < Re[\beta]$, $\varepsilon_I < \varepsilon_R$) and far from the surface plasmon resonance ($\varepsilon_2 < |\varepsilon_1|$), Eq. 1.46 can be written,

$$M_1 = \frac{\sqrt{\beta^2 - k_0^2 n_2^2}}{Im[\beta]} = \frac{\sqrt{Re[n_{eff}]^2 - n_2^2}}{Im[n_{eff}]} \tag{1.47}$$

The numerator of 1.47 represents ($\approx$) the distance, at a given frequency, between the SPP dispersion relation and the light line in the dielectric material. This wavevector mismatch qualitatively gauges the confinement of the surface mode. It vanishes at low frequencies and it is maximal at ω_{sp}. Using the following approximation to Eq. 1.19 [19][3]:

$$Re[n_{eff}] = \frac{Re[\beta]}{k_0} \cong \left(\frac{\varepsilon_R \varepsilon_2}{\varepsilon_R - \varepsilon_2}\right)^{1/2} \tag{1.48}$$

$$Im[n_{eff}] = \frac{Im[\beta]}{k_0} = \frac{\varepsilon_I}{2\varepsilon_R^2}\left(\frac{\varepsilon_R \varepsilon_2}{\varepsilon_R - \varepsilon_2}\right)^{3/2} \tag{1.49}$$

Substituting the above in Eq. 1.47 yields:

$$M_1 \cong \frac{2}{\sqrt{\varepsilon_2}} \frac{\sqrt{\varepsilon_R}}{\varepsilon_I} (\varepsilon_R - \varepsilon_2) \tag{1.50}$$

that for $\varepsilon_R > \varepsilon_I$ can be reduced to:

$$M_1 \approx \frac{2}{\sqrt{\varepsilon_2}} \frac{\varepsilon_R^{3/2}}{\varepsilon_I} \tag{1.51}$$

Assuming the Drude model for the dielectric function of the metal expressed in Eq. 1.38 and Eq. 1.39, in the limit of frequencies lower than

the plasma frequency ($\omega \ll \omega_p$) but larger than the characteristic collision frequency ($\omega \gg \gamma$) we obtain,

$$M_1 \approx \frac{2}{\sqrt{\varepsilon_2}}\omega_p\tau. \tag{1.52}$$

From Eq. 1.52 M_1 does not depend on the wavelength of operation in the Drude region, This implies that any increase in confinement, measured as the inverse mode size ($1/\delta_d$) is perfectly balanced by an increase in attenuation as λ_0 decreases. M_1 increases as ε_2 decreases, implying that the confinement ($1/\delta_d$) decreases less rapidly than the attenuation. In summary, maximizing M_1 means choosing a metal which maximizes the product $\omega_p\tau$.

In Fig. 1.13 the figure of merit M_1 is plotted using Eq. 1.51 in the specific case of a gold/air interface and a gold/InP interface.

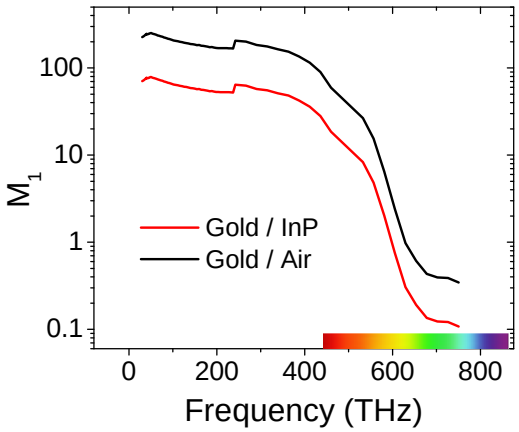

Figure 1.13: Figure of merit M_1 as function of the frequency. M_1 is roughly constant in the NIR and decreases dramatically in the visible.

The figure of merit is roughly constant for frequencies in the infrared, included telecom frequencies, but strongly decreases for frequencies in the visible. SPPs in the visible show a very strong confinement in the vertical direction, but this confinement increases more slowly than the attenuation in the propagation direction. Thus, SPP in the visible range are not suitable for circuitry applications.

1.4.4 Toward a lossless plasmonics

We highlighted before that silver and gold are currently the best metals for plasmonic applications, because of their larger time τ, which is directly proportional to the figure of merit (Eq. 1.52). However, both those metals are not compatible with present semiconductor technology, restraining applications. Efforts are hence dedicated to develop alternative plasmonic materials with improved optical properties, easier fabrication and integration capabilities.

Because plasmonic losses partly arise from large electron densities, an overall approach would be either to reduce the electron density in metals or to increase it in semiconductors [39]. It is possible to reduce the carrier concentration in metals, for instance, by mixing them with nonmetals and giving rise to intermetallics (silicides, germanides, borides, nitrides, oxides, and metallic alloys). A recent proposal is titanium nitride, which can provide performances comparable to gold [40].

Even if the perfect material for plasmonics remains elusive, theoretical studies suggest that advances in nanoassembly may permit the development of "lossless" metals. Indeed it was identified that the transition to the lossless regime occurs when the interatomic distances in the lattice exceed certain values, typically a factor of two larger than those occurring in nature [41].

1.5 Conclusions

This chapter is dedicated to an introduction to SPPs.

We solve the Maxwell equations at an interface and we discuss then the existence of a guided mode. A SPP exists only at the interface between a dielectric and a metal. The SPP dispersion relation is inferred, showing the field distribution. Since the dispersion relation strongly depends on the metal index we discuss in details the electromagnetic response of metals comparing the Drude model and the experimental results from the literature. After examining the SPPs properties and the energy confinement, a figure of merit is introduced to quantitatively show the advantages of SPPs in the telecom wavelength range over the mid-IR wavelengths range. At telecom frequencies losses dramatically increase, but SPPs exhibit their peculiar property: a sub-wavelength confinement.

Along this thesis we will develop strategies for a loss compensation in order to benefit of the confinement properties.

Chapter 2

Generation of SPPs

Surface plasmon polaritons propagating at the interface between a conductor and a dielectric are two-dimensional electromagnetic waves. In analogy with photons, which are light quanta, SPPs can be considered as quanta of surface modes. An energy quantum of $h\omega$ must be provided, to excite a SPP mode at the frequency ω. However, the SPP wavevector β is larger than the wavevector k_0 of a free photon propagating in the dielectric. Hence, a direct excitation is not possible. Momentum matching must be engineered, or alternatively, end-fire coupling techniques can be employed. These latter ones rely on spatial mode-matching rather than momentum-matching.

2.1 Conversion of electrons to SPP

SPPs were originally experimentally observed in electron energy loss spectra [42]. Beside the expected 3D plasmon absorption signal peak at the energy $h\omega_p$, an additional peak at a lower energy ($h\omega_{sp}$) was also observed. This peak was shifting in energy following the surface oxidation, confirming its surface character. As a matter of fact the oxide at the surface modifies the effective dielectric constant seen by the surface plasmon and consequently the resonance frequency (see Eq. 1.41).

The generation of SPP by electronic excitation has also been demonstrated by focusing an electron beam in order to create a highly localized source down to 5 nm of diameter [43]. The SPPs were then detected by cathodoluminescence spectroscopy or by the use of gratings [44]. Recently, thanks to the use of a scanning tunneling microscope (STM), it has been pos-

sible to generate SPPs with a spatial resolution smaller than one nanometer. Their propagation was confirmed by leakage radiation microscopy [45].

It was also recently demonstrated the possibility to excite SPPs on a gold nanowire with low energy tunneling electrons [46]. This method only requires electrodes, which can be easly integrated in a planar geometry.

However, using the electron diffraction it is only possible to excite SPP with zero group velocity, allowing to only explore a small range of frequencies close to ω_{sp}.

2.2 Conversion of photons to SPPs

An alternative strategy to excite a SPP is the conversion of photons. This conversion is possible and it allows one to choose the excitation frequency of the SPP.

The general problem is how to couple an electromagnetic wave, guided or propagating in free-space, to a SPP mode. Let's first consider the simplest case of a wave propagating in free-space and impinging on a surface at an angle θ (see Fig.2.1).

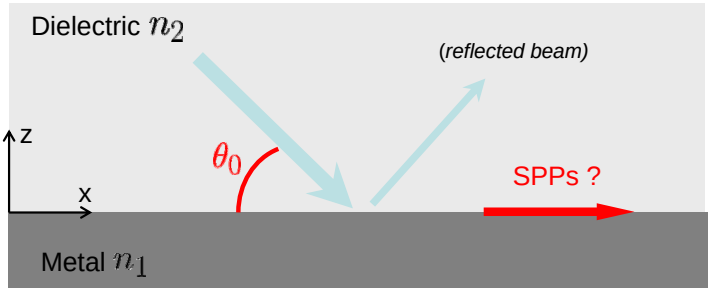

Figure 2.1: Excitation of a SPP by a plane wave.

The impinging plane wave exhibits a phase given by $e^{in_2k_0(x\cos\theta - y\sin\theta) - i\omega_i t}$, where ω_i is the impinging frequency, while the SPP phase is given by $e^{\beta x - i\omega_{sp}t}$. The continuity conditions at z=0 have to be verified for every t and every x, imposing the same dependence in t and x for all the waves in the system. It follows that $\omega_i = \omega_{sp}$ (energy conservation) and that the wavevectors

projection along $\hat{x}$ must be the same:

$$n_2 k_0 \cos\theta = \beta \Longrightarrow n_2 \cos\theta = n_{eff} = n_2 \sqrt{\frac{\varepsilon_1}{\varepsilon_1 + \varepsilon_2}}. \tag{2.1}$$

We know from section 1.2.1 that the confinement of the SPP imposes $n_{eff} > n_2$. The condition of Eq.2.1 is never satisfied. The phase mismatch corresponds, at a given frequency, to the distance between the SPP dispersion relation curve and the light line dispersion in the medium 2, and can be graphically observed (red arrow) in Fig.2.2.

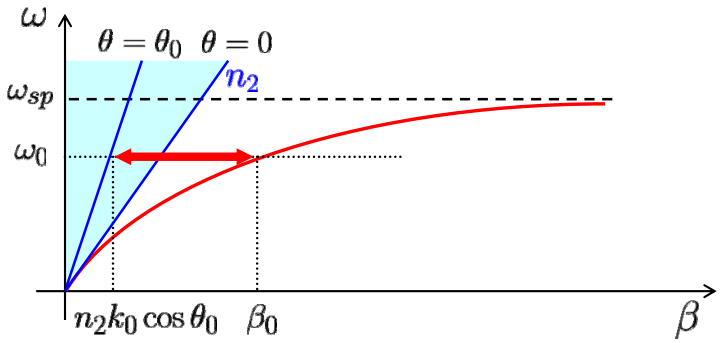

Figure 2.2: Excitation of a SPP by a plane wave. The light cone of medium 2 is colored in light blue. The SPP dispersion relation is at the right of the light cone. It is not possible to directly excite a SPP mode by the use of a free-space propagating beam: the momentum mismatch represented with the red arrow is present for every $\theta > 0$.

2.3 Classic techniques

2.3.1 Prism coupling

It is impossible to excite a SPP at the interface metal/dielectric by the use of a light beam coming from the same dielectric. However, if the light beam is coming from a dielectric medium with higher index ($n_3 > n_2$), the coupling is possible for an angle θ_0 which satisfies $n_3 \cos\theta = n_{eff}$, as shown in Fig.2.3.

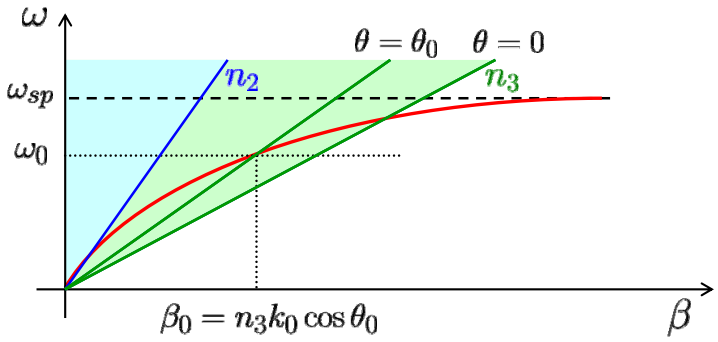

Figure 2.3: Excitation of a SPP by a plane wave coming from a third dielectric medium of higher refractive index than the dielectric at the interface with the metal. The light cone of the higher index material, n_3, is depicted in green and includes the light cone of the lower index, n_2, the same present in Fig. 2.2. The coupling with the SPP at frequency ω_0 is possible only for a precise angle θ.

The polarization of the impinging beam has to be taken into account too because the SPPs are TM polarized. Only the TM component of the wave can excite the SPP.

Two configurations based on prism coupling are shown in Fig.2.4, proposed in 1968 (a) by Kretshmann [47] and (b) by Otto [48]. In the first case (a) the light propagates into the prism and the metallic film has to be thin enough to allow the light to couple with the SPP at the interface. In the second case (b) the prism must be sufficiently close to the metal surface to allow the evanescent wave on the prism surface to couple with the SPP mode (photon tunneling).

The experimental confirmation of the coupling with the SPP comes from the attenuation of the reflected wave. This attenuation can be observed varying the angle of a monochromatic beam (coupling at $\theta = \theta_0$) or varying the frequency of the beam for a given angle (coupling at $\omega = \omega_0$).

The Kretschmann arrangement can be used for sensing applications in the visible providing a high sensitivity that is hardly achievable with other optical techniques [49]. This approach is used in commercial sensor used in biology and medicine to detect interactions in real time [8]. Recently it has been extended to the mid-infrared frequency range for gas sensing,

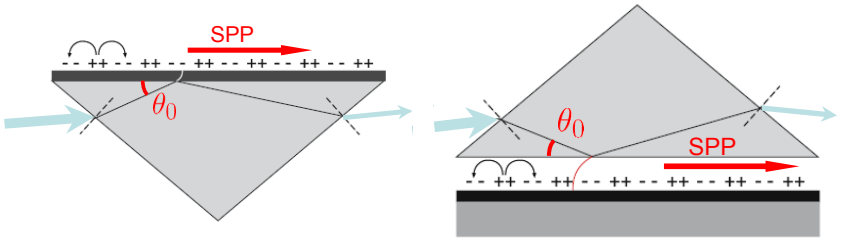

(a) (b)

Figure 2.4: Prism coupling exploiting the total internal reflection in the configuration of Kretschmann (a) and Otto (b).

demonstrating a five time higher sensitivity for CO_2 and N_2 mixtures [50].

2.3.2 Grating coupling

Free-space propagating light (plane waves) can be coupled into the SPP mode *via* a grating, as shown in Fig. 2.5. A shallow grating of grooves or holes with lattice constant a can provide the missing momentum, because the diffracted light at the order ν has a wavevector along the direction $\hat{x}$ given by:

$$k_{x,\nu} = n_2 k_0 \cos\theta + \nu \frac{2\pi}{a} \tag{2.2}$$

The order 0 corresponds to direct reflection. At first order, the wavevector must satisfy the following relation:

$$\beta = n_2 k_0 \cos\theta + \frac{2\pi}{a} \tag{2.3}$$

If the illumination is normal to the surface ($\cos\theta = 0$), the grating period can be chosen to excite the desired wavevector. As for the prism coupling, a TM polarization is needed.

2.3.3 Diffraction coupling

Light diffraction generates evanescent waves with large wavevectors, which can be used to couple with SPP modes. The crucial point is that a plane wave

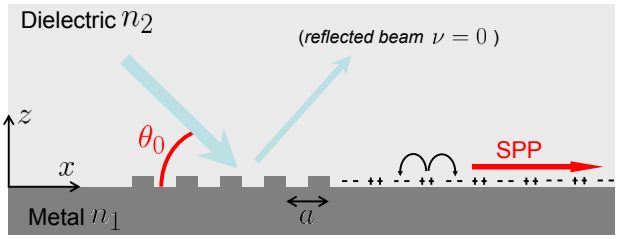

Figure 2.5: Grating coupling

impinging on a sub-wavelength hole generates radiating waves (far-field) and also evanescent waves (near-field).

After the Helmholtz equation the components k_x, k_y and k_z of the wavevector verify the relation $k_x^2 + k_y^2 + k_z^2 = n^2 k_0^2$, where n is the refractive index of the considered dielectric medium. When all the components are real the wave is propagating in the medium. When one of the components has an imaginary part the wave is evanescent or confined. The latter case corresponds to SPPs which are confined in two directions and propagate along the third one. In the case of evanescent or confined wave the real part of the wavevector β is larger than the wavevector of light in the dielectric medium: $\beta > nk_0$. A judicious choice of polarization and dimension of the sub-wavelength hole is possible to couple light to SPP by the use of diffraction. Figure 2.6 shows the schematic of a metallic film with a hole of width $a \approx \lambda_0/n$ illuminated perpendicularly. If the film is not too thick SPP can be excited also on the opposite side of the film.

This principle is used for local SPP excitation through a tip with a sub-wavelength aperture, [12] as shown in Fig.2.7. The technique is based on a tapered optical fiber with an aperture $a < \lambda_0$. Exploiting the piezoelectric stages of scanning microscopy systems, it is possible to select the excitation point with a nanometric precision. The same tapered fiber can also be used for SPP detection exploiting the reverse mechanism. In this case the confined SPP field is scattered into radiating modes that are collected along the fiber. The Near-field Scanning Optical Microscope (NSOM) described in section C.3 is based on this principle.

This configuration was also adopted in the well-known experience of Ebbesen et. al on extraordinary light transmission mediated by SPPs [51]. using SPP to demonstrate the extraordinary light transmission. In 1998 they re-

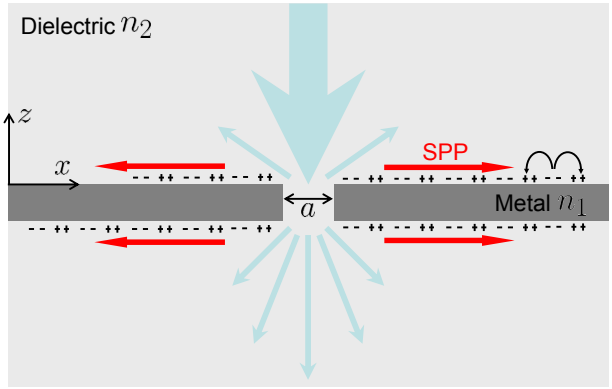

Figure 2.6: Diffraction coupling with a sub-wavelength hole.

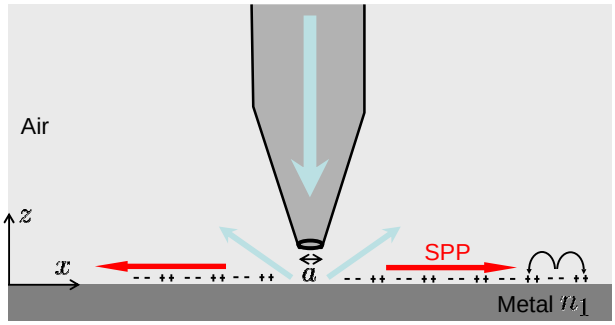

Figure 2.7: Diffraction coupling with a tapered fiber.

port a larger transmission of light through sub-wavelength holes of a metallic film, thanks to the SPP propagation on the metal surface.

2.4 Electrical generation of SPPs

Several experiences have shown in the last decade the increased ability in SPP manipulation. Nowadays SPPs are successfully used in sensing applications and, in the near future, they might be used for optical interconnections. [52, 53]. Plasmonics offers the possibility to squeeze optical systems into sizes not available otherwise, with the advantage of high bandwidths typical of optics. An optical circuitry would include integrated SPP generators, amplifiers and detectors.

To date, SPPs are mainly generated with an external coupling. This strategy requires bulky equipment and an alignment procedure on a sub-wavelength aperture, on a prism or on a grating. While these generation techniques certainly suit research applications, an electrically pumped SPP generator would represent an important building-block for further developments.

In order to achieve this goal two different functions must be engineered. The first one is the generation of photons, which can be provided, for instance, by a semiconductor laser with, for instance, a Fabry-Perot ridge resonator. The laser ridge advantageously provides a waveguided mode and also yields high optical power. The second function is light coupling into the plasmonic waveguide. Hence, the complete device design must allow to couple a dielectric waveguide (based on index contrast) into a plasmonic waveguide. Figure 2.8a illustrates schematically a generic integrated coupling. In particular in a planar geometry, unavoidable for the classical semiconductor top-down fabrication, a transverse magnetic (TM) polarized LED or laser source is needed. The laser source must be chosen carefully because this requirement is not common. Semiconductor lasers based on interband transitions cover a spectrum from 0.4 to 3.3 μm (including telecom wavelengths, 1.310 μm – 1.550 μm). They technically allow both polarizations, but the TE polarization is the most common. An interband laser emitting TM polarized light requires a special conception as detailed in the next chapter (see section. 3.1.3). On the other hand, lasers based on intersubband transitions naturally emit TM polarized light as a consequence of the selection rules. Quantum cascade lasers (QCL), achieved for the first time in 1994 [54], cover the mid-infrared (mid-IR, 3 - 24 μm) [55][56] and the terahertz (THz, 60 - 250μm) spectral ranges [57].

We are now going to present the two techniques represented in Fig. 2.8 (b) and (c). In both cases the goal is to obtain a *monolithic* structure.

The first one (see Fig. 2.8 b) is termed integrated grating coupling and consists in a partial diffraction of the laser mode by the use of a grating. By playing on the grating period it is possible to match the wavevector of the guided laser mode and of the SPP.

The second technique (see Fig. 2.8 c) is termed end-fire coupling and consists in positioning the two waveguides one in front of the other. The end-fire configuration is generally used to couple different samples, made of

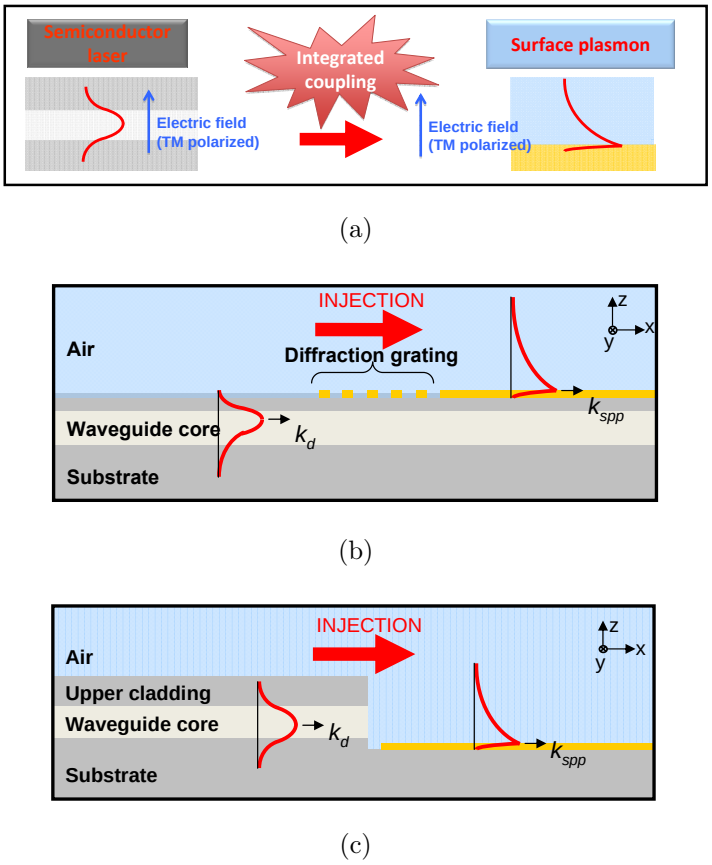

Figure 2.8: (a) General lateral scheme of an integrated coupling between a laser source and a SPP guide. Specific cases are shown in (b), coupling by grating, and in (c) end-fire coupling.

different materials and different waveguide sizes. In our case though, the coupling is on the same substrate. This appears particularly feasible thanks to the simple realization of a gold/dielectric SPP waveguide, achievable with only a metal deposition (metal/air waveguide).

In the next sections we present the results of the integrated grating and end-fire couplings obtained in the mid-infrared at $\lambda = 7.5$ μm. The devices employ a QC laser integrated on the chip. These results inspired the devices operating at telecom wavelengths $\lambda = 1.3$ μm, which we will present further in the thesis. The concept demonstration in the mid-IR, where the SPPs exhibit lower losses and all the laser dimensions are larger, encouraged the

transfert toward telecom devices. We will describe here the experiences in the mid-infrared through the main aspects: design, fabrication and experimental measurements. However, the detailed discussion of the integrated grating and the end-fire geometries will be developped in section 4.1 and 4.2, at telecom wavelengths.

2.5 Integrated device in the mid-infrared

The integrated devices presented in the following two sections are based on a QC structure. QCLs exploit the inter-subband transitions in semiconductor heterostructures. The emitted wavelength is not determined by the semiconductor gap, as for interband lasers, but by a judicious quantum engineering of the energy levels. Thanks to the several semiconductors layers forming the heterostructure, the electrons are spatially confined in the layer planes and their energy is quantized into discrete levels of the quantum well. Playing on the well thickness it is possible to tune the emission frequency of the laser. Since 1994 the QCL performance continued to improve. The first laser operating at room temperature in continuous wave (CW) was demonstrated in 2002 [58]. The emitted wavelength was around 9 μm, and at 298 K the output power between 10 and 20 mW. Nowadays QCL devices can emit more than 100 mW in continuous wave, at room temperature [59]. The majority of these QCLs are built with layers of InGaAs/AlInAs on InP.

The structure chosen for the mid infrared devices lases at $\lambda = 7.5$ μm. To implement the grating coupling configuration a plasmonic waveguide is needed, with the metal extremely close to the active region. Lasing on a surface plasmon mode, in pulsed regime and at room temperature, was demonstrated by our group in 2006 [60]. Successively it was demonstrated the possibility to pattern the top metal contact to obtain single mode operation [61].

2.5.1 Grating coupling

Periodically patterning the top metallic contact of the mid-IR QCL allows to couple the electromagnetic wave propagating in the laser waveguide with that of the metal-air interface [62]. The SPP at the top air/metal interface profits from the optical gain experienced on the other semiconductor side

[63]. We are then able to launch them in counter-propagating directions into a passive plasmonic waveguide (a metallic strip). Importantly, for efficient injection of SPPs into the passive section, the SPP wavevectors must be matched. This is the role of the integrated grating couplers, as schematized in Fig. 2.9. The device includes the three basic components required for a fully integrated plasmonic component: an electrical generator of SPPs, a coupler, and a passive metallic waveguide.

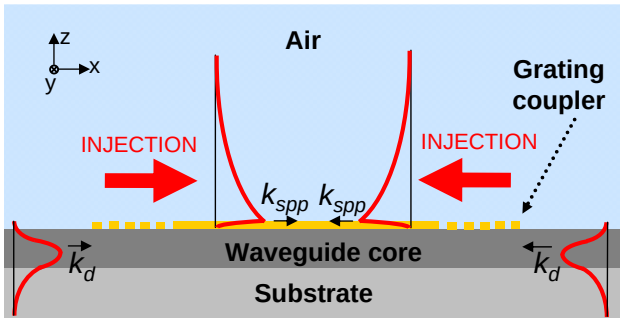

Figure 2.9: Schematic of the counter-propagation design achieved with the grating coupling at $\lambda = 7.5$ μm.

The results of a 2D numerical simulation of a longitudinal cross section of the device is shown in Fig. 2.10. The predicted EM field in the air, above the passive plasmonic waveguide, is a complex pattern given by the superposition of the desired propagating SPPs and also quasi-cylindrical waves (quasi-CW) [64]. The quasi-CWs are propagating waves, but bound to the metallic surface. These waves are unavoidable but do not affect the SPPs measurement and possible applications.

The devices were fabricated into 22-μm-wide, 4-μm-deep mesa ridges, whose top, gold metallic surface is patterned *via* electron-beam lithography followed by lift-off. The electron-beam lithography defines the passive plasmonic waveguide, the two couplers and the top contacts of the laser cavities. The active parts of the device are the two 1^{st} order distributed feedback (DFB) laser sections, which make use of an air/metal top grating to achieve distributed feedback, as described in [63]. Figure 2.11 (a) clearly shows the three different patterns obtained by the electron-beam lithography. Figure 2.11 (b) and (c) are SEM close-up of respectively, a coupler and a cleaved facet of a finished device.

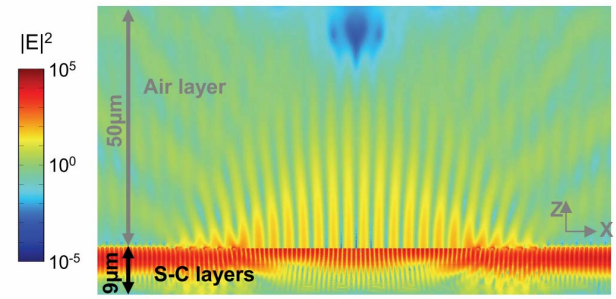

Figure 2.10: 2D numerical simulation performed within a finite-element approach. The color plot shows the electric feld squared modulus (arbitrary units) in logarithmic scale.

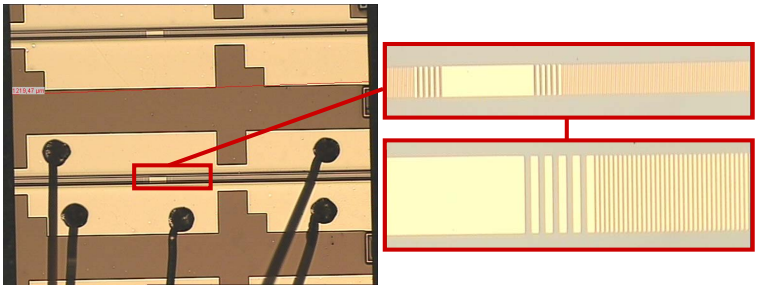

(a)

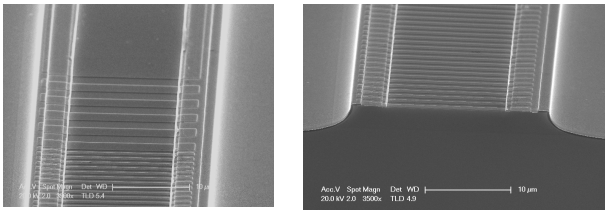

(b) (c)

Figure 2.11: (a) Optical microscope image of the final bonded device. The plasmonic waveguide, the coupling gratings and the metal patterning of the DFB are clearly visible in the insets (images taken after the first lithographic step). SEM image of (b) the grating coupler and (c) of the device facet.

Fig. 2.12 shows the measured laser output collected from one of the two cleaved facets of a typical device as a function of the injected current at room

temperature (RT, 300 K). Lasing is obtained at a threshold current density of 5,5 kA/cm^2. The emission spectrum (see inset in Fig. 2.12) exhibits a single mode emission at $\lambda = 7.58$ μm.

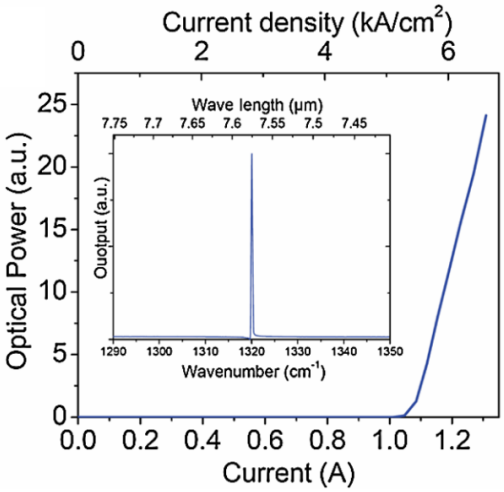

Figure 2.12: Light-current characteristics of a typical device, at RT (300 K). Inset: Typical emission spectrum at RT, at an injection current 50% higher than I_{th}. The measurements have been performed in pulsed mode (50 ns pulses, 84 kHz), using a Fourier transform spectrometer (FTIR)

The electromagnetic near-field distribution of the device was characterized on various regions of the structured metal top surface. All the near-field maps are obtained using a home-built mid-infrared a-NSOM, built by the group of Y. De Wilde [65] (See details in appendix C.1). The images are collected by demodulating the optical signal at the second harmonic of the atomic force microscope (AFM) tip oscillation frequency. In order to unequivocally demonstrate the SPPs generation two devices were measured, one without (reference device, left panels), and with (SPP device, right panels) grating couplers. Panels (a) and (b) of Fig. 2.13 show their schematic cross sections. Panels (c) and (d) show AFM images of their top surfaces. The AFM images cover the passive sections, the 60-μm-long metallic strip and also portions of the gratings, which are clearly visible at the left and right edges of the scans. The a-NSOM signal i.e., the EM near-field is acquired simultaneously with the AFM images with the devices in operation. The results (see panels (e) and (f)) show that while an a-NSOM signal is present on

the grating surfaces in both cases, only the SPP devices present interference fringes which can be clearly distinguished on the metallic strip. The fringes stem from counter-propagating SPP excitations which travel on the surface of the metallic strip, with opposite wave vectors β and $-\beta$. Their presence proves that SPPs are generated and launched into the metallic waveguide. Furthermore, their absence in the reference device without couplers confirms that no light tunneling is possible through the top metallization. Finite element simulations in panel (g) and (h) confirm the experimental results highlighting the extremely different behavior of the two devices.

An additional important information is the wavelength λ_{SPP} of the plasmonic wave propagating on the passive metallic strip. Its value is experimentally measured by taking a 1D section of the a-NSOM and AFM signals in the center of the device. Figure 2.14 reports such a section, in correspondence of the white dashed line in Fig. 2.13 (f). The topographic signal (green dotted curve) permits us to correlate the a-NSOM one (black curve) with the surface metallization. The experimental data are in very good agreement with the simulations obtained within a finite element approach (dark gray curve), which confirm that the couplers are crucial in order to inject the SPP wave into the passive waveguide. A sinusoidal fit of the near-field onto the metallic strip yields a period of 3.89 μm, which corresponds to $\lambda_{SPP} = 7.78$ μm. This value is in good agreement with the wavelength measured in the far-field (Fig. 2.12).

The measurement in Fig 2.15 shows the topography signal (a) and the corresponding near-field signal (b) acquired simultaneously in correspondence of the DFB grating regions, while the device was operated above threshold. The presence of an (evanescent) electric field detected on top of the metallic fingers confirms that lasing is achieved on the grating mode mode with the field maximum under the metallic finger: the mode leaks through the grating on top of the device surface.

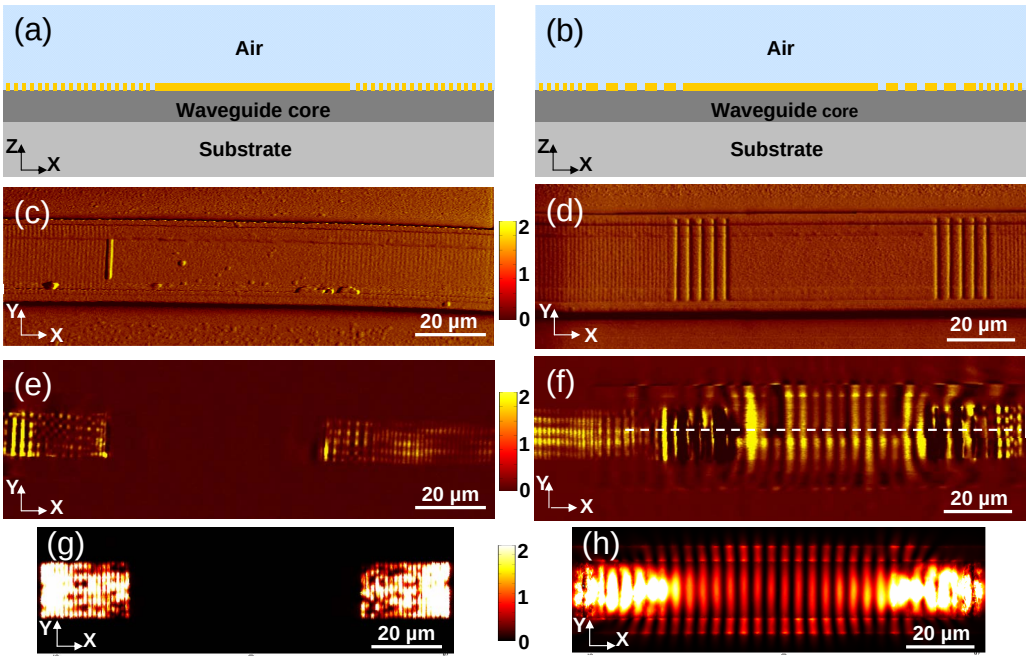

Figure 2.13: Comparison between a device without coupler (left column), and with coupler (right column). (a), (b) Schematic structure of the devices. Without the grating coupler [panel (a)] the wave vector mismatch prevents efficient injection of SPPs into the passive central strip. The grating coupler [panel (b)] adapts the wave vectors, and it allows for efficient SPP launching. (c), (d) AFM images of the center of the devices. (e), (f) a-NSOM images. When the coupler is present, interference fringes are clearly present onto the passive region (the metallic strip) in the EM near-field. When the coupler is missing, SPPs are clearly not injected into the passive section. (g), (h) The finite element simulations, showing a map of $|E^2|$, confirm the observed experimental results.

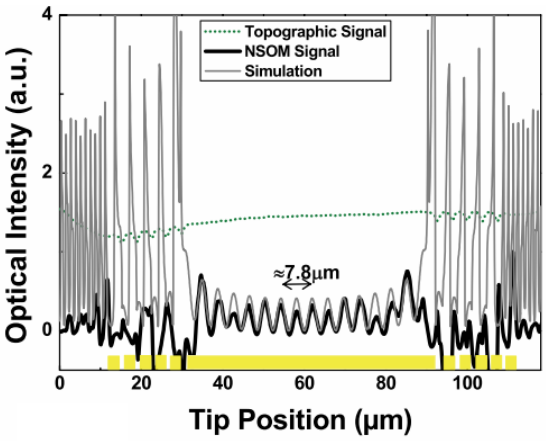

Figure 2.14: Intensity of the EM near-field (a-NSOM signal) at the device top surface. The measured data (black curve) correspond to a 1D cross-section taken in correspondence of the dashed white line in Fig. 2.12 (f). The numerical simulation (dark gray curve) is a 1D cross-section of Fig. 2.10 taken 100 nm above the metallic top-surface. The topographic signal (dotted green curve) allows one to correlate the EM near-field with the top metallization.

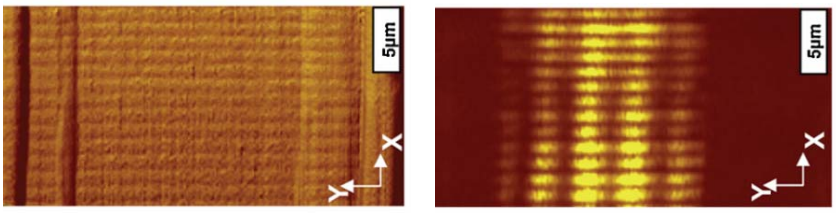

(a) (b)

Figure 2.15: (a) AFM topography of the 1st order DFB region. (b) a-NSOM image recorded simultaneously with the AFM image of panel (a). An evanescent electric field is clearly present on top of the metallic fingers which constitute the DFB grating.

2.5.2 End-fire coupling

In this section we present the results of the integrated end-fire coupling, which I obtained in the mid-infrared at $\lambda = 7.5$ μm [66]. The critical aspects of the device realization are the combination of the design and the fabrication, in order to obtain a good coupling.

The design aims at maximizing the coupling, playing on the position of the plasmonic waveguide with respect to the laser waveguide. The relative height h and relative distance d, (see schematic in Fig. 2.16) were chosen based on the results of numerical simulations and, at the same time, in comparability with the available fabrication techniques. The SEM image (Fig. 2.17) shows

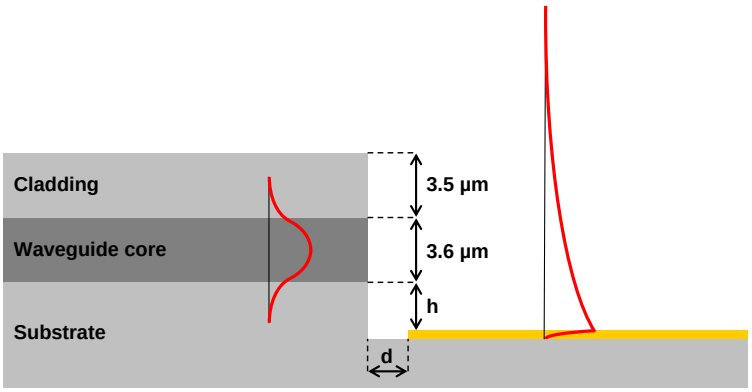

Figure 2.16: Schematic of the end-fire architecture at $\lambda = 7.5\mu$m. The parameters d and h must be chosen to optimize the coupling between the laser and the SPP modes.

the SEM images of the facets and an optical image of the whole device. Clearly the depth of the etching (h) must be sufficient to expose the active region, allowing the laser mode to be injected into the SPP waveguide. The active region contains 50 repetitions of a two-phonon-resonance design with nominal emission at $\lambda_0 = 7.5$ μm [67]. The 2.6-μm-thick active region, whose details are reported in [60], is sandwiched between two 0.5 μm-thick low-doped InGaAs cladding layers, thereby forming a 3.6-μm-thick waveguide core. The InP upper cladding is 3.5-μm-thick, entailing an etching depth of more than 6.5 μm ($h > 6.5$ μm). Standard laser ridges 22μm-wide, 1.5-mm-long, and 7μm-deep were defined using inductively coupled plasma (ICP)

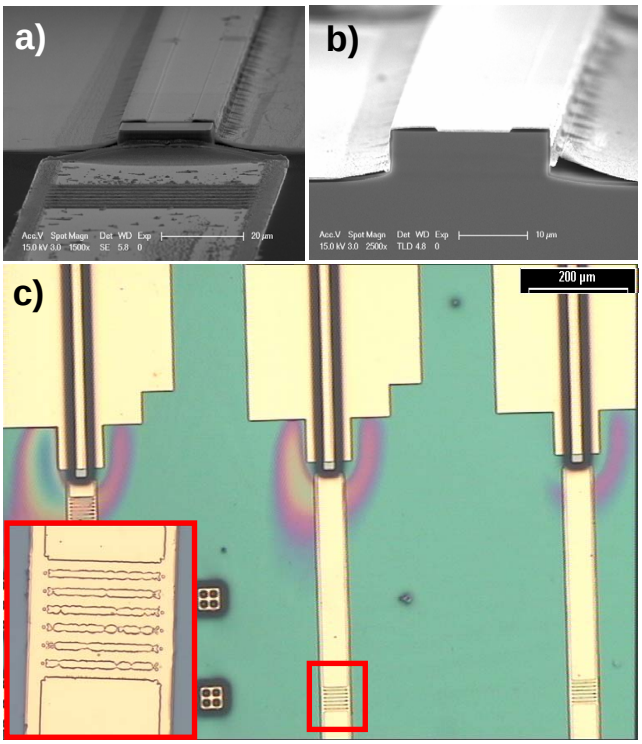

Figure 2.17: SEM images of (a) the facet in front of the plasmonic waveguide, obtained with the ICP etching, and (b) the cleaved facet.(c) Optical images of the completed device showing on the top part the laser cavity and on the bottom part the plasmonic waveguides. The inset highlights a diffraction grating used to probe the SPP presence.

etching [1]. The ICP etching is necessary to have a vertical facet in front of the plasmonic waveguide, hence optimizing the coupling. A wet etching would lead to scanted walls. However, the facet obtained with ICP is not comparable in reflectivity to the cleaved ones and the performances of the laser are affected. Figure 2.18 (a) shows the applied bias and the optical power as a function of the injected current for a 1.3-mm-long laser ridge at RT. The corresponding laser spectrum is shown in Fig. 2.18 (b). The laser threshold current density is J_{th}= 3.5 kA/cm^2. This value is almost twice as high as for a laser with two cleaved facets and of the same length. The

1. The ICP etching was performed in the LPN laboratory, in collaboration with the group of I. Sagnes.

threshold increase is possibly due to the reduced reflectivity of the dry-etched laser facets.

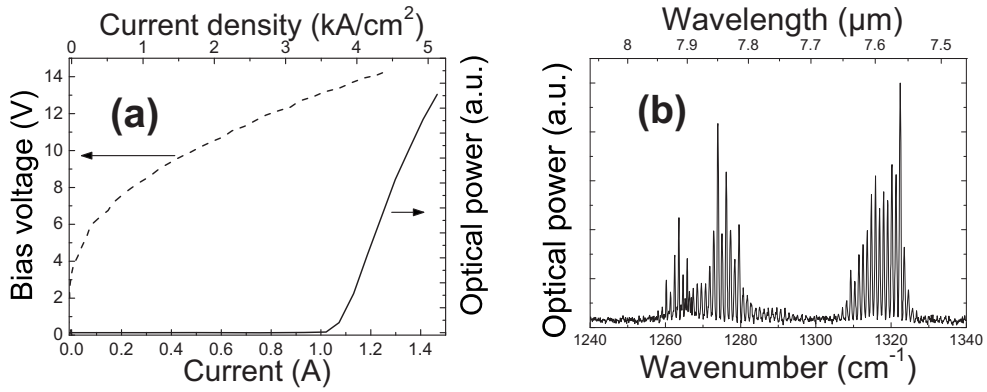

(a) (b)

Figure 2.18: (a) Current-voltage and light-current characteristics at RT (300 K) for a typical device. (b) Emission spectrum of the same device, acquired at 300 K just above the laser threshold. These measurements are performed under pulsed current injection (50 ns duration and 84 kHz repetition rate).

The demonstration of SPP generation is obtained via two different techniques, based on far-field and near-field imaging, respectively. Both techniques rely on the introduction of a local scatterer of the SPP wave.

The first technique exploits second-order gratings, positioned along the metallic SPP waveguide. The gratings vertically diffracts the SPP light, converting an evanescent wave into a radiating field. Each grating acts as a localized probe, of the SPP presence, permitting a detection in the far-field through a microbolometer camera. The SPP mode propagation is affected, but the grating only diffracts a fraction of the SPP wave.

Several gratings can be built on the same plasmonic waveguide to "detect" the SPP presence at different distances. We demonstrated a device with up to two gratings (see Fig. 2.17), at 500 μm and 1000 μm from the beginning of the plasmonic waveguide. The far-field is measured with an infrared camera, based on a matrix of bolometric detectors sensitive to the temperature variations induced by the radiation. Figure 2.19 (a) shows the optical system used to obtain the image. The camera is fixed; the position of the two germanium lenses can be adjusted to focus/zoom.

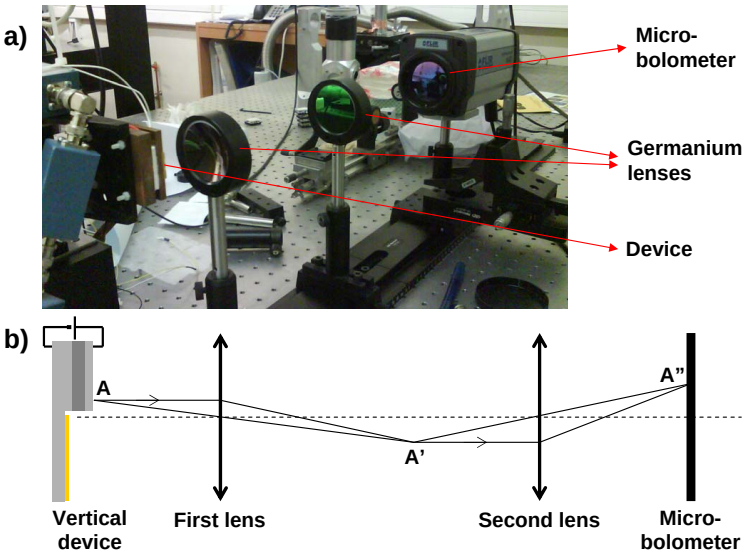

Figure 2.19: (a) Picture of the far-field set-up. (b) Schematic to illustrate the image formation on the μ-bolometer. A' is the image of A after the first lens and A" is the one formed thanks to the two lens combination.

The camera snapshot in Fig. 2.20 shows the far-field infra-red images with the relative optical image for 4 different devices. Each measurement presents an intense central spot which corresponds to light scattered at the laser facet. The smaller spots on the right correspond to light originating from SPPs that are diffracted by the metal gratings. The red solid line is a one-dimensional section of the infrared image (the gray scale of the pixels along the metal strip is represented). The absence of light diffraction at the grating locations in the reference device (Fig. 2.20d) proves that the electromagnetic energy is transferred to the localized probes *via* the metal waveguide only, and consequently *via* SPP waves. In Fig.2.20c we observe a difference in intensity between the first and the second grating. Since the plasmon should propagate without relevant losses along 1 mm the decay can be explained thanks to the losses due to the first grating and to the roughness of the SPP waveguide (the gold is evaporated on the surface bombarded by the ions of the ICP etching). A quantitative experimental estimate of the SPP attenuation coefficient can be obtained from the camera image and it yields α_{SPP} 5.5 cm^{-1}. This value is roughly one order of magnitude higher

than what is expected from a theoretical estimate of the SPP decay length at $\lambda = 7.5$ μm on a plain gold surface, which gives ≈ 2.6 cm.

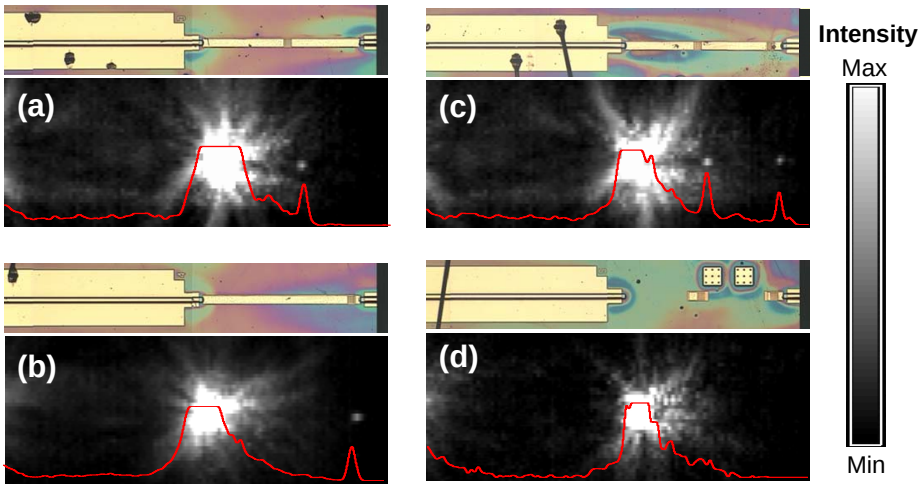

Figure 2.20: Infrared image and corresponding optical image for four devices operating in laser regime: (a) with the metallic waveguide and a grating at half way. (b) with the metallic waveguide and a grating at the end. (c) with the metallic waveguide and two gratings (d) without the metallic waveguide, but with two gratings. A section of the infra-red image passing through the laser facet and the gratings is shown in each image (red line). The infra-red images are taken at room temperature with a FLIR micro-bolometric camera.

We have also directly detected the EM field intensity at the device surface using the apertureless near- field scanning optical microscope (a-SNOM) able to operate in the mid-IR range of the EM spectrum (described in appendix C.3). Figure 2.21 shows (a) the atomic force microscopy (AFM) topography of a portion of the metal waveguide and (b) the intensity of the electromagnetic near-field when the device is in operation, respectively. A surface wave is clearly detected on the surface of the metallic strip, while no signal is present where the metallization is absent. The near-field signal stems from a SPP wave which is launched by the laser device into the passive waveguide and propagates along it. The direct observation of a SPP wave on the metallic surface complements and corroborates the detection obtained with far-field techniques.

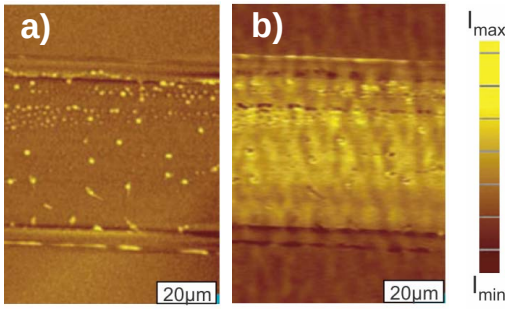

Figure 2.21: Experimental results of the a-SNOM: topography (AFM signal) and the near-field intensity signal corresponding to a zone of 100x100 μm^2.

2.6 Conclusions

The standard techniques for SPP generation are reported. We then introduce the concept of electrical generation of SPPs and we discuss the demonstration of two architectures in the mid-IR. This result validates our semiconductor approach that presents advantages for future applications, in term of compactness and integrated alignment. The results in the mid-IR are of particular relevance for the transfer toward shorter wavelengths, where the SPPs feature a sub-wavelength confinement. At the same time the losses dramatically increase.

The challenge is to find an analogous TM polarized laser source at telecom wavelengths, to compensate the larger metallic losses. The implementation of our approach for SPP generation at shorter wavelength can benefit of well developed technologies.

Chapter 3

Laser active region

This chapter is devoted to the conception and development of the semiconductor light source used for SPP generation at telecom wavelengths. To this scope we need a semiconductor laser source, which guarantees gain and a sufficient power for the SPP observation.

In the first part of this chapter we present the laser active region based on semiconductor tensile-strained quantum wells. The strain applied to the QWs not only improves the laser performance, but it also allows one to select the polarization of the emitted light. Semiconductor lasers for telecommunications typically operate in transverse polarization (TE). However, a transverse magnetic (TM) polarization can be obtained thanks to the strain. SPPs are transverse magnetic (TM) polarized, therefore strained QWs represent an excellent candidate as gain material for SPP amplification.

In the follow we characterize the laser source by assessing the effect of the metal proximity to the active region. We demonstrate a suitable *thin cladding* structure for plasmonic applications and we perform a detailed analysis of the laser waveguide losses. In order to estimate them, we performed passive measurements on two types of ridge structures with different cladding thickness. The results allowed us to fine tune the material indexes for the numerical simulations.

Finally, we show laser operation of the devices by electrical injection. We perform gain measurements – using the Hakki Paoli technique – in order to estimate a loss value also for the waveguides not measurable with passive techniques. These experimental results validate the reliability of our finite element simulations tool, which will be used in the further experiences.

3.1 Semiconductor lasers

Compared to other light sources, semiconductor lasers present advantages in terms of compactness, electrical pumping, directional emission and output power. Furthermore semiconductor lasers benefit of the well developed semiconductor device technology. The developments in semiconductor growth always led to improvements of the lasers performance, for instance in laser threshold [68].

The first semiconductor lasers were demonstrated in 1962 using homojunctions. They had a high threshold current density (e.g. 19000 A/cm^2) and operated at cryogenic temperature [69]. In 1969-1970 was built a laser based on the concept of the semiconductor heterojunction. The laser could operate at room temperature with a low threshold current density (1600 A/cm^2)[70]. The double-heterostructures diode lasers provide both carriers and optical confinements, which improve the efficiency of stimulated emission, and enable applications to optical communications. Heterostructures allow one to control crucial parameters in semiconductor crystals and devices, such as the bandgap width, the effective masses and mobilities of carriers [71]. Indeed it is by refining the concept of heterostructure that in the late 1970s quantum-well (QW) structures were proposed and experimentally achieved. The threshold current density was reduced to about 500 A/cm^2 [72]. The reduction of the confinement region for the electron-hole pairs to a tiny volume in the quantum well region improved the laser performance significantly. In the late 1980s strained quantum-well lasers were proposed to improve the laser performance [73]. Diode lasers using strained quantum wells reduced the threshold current density to 65 A/cm^2 at room temperature ($\lambda \approx 1$ μm) [74].

The threshold current density of semiconductor lasers has improved by approximately one order of magnitude per decade since their invention in 1962. The improvements also resulted from the development of novel ideas and technology such as liquid-phase epitaxy (LPE), molecular beam epitaxy (MBE) or metal organic chemical vapor deposition (MOCVD). In particular, the control of single atomic layers provided by the MBE allowed in the 1994 the demonstration of the first quantum cascade laser (QCL) [54]. The growth of QCLs is extremely delicate because it necessitates an heterostructure with several identical periods.

In order to understand the effect of strain in semiconductor diode lasers, we discuss first the case of a bulk semiconductor, introducing the QW structures in the following.

3.1.1 Bulk semiconductors

The expression of interband gain G as a function of the photon energy $\hbar\omega$ in a semiconductor crystal is as follows [75]:

$$g(\hbar\omega) = \frac{\pi e^2 \hbar}{c n_r m_0^2 \varepsilon_0 (\hbar\omega)} |p_{if}|^2 \rho_{cv}(\hbar\omega)[f^e(E^e) - (1 - f^h(E^h)] \tag{3.1}$$

where e is the electron charge, $\hbar$ is the reduced Plank constant ($\hbar = h/2\pi$), n_r is the refractive index of the crystal, c is the speed of light, m_0 is electron effective mass, ε_0 is the vacuum permittivity, $|p_{if}|$ is the transition matrix element and ρ_{cv} is the joint density of states (DOS) for an electron gas. E^e is the energy of the electrons respect to the conduction band energy minimum energy and f^e is the Fermi function for the electrons. If $f^e(E^e) = 0$ there are no electrons in the conduction band. Analogously E^h is the energy of the holes respect to the valence band energy maximum energy and and f^h is the Fermi function for the holes. If $f^h(E^h) = 0$ there are no holes in the valence band. If $f^e(E^e) = f^h(E^h) = 0$ the gain is negative, corresponding to losses. This is the case of a semiconductor in equilibrium. A positive value of gain appears when the following condition is satisfied:

$$f^e(E^e) > 1 - f^h(E^h), \tag{3.2}$$

which is called inversion. If in 3.2 the equality is satisfied, g is zero and the transparency regime is reached.

For bulk semiconductors ρ_{cv}^{3D} depends on the photon energy $\hbar\omega$ as follows [75]:

$$\rho_{cv}^{3D}(\hbar\omega) = \frac{\sqrt{2}}{\pi} \left(\frac{m_r}{\hbar^2}\right)^{3/2} \sqrt{\hbar\omega - E_g} \tag{3.3}$$

with E_g the bandgap energy, and m_r the reduced effective mass between the electron (m_c) and the hole (m_v) masses.

It can be shown that the requirements for optimum gain performance – minimal transparency current density and maximal differential gain – are

a small effective mass and a symmetric band structure with $m_c = m_v$ [76]. Bulk III-V semiconductors do not fulfill these optimum gain requirements. Furthermore, at long wavelengths the complex valence subband structure facilitates substantial non-radiative recombinations through Auger processes and intervalence band absorption [77]. There is room for improvement.

3.1.2 Quantum well structures

The laser gain can be improved by increasing the DOS, which depends on the system dimensionality. Compared to 3D systems, 2D systems exhibit a step-like DOS, useful to decrease the laser threshold. In semiconductors, quantum confinement can be obtained with QWs. By creating a well-shape in the potential profile the electron kinetic energy for motion normal to the direction of the interfaces (z-direction) becomes quantized into discrete energy levels. Every quantum number corresponds to one conduction band and three valence band levels, the light hole (lh), the heavy hole (hh) and the split-off (so) band. In Fig. 3.1 we represent the schematics of a quantum well and the reduced density of states (ρ_{cv}^{2D}), as a function of the energy, with a typical steplike behavior.

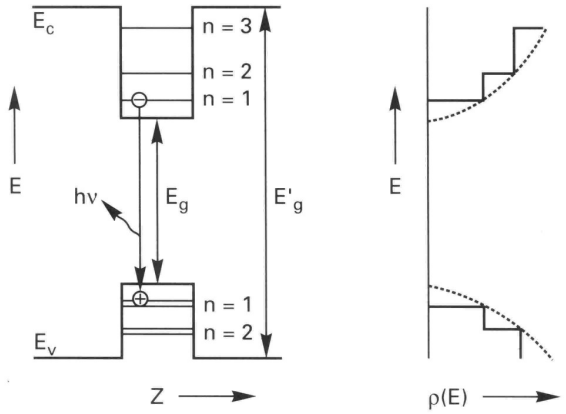

Figure 3.1: Energy scheme (left) and density of states (right) for a quantum well of e.g. InGaAsP embedded in InP. Due to the confinement, along z, the kinetic energy of carriers is quantized into discrete energy levels. The density of states for non-quantized carriers is shown by the dashed curves. The quantization modifies it into the solid step-like curves [76].

Due to the confinement in one direction (quantization direction) the DOS in a 2D system is modified as follows [75]:

$$\rho_{cv}^{2D}(\hbar\omega) = \frac{m_r}{\pi\hbar^2} \tag{3.4}$$

where in this case m_r is the e-h system reduced mass in the plane parallel to the quantization direction. The density of states of a 2D electron gas is independent of the carrier energy and it is proportional to the effective mass in the QW plane (x-y plane).The QW gain as a function of the carrier energy changes, hence the dependence of the gain on the current (g-current characteristic), is modified too (Fig. 3.2). For bulk active layers the spectral

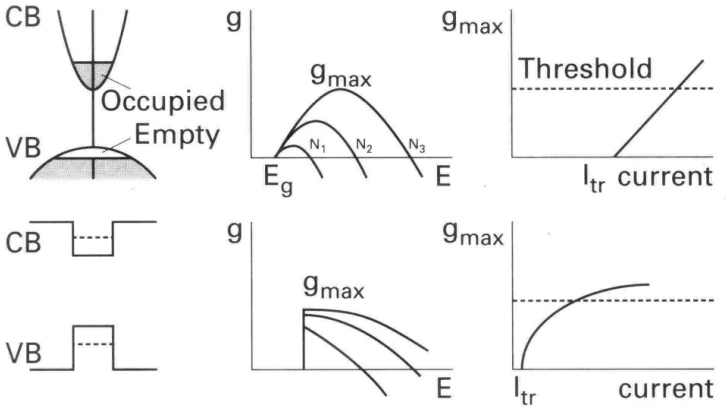

Figure 3.2: Schematics of band filling, gain formation under increased injection, and gain-current characteristics for semiconductor lasers with bulk (top) and QW (bottom) active layers (CB = conduction band, VB = valence band) [76].

gain bandwidth increases with carrier density and above transparency the peak gain is linearly proportional to the injection current. In contrast, the step-like density of states in QWs induces a steep onset of the gain at the effective bandgap energy. Positive gain appears for smaller values of the injection current compared to bulk active layers. At high injection currents, however, the gain saturates following a logarithmic gain-current relation [78]:

$$g = G_0 ln\left(\eta_i \frac{J}{J_0}\right) \tag{3.5}$$

where G_0 is a constant, η_i is the internal quantum efficiency and J_0 is the transparency current density. This empirical logarithmic gain-current density relation is a reasonable approximation. It is independent of recombination kinetics, and it leads to a *differential gain* which is inversely proportional to the current density:

$$\frac{\delta g}{\delta J} = \frac{G_0}{J} \tag{3.6}$$

3.1.3 Strained multi quantum wells

The application of strain allows one to engineer the electronic bands of the material. It has two main effects: (i) it lowers the in-plane valence band effective mass, hence increasing the symmetry between valence band and conduction bands. This largely enhances the AR performance. (ii) the strain can increase the splitting between the heavy-hole (HH) and light-hole (LH) subbands. This enables a polarization-selective gain: transverse electric (TE)-gain is favored in compressively strained structures and transverse magnetic (TM)-polarized gain in active layers with (a large enough) tensile strain.

The principle is schematically depicted in figure 3.3 for a bulk material. By applying a tensile strain the LH band energy increases. The transition between the conduction band and the LH valence band is favored and the majority of the emitted photons are TM polarized.

Tensile strained MQW structures for lasers emitting at telecom wavelengths (1.33 μm - 1.55 μm) are generally based on a quaternary alloy of III-V materials. They have been investigated theoretically and experimentally, with measurements of the differential gain and the external quantum efficiency [79]. Structures based on $In_{1-x}Ga_xAs_yP_{1-y}$ are more common. However, due to superior gain performance and reduced temperature sensitivity [80], our choice fell on a structure with 9 QWs based on $In_{1-x-y}Ga_xAl_yAs$. Although Aluminum is more difficult to handle, structures based on $In_{1-x-y}Ga_xAl_yAs$ exhibit other advantages [76]:

- It is a type 2 structure, spatially separating the electrons from the holes. The negative influence of hh-carriers on the lh band curvature at the band edge can be completely eliminated. The effective mass of the light holes decreases.

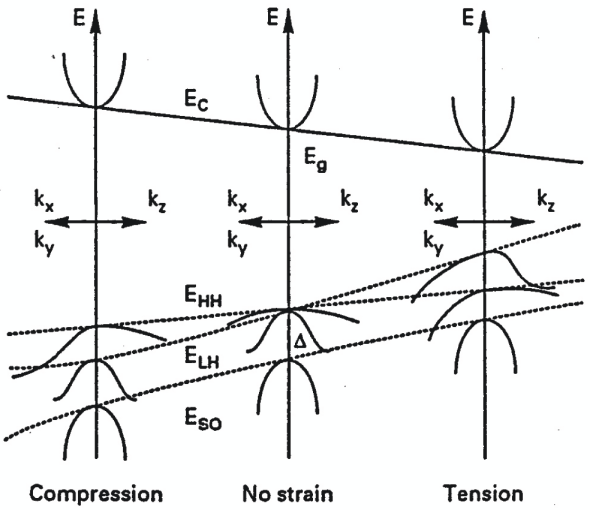

Figure 3.3: Schematic representation of the bulk band dispersion of a III-V semiconductor under compression, lattice matching, and tension [76].

– It offers a better control of the strain and the interfaces between wells and barriers are more abrupt.

3.2 Employed heterostructures

In this section we detail the heterostructures employed in this work. We always use the same AR to provide gain. However, the waveguide claddings differ in thickness, composition and doping. All the epitaxial growth have been performed by Alcatel-Thales III-V Lab, in collaboration with J. Decobert, F. Lelarge, J-L Gentner and G-H Duan.

3.2.1 Active region

Alcatel-Thales III-V Lab developed tensile strained $In_{1-x-y}Ga_xAl_yAs$ - InP MQW active structures, emitting at ≈ 1.3 μm [81]. The material has been grown by metal-organic vapor phase epitaxy (MOVPE). The active region consists of nine 10 nm-thick, undoped, -1.70% tensile strained QWs surrounded by ten 20 nm-thick, +0.69% compressive strained barriers. A lattice-matched InGaAsP layer of 15 nm serves as separate confinement het-

	Type	Composition	Strain	Thickness	Doping (cm^{-3})	
Clad.	spacer	InP		50 nm	n.i.d.	
	SCH-sup	GaInAsP		15 nm	n.i.d.	
AR	Barrier	AlGaInAs	0.69%	19.6 nm	n.i.d.	x 9
	Well	AlGaInAs	-1.70%	9.5 nm	n.i.d.	x 9
	Barrier	AlGaInAs	0.69%	19.6 nm	n.i.d.	
Sub.	Buffer	InP		750 nm	n=$1 \cdot 10^{18}$	
	Substrate	InP		$\approx$ 500 μm	n	

Table 3.1: The active region used for all the devices in the manuscript. It is a structure based on AlGaInAs MQWs with high tensile strain [81]. The AR thickness is $\approx$ 300 nm. The acronym *n.i.d.* stands for *not intentionally doped*.

erostructure (SCH) layer above the MQW active region (see Tab. 3.1). The total thickness of the AR is $\approx$ 300 nm, excluding the top InP spacer. The AR is grown on a n-doped substrate.

Preliminary verifications of the AR quality and wavelength emission were performed with luminescence measurements, reported in appendix A. The measurement performed by B. Habert in the *Institut d'Optique* show a good spatial homogeneity of the luminescence signal and a maximal peak at λ = 1300 nm.

3.2.2 Claddings

In a diode laser device the cladding accomplishes two functions: (i) it separates the top metal contact from the AR, providing at the same time an index contrast to confine the mode (ii) it acts as a charge reservoir for the p-n junction. Our goal here is to elucidate the effect of the proximity of a metallic layer/contact to the gain region. We use three structures with different cladding thicknesses:

- *Thick cladding* structure: total cladding thickness $\approx$ 2800 nm. Typical of standard lasers (see Tab. 3.2)
- *Thin cladding* structure: total cladding thickness $\approx$ 450 nm (see Tab. 3.3)
- *Ultra-thin cladding* structure: total cladding thickness $\approx$ 250 nm (see

Thick cladding	Thickness (nm)	p-doping (cm^{-3})
InGaAs	300	$3 \cdot 10^{19}$
InP	2000	$1.4 \cdot 10^{18}$
InP	450	$7 \cdot 10^{17}$
InP	50	n.i.d.
Active region		

Table 3.2: *Thick cladding* of total thickness 2850 nm (considering also the 50 nm thin layer of n.i.d InP grown on the AR top).

Thin cladding	Thickness (nm)	p-doping (cm^{-3})
InGaAs	15	$3 \cdot 10^{19}$
InGaAsP	80	$2 \cdot 10^{19}$
InP	295	$1.4 \cdot 10^{18}$
Active region		

Table 3.3: *Thin cladding* of total thickness $\approx$ 450 nm (considering also the 50 nm thin layer of n.i.d InP grown on the AR top).

Tab. 3.4)

We stress that a heavily p-doped InGaAs top layer is unavoidable for efficient electrical injection. Contrary to InP and InGaAsP, InGaAs is excellent for ohmic p contacts [82]. However, due to interband absorption at $\lambda = 1.3$ μm, it is also extremely absorbing. Hence, extremely thin InGaAs layers (15 nm) are used in the *thin* and *ultra-thin cladding* structures where the InGaAs is close to the AR. A second peculiarity in the thinner cladding structures is the presence of a highly-doped InGaAsP layer, necessary for electrical reasons. Thinning the cladding reduces the reservoir of p-carriers: a higher layer doping is thus necessary to maintain a sufficient total doping.

In the course of my work I developed other structures to further enhance the proximity of the metal to the AR. However, issues related to electrical injection arise. These attempts are briefly detailed in appendix E.

Ultra-thin cladding	Thickness (nm)	p-doping (cm^{-3})
InGaAs	15	$3 \cdot 10^{19}$
InGaAsP	80	$2 \cdot 10^{19}$
InP	100	$1.4 \cdot 10^{18}$
Active region		

Table 3.4: *Ultra thin cladding* of total thickness $\approx$ 250 nm (considering also the 50 nm thin layer of n.i.d InP grown on the AR top).

3.3 Characterization of the ridge resonators

This preliminary analysis lays the foundation for the realization of active plasmonic devices in the telecom frequency range, where the *thin* and the *ultra-thin cladding* structures are employed as gain media. We aim at demonstrating the viability of this approach, and at bench-marking the laser performance, losses and achievable gain. This analysis is based on the comparison of *thick cladding* vs. *thin cladding* structures.

I fabricated both structures into ridge waveguide resonators. The semiconductor claddings are etched until the SCH layer above the AR. A 300-nm-thick Si_xN_y insulating layer is deposited by plasma-enhanced chemical vapor deposition (PECVD) and opened with reactive ion etching (RIE) on the top device surface. Ti/Au layers 3/200-nm-thick are e-beam evaporated to provide the electrical contact and - after polishing and back-contact deposition - the samples are cleaved and Indium-soldered onto copper blocks for characterizations. The laser ridges are typically 9-μm-wide, while their length L ranges from 350 μm to 4 mm. SEM images of the cleaved facets of two typical devices are shown in Fig. 3.4a (*thick cladding*) and Fig. 3.4b (*thin cladding*) [83].

An additional useful configuration for the study of the metal effect is the air confinement waveguide [84]. This guide was fabricated exclusively on the *thin cladding* structure. We will since now refer to the air confinement waveguide on the *thin cladding* structure with the only name *air confinement*. In this case only narrow (1 μm-wide) lateral electrical contacts are present on the ridge top, leaving a 4 μm-wide central top region not covered by metallization layers (see Fig. 3.5).

Details of the fabrication process can be found in the appendix B.

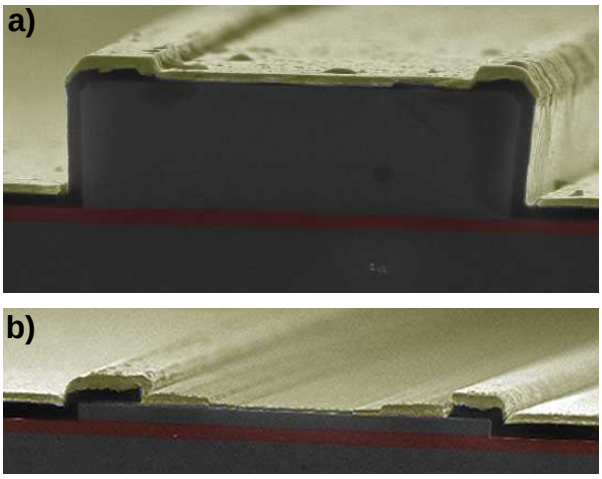

Figure 3.4: SEM images of the cleaved 9 μm width facets of (a) a *thick cladding* and (b) a *thin cladding* laser. The images are colorized to highlight the different layers: yellow is gold, dark green is the Si_xN_y insulating layer, red is the active laser core. [83]

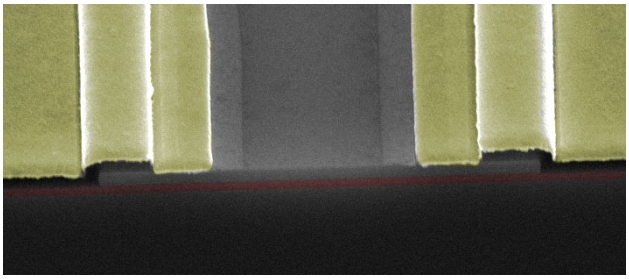

Figure 3.5: SEM image of an *air confinement* waveguide. No metal is present on the top of the device (current injection is provided by lateral contacts).

3.3.1 Passive measurements

Passive transmission measurements aim at quantifying the optical waveguide losses of our devices and have been performed with no current injected in the laser. Linearly polarized light from a frequency tunable laser is injected in the ridge resonator using a polarization-maintaining optical fiber, whose end is tapered and equipped with a micro lens. The transmitted signal is collected from the opposite facet with a microscope objective and focused

onto a power-meter. A second polarizer is placed between the objective and the power-meter. It allows one to select the same polarization as the input signal, hence avoiding unwanted contributions from reflections and diffractions. These results were obtained in collaboration with M. Fevrier and B. Dagens. Further details on the set-up for passive measurements can be found in appendix C.1.

Preliminary transmission measurements were performed on a broad wavelength range ($1.27\ \mu\text{m} < \lambda < 1.35\ \mu\text{m}$) to determine the polarization-dependent energy gap of the tensile-strained QWs. In order to minimize the background signal (due to multiple-reflections of the input signal) we measured 4-mm-long resonators. These long cavities can be measured only if the optical mode suffers weak losses. This corresponds to the case of the *thick cladding* waveguides, where the top metallic contact is far from the AR. Figure 3.6 shows the polarization dependent transmission signal at wavelengths close to the energy gap. The absorption edge for TM polarization appears at lower energy than for TE polarization. These preliminary measurements prove that tensile strained QWs correctly exhibit a smaller energy gap for TM than for TE polarization.

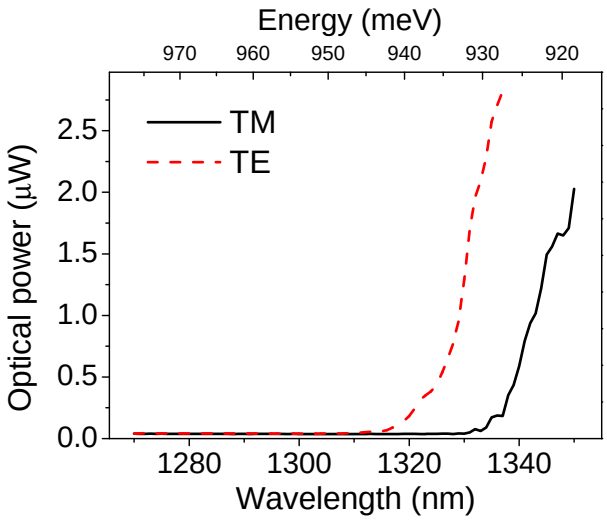

Figure 3.6: Transmission curves for the TE (red dashed curve) and TM (black solid curve) polarization in a *thick cladding* device of length L= 4 mm. The absorption edge shift confirms that the energy gap for TM is lower than for TE polarization.

In order to collect a stable transmission signal for both TE and TM polarizations, we performed the measurements in a wavelength range of about two nanometers around $\lambda = 1420$ nm. This wavelength range is below the energy gap of the QWs. Inter-band absorption is absent, and we assume that the transmission losses at $\lambda = 1420$ nm are similar to the waveguide losses at the shorter laser emission wavelength. An example of a high-resolution transmission scan is shown in the inset of Fig. 3.7. The free spectral range ($\Delta\lambda$) depends on the length of the laser cavity and it is given by:

$$\Delta\lambda \simeq \frac{\lambda^2}{2n_{eff}L} \tag{3.7}$$

where λ is the wavelength, n_{eff} the mode group index and L the cavity length. The oscillations in the transmitted signal are due to interferences in the Fabry-Perot cavity. The transmission contrast, defined as the ratio between the minimum (P_{min}) and the maximum (P_{max}) of the transmitted power, allow one to measure waveguide losses [85]. We use the following equation:

$$Y = ln\left(\frac{1-\sqrt{P_{min}/P_{max}}}{1+\sqrt{P_{min}/P_{max}}}\right) = ln(R) - \alpha_W^{TE/TM}L \tag{3.8}$$

where R is the mirror power reflectivity. The Y parameter is extracted from the measured transmission contrast and it is linked to the waveguide losses α_W, both for TE and TM polarizations. Transmission measurements on different cavity lengths yield, *via* a linear fit, the waveguide loss and also the reflectivity coefficient R.

Fig. 3.7 shows the Y parameter as a function of cavity lengths and polarization for *thick cladding* devices. We have measured at least two different devices for every length. The linear fit yields the waveguide losses: $\alpha_W^{TE} = 3.7$ cm^{-1} and $\alpha_W^{TM} = 5$ cm^{-1}. The facet reflectivity, inferred from the linear fit, is lower for the TM than for the TE mode, in reasonable agreement with results in the literature [86].

The same method allowed us to measure the optical losses for the TE polarization for a *thin cladding* cavity, $\alpha_W^{TE} = 13$ cm^{-1}, and the *air confinement* cavity, $\alpha_W^{TE} = 18$ cm^{-1}. At first sight it is strange that the losses α^{TE} are higher in the cavity with less metal on the top contact. Indeed the spatial field distribution of the modes (see section 3.4) shows that in the air

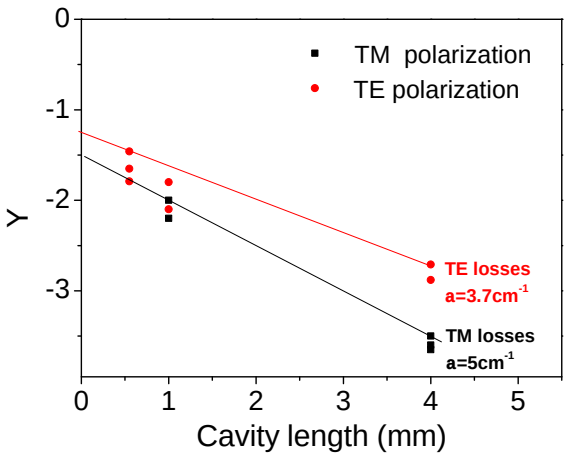

(a)

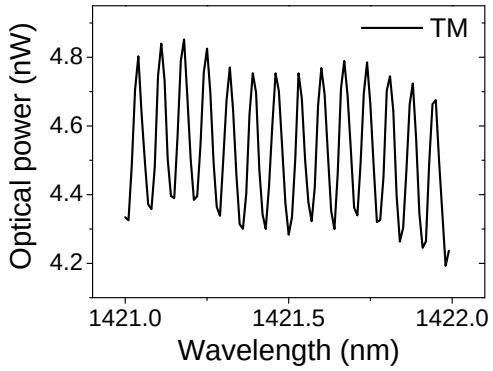

(b)

Figure 3.7: (a) Loss measurements on different cavity lengths (*thick cladding* device) allows one to extrapolate the losses of the Fabry-Perot cavity. The line slopes correspond to the cavity loss. (b) Typical transmission measurement in a narrow wavelength range around λ=1420 nm.

confinement cavity the mode has a larger overlap with the contact cladding (p-doped InGaAs and InGaAsP) than in the fully metallic cavity (the field is zero at the metal interface for a TE mode).

With this passive technique it was not possible to asses the losses in the TM polarization, α^{TM}. These are too high and not enough light is transmitted trough the cavities to allow measurements. The results of the passive measurements are summarized in Tab. 3.5.

Waveguide cavity	Exp. losses (cm^{-1}) λ=1420nm	
	TE	TM
Thick cladding	3.7	5
Thin cladding	13	N.A.
Air conf. on *thin cladding*	18	N.A.

Table 3.5: Experimental optical losses values expressed in cm^{-1}. In two cases it was not possible to measure the TM losses due to the extremely high absorption values.

3.4 Laser simulations

Finite element electromagnetic simulations performed in 2D [87] and 1D [33] allow one to visualize the mode shape and calculate the mode optical losses, α_W. We show that the materials optical indexes used in the simulations can be finely tuned to reproduce the experimental α_W, at $\lambda = 1420$ nm on the *thick cladding* devices, both for TE and TM polarization. These indexes are then used to extract the α_W at $\lambda = 1300$ nm.

2D Simulations at $\lambda = 1420$ nm

We performed two dimensional simulations of the waveguided mode in our structure at $\lambda = 1420$ nm. Figure 3.8 shows the squared electric field, and the direction of the electric field (arrow), for the TE and TM polarized lowest loss modes in:

- (a)-(b) a *thick cladding* waveguide
- (c)-(d) a *thin cladding* waveguide
- (e)-(f) a *air confinement* waveguide

The optical complex indices used for the simulations are reported in Tab. 3.7.

While in TE polarization the low-loss mode shows always one central lobe, in TM polarization the metal strongly acts on the mode shape. The TM low-loss mode in the *thin cladding* waveguide tends to concentrate on the ridge borders, under the insulator layer. In the following device fabrications

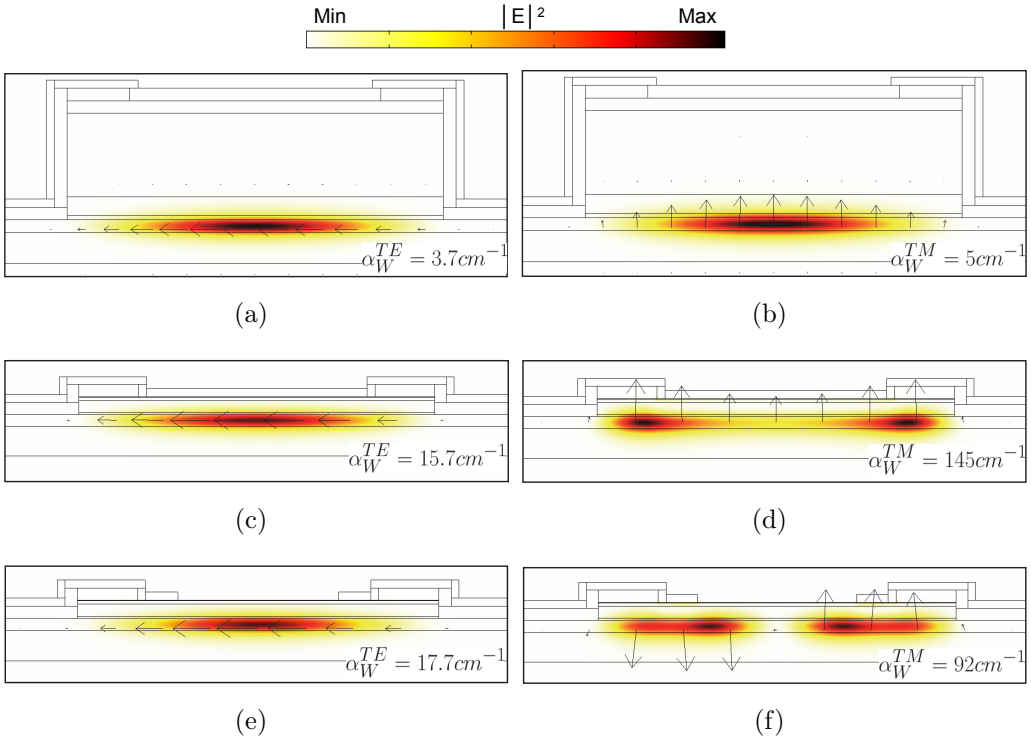

Figure 3.8: Simulated squared electric field, at λ= 1420 nm, for both polarizations (TE on the left and TM on the right): (a)-(b) *Thick cladding* waveguide. (c)-(d) *Thin cladding* waveguide (e)-(f) *air confinement* waveguide. The direction of the electric field is shown with black arrows.

we opened large windows in the insulator, almost of the same width of the ridge, to prevent this split shape. This precaution becomes more and more important as the cladding thickness is further reduced. Note that the low-loss mode of the air confinement waveguide has two lobes.

The losses of each mode (written in the bottom-right corners in Fig. 3.8) are extracted from the calculated complex effective index. The α_W is linked to the imaginary part of the effective index, k through,

$$\alpha_W = \frac{4\pi k}{\lambda} \tag{3.9}$$

The value of the imaginary part k in the simulation can tunes in agreement with the experimental value, acting on the layer index. Every layer is characterized by a complex index of refraction, with the imaginary part

Waveguide cavity	Exp. losses (cm^{-1}) λ=1420nm		Sim. losses (cm^{-1}) λ=1420nm		
	TE	TM	TE	TM	
Thick cladding	3.7	5	3.7	5	Fit
Thin cladding	13	x	15.7	145	No adjusted param.
Air conf. on *thin cladding*	18	x	17.7	92	

Table 3.6: Experimental and calculated optical losses values, at λ = 1420 nm, expressed in cm^{-1}.

linked to the material optical losses.

The absorption losses for the n-doped InP buffer are estimated using a Drude-Lorentz model. The losses for the p-doped layers are estimated *via* the experimental measurements reported in Ref. [88], while the absorption coefficient in the thin InGaAs contact layer are taken from Ref. [89]. Finally, the index for gold n_{gold} = 0.48-i·9 (at λ = 1420 nm) is taken from Ref. [35], the data presented in Fig. 1.6. In the *thick cladding* structures the electric field intensity at the top metal-semiconductor interface is negligible hence the losses are exclusively determined by absorption in the semiconductor layers. In order to reproduce the experimental data of the *thick cladding* waveguides, we find that the absorption coefficient in the InP p-doped layers needs to be increased 2.5 times with respect to the values found in the literature [88]. The inferred material parameters are presented in Tab. 3.7 and they will be used in the rest of this manuscript to perform the numerical simulations.

Table 3.6 updates the experimental loss values with the calculated values at λ = 1.420 μm. For TE polarization the agreement is good, for both *thin cladding* and *air-confinement* devices. We can reliably predict the optical absorption due to the cladding losses. However, for TM polarization the presence of the metal considerably increases the losses up to more than 100 cm^{-1}. This level of attenuation is incompatible with a passive loss measurement technique. Only active measurements combined with simulations can lead to an improved understanding of the system.

Thick clad.	t (nm)	Doping (cm^{-3})	index @1420nm	index @1300nm
Gold	200		0.48 - i·9	0.403 - i·8.25
InGaAs	300	p=$3 \cdot 10^{19}$	3.2 - i·2.26×10^{-1}	3.2 - i·2.07×10^{-1}
InP	2000	p=$1.4 \cdot 10^{18}$	3.2 - i·8.84×10^{-4}	3.2 - i·5.93×10^{-4}
InP	450	p=$7 \cdot 10^{17}$	3.2 - i·3.83×10^{-4}	3.2 - i·2.68×10^{-4}
InP	50	n.i.d.	3.2	
InP	50	n.i.d.	3.2	
AR	300	n.i.d.	3.45	
Buffer	750	n = $1 \cdot 10^{18}$	3.2 - i·1.77×10^{-5}	3.2 - i·1.36×10^{-5}
Substrate	2000	n	3.2	

Thin clad.	t (nm)	Doping (cm^{-3})	index @ 1420nm	index @ 1300nm
Gold	200		0.48 - i·9	0.403 - i·8.25
InGaAs	15	p=$3 \cdot 10^{19}$	3.34 - i·2.26×10^{-1}	3.34 - i·2.07×10^{-1}
InGaAsP	80	p=$2 \cdot 10^{19}$	3.34 - i·5×10^{-3}	3.34 - i·3.3×10^{-3}
InP	295	p= $1.4 \cdot 10^{18}$	3.2 - i·8.84×10^{-4}	3.2 - i·5.93×10^{-4}
InP	50	n.i.d.	3.2	
AR	300	n.i.d.	3.45	
Buffer	750	n = $1 \cdot 10^{18}$	3.2 - i·1.77×10^{-5}	3.2 - i·1.36×10^{-5}
Substrate	2000	n	3.2	

Table 3.7: Optical indexes of the *thick* and the *thin cladding* structure, at λ = 1420 nm and λ = 1300 nm.

2D Simulations at $\lambda = 1300$ nm

Since the lasers operate at $\lambda \approx 1.3$ μm, it is necessary to know α_W at this wavelength. The complex indices at $\lambda = 1.3$ μm are shown in Tab. 3.7 and the results of the 2D simulations are reported in Fig. 3.9. A summary of the losses can be found in Tab. 3.8.

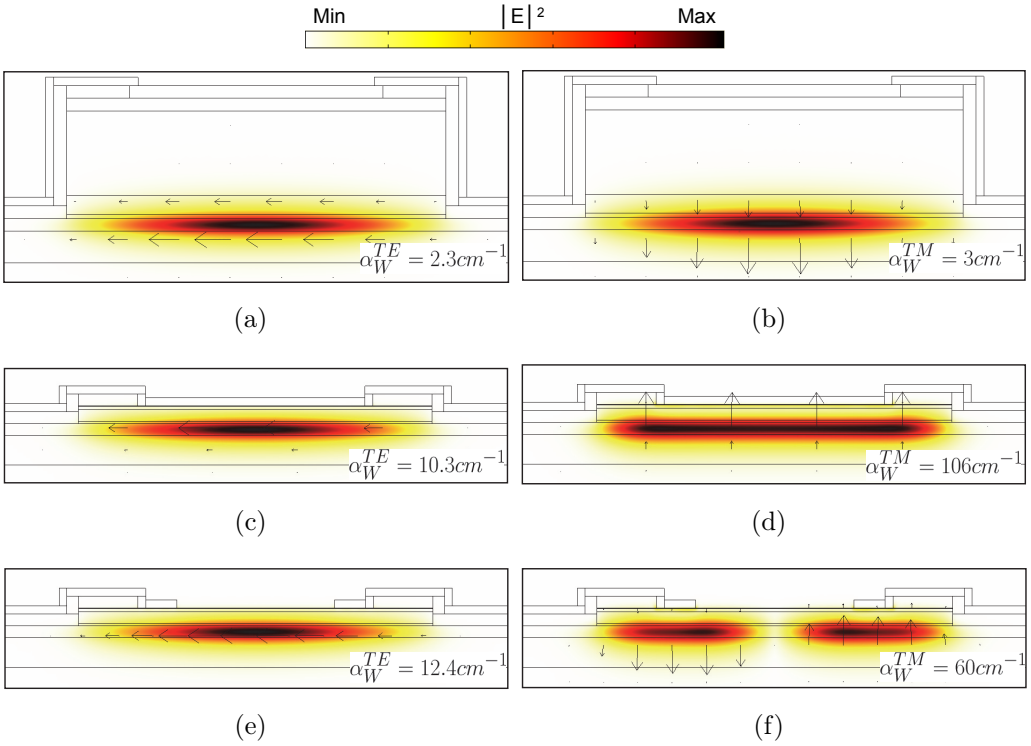

Figure 3.9: Simulated squared electric field, at λ= 1300 nm, for both polarizations (TE on the left and TM on the right): (a)-(b) *Thick cladding* waveguide. (c)-(d) *Thin cladding* waveguide (e)-(f) Air confinement waveguide on the *thin cladding* structure. The direction of the electric field is shown with black arrows.

1D Simulations at $\lambda = 1300$ nm

The shape of the TM polarized mode in the *thin cladding* waveguide (Fig. 3.9d) shows a relevant fraction of the electric field at the metal/semiconductor interface. The overlap of the field with the metal is responsible for the large

Waveguide cavity	Exp. losses (cm^{-1}) λ=1420nm		Sim. losses (cm^{-1}) λ=1420nm		Sim. losses (cm^{-1}) λ=1300nm	
	TE	TM	TE	TM	TE	TM
Thick cladding	3.7	5	3.7	5	2.3	3
Thin cladding	13	x	15.7	145	10.3	106
Air conf. on *thin cladding*	18	x	17.7	92	12.4	60

Table 3.8: Experimental and calculated optical losses values expressed in cm^{-1}. The first two columns refer to λ = 1420 nm. The last column refers to λ = 1300 nm.

Thin cladding	α_W^{TM} at λ=1300nm (cm^{-1})	
	2D	1D
without 3 nm of Ti	106	114
with 3 nm of Ti	x	144

Table 3.9: Comparison between the optical losses of TM polarized modes of the *thin cladding* waveguide resulting from the 2D and the 1D simulations. Considering the 3nm of Ti is not possible to calculate the optical losses with a 2D simulation.

calculated losses.Since even extremely thin layers at the interface play a relevant role, we need to take into account the extremely thin layer of Ti (3nm) used to stick the gold to the surface. Due to the reduced thickness we employed 1D simulations. The simulation at λ = 1300 nm, without the Ti layer yields $\alpha_{W\_1D}^{TM}$ = 114 cm^{-1} (consistent with α_W = 106 cm^{-1} of the 2D simulation). Including the Ti layer, with an optical index n = 3.645 - i·4.262 [90], leads to $\alpha_{W\_1D}^{TM}$ = 144 cm^{-1}. The results are summarized in Tab. 3.9.

With the Ti layer a loss difference between the TM modes of the *thin* and the *thick cladding* waveguide of $\Delta\alpha_W^{TM} \approx 140$ cm^{-1} is numerically estimated. This represents a lower limit since the real metal roughness, not included in the simulations, can increase the losses of the *thin cladding* device. This result will be compared later with the measured gain necessary to compensate the losses in the two waveguides architectures.

3.5 Active measurements

Active measurements are performed upon electrical pumping of the devices, in pulsed or in continuous wave (CW) regime. The device light emission is collected using a cleaved multimode optical fiber which is either coupled to a high sensitivity power-meter (for light-current characterizations) or to an optical spectrum analyzer. Further details on the set-up for passive measurements can be found in appendix C.2. In Fig. 3.10 we show typical light-current-voltage (LIV) characteristics of *thick*- and *thin*-cladding devices. Note that the measured output powers are not representative of the total device output since we collect the signal with cleaved fibers in order to feed an optical spectrum analyzer. The measurements are performed at room-temperature (RT), in pulsed regime with a 2% duty cycle. Both devices reach laser threshold, even the *thin cladding* devices which exhibit extremely large α_W [83]. This is a promising result for the development of plasmonic devices at λ =1.3 μm. Typical thresholds (J_{th}) for *thick cladding* devices are 1 - 1.5 kA/cm^2, while the *thin cladding* devices exhibit J_{th} between 2.8 and 4 kA/cm^2.

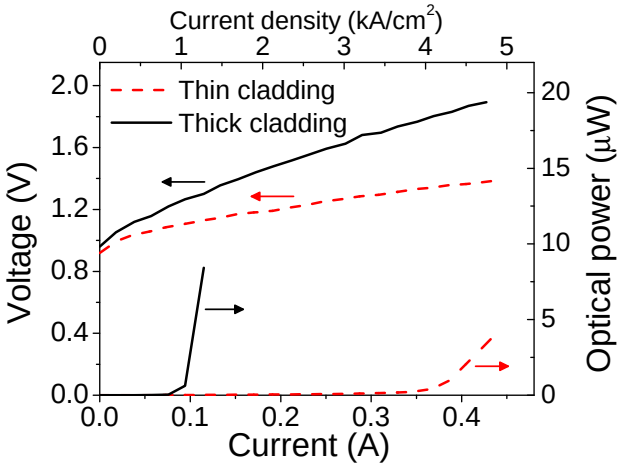

Figure 3.10: Typical current-voltage (black-solid line) and light current (red-dashed curve) laser characterizations. The devices are 1000 x 9 μm^2 and they are measured at RT with 200-ns-wide pulses at a frequency of 100 kHz (duty cycle = 2%).

Fig. 3.11 shows typical spectra at different sub-threshold injected currents

for the *thin cladding* device. The spectra of the device operating in laser regime are shown in Fig. 3.12.

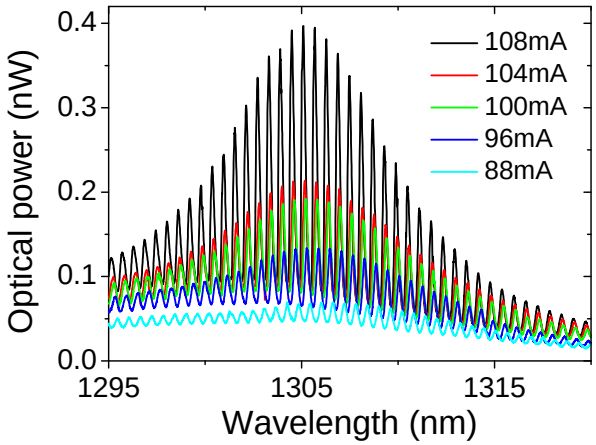

Figure 3.11: Spectra of a *thin cladding* device (350 μm long) at different current values below threshold. The spectra are collected in pulsed regime (frequency 1 MHz and pulse width of 100 ns, corresponding to a duty cycle of 10%).

3.5.1 Differential gain calculation

We have applied the Hakki-Paoli method to experimentally measure the AR modal gain as a function of the emission wavelength [91]. The gain can be determined as a function of the injected current by collecting spectra below and above J_{th}. The contrast between the interference fringes is defined as follows: $r(\lambda) = P_{min}(\lambda)/\ P_{max}(\lambda)$, where P_{min} and P_{max} are the minimum and maximum values of the Fabry-Perot spectrum. The modal gain can then be inferred using the following formula [91]:

$$\Gamma g(\lambda) = \frac{1}{L} ln \left(\frac{\sqrt{r(\lambda)} + 1}{\sqrt{r(\lambda)} - 1} \right) + \frac{1}{L} ln(R) \tag{3.10}$$

Where R is the facet power reflectivity and Γ is the guided mode overlap factor. The R is calculated using the approximation [68],

$$R = \frac{(n_d - n_{air})^2}{(n_d + n_{air})^2}, \tag{3.11}$$

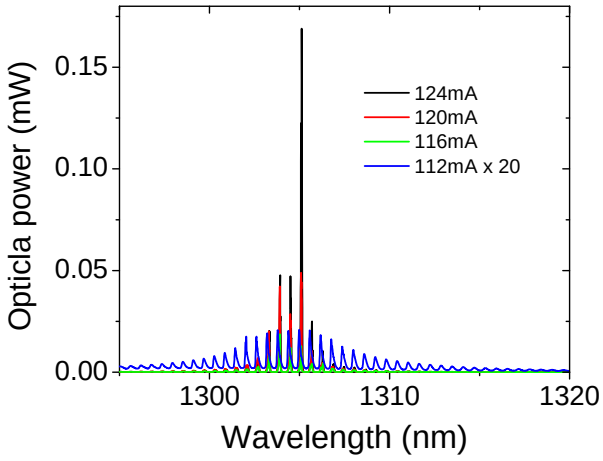

Figure 3.12: Spectra of a *thin cladding* device (350 μm long) at different current values above threshold. The spectra are collected in pulsed regime (frequency 1 MHz and pulse width of 100 ns, corresponding to a duty cycle of 10%). The curve at 112 mA is multiplied by a factor 20 to be plotted on the same scale of the spectra at higher currents.

where n_d is the effective index of the dielectric waveguided mode and n_{air} is the air index. We employ Γ=0.55 for both *thick* and *thin* cladding waveguides. This confinement factor is calculated through the finite element simulations presented in section 3.4. By applying this formula to every under-threshold spectrum shown in Fig. 3.11 we calculated the curves of Fig. 3.13 in which the gain is plotted as function of the wavelength. We stress that the measurements in Fig. 3.11 have been performed at a duty cycle of 10% and not in CW as hypothesized by Hakki and Paoli. Indeed the injection regime does not affect the method validity that is based on the fringes contrast. On the other hand we will show later that the devices operating in CW have lower gain performance due to heating effects.

As anticipated in section 3.1.2 an important factor in a laser is the evolution of the optical gain with the injected current, whose slope represents the differential gain with respect to the current density, $\delta g/\delta J$. The differential gain is experimentally extracted by collecting the gain values at the laser emission wavelength (for instance in Fig. 3.13a at λ=1305 nm) and then plotting them as function of the current density. As shown in Fig. 3.13b the

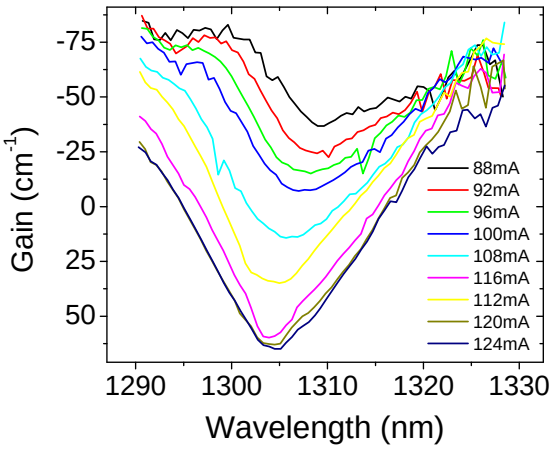

(a)

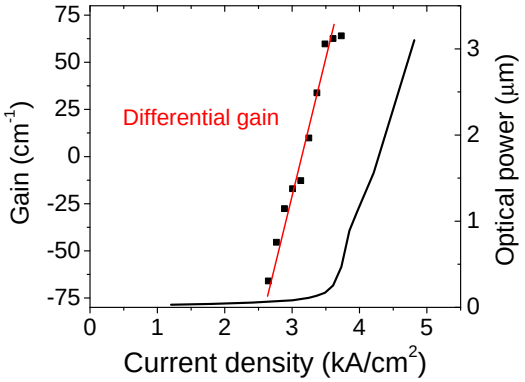

(b)

Figure 3.13: (a) The gain-curves are calculated through the Hakki-Paoli formula from the spectra of Fig. 3.11. Note: increasing the injected current the peak of the gain curve blue-shifts. (b) The gain values at λ=1305 nm are plotted as function of the current density. The linear slope below the threshold is defined as the differential gain at threshold.

differential gain below threshold has approximately a linear behavior, while above threshold it clamps to a constant value. The gain clamps when the waveguide losses and the mirror losses are compensated. In Fig. 3.13 the gain is clamping at a value corresponding to the mirror losses (see Eq. 3.10) which are determined by the cavity length L and by the power reflectivity coefficient (R) of the facets.

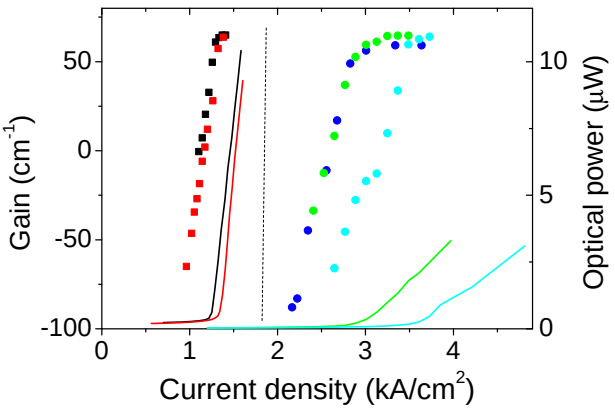

Figure 3.14: Laser output as a function of injected current density (solid lines). The square and round dots represent the AR gain values for respectively *thick* and *thin cladding* as inferred from Hakki-Paoli measurements. All the laser cavities have a length of 350 μm.

Fig. 3.14 shows the results of Hakki-Paoli measurements on *thick* and *thin cladding* devices with cavity lengths of L=350 μm. A more careful analysis of Fig. 3.14 highlights that the differential gain decreases with the current density threshold, denoting a lower efficiency of the radiative recombination at high current densities. This is in agreement with standard diode laser behavior.

Hakki-Paoli measurements were performed on several devices with different cavity lengths and under pulsed or CW operation. *Thin cladding* devices only operate in pulsed mode, while *thick cladding* ones could be measured in both pulsed and CW regime. Operating in CW naturally reduces the differential gain, as well as operating longer-cavity devices, because of the AR heating which decreases the efficiency of the radiative recombination. For this reason we concentrate on pulsed measurements in Fig. 3.15, which reports the results of gain measurements on several lasers with cavity length of 350 μm (this allows us to neglect heating effects). The differential modal gain is plotted as a function of the current density. At high injection currents the optical gain shows a saturation behavior and the differential gain decreases. Since the differential gain is inversely proportional to the current density, we use Eq. 3.6 to fit the data on 350-μm-long lasers, which cover a broad span of J_{th}. We obtain $G_0 = 465 \pm 25$ cm^{-1}, in excellent agreement with the value

found for a very similar AR (AlGaInAs/InP) by Van Parys and collaborators [76].

We can now estimate the losses of the *thin cladding* lasers using the differential gains extracted from Hakki-Paoli measurements. By integrating the differential modal gain with respect to the current density the gain value of the laser can be calculated. The integration of $\Gamma\delta g/\delta J$ from typical thresholds of *thick cladding* devices (J_{th_thick}=1.3 kA/cm^2) to typical thresholds of *thin cladding* devices (about J_{th_thin}=2.8 kA/cm^2) yields a gain difference of $\Delta g \approx 200$ cm^{-1}. This corresponds to the area of the shadowed surface in Fig. 3.15:

$$\Delta g = \Gamma G_0 \int_{J_{th\_thick}}^{J_{th\_thin}} \frac{1}{x}\,\mathrm{d}x = 0.55 \cdot 465 \int_{1.3}^{2.8} \frac{1}{x}\,\mathrm{d}x = 196 cm^{-1}. \qquad (3.12)$$

In conclusion the AR must generate additional ≈ 200 cm^{-1} of gain with respect to to a *thick cladding* device to fully compensate the losses in the *thin cladding* laser. This value can be directly compared with the calculated $\Delta\alpha_W^{TM}$, showing a reasonable agreement (30%, see Tab. 3.10).

Differential gain for CW injection

We dedicate this subsection to the measurements of the differential gain in CW injection regime.

The proximity of the metal to the AR prevents the *thin cladding* device to lase in CW. The metal/semiconductor interface heats the AR, deteriorating the laser performance, increasing the non-radiative recombinations. Even the *thick cladding* structure is strongly affected by the injection regime. As shown in Fig. 3.16 the differential gain in CW regime of 350-μm-long lasers decreases compared to the one on pulsed regime. A differential gain reduction is also observed in 1000-μm-long lasers, since the higher current threshold entails a larger heating. Another consequence of the heating is the red-shift of the emission wavelength [32]. The 350-μm-long lasers emit in a range of wavelengths 1300 nm $< \lambda <$ 1305 nm, while the 1000-μm-long lasers emit between 1312 nm $< \lambda <$ 1318 nm.

Solutions are available to improve the heating dissipation, like using a good thermal conductor layer on the device surface, or using a thermo-electric cooler. However, in view of our goals, we chose to operate the devices in

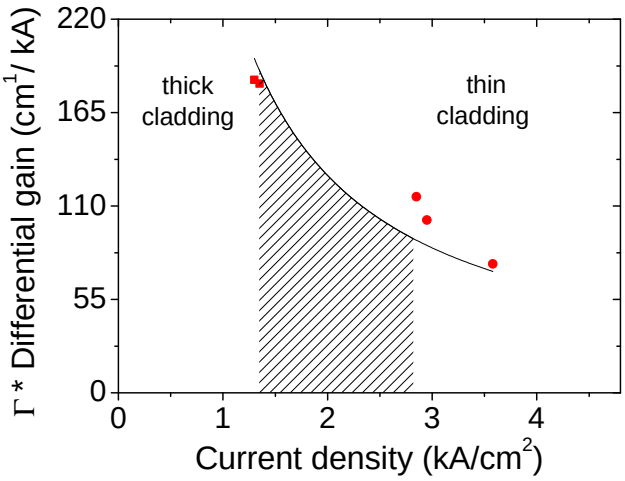

Figure 3.15: Differential modal gain (with respect to the injected current density) of 350-μm-long lasers as a function of the threshold density current. The values are obtained from Hakki-Paoli measurements. The general, expected trend is a decrease of the modal differential gain with the injected current density. The area of the shadowed surface corresponds to the gain needed to compensate the increased losses of *thin cladding* devices, and it amounts to ≈ 200 cm^{-1}.

pulsed regime with small duty cycles to avoid heat generation. In the following chapters we will show that the pulsed regime provides sufficient power to clearly detect the SPPs into the near-field.

3.5.2 Model consistency

An additional validation of the loss calculation can be given by anticipating a result from chapter 5. We demonstrate an *ultra thin cladding* device, with some special "trick", operating at room temperature in pulsed regime. The lowest measured threshold is J=15 kA/cm^2. By using the function 3.12 to estimate the gain necessary to compensate the losses between the *thin cladding* and the *ultra thin cladding* we obtain:

$$\Delta g = \Gamma G_0 \int_{J_{th\_thin}}^{J_{th\_ultrathin}} \frac{1}{x}\,\mathrm{d}x = 0.53 \cdot 465 \int_{2.8}^{15} \frac{1}{x}\,\mathrm{d}x = 414 \quad cm^{-1}. \qquad (3.13)$$

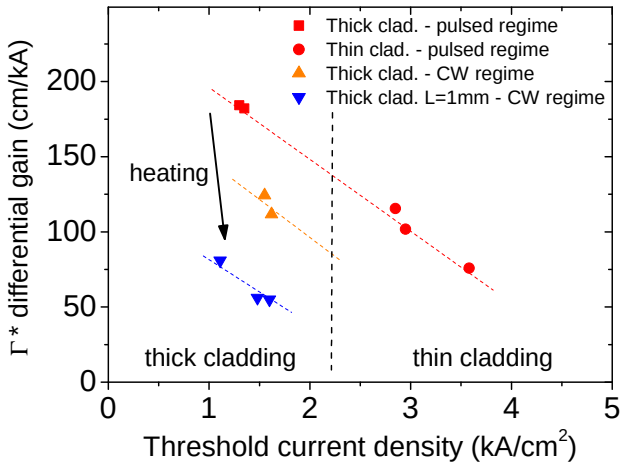

Figure 3.16: Differential modal gain (with respect to the injected current density) of lasers as a function of the threshold current density. Red dots, data already plotted in Fig. 3.15 (350-μm-long lasers). Triangles, data in CW regime: in orange the 350-μm-long lasers and in blue the 1000-μm-long lasers. The arrow highlights that the differential gain decreases with the device heating.

On the other hand the calculated losses, with the simulations, for the *ultra thin cladding* are 487 cm^{-1}. This corresponds to a difference between the two waveguide modes of $\Delta\alpha \approx 300$ cm^{-1}. The measured gain is in fair agreement (30%) with the calculated losses (see Tab. 3.10).

	Calculated $\Delta\alpha_W^{TM}$ (cm^{-1})	Measured Δg (cm^{-1})
Thick and *thin cladding*	140	200
Thin and *ultra-thin cladding*	300	410

Table 3.10: Comparison between: *thick cladding* / *thin cladding* devices and *thin cladding* / *ultra-thin cladding*. Data in cm^{-1}.

3.6 Conclusions

We have presented the employed AR and the structures with thin top claddings. The ridge devices based on these structures feature a top metal contact extremely close to the AR. However, the optical losses can be compensated thanks to the high quantum wells gain and laser operation at RT of the *thin cladding* ridge device is demonstrated.

The differential gain of the AR region is measured through the Hakki-Paoli thechnique. Thanks to passive measurements we extrapolate an experimental value for the waveguides losses. The proposed finite element model is in fair agreement with the experimental results.

The *thin cladding* structure will be used for the demonstration of the SPP generation. The validated simulation tool can be used as a design instrument and to interpret the experimental results.

Chapter 4

Semiconductor-based generation of SPPs at telecom wavelengths

This chapter is dedicated to the generation of SPPs at telecom wavelengths by electrical injection with a semiconductor device. We explore the two approaches previously described (see section 2.4), experimentally realizing the grating coupling and the end-fire coupling. The first section of the chapter is dedicated to the grating coupling device for the elegance of the concept, its originality and the easiness of the fabrication. Based on a numerical analysis of the coupling mechanism, we study the effect of geometrical parameters, such as the grating and the dielectric waveguide, in order to optimize the experimental phase [92]. In the second section of the chapter we provide the electro-optical characterization of the fabricated devices. The third part of the chapter is dedicated to the end-fire coupling approach at telecom wavelengths.

4.1 Grating coupler approach

We have previously illustrated the demonstration of a semiconductor surface plasmon polariton source exploiting a grating coupler at mid-IR wavelengths. In this geometry the coupler, which is a metallic grating, compensates the momentum difference between the laser mode and the SPP wave. However metals behave differently at telecom wavelengths. This requires a detailed numerical analysis before the experimental realization. The general scheme of a grating coupler device is shown in Fig. 4.1. The light travels in

an optical waveguide and is diffracted by the grating in specific directions. For an optimized device, the grating must be designed to maximize the coupling into the SPP mode. Compared to other configurations, such a coupler is compact [93] and it can be easily integrated [94] since a single metal deposition is necessary. This latter comprises the SPP-carrying strip and the diffraction grating above the dielectric waveguide layers.

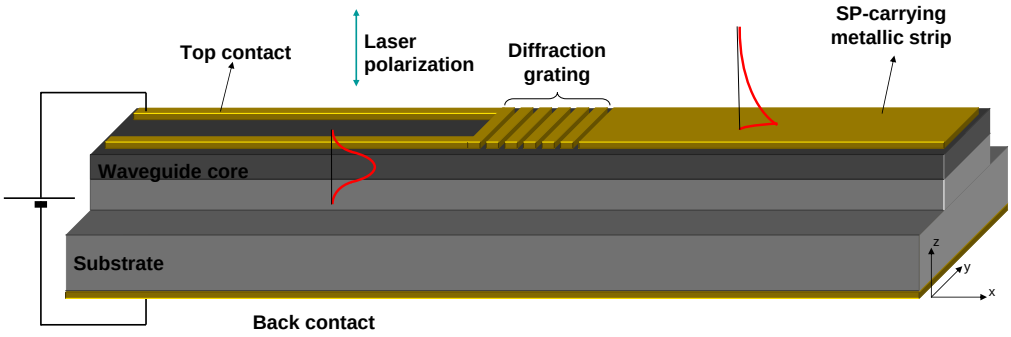

Figure 4.1: SPP source with coupling grating [30]

4.1.1 The coupling mechanism

The grating coupling is based on an interference phenomenon. It diffracts a part of the waveguided mode, hence its period must be chosen in order that constructive interference takes place into the SPP mode.

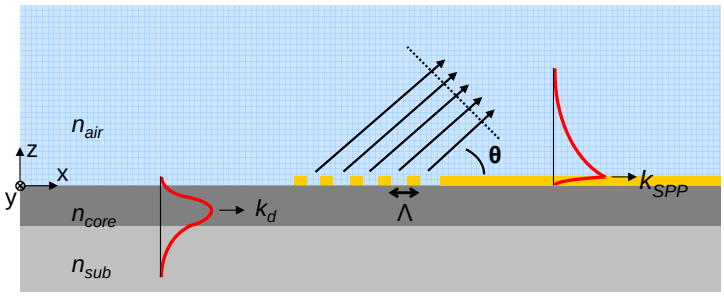

Figure 4.2: Schematics of the grating coupler mechanism [30]

In Fig. 4.2 we show a schematic of the grating. n_d is the effective index

of the dielectric mode, n_{SPP} the effective SPP mode index (the expression is in Eq.1.19) and $k_0 = \omega/c$ is the wavevector of light in vacuum. Every single element of the grating behaves as an elementary scatterer that generates approximately a cylindrical wave. For a certain angle θ the waves will interfere constructively. In order to find this angle we write the difference in phase $\Delta\phi$ between two waves scattered from adjacent grating elements:

$$\Delta\phi = n_d k_0 \Lambda - n_i k_0 \Lambda \cos\theta \tag{4.1}$$

where n_i is the index of the medium in which we consider the diffraction, i.e. n_i=1 for the diffraction in the air ($\theta \in]0, \pi[$), n_i=n_{SPP} for the diffraction in the SPP mode, and n_i=n_{sub} for the diffraction in the substrate ($\theta \in]-\pi, 0[$). The interference is constructive if the waves have the same phase, $\Delta\phi = p2\pi$ with p natural number. By using 4.1 we obtain,

$$\cos\theta_p = \frac{n_d - p\lambda_0/\Lambda}{n_i}. \tag{4.2}$$

We look at the relation 4.2 in the SPP case, θ= 0 and n_i= n_{SPP} at the first order (p=1),

$$n_d = n_{SPP} + \frac{\lambda_0}{\Lambda} \Rightarrow \Lambda = \frac{\lambda_0}{n_d - n_{SPP}} \tag{4.3}$$

In term of wavevectors, this is a phase-matching condition:

$$k_d = k_{SPP} + \frac{2\pi}{\Lambda}. \tag{4.4}$$

where k_d is the wavevector of the guided mode and k_{SPP} is the wavevector of the SPP mode.

For instance, a realistic case with λ_0= 1.3 μm, $n_d \approx$ 3.3 and $n_{SPP} \approx$ 1 yields Λ= 560 nm. This value for Λ also permits other diffracted beams satisfying the condition 4.2:

$$\cos\theta_p = \frac{n_d - p(n_d - n_{SPP})}{n_i}. \tag{4.5}$$

We consider the diffraction in the air, $n_i = n_{air}$, since $n_{SPP} > n_{air} =$ 1 we find for p = 1 a $\cos\theta_p > 1$. Even for p > 1 no solution is allowed. Considering the diffraction in the substrate there are two possible directions for $p = 1$ and $p = 2$. With a n_d= 3.3, n_{SPP}= 1 and n_{sub}= 3.2 the angles are θ_1= -72° and θ_1= -114°.

In conclusion, the theory predicts a diffraction of the grating into the SPP mode and not in the air. However, diffraction in the substrate is unavoidable. In practice the grating has a finite size and there is a parasitic diffusion in all directions. Indeed we will later show a measurement in far-field of the grating diffraction perpendicularly to the surface.

4.1.2 Preliminary simulations

Calculation technique

This numerical study aims at investigating the feasibility of the device by varying the geometrical parameters [92]. We study the robustness of the device as a function of the wavelength and of the geometrical properties of the grating. Since it was performed before the epitaxy of the heterostructures presented in chapter 3.2, we have also considered a variable core thickness (namely the AR). The first simulations are performed with a core thickness of t_{core}= 500 nm (in real devices t_{core}= 300 nm).

For the finite element simulations we consider a dielectric waveguide composed of a high-index core (index n_{core}, thickness t_{core}) sandwiched between two semi-infinite lower-index media: the substrate (index n_{sub}) at the bottom and air (n_{air} = 1) at the top (see Fig. 4.3). The metallic layer (index n_m, thickness t_m) is located above the waveguide core and it comprises both the SPP-carrying film and the grating coupler. Figure 4.3 defines the coordinate

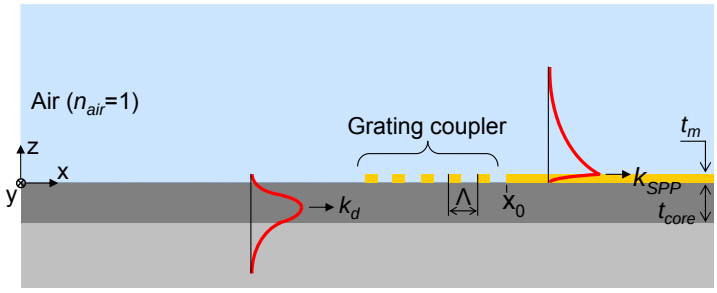

Figure 4.3: Main parameters used in the simulations of the grating coupler geometry [92]. t_m is the thickness of the metal and t_{core} is the thickness of the core layer, where the dielectric mode is guided.

system and the resulting geometry, which is assumed to be infinite along the

y-direction. The grating is characterized by its period Λ that satisfies Eq. 4.3, its duty cycle is d/Λ where d is the width of the metallic fingers, and the number of periods N. The refractive indices of the dielectric layers used in the following ($n_c = 3.45$ and $n_{sub} = 3.2$) are the values for the AlGaInAs tensile-strained multiple-quantum wells (MQWs) and the InP substrate used in the previous chapter (see Tab. 3.7). The frequency-dependent complex refraction index for gold is as presented in the first chapter [35].

All the numerical results were obtained by performing systematic two dimensional (2D) simulations using a finite element approach [87]. Because of the transverse magnetic (TM) polarization of SPPs, we only consider the fundamental TM mode of the dielectric waveguide. The simulation strategy consists in injecting the fundamental TM mode – at a wavelength λ_0 – from the left waveguide boundary, while all the other boundaries feature absorbing conditions. The coupling efficiency is defined as the ratio

$$\eta = \frac{P_{SPP}}{P_d} \tag{4.6}$$

where P_{SPP} and P_d are the electromagnetic power fluxes carried by the SPP mode and by the forward propagating dielectric waveguide mode, respectively.

In order to link these two quantities to the magnetic field distribution that will be numerically calculated, we used the basic formulae for a slab waveguide [68, 92]. The formula are reported in Appendix D. The P_{SPP} is calculated by evaluating the magnetic field amplitude at the metal-air interface $|H_y(x = x_0 + x_e, z = t_m)|$, $x = x_0$ being the left edge of the metallic film. The P_d is calculated from magnetic field in the core layer $< |H_y(x, z = z_{max})| >_x$ (z_{max} corresponding to the position of the mode profile maximum), respectively. The symbol $< \cdot >_x$ stands for the average value over one spatial period of the guided wave. Indeed, the grating coupler induces a reflected wave resulting in a partially standing wave in the dielectric waveguide. Since the boundary condition imposes the total amplitude at a given x, we don't know a priori the forward amplitude and, therefore, the average operation is required to deduce it. Note that with this technique we are able to readily determine the grating-induced reflection coefficient as well. On the other hand, the total field at the metal-air interface corresponds actually to the SPP contribution, provided that the distance x_e is sufficiently large with respect to the wavelength, so that the contribution of the radiating – non-guided –

waves launched from the coupler together with the SPPs becomes negligible [64]. An evaluation of the field at x_0 would include also the cylindrical waves contribution. Therefore, the SPP field at the edge $x = x_0$ is given by $H_{SPP}(x_0, z = t_m) = H_y(x_0 + x_e, z = t_m)/exp(-\mathrm{Im}\{k_{SPP}\}x_e)$ where k_{SPP} is the SPP complex wavevector. The power fluxes P_{SPP} and P_d are then calculated with analytical formulas readily derived from Poynting vector integration [68]. The results presented below are calculated with $x_e = 100$ μm.

Wavelength dependence of the coupling efficiency

First, we investigate the wavelength dependence of the SPP excitation efficiency. Figure 4.4a shows the calculated coupling efficiency in the wavelength range 1.15-1.5 μm. The waveguide core is 500 nm thick, the grating has a 50%-duty-cycle, a period of $\Lambda = 570$ nm, and the metal thickness is 100 nm. The number of periods is spanned from 2 to 20 (for clarity, data are plotted only for some values of N between 2 and 12). As expected from an interference-based coupling, a resonance wavelength appears as the number of periods is increased, while its frequency width narrows around a central value of $\lambda \approx 1.3$ μm. As shown in Fig. 4.4b, the maximum SPP coupling efficiency steadily increases with N, and it reaches a maximum value of about 13% for $N = 12$. For larger values of N, the coupling efficiency saturates: the impinging guided wave is almost totally scattered – into SPPs, but also in the substrate – after roughly 12 periods, making the following periods redundant.

For all the following calculations, we used $N = 10$, which offers a good trade-off between efficiency and compactness: such a coupler is in fact shorter than 6 μm in length. Furthermore, this choice yields a relatively broadband device: $\Delta\lambda/\lambda \approx 10\%$, where $\Delta\lambda$ is the full-width at half-maximum (FWHM). This feature can be particularly useful in the context of telecommunications, if the coupler is employed as a passive photon-to-SPP converter. In view of designing a SPP source based on a quasi-monochromatic laser, the issue of the period-sensitivity is of more practical importance.

Figure 4.4c shows the SPP coupling efficiency as a function of the grating period Λ for various excitation wavelengths. From the plots, which exhibit a resonant behavior which roughly follows Eq. 4.3, a FWHM of about 50 nm is estimated. This value is sufficient to ensure some flexibility for fabrication

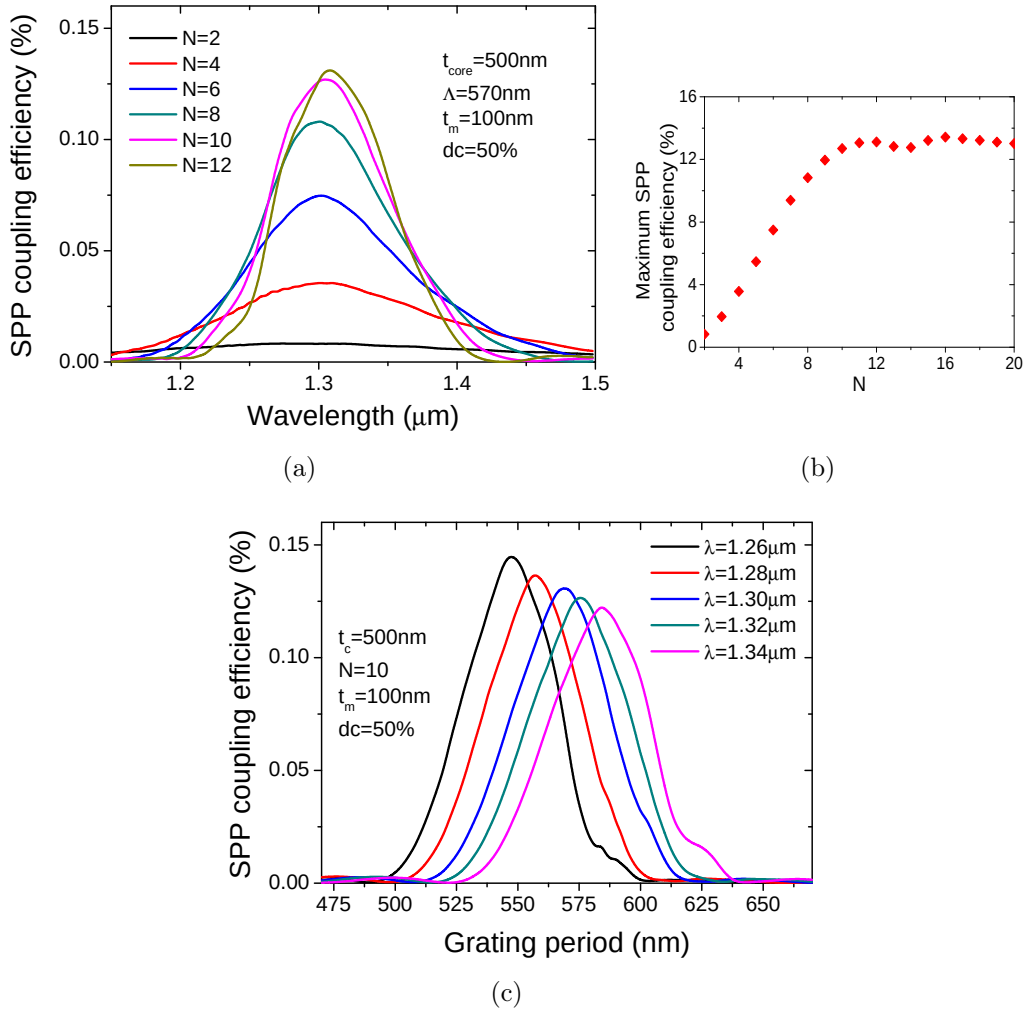

Figure 4.4: (a) Calculated SPP coupling efficiency as a function of the wavelength. Different curves show data for various numbers N of periods composing the grating. (b) Maximum SPP coupling efficiency versus N. (c) Calculated SPP coupling efficiency as a function of the grating period Λ for various wavelengths. The number of periods is fixed to 10.

with standard techniques based on electron-beam lithography.

We also notice that the peak values for η in Fig. 4.4c are wavelength-dependent. This effect possibly stems from the index dispersion of gold, since it disappears when the calculations are performed with a non dispersive dielectric function (data not shown). The intuitive physical reason is that

the SPP mode is more extended in the dielectric at larger wavelengths, hence the SPP excitation via a localized source near the metal-dielectric interface – that is, our coupler – is less efficient. An analogous effect has been rigorously demonstrated in the case of a single slit in a metallic film illuminated at normal incidence [64].

Dependence on geometrical parameters of the grating

We show here that it is possible to further increase the maximum coupling efficiency η by fine tuning the geometrical parameters of the grating coupler, namely its thickness and duty cycle. We have performed numerical simulations of SPP excitation and coupling efficiency with a grating whose duty cycle is varied from 0% to 100%, and the metal thickness spans the 50-250 nm range (see Fig. 4.5). The number of periods ($N = 10$) and the waveguide core thickness ($t_{core} = 500$ nm) are kept constant. The wavelength used for the calculations is $\lambda = 1.3$ μm while the data are shown for various grating periods.

Figure 4.5a shows that the largest SPP coupling efficiencies of $\approx 20\%$ are obtained for duty cycles between 60% and 70%. It also appears that the grating period yielding the highest value is $\Lambda = 560$ nm (60% duty cycle) while it is 570 nm for a 50% duty cycle. This is due to a small variation of the effective index undergone by the impinging guided wave when it propagates under the grating. Hence, the coupling condition Eq. 4.3 depends on the grating shape *via* the effective index modulation. This effect is visible in Fig. 4.5b as well, since the optimal period Λ depends on the grating thickness. In any case, Fig. 4.5b confirms that the very reasonable value close to 100 nm for the metal thickness is a good choice.

Dependence on the input waveguide thickness

The waveguide core thickness is imposed by the laser technology employed (in our case 300 nm). However we also previously investigated the sensitivity with respect to the input dielectric waveguide dimensions. Fig. 4.6 shows the SPP excitation efficiency calculated at $\lambda_0 = 1.3$ μm for a 10-period grating with $t_m = 100$ nm. Various grating periods as well as two different duty cycles are investigated. The dielectric waveguide core thickness is varied between 250 nm, which roughly corresponds to the cut-off thickness for the

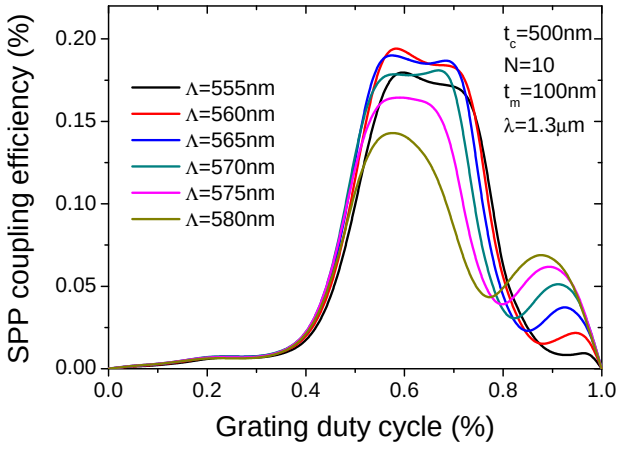

(a)

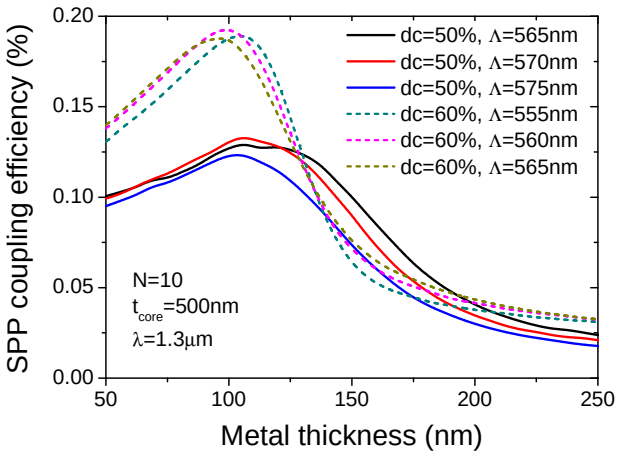

(b)

Figure 4.5: Calculated SPP coupling efficiency as a function of the grating duty cycle dc (a) and the metal thickness t_m (b) for various grating periods Λ. Data in panel (b) are shown for both $dc = 50\%$ and $dc = 60\%$.

fundamental TM mode, and 750 nm.

Since the coupling mechanism relies on the coherent scattering of the impinging guided wave, the SPP excitation efficiency should strongly depend on how this wave interacts with the grating. In particular, we expect the extreme cases to be unfavorable. Near the cut-off thickness ($t_{core} \approx 250$ nm) the mode penetrates excessively into the substrate, while for large values of

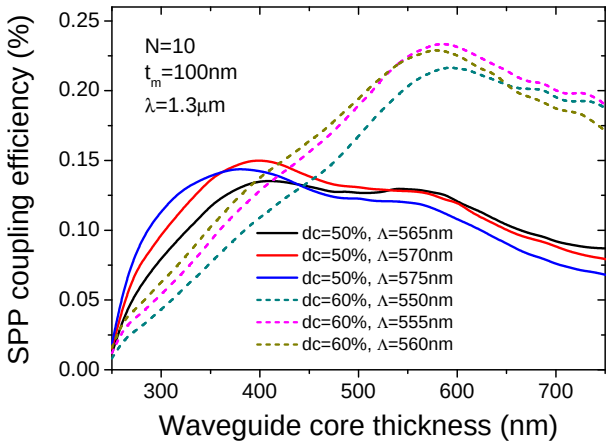

Figure 4.6: Calculated SPP coupling efficiency as a function of the waveguide core thickness t_{core} for various grating periods Λ and for both $dc = 50\%$ and $dc = 60\%$.

t_{core} it is more and more confined in the waveguide core. Hence in both cases the field at the core-air interface is comparatively very weak. The duty cycle also plays a role in this interaction. We find a maximum η of $\approx$ 15% for a 400-nm-thick core layer with Λ = 570 nm and dc = 50%, while with dc = 60%, Λ = 555 nm and tc = 600 nm, the coupling efficiency jumps to 24%. The situation is well illustrated in Fig. 4.5, which highlights the importance of optimizing all the parameters *simultaneously* in order to optimize the coupler. Note that increasing N can further improve the efficiency of a few percents, but to the detriment of a reduced compactness.

We conclude this section by plotting the electric field distribution calculated at λ_0 = 1.3 μm with the aforementioned set of optimized parameters (Fig. 4.7). The SPP wave launched at the metal-air interface is clearly distinguishable, as well as the light scattered in the substrate. Our calculations in Fig. 4.5 showed that $\approx$ 24% of the power propagating in the input waveguide is coupled into the SPP mode. Carefully looking at the diffracted light in the substrate (inset) it is possible to distinguish two main directions that fit well with the angles, found in the paragraph 4.1.1, of the first order(θ_1= -72°, more intense) and of the second order (θ_2= -114°) diffraction.

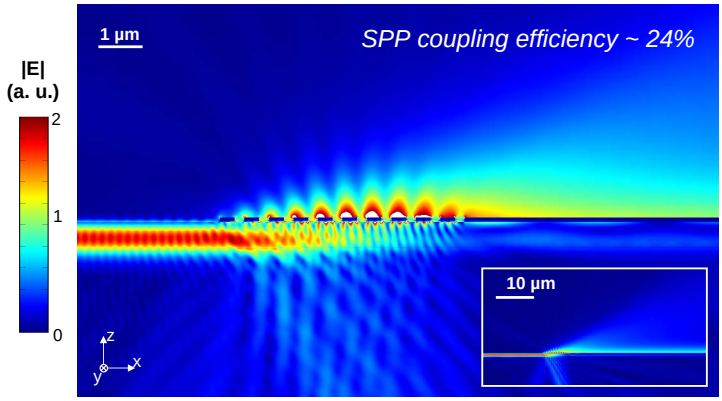

Figure 4.7: Electric field distribution calculated for the problem described in Fig. 4.3 with the optimized parameters $t_{core} = 600$ nm, $N = 10$, $\Lambda = 555$ nm, $dc = 60\%$, $t_m = 100$ nm. The wavelength of the impinging guided wave is 1.3 μm. Data are plotted in linear color scale with an arbitrary unit. Inset: overall view of the simulated area.

4.1.3 counterpropagation device

We present the device experimentally achieved to demonstrate the SPP generation with the grating coupler. The device, shown in Fig 4.8, features two grating couplers along the same direction, both coupling the waveguided mode with the same passive SPP waveguide. Since the SPPs propagate in opposite directions, we call it the *counterpropagation* device. If SPPs are successfully injected onto the passive guide an interference stationary pattern will emerge. This configuration is chosen in order to facilitate the near-field observation and because of its unambiguous answer.

The idea is to realize an electrically pumped version of the double slit experiment. This classic experience of Young was recently revisited in the near-field demonstrating the presence of SPPs on the metal between two slits [96, 97]. In our case the slits are replaced by the gratings to maximize the coupling with SPPs. Furthermore, as in the experiment of Young our light source is coherent since the light is provided by a unique laser (the laser cavity extends also under the SPP metallic passive waveguide).

Compared to the scheme shown in Fig. 4.3 the counter-propagation device presents some important differences. First, the real device must have

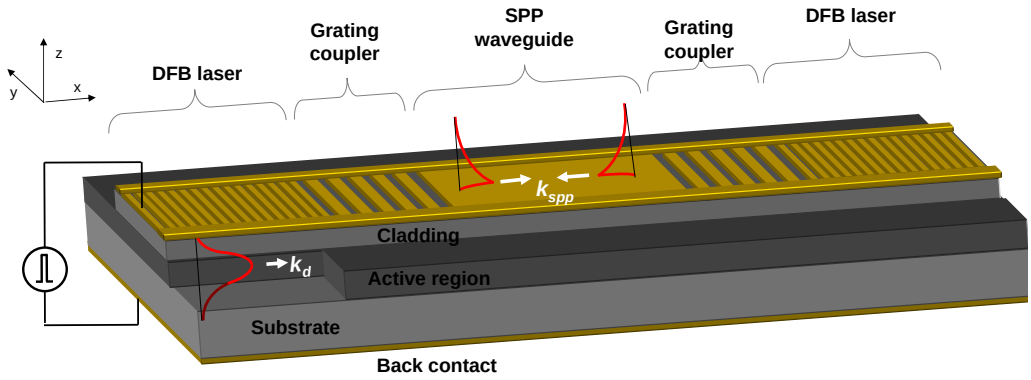

Figure 4.8: Device for the SPP generation based on the counter-propagation geometry [95].

a top cladding. The p-doped cladding is necessary for electrical injection, as a charge reservoir and to create the p-n junction. We adopted the *thin cladding* structure presented in section 3.2.2, which represents a good compromise between cladding thickness and laser threshold values. Secondly, the laser cavity is not a Fabry Perot cavity: the feedback is not based on facet reflection. Instead the resonator exploits a distributed feedback (DFB) mechanism. The DFB resonator is built with a metallic grating, as in [63, 67, 98], along the ridge length (see the lateral schematic in Fig. 4.9c).

Compared to the air confinement resonator (Fig.4.9a) the DFB permits a more homogeneous current injection, because the grating is laterally connected to the top contact and participates to the injection. Compared to the fully-metallic resonator (Fig.4.9b), it allows one to decrease the mode losses and consequently the laser threshold. Furthermore in the DFB resonator the feedback is distributed and the mode is less sensible to the facet quality. Finally, the DFB emission is spectrally single mode, which facilitates the observation of the SPP interference pattern.

Note: the DFB will be discussed in more detail in Chapter 6. Here we consider it as a tool. It is a first order grating that must satisfy the condition $k_d = \pi/\Lambda_{DFB}$, with $\Lambda_{DFB} \approx 200$ nm. Since the core region where the dielectric mode propagates is a laser active region we will re-name k_d as k_{laser}.

The schematic of the device in Fig. 4.10a illustrates the top view of the

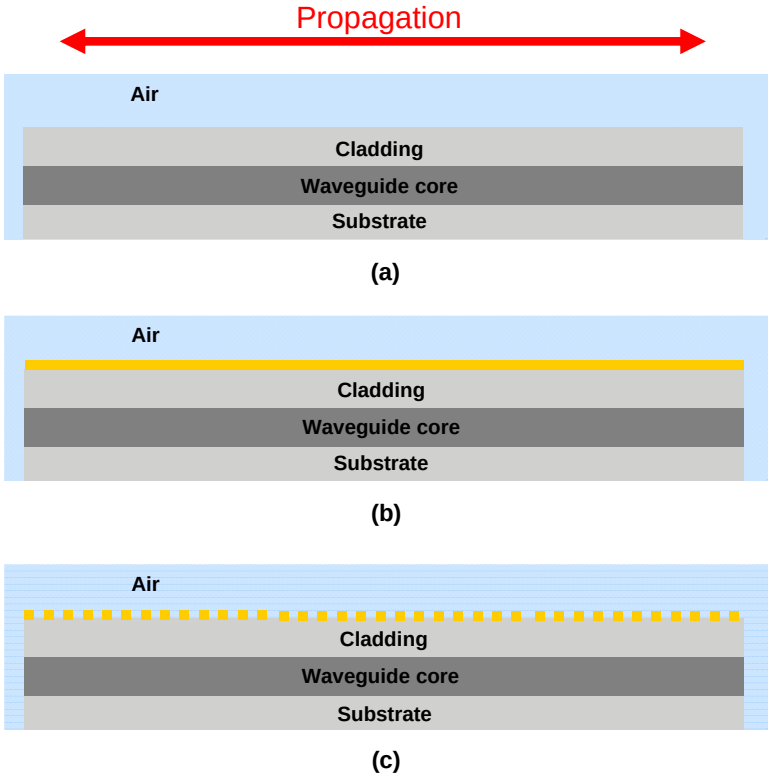

Figure 4.9: Different types of resonators: Fabry-Perot cavity with an air confinement waveguide (a), fully-metal (b), and a DFB resonator with a metallic grating (c). The mode propagates in the plane.

counter-propagation device, highlighting the wavevector matching, from the DFB wavevector (red arrow) to the SPP wavevector (blue arrow) through the coupler (bicolored arrow), $\Delta k = 2\pi/\Lambda = k_{laser} - k_{SPP}$. The first-order grating of the DFB, the coupler gratings, and the passive plasmonic waveguide are all obtained with a single fabrication step, using the electron beam lithography (EBL), evaporation and lift-off. The use of EBL is necessary, because of the extremely small size of the DFB pattern that cannot be achieved with conventional optical lithography. The metallic fingers are $\approx$ 100 nm large, and they are separated by $\approx$ 100 nm. However, even by EBL, it is not straightforward to obtain such a high resolution, subsequently permitting a lift-off. The development of a reproducible processing recipe is one of the technological achievements of this work, detailed in Appendix B.2.

Device fabrication and preliminary characterization

In Fig. 4.10b we show the result of the lift-off after the EBL, imaged with the SEM. The whole metal pattern is 7.8 μm large and it is $\approx$ 1 mm long, but only the central part with the passive SPP waveguide is shown. The DFB gratings continue for $\approx$ 500 μm on each side. In order to obtain a reproducible lift-off we could not deposit the simulated optimal metal thickness (100 nm), but we found a compromise at a total thickness t_m = 70 nm: 3 nm of Ti and 67 of Au. The bottom-right close-up of Fig. 4.10 shows in detail the 4 μm-long-coupler, which is composed of 7 fingers of periodicity 560 nm and duty cycle 55%. We also fabricated devices with couplers of 10 slits, which correctly work. The passive plasmonic waveguide is a strip of length L_{strip}= 30 μm that is long enough to contain several SPP interference fringes (we estimate $\approx$ 45 fringes). This ensures that a relatively wide zone will be free from stray radiation originating from the grating couplers and lead to a clear near-field detection of propagating SPPs.

After the first EBL and lift-off step, the devices are processed as air-confinement devices in order to laterally contact the metal patterning and avoid burying the ridge center. The detailed steps of the fabrication can be found in Appendix B. The devices were processed into 9 μm wide, 450 nm deep mesa ridges and cleaved at a length of 1 mm.

Preliminary measurements of the devices confirm the laser regime and allowed a spectral analysis of the signal emitted from the facets. The emission is collected with a cleaved multimode fiber with the set-up detailed in Appendix C.2. The device is almost entirely covered by the DFB grating and the central part with the couplers and the passive waveguide represents less than the 5% of the total device length. Consequently the emitted spectra corresponds to the DFB, in which the single frequency is imposed by the grating periodicity. Fig. 4.11a shows the collected spectra of several devices with different grating periods Λ_{DFB} = 196-198-199-200 nm. A single mode emission, correctly tuning with the grating period, is obtained.

Figure 4.11b shows the room-temperature (RT) electrical characterization and the optical emission of a 1 mm long counter-propagation device. The laser threshold current density is 4.5 kA/cm^2. The emission spectrum (4.11b, inset) shows single mode operation at $\lambda \approx$ 1300 nm. These measurements are performed in pulsed injection regime at a duty cycle of 1%, with pulse frequency 100 kHz and pulse width of 100 ns. However the device can operate

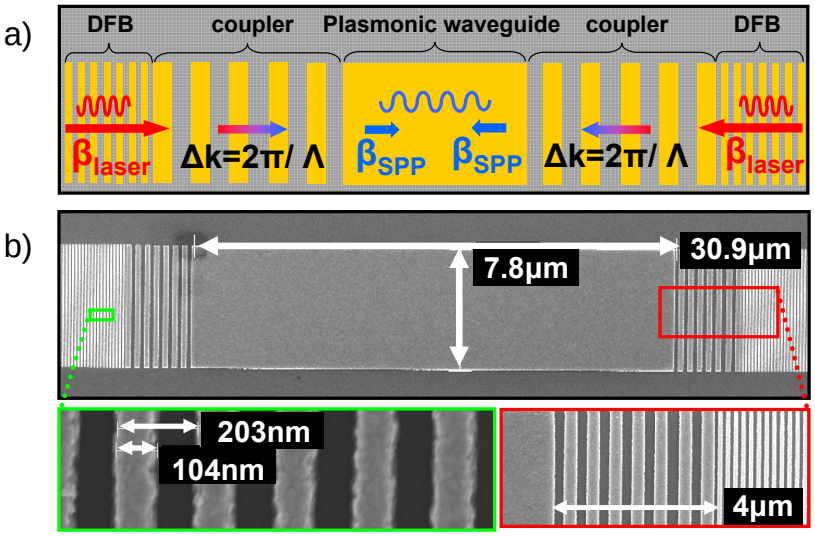

Figure 4.10: (a) Schematics of the top metal patterning which defines the three basic device components: first-order grating for the DFB cavity, the coupler grating, and the passive plasmonic waveguide. The configuration is symmetric in order to inject SPPs from both sides of the passive waveguide (counterpropagation configuration). The red and blue arrows show the propagation direction and are proportional to the wavevector of the DFB mode and of the SPP mode, respectively. The bicolored arrows are proportional to the momentum provided by the couplers to match DFB and SPP modes. (b) SEM image of the top metal patterning with closeups of the coupler and of the DFB grating. The surface is patterned using electron-beam lithography, followed by lift-off of a 70 nm thick metal layer (3 nm Ti, 67 nm Au) deposited with electron-beam evaporation.

up to a duty cycle of 10% with a pulse frequency of 1 MHz.

Far-field characterizations

We performed a far-field characterization of the counter-propagation device using the CCD camera, described in Appendix C.1. The camera is positioned above the operating device allowing to collect the photons emitted in the vertical direction. In laser regime the majority of the light is propagating in the cavity mode with an in-plane wavevector, but a small fraction of light

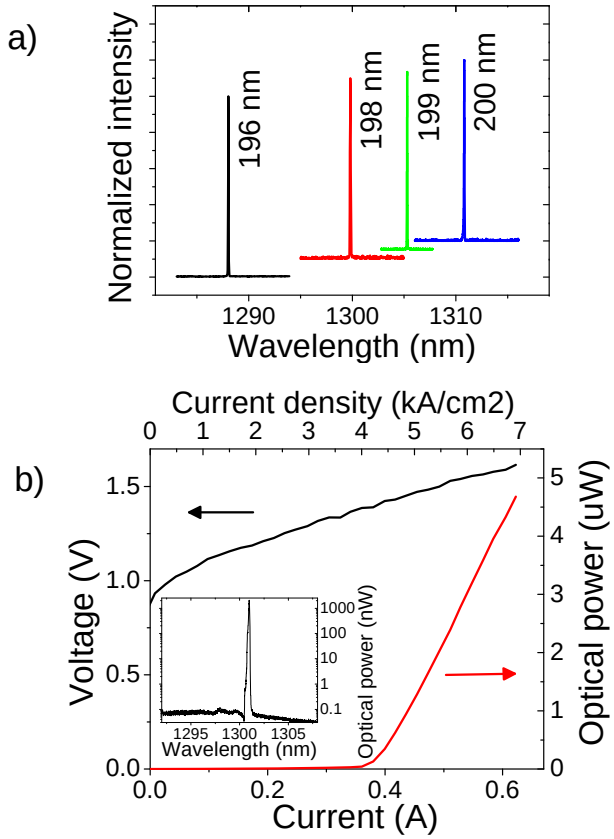

Figure 4.11: (a) Single mode spectra of DFB lasers with different grating periods (196, 198, 199, and 200 nm). The spectra are measured at room temperature (RT) in pulsed regime with an optical spectrum analyzer. They are normalized and a vertical offset is introduced for clarity. (b) LIV characterizations at RT in the pulsed regime (1% duty cycle) of a typical device with $\Lambda_{DFB} = 198$ nm. The inset shows the spectrally single mode emission collected from the device facet at an injection current of 500 mA. The side mode suppression ratio (SMSR) is more than 40 dB, and the full width at half-maximum (FWHM) is $\approx$ 12 GHz (0.07 nm).

is also diffused perpendicularly to the plane. We observe the scattered light in correspondence of the device facets and of the couplers. Indeed not all the light is coupled from the laser waveguide into the SPP passive waveguide, but a fraction of it is diffused in all the space.

Thanks to the spots due to the diffraction on the facets, it is possible

to easily focus the CCD camera on the device surface, and then localize the grating couplers.

Another source of light in the vertical direction is the luminescence of the AR, always present even in the laser regime. The luminescence is isotropic and seeps through the DFB grating. Figure 4.12 clearly shows the luminescence coming from the DFB along the ridge. The interruption at the image center corresponds to the passive SPP waveguide where the luminescence light is completely screened by the continuous metallic strip. The schematic of the metal patterning on the top helps to read the infrared images. The facets are outside of the field-of-view. We observe that increasing the injected current the luminescence coming from the DFB waveguide increases in intensity. Close to threshold, at 350 mA (see LI in Fig. 4.11b), a darker green appears in correspondence to the couplers. In laser regime, at 450 mA, two bright spots stand out against the luminescence which remains more or less constant compared to the threshold (electro-luminescence clamping). Probably small fabrication defects are the causes of the asymmetric brightness of the spots, which should be perfectly equivalent. This characterization validates that the couplers diffract the laser light of the DFB cavity. There are no significant leakages and only the luminescence light is collected, above the first order DFB, correctly clamping in the laser regime.

Near-field characterization

SPPs cannot be observed in the far-field due to their evanescent and non radiative nature. The best way to have a direct evidence of the SPP presence is a near-field analysis. The counter-propagation sample was measured with three different near-field scanning optical microscopes (NSOMs). We first report the two measurements obtained with a tapered fiber NSOM and with an aperture-less NSOM (a-NSOM). We then show the measurement obtained with a transmission NSOM based on an hollow metal coated pyramid [95]. All the set-up are described in more details in Appendix C.3.

The tapered fiber NSOM characterization was performed in INL institute, Lyon, thanks to the collaboration with the group of Segolene Callard. The tapered fiber perturbs the SPP evanescent field, collecting the emitted photons and guiding them toward an InGaAs detector. Thanks to a monochromator we were able to measure the field at a selected wavelength. The result is shown in Fig. 4.13b. The same setup with a metallic coated

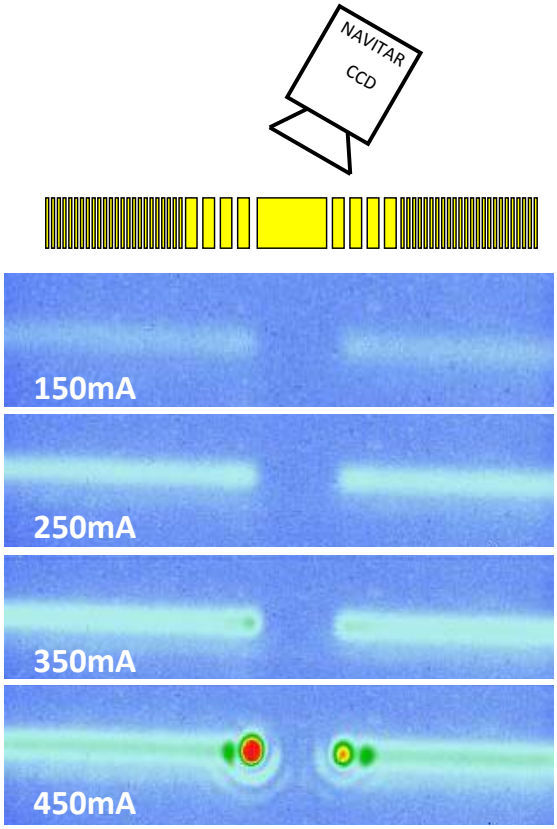

Figure 4.12: The far-field measurements of the counter-propagation device, as a function of the injected current, are obtained with a CCD camera. A schematic of the top metal patterning (top panel, bright yellow) helps the interpretation of the CCD camera measurements. By increasing the injected current the luminescence from the DFB waveguide increases. In the laser regime (450 mA) two intense spots are observable in correspondence of the coupler gratings, while the luminescence coming from the DFB waveguide has about the same intensity. In this case the gratings are diffracting the laser light, coupling with the SPP modes, but also in the vertical direction. Note that no far-field is observable between the couplers, indeed SPPs are non radiative.

fiber gave an analogous result shown in Fig. 4.13c.

The device was then imaged with the a-NSOM used for the mid-IR measurements at the ESPCI institute (see section 2.5.1), but using an InGaAs

detector. In this case the tip scatters the evanescent field of the SPPs, causing a diffusion that is detected in the far-field, focusing the signal on the detector. The result is shown in Fig. 4.13d.

In both measurements we can clearly discern the interference pattern due to the SPP couterpropagation on the passive waveguide. These very encouraging preliminary results pushed us to the development of a more precise near-field analysis that could improve the measurement resolution and prove without any doubts the SPP generation.

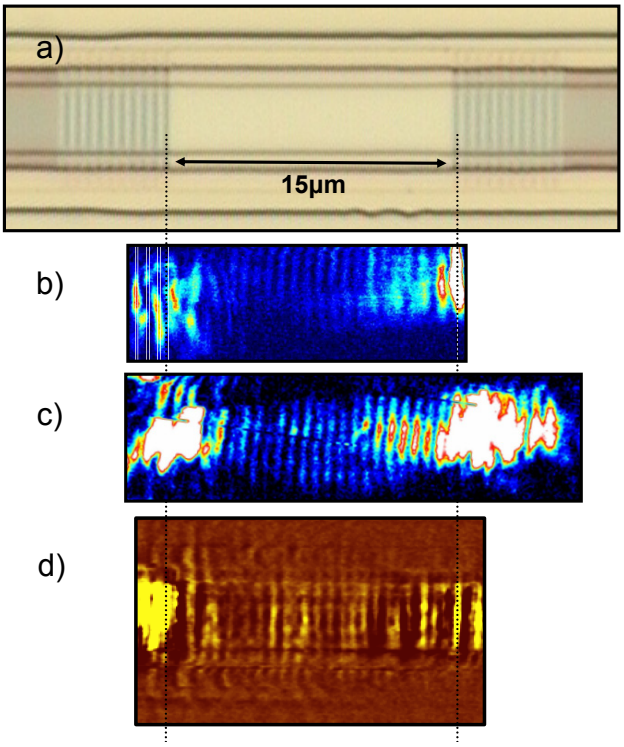

Figure 4.13: (a) Optical microscope image of a device with a SPP waveguide of 15 μm and 10 fingers in the coupler grating. The result of the measurements, obtained with (b) the tapered fiber NSOM, (c) the previous tapered fiber NSOM with a metal coating and (d) the a-NSOM, show the presence of an interference pattern on the SPP waveguide. The measurements in (b) and (c) are collected at $\lambda = 1303$ nm.

Our collaborators at the *Institut Langevin*, ESPCI Paris, developed a transmission SNOM set-up in the telecom frequency range. This technique,

based on a commercial Witec NSOM, is generally used in the visible frequency range and it is for the first time implemented in the NIR. The diffusive tip is replaced by an hollow pyramid that scatters, on its edge, the evanescent SPPs and transmits the light through a nanoaperture of diameter ≈ 100 nm. The sample stage is translated during the scans using piezoelectric translators, while the tip is maintained at a fixed position. The tip-sample distance control relies on the classical beam-deflection principle using a 980 nm laser. The beam is focused through a microscope objective onto the surface of the cantilever, 100 μm away from the pyramid. A dichroic mirror sends the reflected laser into a segmented photodiode which measures the cantilever deflection. The optical signal transmitted through the nanoaperture is collected by the same objective and focused on a multimode fiber connected to a thermoelectrically cooled InGaAs detector. The fiber itself acts as a confocal pinhole which is optically conjugated with the nanoaperture in the hollow pyramid. Further details on the setup can be found in Appendix C.3. The current injected in the device is modulated, hence the collected signal is demodulated at this same frequency. The near-field (xy) images of the SPPs at the device surface are obtained when scanning the device laterally with the apex of the hollow pyramid permanently in contact with the surface.

Identical measurements have been performed on SPP devices and on *reference* devices (i.e., devices – processed simultaneously from the same wafer – where the passive metallic waveguide is missing). Panels a and b of Fig. 4.14 show the optical microscope images of a reference and SPP device, respectively. The topographic signal for both devices – collected *simultaneously* with the near-field signal – is shown in Fig. 4.14c and d. Finally, Fig. 4.14e and f shows the near-field images. Plasmonic interference fringes are clearly visible on the passive metallic waveguide between the two couplers in the SPP device only, while no analogous fringes can be observed on the reference device, since SPPs do not exist at the interface between air and a dielectric. The fringes stem from counter-propagating SPP waves traveling on the surface of the metallic strip, with opposite wave vectors $+k_{SPP}$ and $-k_{SPP}$. Their presence proves that SPPs are generated and launched into the passive metallic waveguide. The couplers simultaneously inject SPPs into the passive waveguide and diffract part of the light from the laser cavity into free space, as witnessed by the bright spots observed above the coupler areas.

We have performed 2D finite element electromagnetic numerical simula-

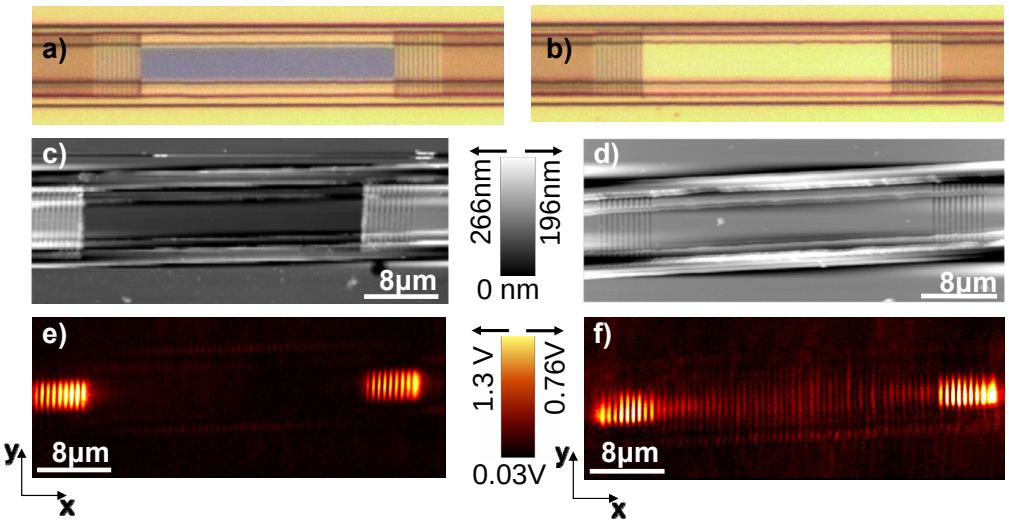

Figure 4.14: (a, b) Optical microscope image of a reference device (no passive metallic waveguide) and a SPP device. (c) Topographic image on the reference device (subtraction filter applied). (d) Topographic image on the SPP device (subtraction filter applied). (e, f) Near-field optical image on the reference (panel e) and SPP (panel f) device. The near-field optical signal is acquired simultaneously with the topography. Both devices are measured at room temperature in pulsed mode (duty cycle = 10%) at an injected current of 800 mA. The near-field optical image on the SPP device clearly shows the presence of the plasmonic interference pattern on the passive metallic waveguide, while no similar signal is visible on the reference one. A careful analysis of panel (e) reveals interference fringes on the ridge sides between the two couplers. These oscillations stem from SPPs propagating on the lateral gold contacts used for the current injection. This subtle observation further strengthens the result.

tions of the lateral (x,z) section of the device, supposing an infinite width of the ridge. The 2D character of the simulation reduces the computational load and allows one to take into account the reduced thickness of the metallic layers (70 nm) and at the same time the considerable length of the full structure (more than 50 μm). In the simulation we do not take into account the DFB grating, replacing it with a guide without metal on the top, as in Fig. 4.9a. The lateral profile of the DFB mode and the mode without metal

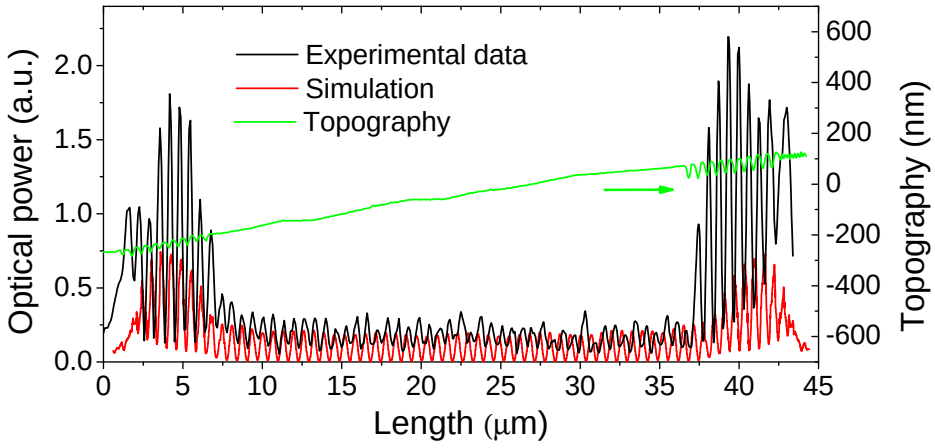

Figure 4.15: Intensity of the near-field optical signal at the device top surface compared with simulations. The measured data (black curve) correspond to a 1D cross section taken from Fig. 4.14f. The numerical simulation (red curve) is a 1D cross section of the squared modulus of the electric field taken 10 nm above the device surface. The topographic measured signal (raw data, green curve) allows one to correlate the EM near-field with the top metallization. The slight slope of the topography corresponds to an angle of $\approx 0.5°$, and it does not affect the optical measurements.

on the top is similar and the confinement factors almost identical. This reasonable approximation simplifies the simulation, without meshing the lateral section of the DFB finger, that has a size of 70 x 100 nm. The fundamental TM modes are injected from the left and the right side of the simulation box, exactly as in the simulation of the single coupler in section 4.1.2.

Figure 4.15 (red line) shows a longitudinal cross section – taken at 10 nm above the device surface – of the electric field squared modulus obtained from the simulation. The agreement with the experimental near-field signal (black line) taken from Fig. 4.14f is excellent, in terms of SPP wavelength and global trend of the signal. The relatively larger signal on the coupler zones with respect to the simulation possibly stems from higher light scattering, due to fabrication non-idealities.

The numerical simulation also provides the extension of the interferential plasmonic pattern in the x - z plane. Figure 4.16a shows the axis definition and a schematic view of the simulation domain. The result of the simula-

tion (Fig. 4.16b) reveals that the full interference pattern is composed of a pure SPP component, highly confined up to ≈ 800 nm close to the metallic surface, and a quasi-cylindrical wave component [64]. As mentioned for the double slit experiment, the latter waves originate from the couplers and counter-propagate on the metallic waveguide like the SPPs, with identical wavevector magnitude. The NSOM system employed in this work can perform measurements as a function of the tip-to-surface distance, in a plane perpendicular to the device surface to record (x - z plane) cross sections of the field distribution, thus experimentally reproducing the simulation conditions. Figure 4.16c presents such measurement, which is in excellent agreement with the theory. It is even possible to qualitatively distinguish the presence of the quasi-cylindrical waves that extend up to several micrometers from the surface. The maximum of the intensity at the metal-air interface provides evidence of the SPP presence.

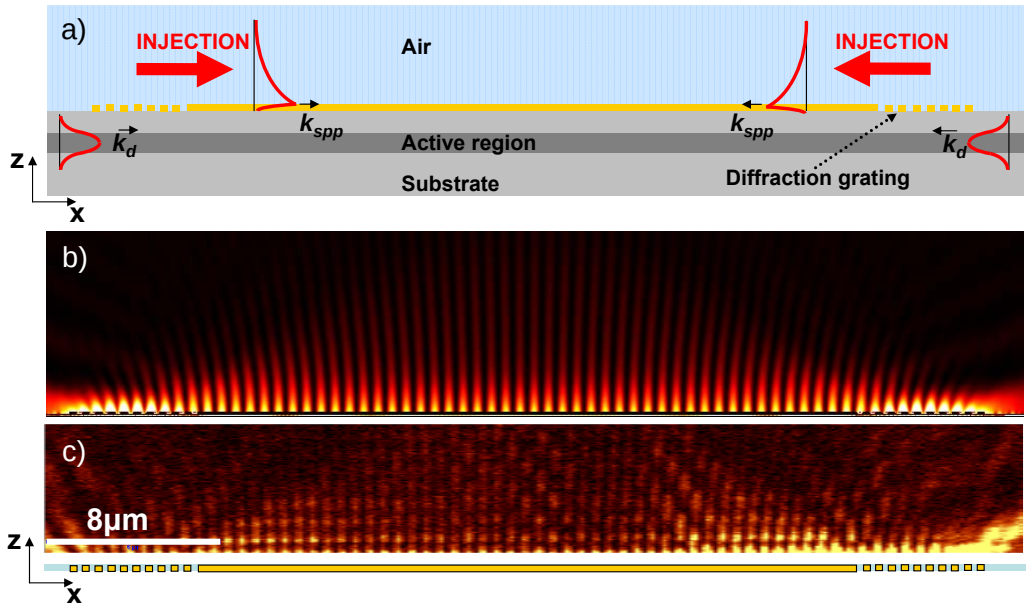

Figure 4.16: (a) Schematic side view of the device. The red curves schematically represent the mode profiles of waveguided SPP modes. (b) Color-plot of the calculated squared modulus of the electric field in the x-z plane (SPP interference pattern). (c) NSOM measurement in the x-z plane, i.e., NSOM signal as a function of the tip-to-surface distance at several x-positions on the sample. The measurement qualitatively agrees with the simulation in panel b. The vertical intensity modulation is a perturbation due to interference between light directly transmitted through the nanoaperture and light scattered by the pyramid apex and back-reflected on the device surface into the nanohole.

4.2 End-fire coupler approach

The end-fire coupling is an alternative solution to generate SPPs using a dielectric mode, as shown in the schematic in Fig. 2.8. A schematic of the integrated *end-fire* device is represented in Fig. 4.17. A similar device has been already investigated in the literature by the group of J. Meyer [99].

In this device most of the light is reflected at the facets of the Fabry-Pérot cavity, in order to provide optical feedback for the laser regime. However a fraction of the waveguided mode is transmitted through the facets, in partic-

ular we consider the right facet in Fig. 4.17. The transmitted light couples with radiative waves, but also with the SPP mode of the passive waveguide in front of the Fabry-Perot cavity. The effort in the device design is toward a maximum coupling into the SPP mode. In the following we describe the device and we report the device characterization in the far field.

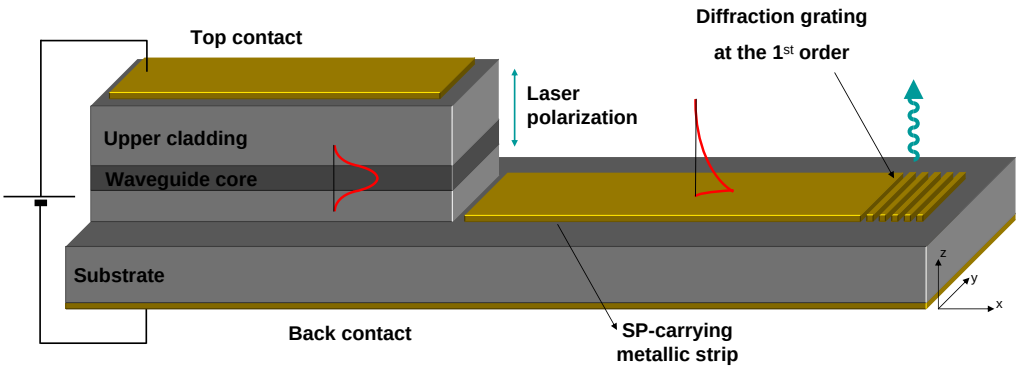

Figure 4.17: Device for the SPP generation based on the end-fire geometry.

4.2.1 Design and simulations

In the grating coupling we paid particular attention to the phase matching condition between the waveguided mode and the SPP mode. On the other hand in the end-fire coupling the wavevector is not conserved and no tool is required for the wavevector adaptation between the dielectric mode of the cavity, $k_d = n_d k_0$, and the SPP mode, $k_{SPP} \approx k_0$. The difference in wavevectors, or equivalently in the effective indexes, only changes the fraction of the transmitted and reflected light (see formula 3.11). In the end-fire configuration it is possible to play on the mode overlap to increase the coupling efficiency. The geometry of the dielectric waveguide is given by the adopted laser. The only tunable geometric parameter available is the relative position between the waveguides. The profile of the laser mode is approximately a gaussian with a width of less than 1 μm, comparable with the extension of the SPP in the air.

Figure 4.18 shows a schematic of the profile of the two modes. We can vary the vertical height (h) of the SPP waveguide with respect to the center of the AR. This height must be sufficiently large to let transmit the laser light,

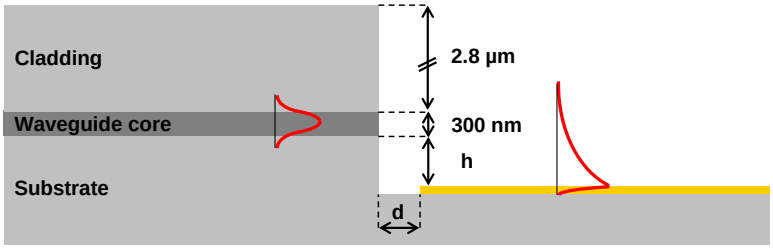

Figure 4.18: Schematic view of the end-fire geometry.

but also not excessively large in order to maintain a spatial overlap between the modes. The horizontal distance (d) between the facet and the passive strip must be as short as possible, leaving at the same time a reasonable gap, compatible with the precision of an alignment with optical lithography (in the simulations we fixed this value to 1 μm).

Analogously to the grating coupling simulations (section 4.1.2), we performed finite element simulations injecting the fundamental TM mode from the left side of the laser waveguide. We can define a coupling efficiency as the ratio between the intensity of the SPP and the intensity of the dielectric mode. Complete conversion into the SPP mode is η=100%. However, being a non-resonant coupling, we did not perform a systematic study of the efficiency, which weakly depends on h.

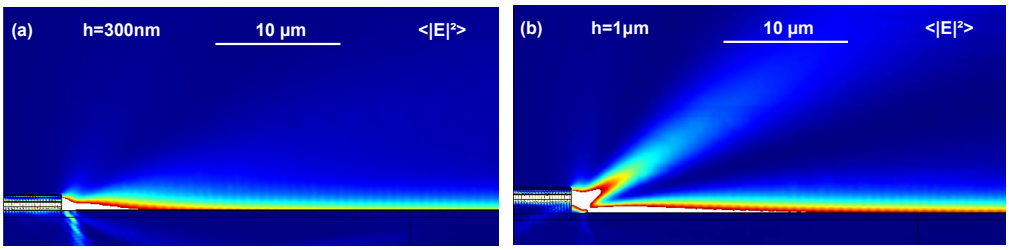

Figure 4.19: Finite element simulations representing the squared modulus of the electric field in an end-fire device with (a) h = 300 nm and (b) h = 1000 nm. In both cases the dielectric mode couples with the SPP, but in the first case we observe a leakage in the substrate, while in the second a reflection on the gold layer that originates a beam at an angle of $\approx 30°$.

Figure 4.19 presents the result of the simulations for $d = 1$ μm and two

values of h: (a) h = 300 nm and (b) h= 1 μm. We plot the square of the electric field modulus (saturated color plot) to highlight the SPP propagation along the metallic strip. To avoid undesired reflections we used absorbing layers at the simulation box boundaries: in the air, in the substrate and at the SPP waveguide end. Nevertheless a weak modulation of the SPP intensity can be identified as a consequence of SPP reflection at the right boundary. In Fig. 4.19a we have a good coupling, with an efficiency of $\eta \approx 20\%$, but some photons are also lost in the substrate. In Fig. 4.19b the coupling efficiency is higher, $\eta \approx 40\%$, no light is lost in the substrate, but we observe a light reflection on the gold layer into a radiative mode in the air.

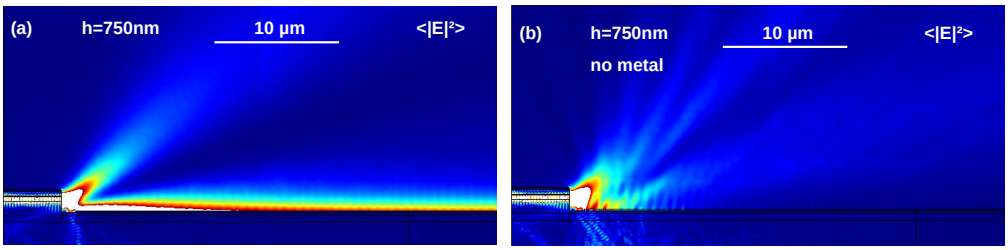

Figure 4.20: Finite element simulations representing the squared modulus of the electric field in an end-fire device with h = 750 nm. In (a) we show the coupling with the SPP giving an efficiency close to 40%. In (b) the metallic strip is absent. As expected no SPP is generated in this case.

Figure 4.20 shows the simulation for an h = 750 nm, (a) with and (b) without SPP waveguide. In (b) the SPP waveguide is replaced by air, the SPP clearly does not propagate and also the radiation in the air is modified.

If the etching is much deeper, reaching a h = 2.4 μm, the light is emitted in the air at three different angles and only a fraction is coupled into the SPP mode. This case is represented in Fig. 4.21 and the estimated efficiency is $\eta \approx 15\%$. In conclusion, the end-fire geometry shows a weak dependence of the coupling efficiency on the h parameter that provide in all case a good coupling. This tolerance is extremely good for fabrication

The SPP detection in this system requires a careful consideration. We saw in the counter-propagation that the SPP interference pattern facilitates the near-field observation, but this solution is not possible with the end-fire coupling geometry. We need here to detect propagating SPPs. In the mid-IR

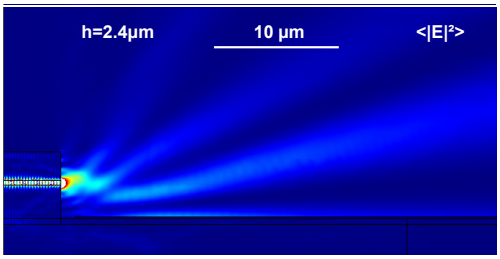

Figure 4.21: Finite element simulation representing the squared modulus of the electric field in an end-fire device with extremely large h = 2.4 μm. Even if more radiative modes are observable the coupling efficiency with the SPP is close to 15%.

frequencies we could measure with an a-NSOM an average SPP signal on the passive strip (see Fig. 2.21).

However to detect the SPP presence without the need of a near-field analysis, we designed the device to detect also in far-field the SPP presence. The idea is to indirectly observe the SPP, by measuring the photons originated by the diffusion of the SPP. In particular the SPP diffuses at the end of the passive strip, as shown in Fig. 4.22a. To enhance the measurable signal we can position a grating with a periodicity equal to the wavelength of the propagating SPP. This second order grating mainly emits in the vertical direction, simplifying the far-field detection. In Fig. 4.22c we report an example of finite element simulation of a second order grating. We show a closeup of the resulting field intensity on a grating composed of 5 periods of 1.3 μm. We clearly observe a reflection of the SPP, providing a modulation on the left of the grating, and diffraction in the vertical direction. Additional finite-difference time-domain (FDTD) simulations [100] indicate a grating scattering efficiency of $\approx 3\%$.

4.2.2 End-fire device

The device was processed on the *thick cladding* structure presented in section 3.2.2. The fabrication, detailed in Appendix B.3, requires ICP etching to obtain a vertical facet in front of the SPP waveguide. The etching is performed in collaboration with LPN by I. Sagnes using an inductively coupled plasma (ICP) reactive ion etching (RIE). This technique allows more

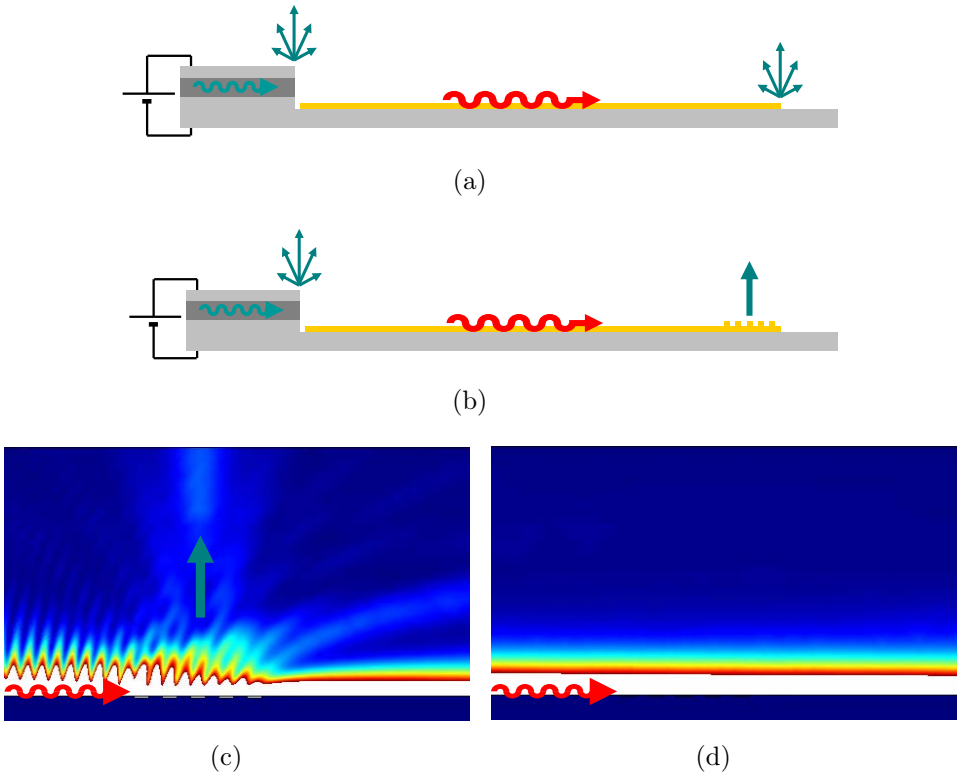

Figure 4.22: Schematic that illustrates the possibility to indirectly detect the SPP *via* a camera in the far-field. (a) The SPP scatters off at the edge of the metallic passive strip (b) The vertical emission can be engineered with a second order grating. Result of the finite element simulation showing the intensity of the electric field on a second order grating (c) and on a flat surface (d). Note: the grating partially reflects the SPP wave.

isotropic profiles compared to the simple RIE and compared to the wet etching (see section B.3). The excellent result of the ICP etching is shown in Fig. 4.23: it is possible to perfectly discern the 9 quantum wells of the AR. The etching rate of the ICP, faster than expected, gave an $h = 2.4$ μm, as in the simulation presented in Fig. 4.21.

The top view of the final device is presented in Fig. 4.24, showing the 22-μm-large ridge on the left and the 60-μm-large SPP waveguide on the right. The Fabry Pérot cavity is typically 1 mm and terminates with a cleaved facet, not visible in the figure. The SPP waveguide is close to the laser

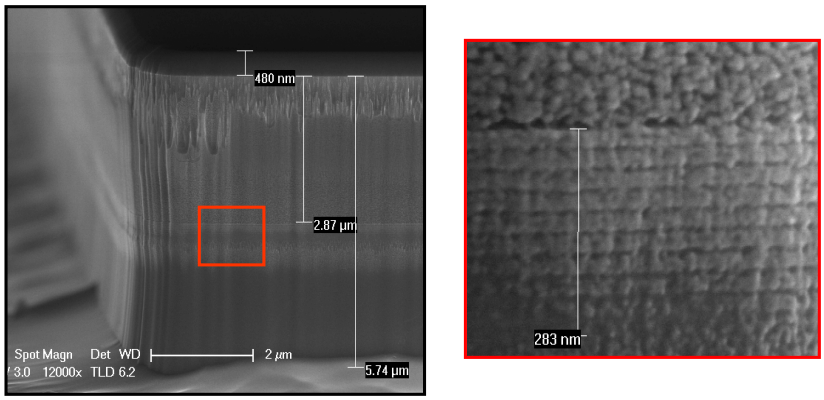

Figure 4.23: SEM image of the ICP etching result. The close up allows to discern the nine QWs of the AR.

facet leaving no appreciable gap in this picture. The surface of the sample presents a notable roughness caused by the dry etching. This increases the propagation losses of the SPP and also induces some radiative scattering.

Figure 4.25 shows the light-current-voltage (LIV) characteristic of an end-fire device, with the light signal collected from the cleaved facet. The measurement is performed at RT in pulsed regime with a duty cycle of 1%. However, the device can also operate at a duty cycle of 10%.

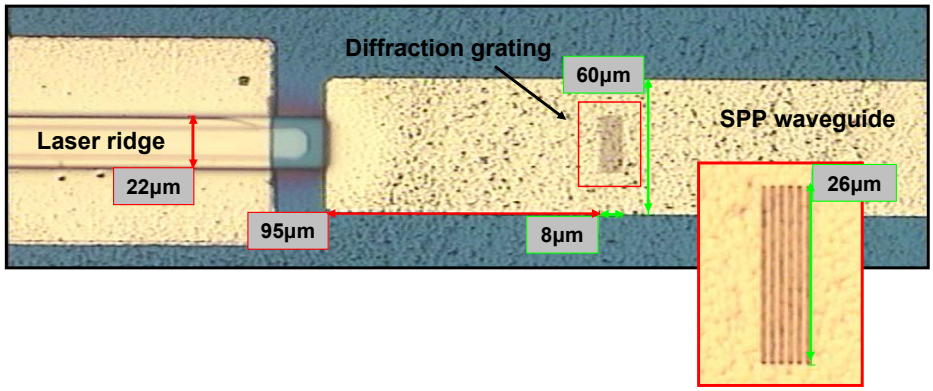

Figure 4.24: Optical microscope image of an end-fire device for SPP generation.

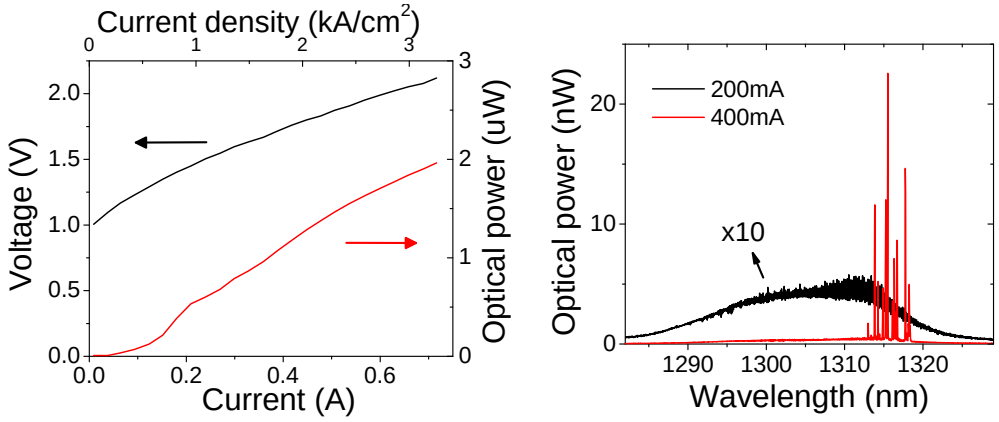

(a) (b)

Figure 4.25: Characterization of an end-fire device. The LIV (a) is taken in pulsed regime at a frequency of 100 kHz and a pulse width of 100 ns (1% of duty cycle). In (b) a luminescence (multiplied by 10) and a laser spectrum.

Far-field characterizations

We were not able to obtain a measurement of the SPP propagation in near-field analogously to the measurement in the mid-IR shown in Fig. 2.21. Our analysis is limited to the far-field characterization, performed with an infrared CCD camera (the set-up details can be found in Appendix C.2). The device is operated in pulsed regime at a frequency of 1 MHz and pulses of 100 ns (duty cycle of 10%). Figure 4.26 shows the CCD image of the whole device. The top metal contact and the SPP waveguide result in dark blue, standing out against the light blue of the laser diffused light. Two bright spots are visible at the facets. The brightest one is in front of the SPP waveguide. The dry etched facet is less sharp-cut than the cleaved one and diffuses more light. Figure 4.26c shows a measurement in far-field of the cleaved facet of the laser at 400mA. The image, obtained with a CCD camera, shows a uniform emission along the ridge width.

The proof of the SPP generation is provided by the spots on the SPP waveguide originating from the two 2^{nd}-order gratings. The gratings are located at 100 μm and 200 μm from the laser facet. The close up in Fig.4.26b clearly shows that the first grating emits more light than the second one, because, as expected, the SPP loses intensity along the propagation on the

passive waveguide. Moreover, the close-up in Fig.4.26b allows one to indirectly observe the surface roughness thanks to the scattered light coming from the superficial imperfections.

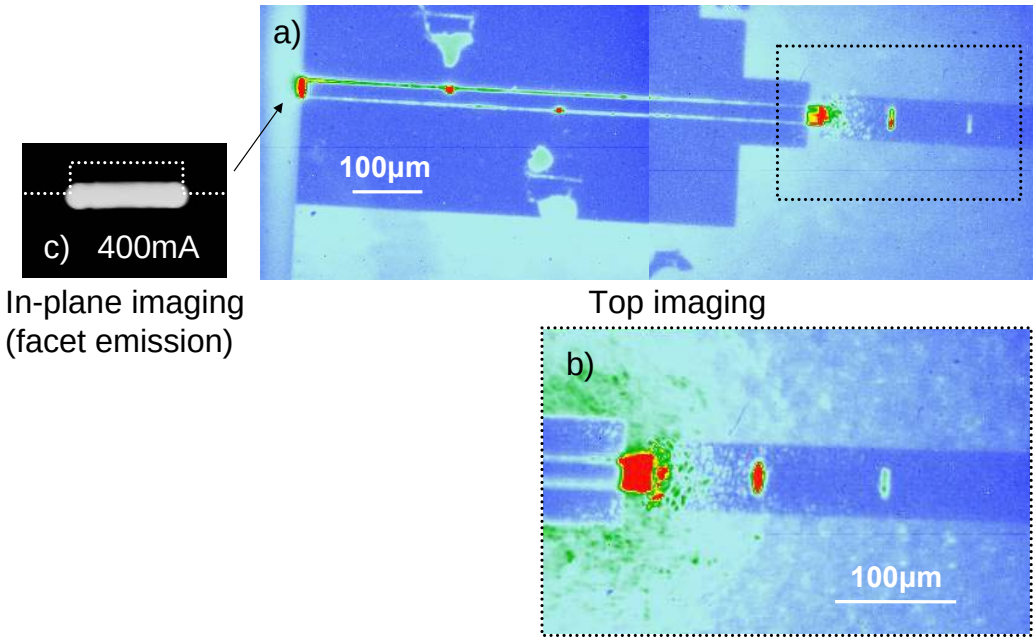

Figure 4.26: Infrared images of the top of the end-fire device. (a) The whole device (b) The close-up of the cavity facet and the gold strip with the two gratings. As expected the gratings are vertically diffracting the propagating SPPs. (c) In-plane infrared image of the laser facet obtained using a CCD camera. The white dotted line roughly indicates the facet profile.

4.3 Conclusions

A semiconductor-based techniques for SPPs generation, by electrical injection and at telecom wavelengths, is developed and demonstrated.

We demonstrate an end-fire configuration probing SPPs by diffraction gratings.

We also develop an original integrated configuration based on grating couplers. This elegant design is demonstrated by NSOM measurements, which also permits to gauge the vertical extension of the SPP extension. A main

advantage of this geometry is the accessibility of the plasmonic field on the device top.

Chapter 5

Amplification of SPPs

This chapter is dedicated to the amplification of surface plasmons. Our results are reported after a necessary contextualization of the current state of the art.

The first section introduces the state of the art for SPP amplifiers and lasers, by summarizing the experimental milestones. We explain the concept of SPP amplification by stimulated emission of radiation, called SPASER, in analogy to the LASER. The review concerns SPPs propagating on a single interface, also with examples of sub-wavelength confinement in one or two directions. For the sake of completeness we dedicate the last part of the review to the amplification of SPPs confined in all the three dimensions, used to achieve nanolasers. Indeed the stimulated emission of SPPs is a concept of great interest in the field of nano-optics because it can allow the demonstration of the laser effect in a sub-wavelength volume smaller than the diffraction limit.

In this context we propose a compact semiconductor approach for the amplification of propagative SPPs and we demonstrate a laser operating on a hybrid plasmonic mode, by electrical injection and at room temperature. We performed original near-field optic measurements to directly prove the plasmonic character of the hybrid mode.

5.1 Experimental state of the art

We review the experimental milestones of SPP amplification, for the single interface arrangement and other types of waveguides, as the long-range SPP,

and the dielectric-loaded SPPs. Other theoretical studies and estimates of the plasmonic losses can be found in the review by Berini et al. [101].

The concept of SPP amplification was firstly introduced in 1979 by Plotz et al. [102]. They theoretically proposed to amplify the total internal reflection by pumping a SPP with a dye solution. The SPP would be generated in the Kretschmann arrangement within a thin film of Ag (about 50 nm) as shown in Fig. 5.1a. The dye solution is in contact with the metal layer. The computed reflectance as a function of the angle, shown in Fig. 5.1b, increases more than one by increasing the gain (here called α). The calculation are performed at $\lambda \approx 1$ μm.

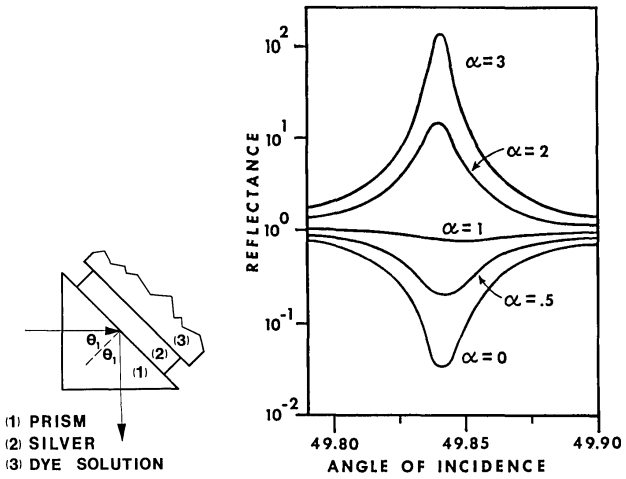

(a) (b)

Figure 5.1: (a) Proposed geometry to enhance reflectance using surface-plasmon excitation [102]. (b) Reflectance *vs* angle of incidence, near the surface-plasmon angle, for several values of the gain parameter α (defined in [102]).

5.1.1 Single interface SPP

The first SPP laser effect was demonstrated in a quantum cascade laser structure at far-infrared wavelengths [103]. However, this device owes its success partly to the low absorption of metals and poor field confinement at such wavelengths (see Tab. 1.2). The stimulated emission of SPPs at

optical frequencies was experimentally proven in 2005 in the Kretschmann configuration [14]. In Fig. 5.2a we see, coming from the right, a pump probe that excites the dye solution of cresyl violet in ethanol. The dye relaxes emitting a photon with the same energy as that of the probe beam, $\lambda = 633$ nm. The stimulated emission is shown in Fig. 5.2b with a reflectivity larger than one in the case of a 39 nm-thick Ag film. If the metallic film is too thick (67 nm) the reflectivity decreases.

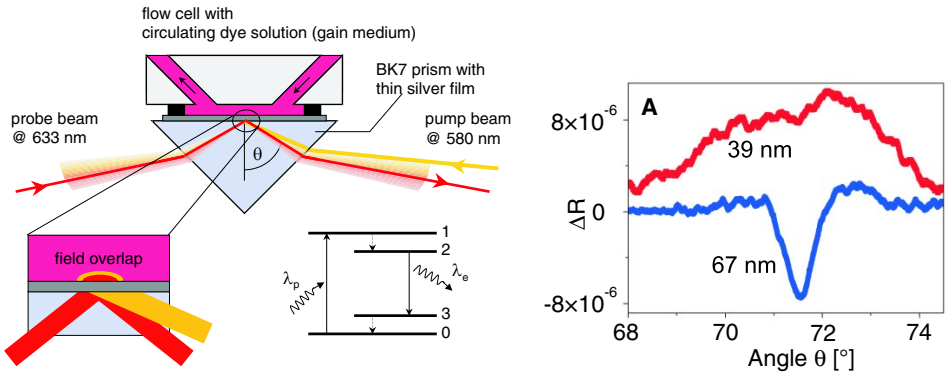

(a) (b)

Figure 5.2: (a) Dual SPP pump-probe arrangement. (b) Measured differential reflectance ΔR for cresyl violet (N $= 7 \cdot 10^{17}$ cm^{-3}) in ethanol as the gain medium, as a function of the probe incidence angle θ. The red and blue curves correspond to silver film thicknesses of 39 nm and 67 nm, respectively [14].

Noginov et al. investigated a structure similar to the Kretschmann configuration, but with the gain medium comprising a 10-μm-thick layer of PMMA highly doped with rhodamine 6G [104]. The structure is strongly pumped at $\lambda = 532$ nm ($\approx$ 18 mJ pulses, $\approx$ 10 ns duration) and probe SPPs were excited *via* the prism at $\lambda = 594$ nm. An increase in reflectance was measured at the SPP excitation angle due to the stimulated emission of SPPs. A loss reduction of 35% and a material gain of ≈ 420 cm^{-1} were estimated.

The amplified stimulated emission of SPPs was also investigated by Bolger et al. [105] using a 100-nm-thick gold film coated with 1 μm of PMMA doped with PbS quantum dots (QDs). A grating in the metal film was created and it was used to out-couple SPPs at wavelengths near the QD emission peak

(same technique used in our end-fire device). The output spectra narrowed as the pump power increased (see in Fig. 5.3) indicating the stimulated emission.

In this last case we can rigorously speak of amplification of the single-interface-SPP, because the metallic film is thicker than the skin depth while this is not the case for the Kretschmann configuration.

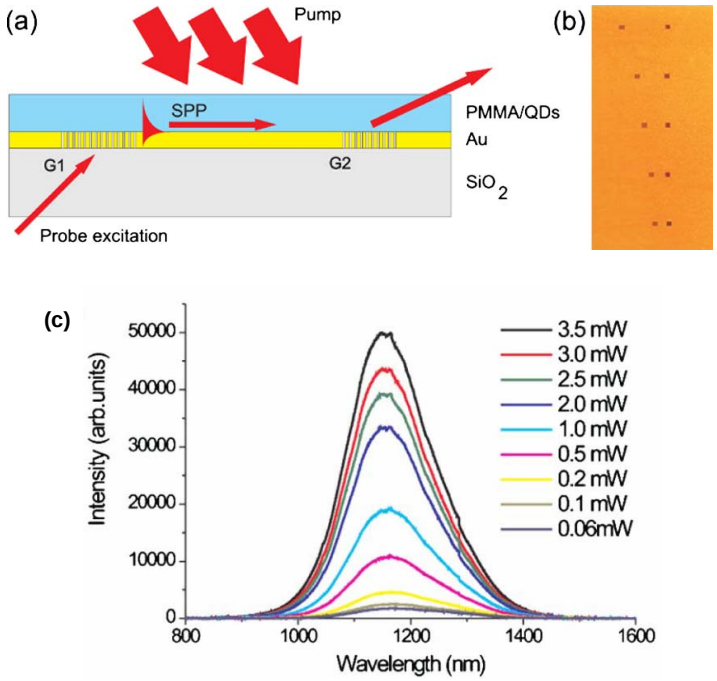

Figure 5.3: (a) Experimental setup for the optical measurements: a He-Ne laser light is coupled to SPPs on the G1 grating and excites signal SPPs via QD fluorescence. The amplifying medium is continuously pumped with a second He-Ne laser. The signal from the 2^{nd} grating (G2) is collected into an optical fiber connected to the spectrometer. (b) Optical images of the in/out-coupling grating pairs with different distances between them. (c) SPP emission spectra for different pump intensities [105].

5.1.2 Long range SPPs

Another typical waveguide used in plasmonics is obtained with an extremely thin metallic film sandwiched in two media with the same optical

index. The two SPPs propagating at the interfaces of the film form symmetric and an anti-symmetric modes, which are respectively called long-range and short-range SPP. The long range SPP (LRSPP) is less confined with respect to a single-interface SPP and can exhibit only few cm^{-1} of losses. The stimulated emission of LRSPPs was first observed at λ= 1.532 μm on a gold stripe (20 nm thick and 8 μm wide) embedded in erbium-doped glass in a co-propagating LRSPP pump-probe arrangement [106]. The first measurements of LRSPP amplification were demonstrated by De Leon et. al [107] using an insertion arrangement (see Fig. 5.4) The structure consisted of a gold stripe (20 nm thick, 1 μm wide and 2.7 mm long) on SiO_2 covered by 100 μm of IR-140 dye ($N = 6 \cdot 10^{17}$ cm^{-3}) in a solvent index-matched to SiO_2.

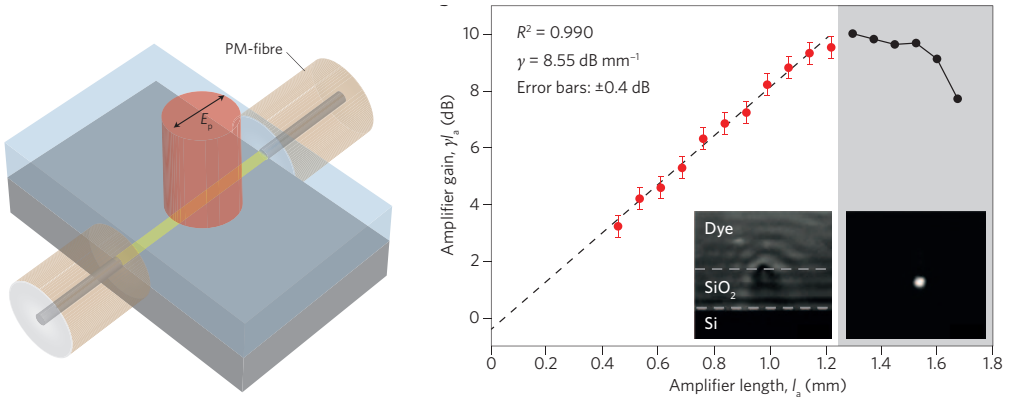

(a) (b)

Figure 5.4: (a) LRSPP amplifier comprising a gold stripe on SiO_2 (on silicon) covered by a dye gain medium (IR-140). The pump is polarized along the stripe length (E_p) and applied to the top of the structure. End-fire coupled input/output polarization-maintaining fibres are also shown. (b) Measured amplifier gain at a probe wavelength of λ = 882 nm versus amplifier length; the slope of the curve indicates the LPSPP mode power gain (γ = 8.55 dB mm^{-1}). The inset images show the output of a structure with the pump on but probe off (left), and the pump off but probe on (right) [101].

LRSPP lasing was reported by Flynn et al. [108] at $\lambda \approx 1.46$ μm in a symmetric InP-based structure consisting of a 15-nm-thick gold film placed between multiple tensile-strained quantum well stacks providing TM gain, as

shown in Fig. 5.5a. Lasing was observed as TM-polarized light emitted from an end facet of a 1-mm-long, 100-μm-wide Fabry-Perot cavity while pumping from the top ($\lambda = 1.06$ μm, 140 ns pulses), as shown in Fig. 5.5b. This is an example of SPASER, a LASER based in this case on LRSPP, even if the LRSPPs are not sub-wavelength. This device is optically pumped (threshold at ≈ 60 kW/cm^2) but an electrical injection is imaginable with the same architecture, as in the integrated end-fire device proposed by the same group [99].

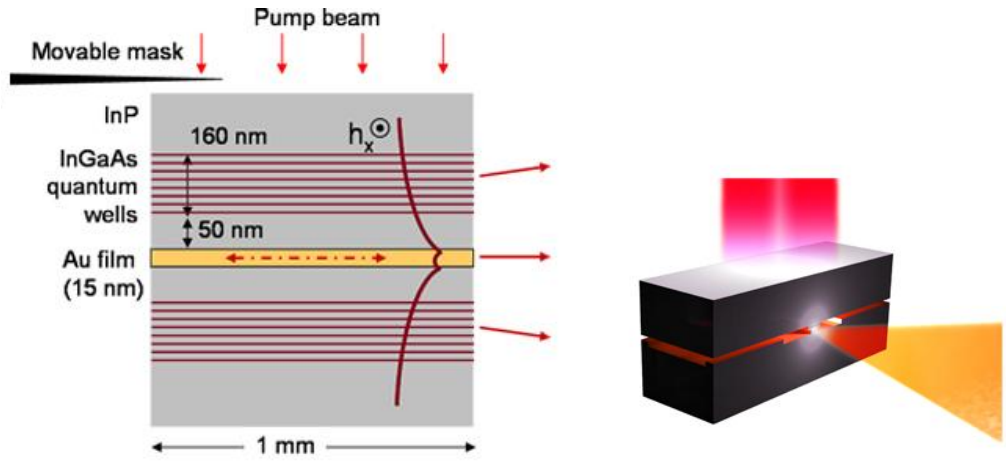

(a) (b)

Figure 5.5: (a) Side view (not to scale), showing the Au-film plasmonic waveguide sandwiched between two dies containing the QW stacks. The stacks are immersed in the evanescent field of the long-range SPP mode represented by the transverse optical magnetic field (perpendicular to the figure plane). Arrows to the right indicate the radiation emitted when SPPs reflect from the end facet [108]. (b) Rendering of the bonded dies pumped from above and emitting radiation to the right.

For active devices based on LRSPPs, where the material gain is in contact with the metal film, it was shown that the lifetime of the gain material is affected by the presence of the metal. Close to the metal there are other channels for dipolar decay, which decrease the gain experimented by the LRSPP mode. In [109] De Leon et al. developed a model that incorporates two important distributions. First, the position-dependent dipole lifetime, that is strongly affected by the possibility of non radiative decays in the

metal, radiative modes in the dielectric and others mode different from the SPP. Secondly, the inhomogeneous optical pump intensity distribution, in which the reflectance on the metal surface is taken into account, because it forces a zero of the impinging electric field at the interface. It was found that if both distributions were neglected, the gain required for lossless propagation would be underestimated by a factor of ten.

In an electrically pumped device, in contrast with an optically pumped one, the pumping distribution can be considered fairly homogeneous. However the other channels for the dipole decay must be taken into account. The gain dipole can non-radiatively decay in the metal, decreasing the dipole lifetime. This effect is called *quenching* and it decreases the effective gain experimented by the SPP. The typical length scale of the *quenching* is 10 - 20 nm.

5.1.3 Laterally confined structures

Confinement of the SPP in the lateral direction can be obtained with a dielectric contrast, for instance by patterning a thin dielectric layer on a metal film. Such structures, known as dielectric-loaded SPP (DLSPP) waveguides, have confinement and attenuation levels comparable to those of a single interface SPP. The dielectric layer is a natural host for a gain material as dipolar emitters (dyes, quantum dots,...).

Grandidier et al. [110] investigated waveguides consisting of PMMA stripes (cross-section of 600 nm x 400 nm) doped with PbS QDs on a 40-nm-thick gold film (see Fig. 5.6). The researchers conducted measurements of spontaneous and stimulated SPP emission using Fourier-plane leakage radiation microscopy at $\lambda \approx 1.550$ μm (near the QD emission peak) while pumping at $\lambda = 532$ nm. They measured the SPP propagation length as a function of pump intensity while probing at $\lambda = 1.550$ μm, observing a distinct threshold beyond which the propagation length increased linearly (up to 27% in this work) with the pump power.

A strong lateral confinement has also been obtained by Oulton et al. with a semiconductor nanowire. They demonstrated a laser-like behavior at cryogenic temperatures in SPPs propagating on a silver film covered by a thin MgF2 layer supporting a CdS nanowire serving as the gain medium and thus defining a Fabry-Perot cavity [111]. The lasing mode is a hybrid mode

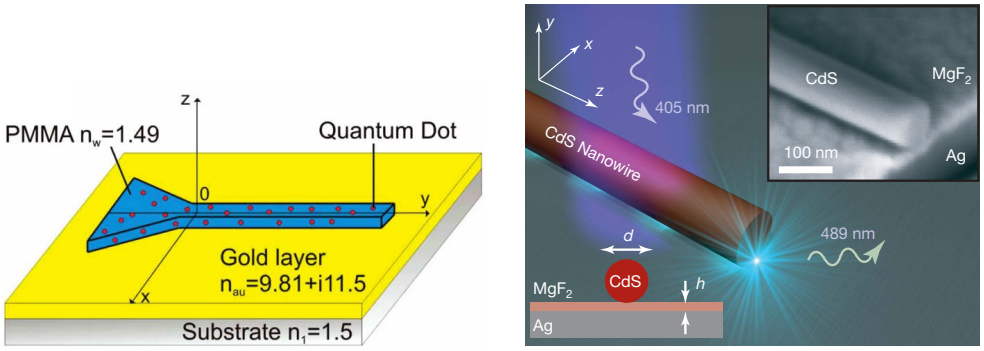

(a) (b)

Figure 5.6: Dielectric loaded SPP waveguide configuration. A PMMA strip confines the plasmon at the gold/polymer interface. An additional tapering structure is designed to efficiently excite the SPP guided mode with an external infrared laser. The effectives indices of the materials are indicated on the figure. (b) The hybrid plasmonic laser consists of a CdS semiconductor nanowire on top of a silver substrate, separated by a nanometre-scale MgF_2 layer of thickness h= 5 nm [111].

[112] partially overlapping the metal and the nanowire (Fig. 5.6b).

The lateral confinement can also be obtained by the use of two metallic walls. Hill et al. [113] demonstrated an electrically pumped SPP laser, using narrow vertical structures formed on rectangular InGaAs pillars coated with a 20-nm-thick SiN passivation layer followed by a silver layer, as shown in Fig. 5.7a. Due to its long and thin shape the design was named *goldfinger*. The lateral metallic walls provide a strong confinement along the horizontal dimension and an index confinement occurs along the vertical dimension. Mirror reflections at the end facets defines a Fabry-Perot cavity. The laser emission was detected as leakage radiation through the substrate. Figure 5.7b shows the measured spectra at low temperature (10 K) above and below the lasing threshold. The structure is 6 μm long and approximately 130 nm wide.

We highlight that until now no laser effect has been observed in propagative single interface SPP at telecom or visible frequencies, with an electrical injection. The electrical injection would represent a big advantage in terms of compactness and for applications. To date the stimulated emission of propagative SPPs by electrical pumping has only been considered theoretically

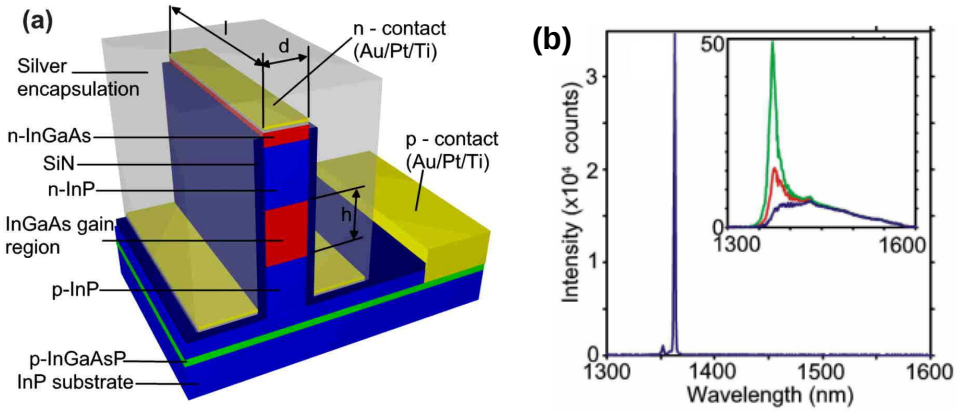

Figure 5.7: (a) Schematic showing the device layer structure formed by a rectangular semiconductor pillar encapsulated in silver [113]. (b) Emission spectrum above threshold for a 3 μm long device with semiconductor core width d $\approx$ 130 nm ($\pm$ 20 nm), with pump current 180 μA at 78 K. Inset: emission spectra at 20 (green), 40 (blue) and 60 (red) μA injection current, all at 78 K.

at $\lambda \approx 3$ μm [114] for a possible integration in optical circuitry [115].

5.1.4 Nanolasers

For the sake of completeness we report some experimental demonstrations of confinement in three dimensions, essentials for the realization of extremely small lasers, called "nanolasers". The sub-wavelength confinement in all the three spatial dimensions can be only achieved with a plasmonic mode, for instance on small metal particles. SPP modes are characteristic of the particle's shape, size and composition, and also of the surrounding dielectric [116]. The fundamental resonant mode of a metal nanosphere, for example, is dipolar, with densities of opposing charge forming at opposite spherical caps. Resonances are excited by an applied laser field or by near dipolar emitters. On resonance, the electric field in the vicinity of the particle is strongly enhanced (10-100 times) relative to the applied field. Coupling this resonance with a gain material *via* near-field, leads to a nanolaser. The concept of amplification by stimulated emission of a SPP mode was proposed by Bergman and Stockman [4]. They spoke for the first time of SPASER and

they proposed a system with a dielectric-core/Ag-shell nanoparticle coated with QDs [117]. In Fig. 5.8a we report the proposed energetic levels of the system, where the excitonic level of the QD is in resonance with the energy of the SPP.

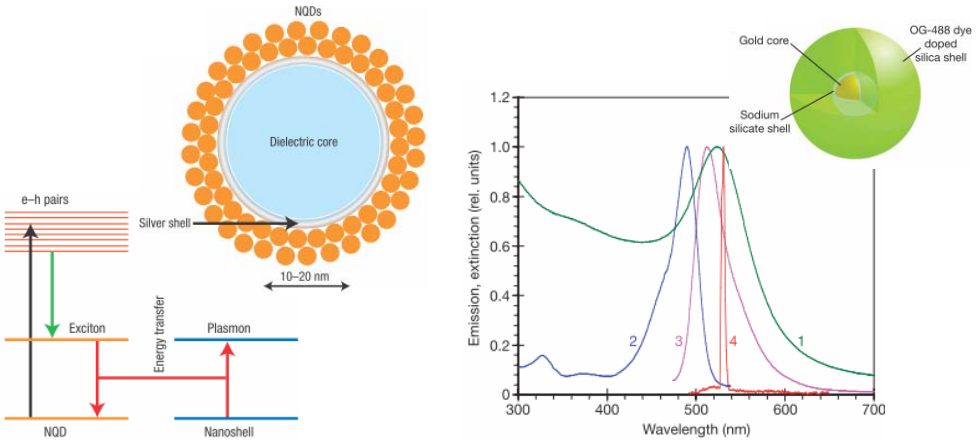

(a) (b)

Figure 5.8: (a) Schematic of the spaser and of levels and transitions in the system [118]. The spaser is made of a silver nanoshell on a dielectric core (with a radius of 10-20 nm), surrounded by two dense monolayers of nanocrystal quantum dots (nQDs). In the energy level schematic the external radiation excites the transition depicted with a vertical black arrow. The excitonic transition allows to convert the energy into the SPP excitation with a resonant coupling [117]. (b) Experimental normalized extinction (1), excitation (2), spontaneous emission (3), and stimulated emission (4) spectra of Au/silica/dye nanoparticles. In the inset the diagram of the hybrid nanoparticle architecture (not to scale), indicating dye molecules around the silica shell.

The SPASER was investigated experimentally by Noginov et al. [118], who observed laser-like emission from spherical spaser particles. Such a particle, shown in the inset of Fig. 5.8b, consisted of a 14 nm gold core coated with a 15 nm SiO_2 shell doped with around 2700 molecules of Oregon Green 488 dye ($N = 6.25 \cdot 10^{19}$ cm^{-3}). The dye emission ($\lambda \approx 510$ nm) overlapped well with the broad resonance of the particles ($\lambda \approx 520$ nm). The researchers measured a threshold behavior, shown in Fig. 5.8b independent of the parti-

cle concentration. This suggests a contribution of several individual particles and tends to exclude a collective effect.

M. C. Gather recently warned: "*careful modelling and experimental design are critical to substantiate spaser claims but will also guide the development of future, more efficient and ever smaller lasers*" [119]. Indeed a clear demonstration should come from an individual spaser particle and should be corroborated by a suitable model. Furthermore a near-field microscopy investigation, which provides the local optical response, could guarantee an incontrovertible demonstration of a threshold behavior.

The amplification with dyes is adequate for a proof-of-concept, but a semiconductor approach is needed for a compact device, electrically pumped and suitable for applications. The smallest semiconductor laser operating with electrical pumping is obtained by exploiting the same *goldfinger* design as reported in the experiment of M. T. Hill (see Fig. 5.7). Researchers demonstrated the first electrically pumped laser emitting CW at room temperature on an optical mode smaller than λ_0^3, where λ_0 is the wavelength in the vacuum [120]. An etched pillar was coated with a 20 nm layer of SiN, producing a structure 0.34 μm wide, 3 μm long, and 1.53 μm high. The structure was then coated with a layer of Ag (see Fig. 5.9) and the laser emission detected trough the substrate. The emission wavelength was 1.554 μm, corresponding to 0.42 times the cube of the wavelength in vacuum.

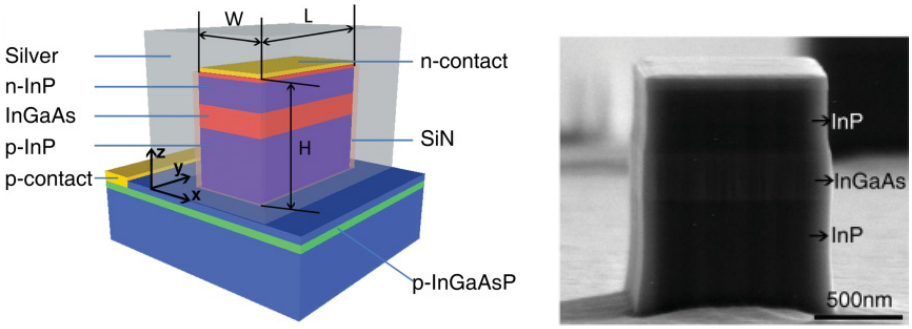

(a) (b)

Figure 5.9: (a) Semiconductor pillar of rectangular cross section encapsulated in silver to form a metallic cavity. (b) Scanning electron microscope image showing the semiconductor pillar before SiN and silver coating [120].

Even if in the last example the mode is extremely small it is however larger than the diffraction limit. We report in the following two examples of semiconductor based lasers that allow, in optical pumping, a sub-wavelength confinement in volumes smaller than the cube of the wavelength in the material, $(\lambda/n)^3$.

The optically pumped coaxial nanolaser structure emits CW at room temperature [121] and has an almost thresholdless emission near 1400 nm at a temperature of 4.5 K. Its center is a metal rod, like the central conductor of a coaxial cable. As shown in Fig. 5.10, a ring of semiconductor surrounds the rod and is in turn coated with metal like the outer shield of a coaxial cable. As in the *goldfinger* structure, the semiconductor structure is layered, with light generated in six InGaAsP quantum wells with gain at telecom frequencies.

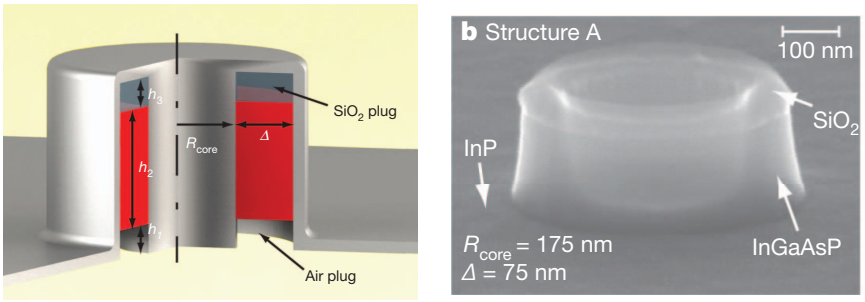

(a) (b)

Figure 5.10: (a) Diagram of a coaxial laser cavity; the gain medium is shown in red. (b) Scanning electron microscope images of the constituent rings in structure. The rings consist of SiO_2 on top, and a quantum-well gain region underneath [121].

The second example of laser emitting CW under optical pumping is reported in [122]. The idea is to optically excite laser emission in a semiconductor nanorod lying on a metal slab covered with a thin insulating layer, as already seen in the experiment in Fig. 5.6b. In this case the GaN wire has an hexagonal section and the AR, in InGaN, is only 170 nm long. It rests on a 5 nm silica film deposited on a 28 nm layer of single-crystal silver with an atomically smooth surface, as shown in Fig. 5.11. The single-crystal silver reduces the laser threshold by three orders of magnitude compared to

the polycrystalline metal used in earlier experiments. The laser effect at 510 nm, below 80 K, make it the world's smallest semiconductor laser.

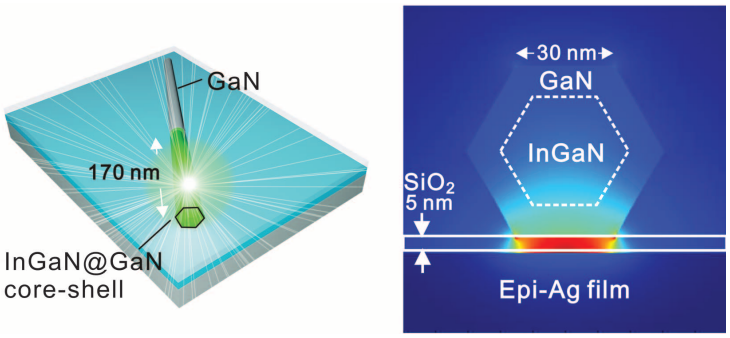

Figure 5.11: Schematic of device: a single InGaN-GaN core-shell nanorod on a SiO_2-covered epitaxial Ag film (28 nm thick). On the right the energy-density distribution [122].

In conclusion, an electrically pumped nanolaser with a confinement below the wavelength in the material for all the three dimensions is still missing. Nanolasers can be small in two dimensions, but they must be long enough in a third dimension to hold at least a half wavelength in the material. Metal can confine light, but decreasing the cavity volume pushes more light into the metal, where it suffers very high losses, raising the threshold. For electrical excitation, Khurgin et al. [123] calculate that the threshold current would be $\approx$10 μA, corresponding to an impractical current density of $\approx$100 kA/cm^2. They rather proposed a nano-source based on a sub-miniature version of the LED, a *Surface Plasmon Emitting Diode* (SPED). A SPED would have both speed and efficiency required in nanophotonics circuit applications.

5.2 Hybrid SPP laser

I will first motivate the hybrid mode choice and present an example to introduce the hybrid plasmonic mode concept. Our semiconductor-based approach to compensate plasmonic losses will be then presented.

I demonstrate a laser device operating - at telecom wavelengths - on a hybrid plasmonic mode. The device operates by electrical injection at room temperature. Compared to the previously reviewed experiments, we origi-

nally propose a near-field imaging of the laser facet, providing the evidence of the stimulated emission into the hybrid mode and confirming the prediction of the numerical simulations [124].

5.2.1 Why hybrid modes?

A full compensation of plasmonic losses at telecom wavelengths is a formidable task: for a SPP propagating, at λ= 1.3 μm, along the interface between air and gold (n_{air}= 1 and n_{gold}= 0.403 - i·8.25, from [35]) losses are estimated to be only 80 cm^{-1}. However, compensating the SPP losses requires replacing air with a gain medium that is necessary denser and has higher optical index. Plasmonic losses roughly scale with the optical index of the dielectric to the 3^{rd} power [19], leading to prohibitively high values. For instance, losses larger than 2000 cm^{-1} are obtained for an interface between a dielectric with n= 3 and gold (λ= 1.3 μm). Even with state-of-the-art semiconductor active regions, which represent one of the best available gain media, gain values that can compensate such losses are unattainable. A viable trade-off for full loss compensation is to rely on hybrid waveguide modes stemming from the coupling of a dielectric and a plasmonic mode [112]. A hybrid mode presents advantageously lower losses compared to a pure SPP and it allows, at the same time, a good overlap with the gain medium [125].

In our case the strategy is to to reduce, as far as possible, the top cladding of our heterostructure, increasing the proximity of the metal to the AR gain. Thinning the caldding the laser mode will overlap the metal changing its shape. In the extreme case in which the cladding is eliminated, the AR would be in contact with the metal and the SPP mode would be directly pumped. However, the laser operation is strongly modified by the thinning of the cladding. The mode losses dramatically increase, tending to the SPP losses and entailing an increase of the laser threshold. Furthermore the p-doped reservoir of charges decreases limiting the diode performance. This approach is obviously not adapted for a full SPP loss compensation, since the diode laser cannot operate without top cladding. However, it permits to amplify a mode given by the superposition of a dielectric confined mode and a SPP mode. The modes obtained from the *mix* between two modes are called hybrid modes.

5.2.2 Hybrid plasmonic modes

Hybrid modes result from the superposition of two different modes that spatially overlap. An advantage of the hybrid modes is the possibility to engineer the relative weight of the two components. In the case of a hybrid mode composed by a dielectric and a SPP component it is possible to choose the mode losses, essentially determined by the SPP component. The relative weight of the plasmonic/dielectric components can be deduced from the uncoupled dispersion relations. The "closer" the dispersion relations are, the stronger the mode hybridization is. Some systems allow a crossing of the two uncoupled dispersions, giving raise to hybrid modes with an equal weight for the two components.

We report the example of Ref. [126], in which researchers propose a coupling between a LRSPP waveguide and a dielectric one, both embedded in a benzocyclobutene (BCB) layer. The gold layer and the SU-8 waveguides are shown in the system cross-sectional view of Fig. 5.12a. In that specific case the dispersions of the coupled modes show a typical "anti-crossing" behavior (see Fig. 5.12b): the dispersion relations of the uncoupled modes cross each other at a given value of the BCB thickness t, but the crossing disappears when the modes are coupled. At the anticrossing both the hybridized modes have an equal repartition of "dielectric" and "plasmonic" characters, as shown from the intensity profiles in Fig. 5.12b.

In our device the hybrid mode stems from the coupling between (i) a classical (TM polarized) mode guided within the AR by the dielectric claddings; and (ii) a SPP mode, guided at the interface between the upper cladding and the top metal contact of the device (Fig. 5.13). The coupling strength between the two modes depends on the materials index of refraction, the ridge width, and can be precisely tuned with the upper cladding thickness (t_{cl}). Large cladding thicknesses lead to uncoupled "dielectric" and "plasmonic" modes (Fig. 5.14a). Instead, when t_{cl} is comparable to the modes extent, hybrid modes appear thanks to their overlap (Fig. 5.14b). The hybrid modes obviously present both "dielectric" and "plasmonic" characters, and can be labeled as symmetric and anti-symmetric, according to the relative sign of the two components.

The anti-crossing existence is determined by the system geometry and the used materials, namely by the material indexes and ridge widths. In our case the dispersion relations do not cross, but - as discussed later - are sufficiently

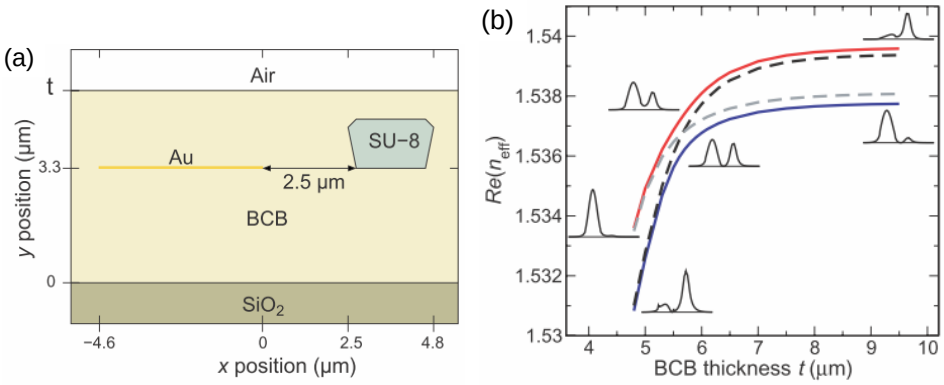

Figure 5.12: (a) Cross-sectional view of a coupler. The Au stripe is separated from the SU-8 waveguide by a gap of 2.5 μm. (b) Dispersion of the two eigenmodes as a function of the BCB thickness t. Real part of the effective index for the symmetric eigenmode (red), the antisymmetric eigenmode (blue), the LRSPP of the isolated Au stripe (gray dashed curve) and the guided mode of the isolated SU-8 waveguide (black dashed curve). The plots of the intensity of the hybrid modes are shown close to the curves. Figures taken from Ref. [126].

close to yield a measurable hybridization. This is actually an advantage, since a perfect "anti-crossing" situation would lead to two extremely high-loss modes. They would both be half "plasmonic", exhibiting losses dominated by the extremely damped "plasmonic" component. Instead, if the dispersions do not cross – as in our case – it is possible to tune the coupling between the modes, modifying the dispersion diagrams at the laser operating frequency, and consequently to engineer the mode losses.

5.2.3 Device simulation

We experimentally reduced the cladding thickness to the minimum possible value in order to have an operating device with a net amplification and maximize the plasmonic character of the hybrid mode. The adopted structure is the *ultra-thin cladding* structure, described in section 3.2.2. This section is dedicated to the finite element simulations of the *ultra-thin cladding* device. We obtained the dispersion relation of the system modes. No anti-crossing behavior is observed, but we show, by simulations, that it can be

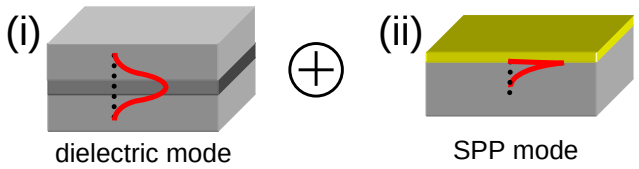

Figure 5.13: Schematics of the magnetic field distribution (H_y component) of the two waveguided modes: (i) the dielectric mode confined in the AR and (ii) the SPP mode at the metal-semiconductor interface.

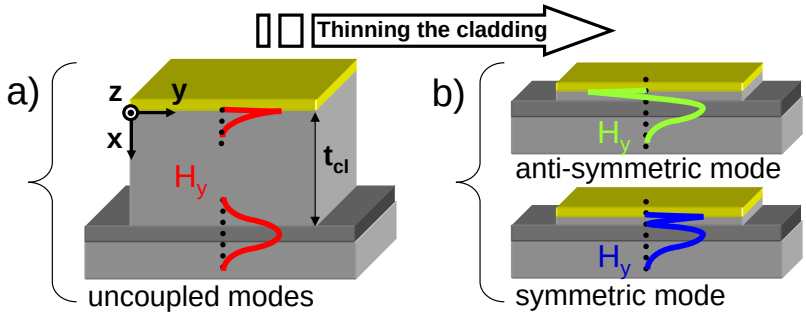

Figure 5.14: Schematics of the magnetic field distribution (H_y component). (a) The two modes on the same ridge. They are not coupled since the thick (t_{cl}) upper cladding prevents the coupling. (b) A thin cladding enables mode coupling, yielding two hybrid modes (one symmetric and one anti-symmetric). They both present a "plasmonic" and a "dielectric" component.

introduced by changing the cladding index or inserting a low index material layer between the cladding and the metallic top contact.

The result of the 2D simulation of the *ultra-thin cladding* device facet shows a large presence of the field on the metal. The squared modulus of the electric field is plotted in Fig. 5.15 and a cross section of the field is shown in the inset. The maximum of the "plasmonic" component is about 30% of the mode maximum. The calculated propagation loss is $\alpha \approx 500$ cm^{-1}.

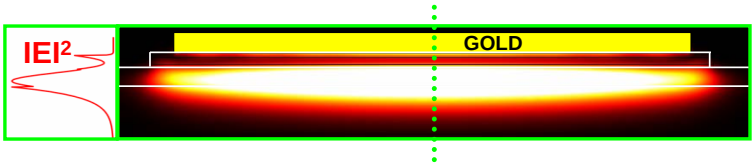

Figure 5.15: Finite elements simulation of the "low-loss" hybrid waveguided mode for a laser with a 250-nm-thick cladding (λ=1300 nm). The electric field squared modulus is plotted and a 1D cross-section is shown on the left.

The consistent presence of the electric field at the metal interface imposes to take into account also the Ti sticking layer of 3 nm. Including this layer the 1D simulations [33] predict a dramatic loss increase of ≈ 170 cm^{-1}. The removal of the Ti layer will be essential to reach laser threshold at RT.

Figure 5.16 reports the calculated dispersion curves of the *ultra-thin cladding* device (t_{cl}= 250 nm) using the 1D finite element simulation software. The color code corresponds to the scheme in Fig. 5.14b for ease of reading. The uncoupled mode dispersions (red dots) do not cross, hence only a small shift is expected upon coupling, as highlighted in the picture inset. At λ= 1.3 μm the hybrid modes (green and blue lines) exhibit a slightly modified wavevector. Note that the anti-symmetric hybrid mode (green line) presents a plasmonic component which is smaller compared to the symmetric hybrid mode. This perturbative regime allows the anti-symmetric mode to have a plasmonic component, but at the same time a good overlap with the AR (Γ= 53%) and with acceptable total optical losses ($\alpha \approx 500$ cm^{-1}).

The losses as a function of the wavevector are plotted in Fig. 5.17. By increasing the wavevector value the modes decouple, because they are more confined and, at a given t_{cl} the overlap decreases. The losses of the hybrid modes tend to the losses of the uncoupled modes. In particular the losses of

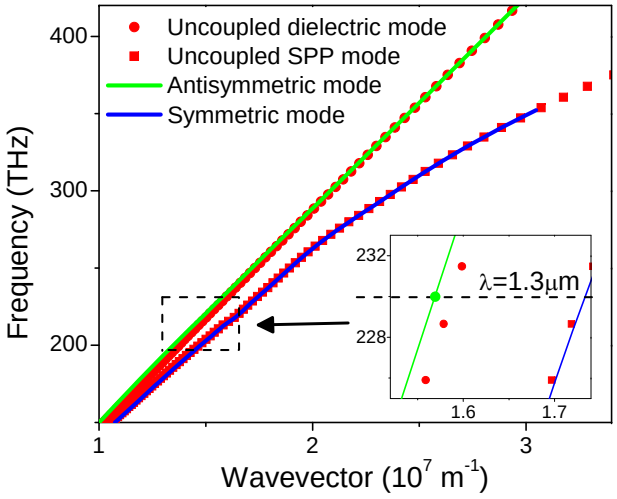

Figure 5.16: Mode dispersion curves for the *ultra-thin cladding* device (250-nm-thick cladding), calculated using a finite elements 1D simulation. The gold index dispersion is taken from Ref. [35]. The dispersion relations of the uncoupled modes do not cross: the mode coupling induces only a slight perturbation, which is best visible in the inset. The antisymmetric hybrid mode highlighted by a green point in the inset corresponds to the mode plotted in Fig. 5.15.

the symmetric mode are always large (> 2000 cm^{-1}), while the antisymmetric mode features maximal losses of ≈ 600 cm^{-1}. The antisymmetric mode at $\lambda = 1.3$ μm is highlighted with a green dot.

Anticrossing behavior by changing the cladding index

We simulated a system featuring an anticrossing behavior. Decreasing the cladding index the uncoupled SPP dispersion is pulled toward low wavevectors. This entails a crossing of the two dispersions at a given wavevector.

We consider the *ultra-thin cladding* structure where the whole 250 μm-thick-cladding has a refractive index $n_{cl} = 3$ (instead of $n_{InP} = 3.2$). The dispersion relations of the uncoupled and coupled modes are shown in Fig. 5.18. A close up of the anticrossing, at a $\lambda = 1$ μm, is shown in the inset.

In practice it is extremely hard to modulate the cladding index, but this study shows the possibility to engineer the system dispersion relations and

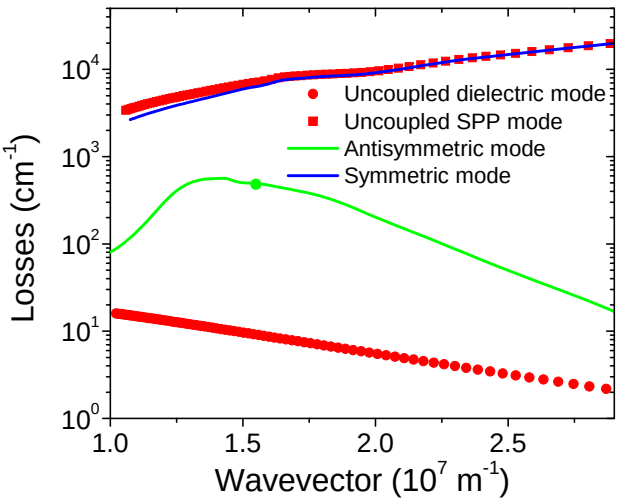

Figure 5.17: Losses of the uncoupled modes (in red color) and of the coupled hybrid modes. As expected, for larger wavevector values the losses of the hybrid modes tend to the losses of the uncoupled modes. For low wavevectors values the losses of the antisymmetric mode decrease because the mode is pushed away from the AR and the confinement factor tends to zero. The antisymmetric hybrid mode highlighted by a green point corresponds to the mode plotted in Fig. 5.15.

the spatial localization of the modes.

Anticrossing behavior by adding a low-index layer

To concentrate the field in a small region of space we can imagine to insert a low-index dielectric layer between the cladding and the top metal. The system behaves then similar to the one proposed by Oulton et al. [112] and reported in Fig. 5.6b, with the gain region separated from the metal by an extremely thin dielectric layer. We limit our analysis to numerical calculations. We study the mode dispersions, and the associated losses, varying the dielectric layer thickness. From an experimental point of view, it is easier to deposit a dielectric layer than to change the index of the cladding as proposed in the previous paragraph. Obviously this layer would prevent electrical injection in the heterostructure, but it is always possible to implement a lateral injection scheme (cfr air confinement waveguides).

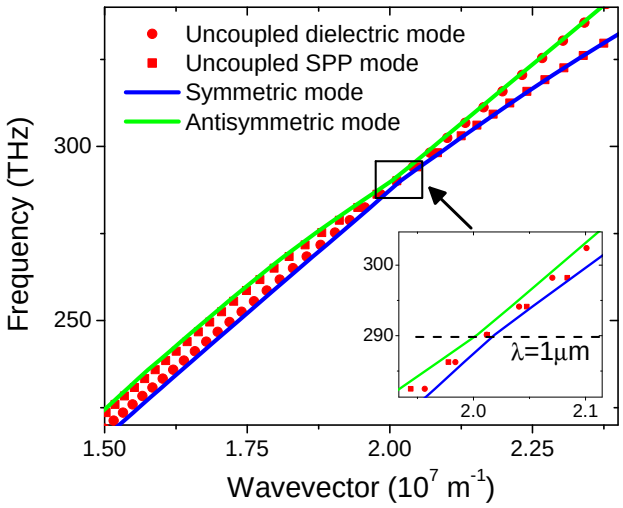

Figure 5.18: Mode dispersion curves for the *ultra-thin cladding* device, where the 250-nm-thick cladding has a refractive index of $n_{cl} = 3$, calculated using a finite elements 1D simulation. The gold index dispersion is taken from Ref. [35]. The dispersion relations of the uncoupled modes cross. The anticrossing is visible in the inset.

We consider a system with a dielectric layer of SiN, $n_{SiN} = 2$. As shown previously without SiN ($t_{SiN} = 0$) the system does not feature an anticrossing. However, an anticrossing behavior can be obtained at a $t_{SiN} \approx 10$ nm as shown in Fig. 5.19. Since in this case the geometry is changing, we fixed in the numerical calculations a frequency of 230 THz (corresponding to $\lambda = 1.3$ μm). Note: the anticrossing is not represented in the ω/k plane but in the k/t_{SiN} plane. At the anticrossing, the energy is equally divided in the SPP component, in the SiN, and in the "dielectric" component. We observe that the losses of the antisymmetric mode, starting at ≈ 500 cm^{-1} increase as the SiN layer thickness increases. At the anticrossing the losses are approximately the same for both modes and exceed 1000 cm^{-1}.

The thickness at which the anticrossing takes place can be controlled by the refractive index of the dielectric layer. By increasing the index of the dielectric layer the anticrossing, and the cut-off of the antisymmetric mode, are shifted at larger thicknesses. In Fig. 5.20 we show with an arrow the anticrossing for the previously discussed dielectric layer of SiN and other two larger refractive indexes. We observe that dielectrics with higher refractive

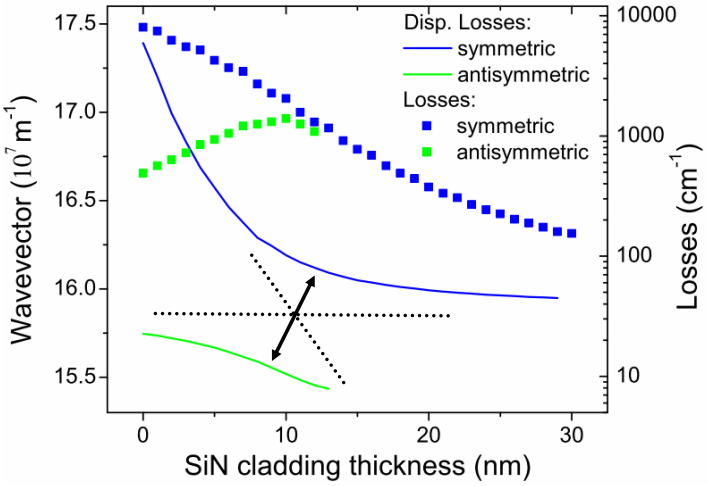

Figure 5.19: Wavevector as a function of the SiN layer thickness and associated losses of the two hybrid modes. The frequency is fixed at 230 THz. The antisymmetric mode has a cut-off at $\approx$ 10 nm of SiN, but it is sufficient to observe that the wavevectors tend to a similar value (dotted black lines).

indexes need to be thicker in order to obtain the anticrossing point. It is easy to imagine that, for an index of the dielectric layer matching the one of the cladding, the anticrossing will shift at infinite values of thicknesses. In other words it will not exist anymore.

5.2.4 Device characterization

The *ultra-thin cladding* devices were processed in ridge resonators analogously to the devices presented in section 3.3. The etched ridges are 9-μm-wide, 750-μm-long. Electrical insulation was provided by a 300-nm-thick SiN layer which was opened above the ridges before the top metal contact evaporation. To eliminate the Ti sticking layer I deposited a gold layer directly after the SiN opening, encapsulating it in the top metallic contact. This supplementary step in the processing largely reduces the metallic losses. The result of the fabrication is shown in Fig. 5.21. The insulator opening leaves only $\approx$ 500 nm of Sin on the ridge edges. This is important to avoid that parasitic modes can lase on the edges, far from the metal. These modes could have lower losses, and consequently a lower threshold, than the hybrid mode.

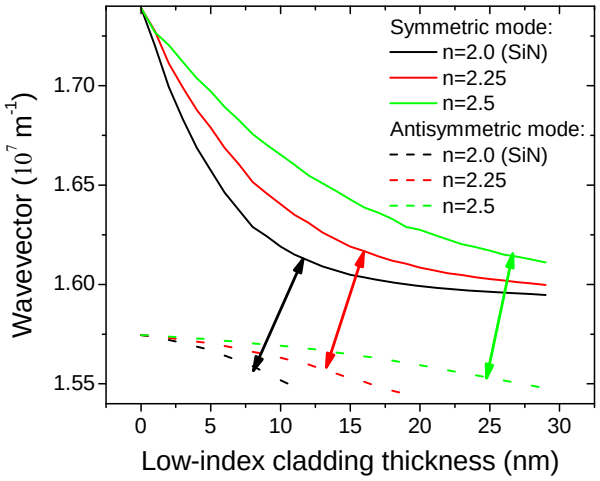

Figure 5.20: Hybrid modes wavevectors as a function of the dielectric layer thickness, for different values of the layer index. The anticrossing shifts toward large thicknesses as the optical index increases.

The *ultra thin cladding* device operates in laser regime at RT in pulsed injection. The threshold behavior is evident in the light-current density (LJ) characteristics, shown in Fig. 5.22 (black curve). We add to the figure also the LJ of the previously presented devices (*thick* and *thin cladding*) to allow a direct comparison. As expected the threshold increases by decreasing the cladding thickness. Figure 5.23 shows a typical laser spectrum of the thinnest device, which correctly emits at λ= 1.3 μm. The comparison with an electroluminescence spectrum (thickest device) allows one to appreciate the spectral narrowing, corroborating the evidence of laser regime.

Near-field characterization

An original feature of the present work is the characterization of the plasmonic hybrid mode by near-field scanning optical microscopy (NSOM), which allowed us to directly visualize the field distribution while the laser is operating. The NSOM measurement were performed by L. Greusard and Y. De Wilde at the ESPCI - *Institut Langevin*. The setup is described in Appendix C.3. The result of the NSOM analysis of the *ultra-thin cladding* device facet is shown in Fig. 5.24. The NSOM signal in Fig. 5.24b is

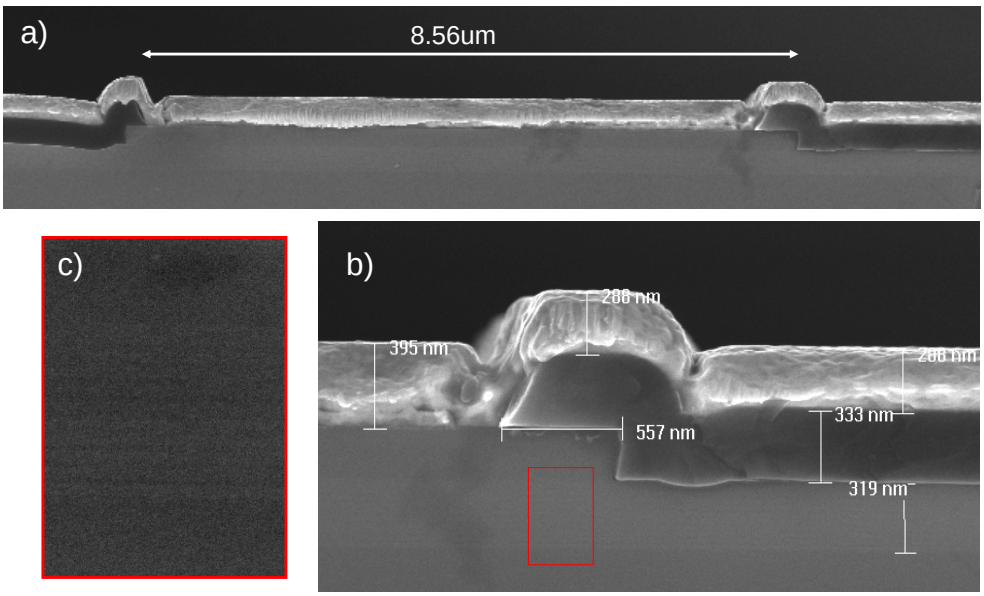

Figure 5.21: a) SEM image of the facet of the *ultra-thin cladding device* device. b) Close-up of the facet side, with typical features sizes. c) Close-up of the QWs on the cleaved facet.

uniformly distributed along the facet. The electric field clearly overlaps the metal, indeed the upper profile of the mode follows the gold topology shown in Fig. 5.24a. A careful observation of (b) reveals that the optical signal is slightly leaking on the right side of the ridge. This confirms the need, for extremely thin cladding structures, of maximizing the metal coverage along the ridge width, to avoid undesired low-threshold higher-order modes. The SiN width of $\approx$ 550 nm, on the right of the facet, appears to be an upper limit.

Two significant NSOM signal's cross-sections, along the x and y direction, are shown in (c) and (d). Figure 5.24c shows the existence of an electric field peak at the metal interface, providing evidence of the SPP component of the hybrid mode. The experimental data are in agreement with the simulated cross section of the squared electric field, taken along the x direction in Fig. 5.15. The horizontal cross-section of the NSOM signal in Fig. 5.24d features a relatively flat behavior with two weak peaks on the sides. We think that the measured signal is given by the contribution of the first two laser transverse modes. On the same image we plot the simulated squared electric field of

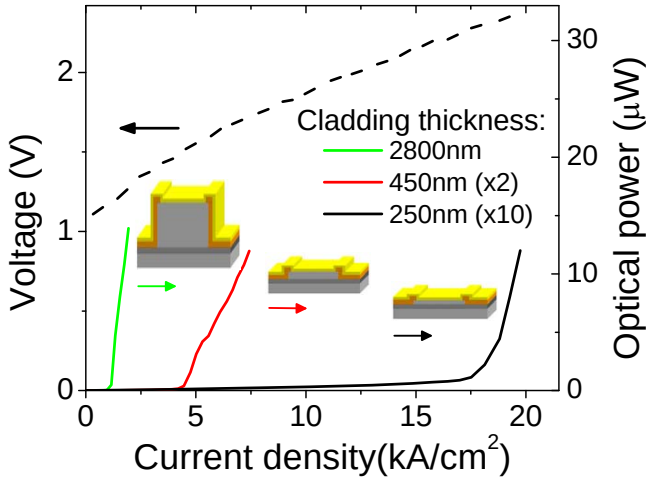

Figure 5.22: Light-current density (LJ) curves, in pulsed regime (DC=1% - 10 kHz repetition rate, 100 ns pulses), for three ridges with different cladding thicknesses: t_{cl}= 2800 nm (green curve), t_{cl}= 450 nm (red curve), and t_{cl}= 250 nm (black curve). Reducing the cladding thickness brings the metal closer to the AR, hence increasing optical losses and laser thresholds. The JV characteristic (dashed black line) is also shown for a device with t_{cl}= 250 nm.

those two modes.

A more precise and comparative analysis of the facet NSOM signal requires to average several cross-sections and to take into account also the other cladding thicknesses, permitting a quantitative comparison as a function of t_{cl}. The results of the NSOM measurements for the three devices are summarized, including the *ultra-thin cladding* device, in Fig. 5.25. For each device we report the SEM image and the associated electromagnetic near-field collected above laser threshold (see Figs. 5.25a,-c). We integrated the NSOM signal along the y-direction. Each normalized integral curve is plotted in Figs. 5.25d-f (red lines) with the corresponding numerically simulated cross-sections of $|E|^2$ (black lines). The "dielectric" components are in excellent agreement with the simulations and for the two devices with thinnest claddings we observe a clear electric field in correspondence of the gold/semiconductor interface. It corresponds to the plasmonic component of the hybrid-mode, which takes advantage of the optical gain experienced

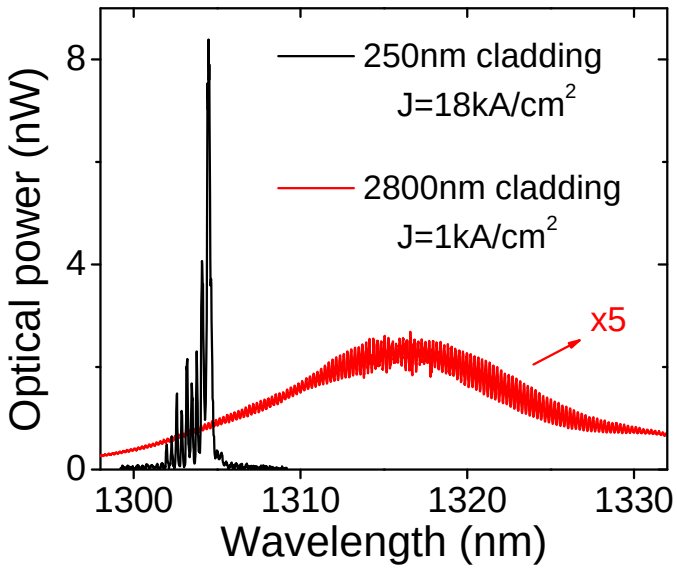

Figure 5.23: Typical laser spectrum (black line) of a device with t_{cl}= 250 nm at an injection current density of 18 kA/cm^2. Luminescence spectrum (red line) of a device with t_{cl}= 2800 nm at J= 1 kA/cm^2.

by the dielectric portion (which overlaps the AR), hence providing a clearly measurable field intensity at the metal-semiconductor interface.

The "plasmonic" component in the NSOM measurement is broadened by the finite diameter (d) of the hole of the aluminum pyramid used in the microscope. The measurement takes into account the total signal coming from a surface of $\pi(d/2)^2$, hence smoothing the abrupt extinction of the plasmonic component at the interface. Additional broadening possibly arises from the diffusion of the SPP at the facet level, where the roughness of the cleaved gold layer prevents a perfect contact-mode of the NSOM pyramid during the scan. Nevertheless the intensity peak of the optical signal at the interface is well reproduced by the simulations (for t_{cl}= 250nm it is one third of the mode maximum). This confirms the plasmonic character of the hybrid mode which is lasing at room-temperature and upon electrical injection.

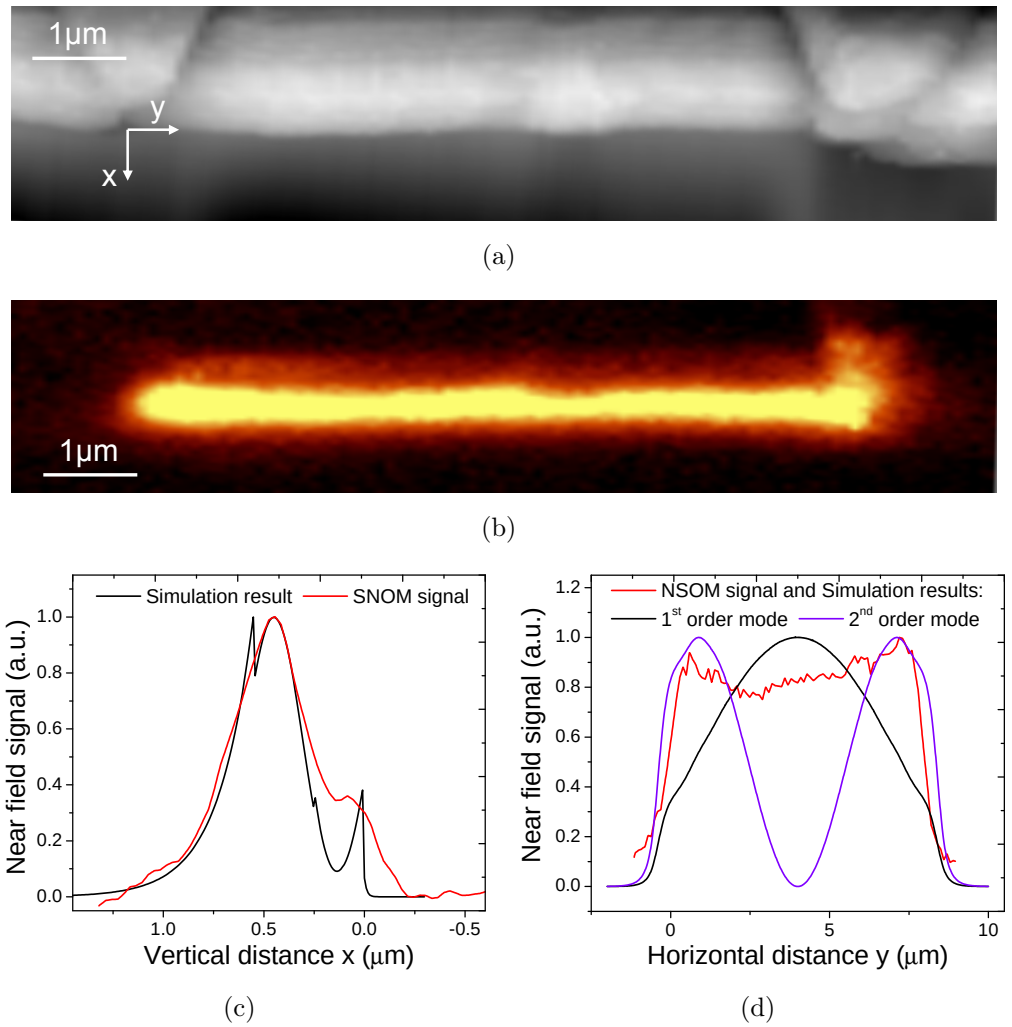

Figure 5.24: (a) Topography acquired simultaneously with the optical measurement. (b) NSOM measurement of the facet. The near-field on the facet overlaps the metal and clearly follows the top contact profile. The origin of the x coordinate is taken at the metal-semiconductor interface and the curves are normalized. (c) Vertical cross-section of the NSOM measurement (in red) compared with the mode cross-section of the simulated intensity (in black) shown in Fig. 5.15 (d) Horizontal cross-section of the NSOM measurement (in red) compared with the cross-sections of the simulated intensities of the first order (in black) and of the second order (in violet) modes.

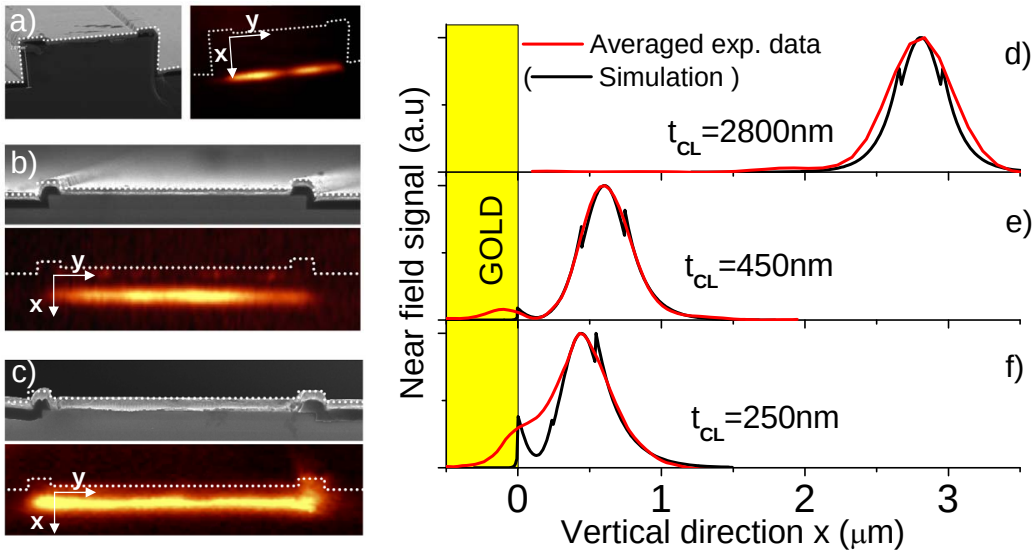

Figure 5.25: (a),(b),(c): SEM images and NSOM measurement of the facets for three different laser types: a) t_{cl}=2800nm, b) t_{cl}=450nm and c) t_{cl}=250nm. The lasing mode can be clearly identified and positioned with respect to the facet. (d),(e),(f): Integrated NSOM signal (red lines, integration performed along the y-direction) and square of the electric field (black line) obtained from 2D finite element simulations. The origin of the x coordinate is taken at the metal-semiconductor interface and the curves are normalized. The agreement between experiment and theory is good, taking into account a tip-induced broadening of the NSOM data, which prevents the system from detecting the extremely sharp decrease of the field at the metal-semiconductor interface.

5.3 Conclusions

In conclusion we have demonstrated a hybrid plasmonic laser emitting at telecom wavelengths. The device presents the advantages of electrical injection and operation at room temperature. Near-field microscopy measurements allowed us to directly measure the mode distribution and to prove the presence of the lasing plasmonic component. We believe that a fundamental study of the metal proximity to a gain media, combined with the electrical injection, represents an important step toward the development of active plasmonic components.

A further thinning of the cladding would allow one to increase the SPP component of the hybrid mode. The complete cladding removal would allow one to directly pump the SPP mode enabling a SPASER. However, the cladding thinning entails a higher doping and, consequently, higher absorption. This cladding absorption and the losses due to the metal become too high for a total compensation.

Moreover a second issue arises. The Schottky barrier, present at the metal/semiconductor interface, approaches the AR. The typical band bending induced by the Schottky barrier can affect the potential shape of the QWs, hence the injection efficiency is affected too. Experimental measurements of the modified injection are reported in Appendix E.

To further thin down the cladding it is best to consider a tunnel junction, which requires a cladding thickness of only a few tens of nanometers [127] [128]. It would also present the advantage of a n-type contact, which is more efficient and less absorbing than a p-type contact.

Chapter 6

Device application: metal patterning for loss reduction

Semiconductor lasers have become essential tools for fiber-optic communications, optical sensing and photonics [129][130][131]. Their compactness, efficiency and wide range of wavelengths are key features of this success. The implementation of a distributed feedback (DFB) resonator enhances their performances, allowing a precise control of the emission frequency and a reduction of the threshold current [132][133]. DFBs are typically implemented by periodically structuring the semiconductor cladding close to the laser AR [75]. An alternative strategy consists in patterning the device top metal electrode into a 1^{st}-order metal grating, without the need for cladding etching and regrowth. This approach was validated at mid-IR wavelengths ($\lambda = 7.5$ μm) [67]. In this region of the electromagnetic spectrum, the metallic ohmic losses are relatively low [134], and the long wavelength requires only a micron-sized lithography. These were significant advantages for a first validation of this concept [63]. In the mid-IR, it was also shown that patterning the metallic layer leads to the onset of an extremely low-loss mode. The extension of this concept to the near-infrared would be of importance, since it would allow one to overcome the huge ohmic losses which are usually encountered when a metallic layer is located near the active region of a diode laser.

In this chapter, we apply the concept of metallic DFB to diode lasers operating at telecom wavelengths ($\lambda = 1.3$ μm).

We first explain the physical idea for the loss reduction by metal pat-

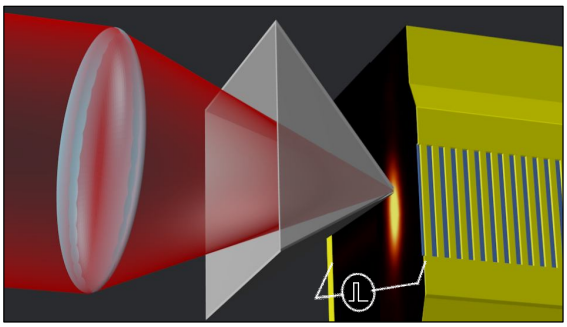

Figure 6.1: Schematic of the facet imaging by the pyramid of the transmission NSOM.

terning. The device design and the fabrication details are presented. We then illustrate the NSOM analysis results of the laser facet imaging (see Fig. 6.1), which leads to the unequivocal identification of the laser mode. Its field distribution analysis also allows us to elucidate the action of the metallic patterning [135].

6.1 Physical discussion on the origin of the low-loss mode

This qualitative discussion allows one to understand how the metal patterning can induce a loss reduction. It was presented for the metallic DFB, achieved by our group, in the mid-IR [63]. However, it is also valid for the structures at telecom wavelengths that feature a top cladding.

The scheme in Fig. 6.2a shows a lateral view of the metal-semiconductor interface and corresponding field plot for E_z, of an unpatterned surface-plasmon structure (a standing wave is considered). A surface plasmon involves the physical motion of electric charges at the metal surface, which is also responsible for the (ohmic) SP propagation losses. After half a period the electric field direction will be reversed, and - in a first approximation - we can assume that charges will have moved following the dotted arrows: charge transfer occurs across the (nodal) regions of zero electric field in the z-direction (white dotted lines). If the top metal is patterned as a grating, symmetric and anti-symmetric modes will appear: in the first case the nodal

lines are located below the metallic fingers (6.2b), in the second case below the air gaps (Fig. 6.2c). Each single metallic finger must be electrically neutral. In the former case charges oscillate as schematized in Fig. 6.2b (black arrows), and correctly one nodal line is present where there is charge transfer. In the second case, however, no charge transfer can occur across since the nodal line is now located below the air gaps (Fig. 6.2c, red crossed arrow). Charges must oscillate within each finger, and the simplest charge distribution imposed by symmetry is schematized in Fig. 6.2c (black arrows). However, in this case the charge oscillation cannot induce additional nodal lines, since this would require a different wavelength. The optical mode must adapt to allow for regions of zero electric field at the metal surface, and is moved into the substrate. This is only an intuitive picture, but it describes correctly the physical mechanism underlying the observed effect.

The net effect of the grating is to "repel" from the metal one of the two modes which originate from the DFB resonator, thus lowering its loss.

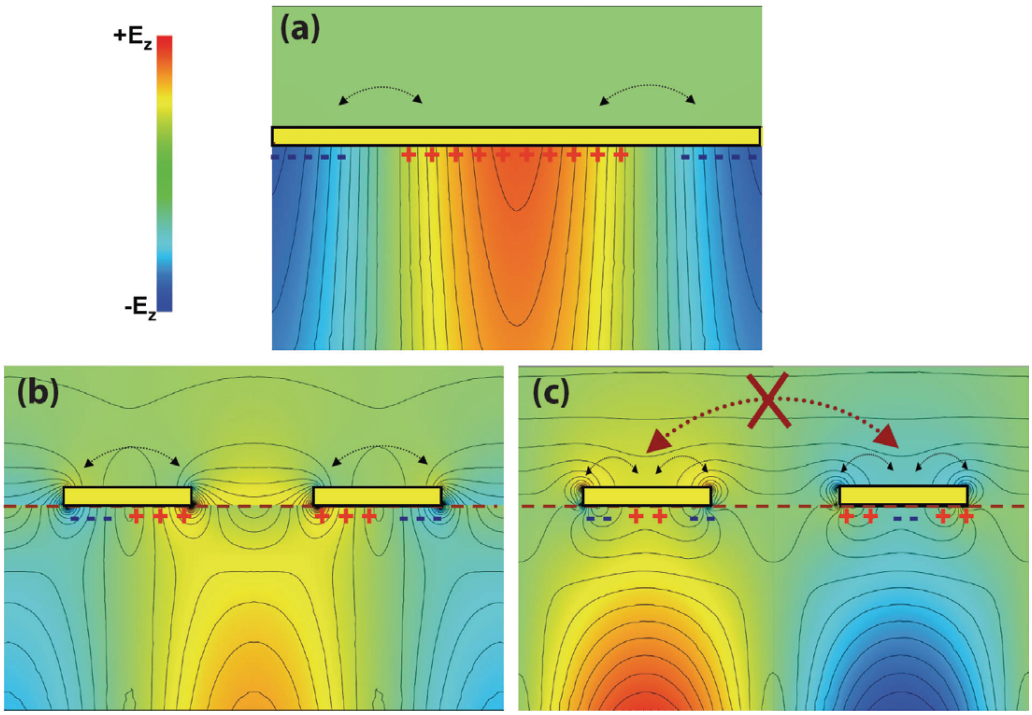

Figure 6.2: Intuitive physical explanation of the loss-reduction effect. Schematic close-up of the metal-semiconductor interface of a surface-plasmon waveguide. The system is considered infinite in the y direction. (a) The case of an unpatterned, continuous metal surface. If mirrors are placed at the left and right edges of the structure, a Fabry-Perot resonator is present and a standing surface-plasmon wave appears. The z component of such a wave is plotted in color scale, together with the surface charge density responsible for the SP. The corresponding charge oscillation is indicated by the dotted curved black arrows. The vertical white dotted lines mark the position of the nodal lines for E_z. Note: the charge oscillation always takes place across the nodal lines. (b), (c) The case of a 1^{st} order grating patterned in the top metal surface only. A symmetric and an anti-symmetric mode appear [63].

6.2 Design and fabrication

The laser design that we have developed for this study is inspired from long mid-IR wavelength QC laser devices ($\lambda = 7.5$ μm) featuring a 1^{st} order metal grating patterned on the top metal contact [67]. The transverse

magnetic (TM) polarized light emitted by the QCL couples with the grating and gives rise to a low-loss mode. The electromagnetic energy density is then localized in the AR, and not at the metal-semiconductor interface, as it would be the case for regular surface plasmon modes and partially for hybrid plasmonic modes shown in the previous chapter.

The introduction of the DFB concept at telecom wavelengths required a preliminary numerical study. We performed 3D finite element simulations of a single period of the DFB imposing periodic conditions on the two facet boundaries. The geometry for the *thin cladding* structure is shown in Fig. 6.3a. The periodicity is 200 nm and the metal finger is 100 nm width (duty cycle 50%). In this case a 3D geometry is required to take into account the periodicity given by the grating. The periodic conditions on the two facets simplify the problem by assuming an infinite length of the DFB cavity.

Figures 6.3b and 6.3d show the squared electric field of the single-lobe low loss mode, which is characterized by an electric field maximum under the metallic finger. The red arrows are proportional to the electric field and show its direction. The other mode, shown in Fig. 6.3c, has an electric field maximum under the air slit, between the metallic fingers. Due to the consistent overlap with the metal, clearly visible in the view of Fig. 6.3e, the losses of this mode are much higher.

The devices were processed into 9-μm-wide ridges both on the *thin cladding* and *ultra-thin cladding* structures. The surface was previously patterned with metal using electron-beam lithography followed by lift-off. The 1^{st}-order grating has a periodicity $\Gamma \simeq 200$ nm for a duty cycle (DC) of $\approx 50\%$. Its thickness (Ti/Au, 3/67 nm) has been chosen thicker than the skin depth at $\lambda = 1.3$ μm. An insulating layer of SiN was deposited and then opened in correspondence of the devices for contact deposition purposes. Figure 6.4a shows the facet of a DFB cavity, on a *thin cladding* structure, with the typical dimensions. We highlight that the SiN opening must be almost as wide as the ridge, to avoid the onset of undesired lateral lobes. The close-up of Fig. 6.4b shows the thickness of the metallic finger of ≈ 70 nm and the thickness of the lateral contacts of more than 250 nm.

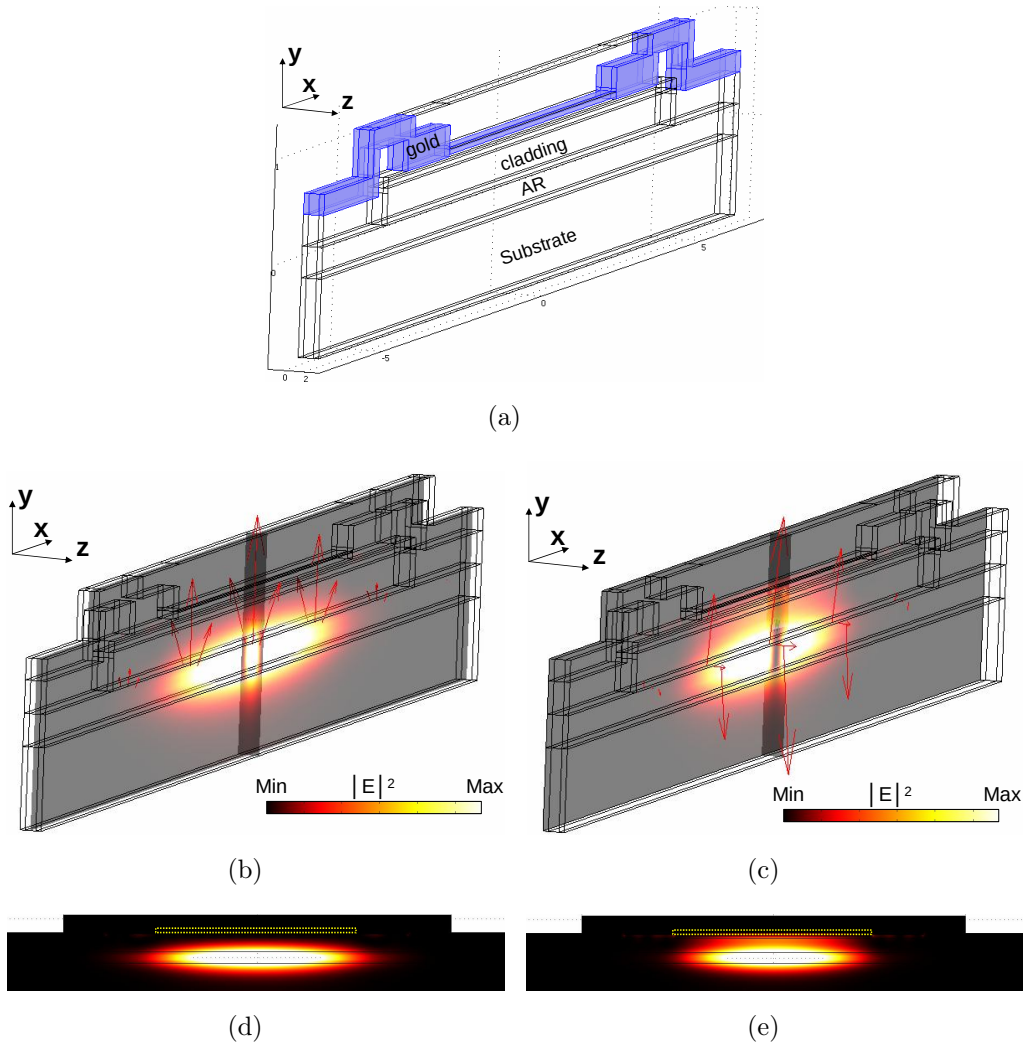

Figure 6.3: (a) Geometry used in the 3D simulation of a DFB period. Simulation results showing two slices (parallel and perpendicular to the facet) of the squared electric field ($|E|^2$) of the mode with a field maximum under: (b) the metallic finger and (c) the air slit. The red arrows are proportional to the electric field. (d) and (e) are a facet view of, respectively, the simulations (b) and (c). The gold finger boundary is colored in yellow.

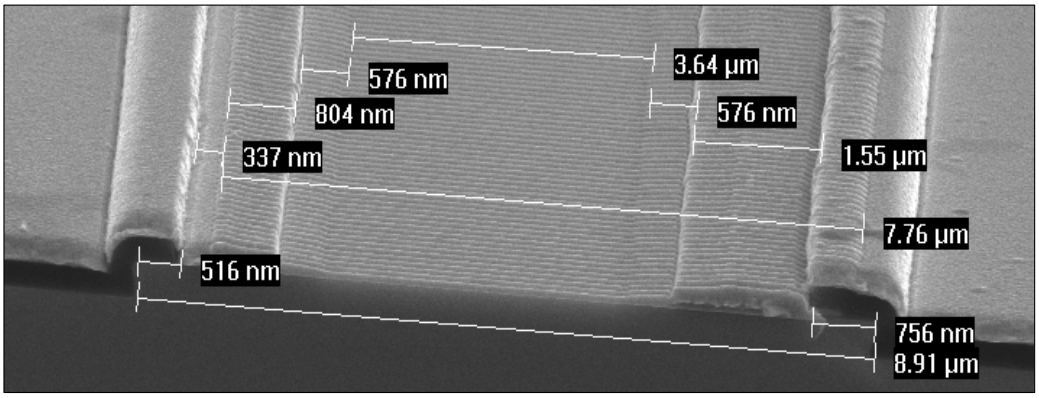

(a)

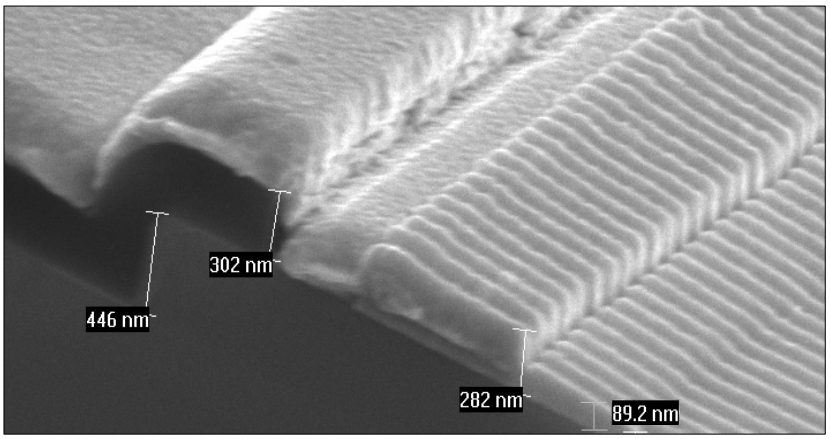

(b)

Figure 6.4: (a) SEM image of a typical DFB device. In this case realized on a *thin cladding* structure. (b) SEM close-up of the facet edge. The ridge is $\approx$ 450 nm deep, the SiN, dark colored, is $\approx$ 300 nm thick and the thickness of the metal grating is $\approx$ 80 nm.

6.3 Device Characterization

We have shown in Fig. 4.11 the characterization of a *thin cladding* device mainly based on a DFB cavity. This device correctly works and the spectra tune with the periodicity of the grating. From now on we will show the characterization of an *ultra-thin cladding* DFB device, in which the grating is even more coupled to the laser mode. The expected loss reduction effect should be larger.

Figure 6.5 reports the typical room-temperature emission spectrum of a 750-μm-long DFB laser with a grating periodicity p of 201 nm. Stable single mode emission at $\lambda \simeq 1300$ nm with a side mode suppression ratio (SMSR) of more than 30 dB is obtained. The measured full width at half maximum is of about 8 GHz (0.05 nm). The emission spectra were measured for different grating periods: 198, 199, 200 and 201 nm. The inset in Fig. 6.5 shows that all the devices are single-mode. The emission correctly tunes with the periodicity of the grating, from $\lambda = 1298$ nm (p=198 nm) up to $\lambda = 1314$ nm (p=201 nm).

6.3.1 Near field imaging of the facet

We have observed the EM near-field distribution of the laser mode with the transmission NSOM, described in detail in Appendix C.3. It is the same setup used for the top imaging of the counter-propagation device, which is equipped of an aluminum pyramid, with a nano-aperture implemented at its apex (diameter ≈ 100 nm). In this case, the device is mounted with its emitting facet oriented towards the objective of the optical microscope, and the pyramid is scanned in contact mode. The photons transmitted through the nano-aperture are collected by the microscope objective and focused into an optical fiber connected to a thermoelectrically-cooled InGaAs detector. The use of a hollow probe allows a very effective suppression of the far-field radiation from the laser facet, which would otherwise saturate the detector.

In Fig. 6.6 we present the near-field analysis of the facet shown in (a). The figures (b), (c), (d), (e) show room temperature near-field measurements of the device facet, at injected current densities of 4, 7, 10 and 13 kA/cm^2. Images (b) and (c) were recorded below threshold, (d) at threshold, and (e) in the laser regime. The white-dotted lines materialize the edges of the ridge. Below threshold (Fig. 6.6b-c) we mainly detect the device luminescence

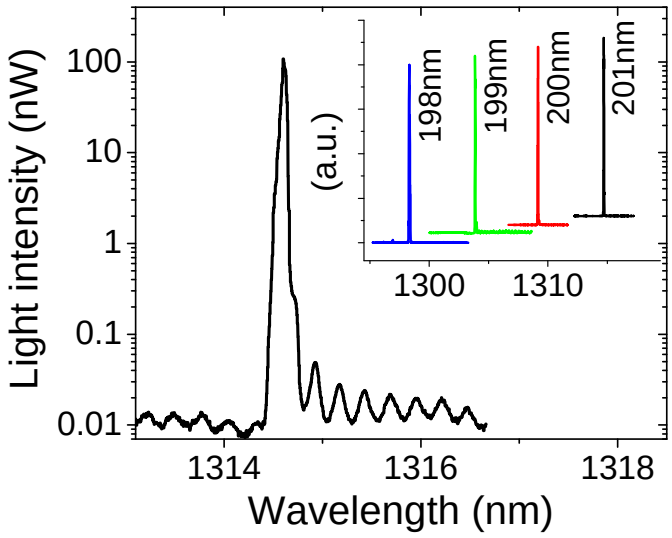

Figure 6.5: Single mode spectra of a DFB laser with a grating periodicity of 201 nm, operating at J=13 kA/cm^2. The SMSR is more than 30 dB. The spectra were recorded by using a cleaved multimode optical fiber which is coupled to an optical spectrum analyzer. The inset shows four normalized spectra of DFB laser with different grating periods, from 198 nm to 201 nm.

which originates from the whole AR. In contrast, when the laser regime is established (Fig. 6.6e), we detect a single lobe which is well confined at the center of the ridge resonator and in the AR layer. The progressive transition from the luminescence to the laser regime is visible in the strong confinement of the mode lobe upon increase of the injected current. Figure 6.6f reports 1D transverse cross-sections - along the x-direction - of the NSOM measurements.

The logarithmic scale highlights the transition from spontaneous to stimulated emission. Below laser threshold, the NSOM detects a diffused luminescence signal along the ridge width, not negligible compared to the central maximum, and increasing with the injected current. Whereas above threshold (J $>$ 10 kA/cm^2) the luminescence signal is clamped and the central lobe has a Gaussian shape. The black dotted line in Fig. 6.6f, taken from the numerical simulation in Fig. 6.3, is in good agreement with the experiment, if the spontaneous emission component on the sides is neglected. Note: the lateral contacts necessary to achieve electrical injection into the grating are continuous stripes which cover the patterned metal. The presence of this con-

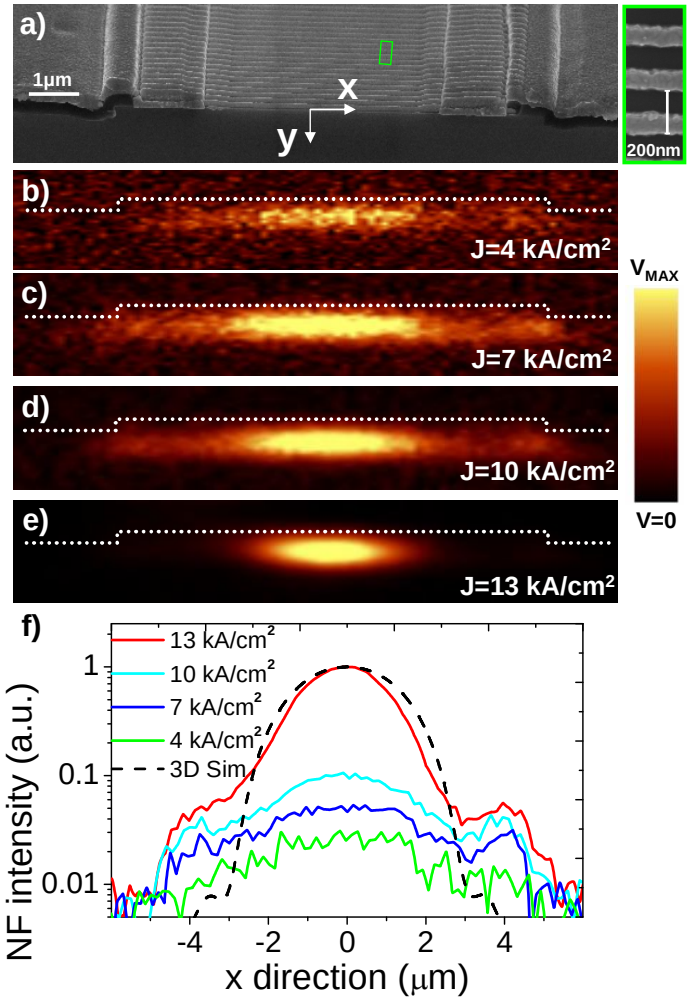

Figure 6.6: (a) Scanning electronic microscope (SEM) image of the DFB laser facet. NSOM images and simulation of the DFB laser facet showing the transversal mode electromagnetic field distribution at different operating currents of the device: (b) far below threshold (J = 4 kA/cm^2, V_{MAX} =0.07 V); (c) below threshold (J = 7 kA/cm^2, V_{MAX} =0.12 V); (d) at threshold (J = 10 kA/cm^2, V_{MAX} =0.24V). (e) at laser regime (J = 13 kA/cm^2, V_{MAX} = 2.25 V). f) Cross-section (along the horizontal direction) of the NSOM measurements plotted in solid colored curves. The experimental cross-section of the laser mode in (f), corresponding to the red solid line, is to be compared with the horizontal cross-sections of the simulated mode, black dashed line.

tinuous metallic region at the resonator sides increases the optical losses for higher order transverse modes. The single-lobed fundamental mode emerges as the favored one for lasing.

6.3.2 Comparison with an un-patterned laser

The peculiar properties of the DFB laser mode (duty cycle = 50%) can be best appreciated in comparison with a laser with an un-patterned top contact layer (equivalent to a DFB laser with DC=100%). If the top metal is not patterned we have the hybrid plasmonic structure of the previous chapter. The corresponding simulated field distributions are plotted in Figs. 6.7a and 6.7b. The insets on the left show the 1D vertical cross-section of the squared electric field along the dotted lines. The cross-section of the 100% duty cycle device shows two maxima, one located at the AR, and the other one at the interface between the dielectric cladding and the metal layer. The DFB laser exhibits instead a single maximum at the AR, similarly to a dielectric confined mode, and no field is present at the metal-semiconductor interface. The simulated field distributions are in agreement with experimental NSOM measurements of the facets, which are shown in figure 6.7c. In particular, this measurement confirms the intuitive picture developed in 6.1: the grating indeed repels the field from the metal.

The different field distribution between the fully metallic and the DFB laser entails a difference in optical losses and consequently a difference in laser threshold. We observed a reduction of the threshold current density (J_{th}) due to the metal patterning. Both devices can operate at RT in pulsed regime (Fig. 6.8). The DFB J_{th} is $\approx$ 8 kA/cm^2, while the fully-plasmonic laser – whose emission is of course multimode – operates at J = 14 kA/cm^2, i.e. a threshold reduction of $\approx$ 40%. The dashed curves in Fig. 6.8 correspond to the light-current characteristics of a fully metallic and a DFB device achieved with the same active region, but with a 200 nm thicker InP cladding [95] (*thin cladding* structure, t_{cl} = 450 nm). Since the metal is farther from the AR, threshold values are lower than the previous case. However, even in this case a slight threshold reduction of approximately 0.5 kA/cm^2 can be observed. The reduction is only of 15% because the grating is less coupled to the optical mode.

Figure 6.8 shows that the DFB laser differential resistance is slightly

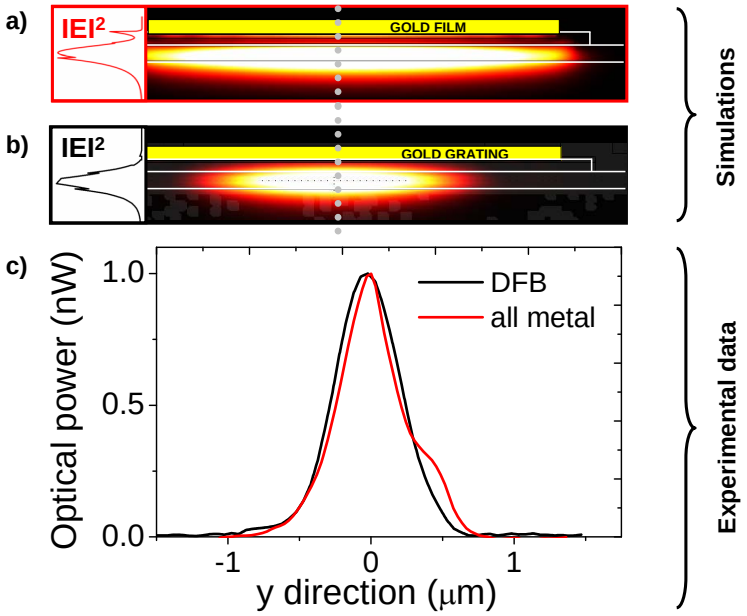

Figure 6.7: Plot of the squared electric field of a facet simulation and inset containing a vertical cross-section for a mode of: (a) A fully metallic cavity. Note the presence of the mode field in the AR and at the interface of the metal. (b) A DFB cavity. The mode shows instead a single maximum, located in the AR. (c) Normalized experimental cross-section along the vertical direction (y-direction, where the zero corresponds to the center of the AR), for the mode of the fully metallic cavity (red line) and the mode of the DFB cavity (black line).

larger than the one of the laser with full metallization (1 Ohm). The non uniformity of the top contact, due to the metal patterning, affects the current injection increasing the total resistance.

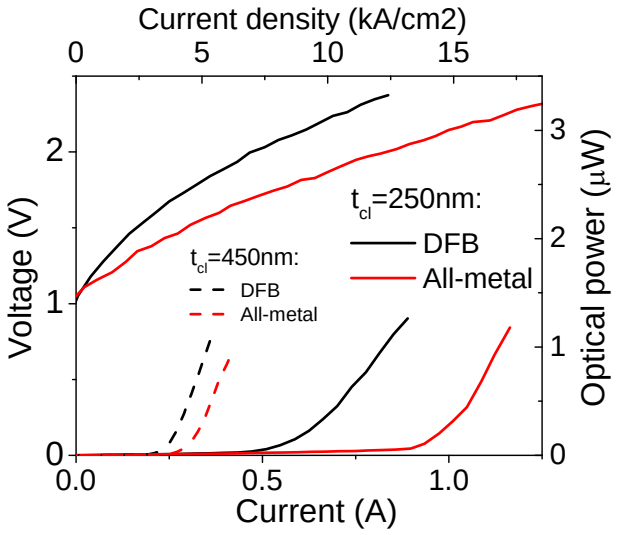

Figure 6.8: Typical Light-Current-Voltage (LIV) characteristics of a DFB laser (black solid curves) and an fully metallic laser, equivalent to a DFB laser with a duty cycle of 100% (red solid curves).The DFB device exhibits a larger differential resistance, but it presents a threshold reduction of more than 5 kA/cm^2 compared to the fully metallic laser. The dashed lines are the light output power of a DFB laser (black dashed curve) and an fully metallic laser (red dashed curve) fabricated on a structure with the same active region but with a cladding 200 nm thicker (*thin cladding* structure). In this case the threshold reduction of the DFB laser compared to the fully metallic laser is of only 0.5 kA/cm^2.

6.4 Calculations of loss reduction

Finite element simulations provide a qualitative understanding of the loss reduction induced by the metal patterning. The simulations are performed in 2D, but are compatible with the 3D simulations of Fig. 6.3. The calculation is performed by solving the 2D Helmholtz equation in a single unit cell, with periodic conditions along the waveguide. A similar analysis is reported in [63], but in this case - because of the presence of a thin top cladding - three different modes a priori exist, considering all the duty cycles, all satisfying the requirement of TM polarization and confinement in the AR larger than 30%.

The optical losses of the three modes (1-2-3) as function of the duty cycle (with a step of 0.2%) are plotted in Fig. 6.9a. Since only two modes exist for a given duty cycle, we show the field distribution at a duty cycle of 50% and 80%. In Fig. 6.9b we depict the low-loss mode 1 (red dots) and the mode 2 (blue squares) for the duty cycle 50%. In Figs. 6.9c we depict the low-loss mode 1 (red dots) and the mode 3 (green triangles) for the duty cycle 80%. The field distributions corroborate the origin of the losses: the field overlaps with the metal. At a duty cycle = 60% the losses of the two modes diverge because in both cases the electric field is pulled toward the metal and the confinement in the AR becomes less than 30%. This behavior is a typical feature of structures with a thin top cladding, as was shown in Ref. [134]. On the contrary, the low-loss mode never has a significant overlap with the metal, hence it is relatively independent of the grating duty cycle. The DFB laser is expected to operate on this latter mode (Fig. 6.9b), as experimentally verified by the NSOM measurement (Fig. 6.6e).

While the operation on the low-loss mode is experimentally confirmed, the finite element simulations predict optical losses of $\alpha = 40$ cm^{-1}, implying a J_{th} of ≈ 2 kA/cm^2 [83]. This value is much lower than the experimentally measured J_{th} (J = 9 kA/cm^2), and the same holds for the thicker structure which should exhibit an even lower J_{th} . There are several possible reasons.

The higher differential resistance exhibited by the DFB device entails more heating by Joule effect and results in a lower efficiency.

The electrical injection in correspondence of the grating – which serves also as top metal contact – is not as efficient as in presence of a continuous metal layer. The DFB device might experience a better current injection under the lateral strips (where a continuous metallization is present), and a less efficient current injection in the device core, where the laser mode is confined.

Furthermore, even in the low-loss mode, a fraction of the field is overlapping the cladding and the metal. Supplementary losses can arise from the Ti layer or the cladding absorption.

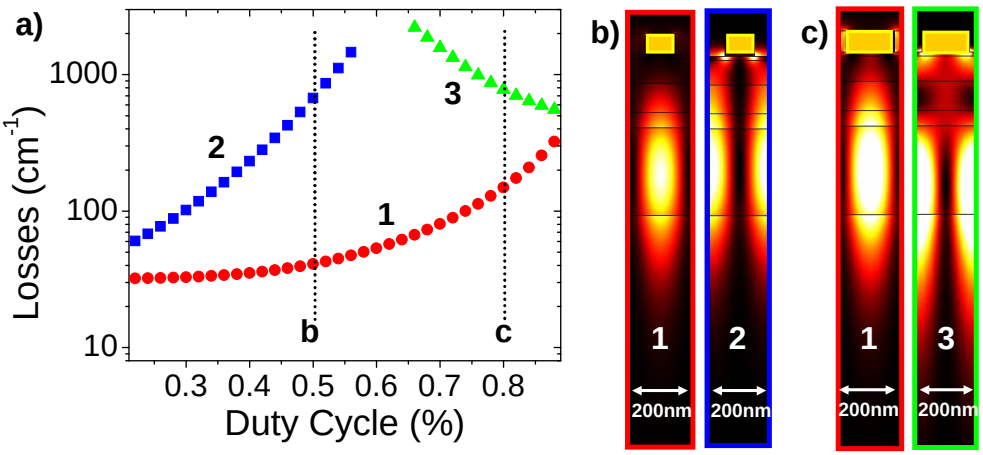

Figure 6.9: a) Results of the 2D finite element simulations showing the modal losses as a function of the duty cycle of the DFB grating. We selected the modes which are TM polarized and have an AR confinement factor of more than 30%. At a duty cycle of 60% the two high-loss modes diverge and the AR confinement factor decreases. This behavior - not observed in Ref. [67] - is in fact typical of DFB lasers with a cladding layer between the AR and the metallic grating [134]. b,c) Longitudinal finite element simulations of a DFB laser period. The squared electric field is plotted for: (b) modes at DC 50%. The low-loss mode 1 (red dots in panel a) and the mode 2 (blue squares in panel a). (c) modes at DC 80%. The low-loss mode 1 and the mode 3 (green triangles in panel a). The electric field for the low-loss mode is located under the metallic fingers and has no consistent overlap with the metal. This is in agreement with the NSOM measurements in Fig. 6.6e. The other modes 2 and 3 have an electric field maximum located under the air slits, between the metallic fingers, and have a consistent overlap with the metal.

6.5 Conclusions

We have demonstrated a DFB laser device operating in single mode at telecom wavelengths with a metal grating extremely close to the active region. The near-field imaging of the facets is completely stray-light free and it provides experimental evidence of the operation on the fundamental, low-loss grating mode. NSOM results are in excellent agreement with the 3D finite

element simulations. Moreover the comparison with the unpatterned device shows a threshold reduction due to the grating. This experimental evidence is noteworthy in the context of plasmonics, but also for device physics. If the problem of non-perfect electrical injection is solved, it will be possible to efficiently combine a simple metallic grating technology with diode laser devices.

Since the electrical injection improvement requires an increase of the cladding doping, entailing an unavoidable increase of the optical losses, we consider for the future a different injection technique. The tunnel junction proposed at the end of Chap. 5 would represent a suitable solution also in this case. It will require a cladding thickness of only a few tens of nanometers and would present the advantage of a n-type contact, which is more efficient and less absorbing than a p-type contact type.

Conclusions and perspectives

In this thesis work I tried to provide experimental answers to the fundamental question on how far we can compensate plasmonic losses with a semiconductor-based active approach. I centered my investigations on the generation and amplification of surface plasmon polaritons (SPPs) at telecom wavelengths, using a semiconductor gain medium with quantum wells. The devices are operated at room temperature and by electrical injection. These conditions provide compactness and ease of use, which are crucial characteristics for further developments.

I first learned fabrication, measurements and numerical techniques used for quantum cascade laser (QCL) devices. I participated to the demonstration of a SPP generator in the mid infrared (Mid-IR) based on an end-fire coupling approach. As a necessary and useful introduction, I also described previous achievements of our group, namely the achievement of a counter-propagation design for SPP generation.

I used this knowledge to transfer the mid-IR concepts at telecom wavelengths. An accurate preliminary study was performed on the active region (AR), based on tensile strained quantum wells, as these semiconductor structures were not previously used in our group. I then developed the fabrication steps necessary to build an edge emitter ridge cavity resonator. In order to study the interaction of the metal with the AR gain, we considered structures with thin top cladding. Of course the metal proximity reduces the device performance but, at the same time, provides gain to SPP modes.

I have built devices with different cladding thicknesses, measuring their differential gain through the Hakki-Paoli technique. Thanks to the support of passive measurements I could validate the numerical simulations, used further in this work. The finite element simulations, with the tuned optical indexes,

allowed to design the SPP generation devices and to precisely estimate the losses for the SPP amplification.

I demonstrated, with two different approaches, SPP generation at telecom wavelengths. The first solution is a device where the source, a standard thick cladding laser, is coupled by end-fire to the SPP waveguide. The second solution instead is a device with the source, thin cladding laser, coupled by a grating to the SPP waveguide. In order to demonstrate the latter device, I developed an electron beam lithography recipe to obtain the lift-off of a reasonably thick (above the skin depth) metallic grating with periodicity 200 nm and duty cycle 50%. The generation of counter-propagating SPPs provides an evanescent interference pattern. The SPP generation was fully confirmed by excellent near-field measurements, which permitted to measure the interference pattern periodicity and its vertical extension. This elegant and original approach allows one to easily access the SPPs, which are on the device top surface.

With the final goal of completely compensating the SPP losses, we reduced as much as possible the top cladding thickness. The metal proximity to the AR induces a hybridization of the waveguided mode, which acquires a plasmonic component. Using a heterostructure with an extremely thin cladding I demonstrated a laser device operating on a hybrid plasmonic mode ($\alpha \approx 500$ cm^{-1}). Like the previous generators, the device operates by electrical injection at room temperature. The near-field imaging of the laser facet provided the evidence of stimulated emission into the hybrid mode and confirmed the predictions of the numerical simulations.

Finally, approaching real applications, I gave a preliminary demonstration of loss reduction due to the patterning of the metallic top contact. We realized a metallic distributed feedback laser with lower threshold compared to an unpatterned contact. Even in this case the results are corroborated by near-field microscopy measurements, which allowed us to directly measure the mode distribution on the device facet, both in spontaneous and stimulated regime.

In perspective, real-applications will be possible by further decreasing the threshold of the device and enabling continuous wave operation. We believe that the top metal patterning combined with a lower absorption in the top cladding could lead to this goal. As explained at the end of Chap. 5, we

believe that the use of a tunnel junction injection would avoid the presence of the InGaAs interband absorption and would permit an efficient n-top-contact. The low-threshold operation would pave the way to devices with high field intensities on their top metallic interface (cfr *counter-propagation* devices) potentially useful for chemical and biological detection.

The tunnel junction will also allow us to further decrease the top cladding thickness. This would enable a direct pumping of the SPP mode, with the aim of demonstrating an electrically pumped semiconductor-based SPASER device.

Appendix A

Photo-luminescence measurement

Our collaborators at the *Institut d'Optique* measured the photo-luminescence (PL) of the active region (AR). The luminescence measurement can be performed on the wafer before the fabrication process.

The setup is composed of a CW laser at $\lambda = 980$ nm (≈ 1 mW) used for sample excitation. An Olympus x100 objective, with numerical aperture 0.95, permits a local excitation within a spot of diameter ≈ 1 μm. The collection is performed with the same objective and the out-coming signal is coupled to a multimode optical fiber. The signal is analyzed with a spectrometer TRIAX 550 (Jobin Yvon) equipped with an InGaAs cooled detector (Princeton instruments). The spectral resolution is 0.3 nm.

This setup was used to measure the AR presented in Tab. 3.1, which is the same for all the devices. The spectra were collected for different sample positions (see Fig. A.1) and feature three main peaks. Each luminescence peak arises from the recombination of the electrons with holes in different valence bands. The most intense peak is at $\lambda = 1300$ nm: it is due to the recombination of the electrons with light-holes (see the schematic in Fig. 3.3). From the selection rule for this transition we know that it mainly emits in TM polarization.

The homogeneity of the luminescence was further investigated scanning the surface for several hundreds of μm^2. The constant signal shown in Fig. A.2 proves the excellent quality of the AR.

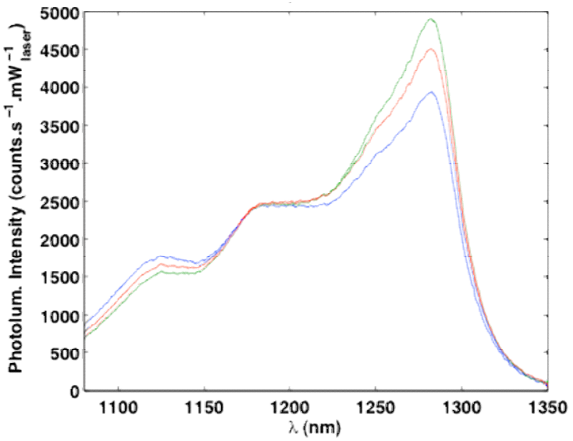

Figure A.1: Three PL obtained at different sample positions. The highest intensity is at $\lambda \approx 1300$ nm. The spectra are similar to the ones measured in [81].

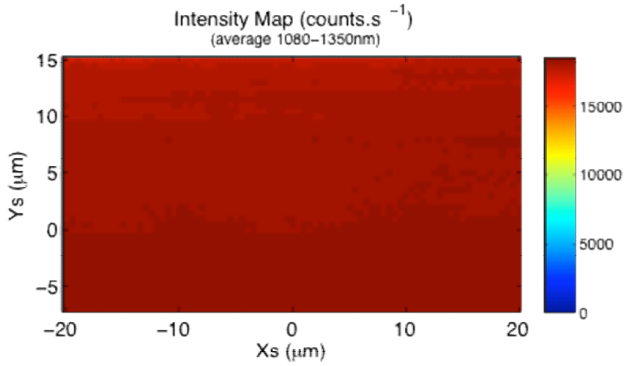

Figure A.2: The spatial scan proves a constant PL emission from all the sample.

Appendix B

Device fabrication

This section describes the fabrication steps that I realized to process the devices used in this work. Except for epitaxial growth, all the fabrication steps are performed in the cleanroom at *Laboratoire d'électronique fondamentale* (IEF), the *Centrale Technologique MINERVE*. We detail all the necessary steps to fabricate the fully-metallic and the air-confinement lasers. The DFB laser fabrication is identical, but with a supplementary initial step of electron beam lithography (EBL) and metal evaporation. The end-fire devices require a specific processing which includes a dry etching step (section B.3).

All the devices are processed on square pieces of substrate, with an approximate size of $\approx$ 1,5 cm x 1 cm. An initial surface cleaning is performed with 40" in a solution of buffered oxide etch (which is a mixture of a buffering agent, such as ammonium fluoride, NH_4F, and hydrofluoric acid, HF).

B.1 Fully-metallic and air-confinement device fabrication

Ridge etch

The ridges are obtained by wet etching after an ultra-violet (UV) lithography. The resist patterns constitute the mask for the etching. In our case the ridges cover all the sample length and are 9-μm-large. A solution of $HBr:HNO_3:H_2O$ is used to etch the InGaAs and the InGaAsP layers. The following etch up to the AR is preformed with a solution of $HCl:H_3PO_4$, that

etches the InP cladding and selectively stops on the SCH-sup layer (see Tab. 3.1).

In the order, the UV lithography requires:

- Sticking layer (HMDS) and the positive resist S1813 (thickness 1,3 μm) are applied with a coating spinner
- Bake at 110°C for 1 min
- Borders removal (the borders of the resist mask are thicker and would prevent a good contact between the chrome mask and the resist on the sample surface)
- Exposure 10" in soft contact
- Development 12" in MF319
- O_2 light plasma for 2'

The etching is checked step by step using a Dektak profilometer. The sample is dipped in:

- HBr:HNO_3:H_2O (1:1:10), etching speed of 800 nm/min
- HCl:H_3PO_4 (1:5), etching speed of 450 nm/min

The result of this step is schematically shown in Fig. B.2b.

Insulator deposition and opening

The complete insulation of the sample with a subsequent opening by UV lithography allows one to electrically insulate the entire sample except the regions chosen for current injection. In our case we want to inject current only in the top of the ridge. A layer of SiN is homogeneously deposited on the surface by plasma enhanced chemical vapor deposition (PECVD), as shown in Fig. B.2c. The successive step is an etching which permits to open the insulator at the ridge center as shown in Fig. B.2d. We leave a 7-μm-large slit on the ridge top.

This lithographic step is critical because it requires micrometric alignment. The resist mask has to be exposed at the center of the ridge leaving symmetrical gaps between the slit and the ridge border. Especially in the *ultra-thin cladding* structures this lateral gap needs to be as small as possible to avoid the onset of parasitic modes under the SiN. Otherwise we can have a mode lasing only under the insulator on the ridge borders. This low loss mode would prevent the study of the compensation of the metal losses .

An SEM image of a device facet is shown in Fig. B.1a. The gap of ≈ 500 nm, visible in Fig. B.1b, is obtained by overdeveloping the resist, in order to

increase the slit aperture from the 7 μm of the mask to more than 8 μm.

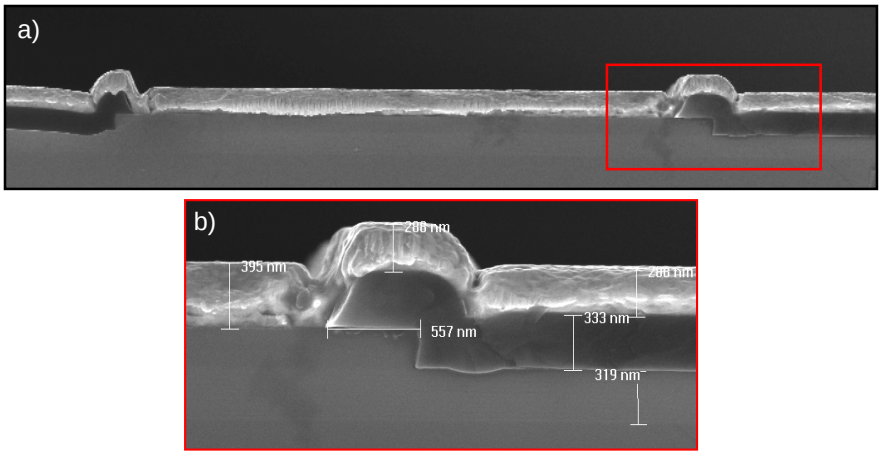

Figure B.1: Typically fully-metallic device realized on an *ultra thin cladding* structure. Section of a cleaved sample of width 9 μm (a). The SiN (dark layer) is opened on the ridge while the gold (light layer) is continuous. The close-up (b) shows the typical thickness of the different layers and the SiN width on the ridge border. Is is also possible to discern the AR, which is lighter than the substrate and the cladding.

Before to start the SiN etching a O_2 light plasma is necessary to clean the surface from traces of undeveloped resist. The SiN is dry etched with reactive ion etching (RIE) using a mixture of CF_4 and O_2. The plasma is performed at high pressure, obtaining skewed SiN borders (see Fig. B.1b), which are more favorable for metal deposition. An interference system based on a diode laser allows to follow in real time the RIE etching and to stop the process when the device surface is reached.

Note - The fabrication of the fully-metallic *ultra-thin* cladding devices requires a top contact without the Ti sticking layer. After the SiN opening the sample is de-oxided (see next section) and a 80 nm-thick-layer of Au only is evaporated. After resist removal the gold remains exclusively on the ridge top. This gold layer will be then encapsulated in the top contact.

Top metal deposition

The deposition of the top contact pads requires a lift-off. A negative resist is more appropriate for this purpose allowing an under-cut once the resist is developed. We chose the resist AZ 5214 E,

- Sticking layer (HMDS) and the negative resist AZ5214 E (thickness 1,4 μm) are applied with a coating spinner
- Bake at 110°C for 1 min
- Borders removal (the borders of the resist mask are thicker and would prevent a good contact between the chrome mask and the resist on the sample surface)
- Exposure 4" in soft contact
- Bake at 120°C for 2 min
- Flood exposure 50"
- Development 15" in AZ400K:H_2O 1:4

Before the evaporation the sample is cleaned with a light O_2 plasma and de-oxided for 40" in a solution of HCl:H_2O 1:4. This step is important to get rid of the layer of natural oxidation of the InGaAs that could affect the electric injection and increase the mode optical losses.

The metal is deposited by electron beam evaporation with a *Plassys* machine.

- 3 nm of Ti (evaporation speed 0.1 nm/s)
- 100 nm of Au (evaporation speed 0.3 nm/s)
- 150 nm of Au with a sample holder tilted at 30°and rotating (evaporation speed 0.3 nm/s)

As shown in the schematics of Fig. B.2e and B.2e2 is possible to chose between a fully metallic contact and an air confinement waveguide, with the metal contacts only on the ridge edges.

Polishing and bottom metal deposition

The sample is mechanically polished up to a thickness of 200 μm. A metal layer of Ti/Au (5 nm/200 nm) is then evaporated on the back side. The sample is then cleaved and mounted on copper supports, as shown in Fig. B.3.

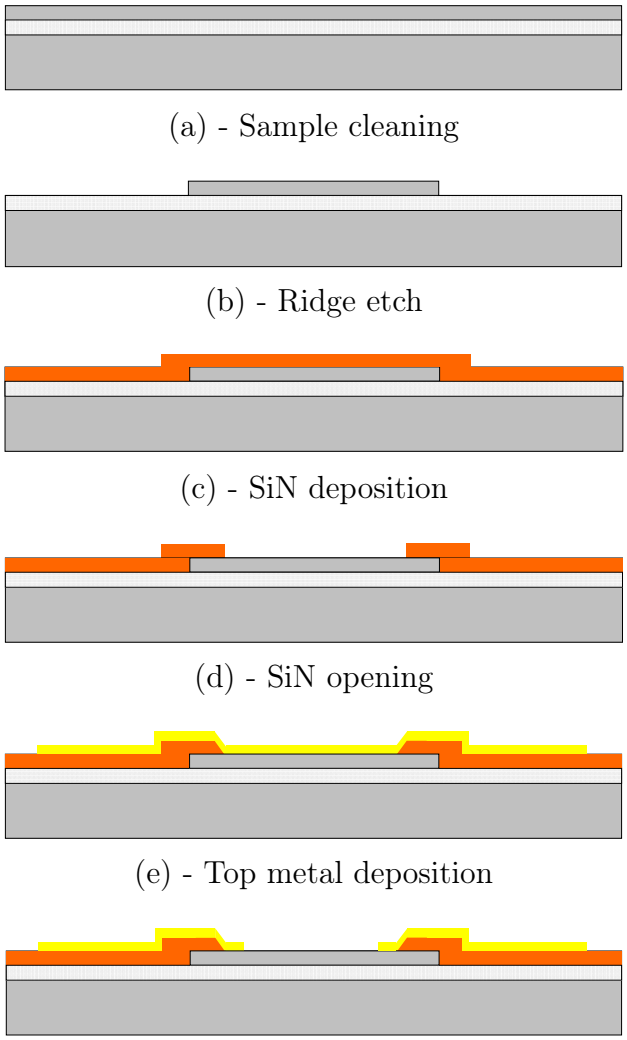

Figure B.2: Fabrication steps for the fully-metallic and the air-confinement waveguide.

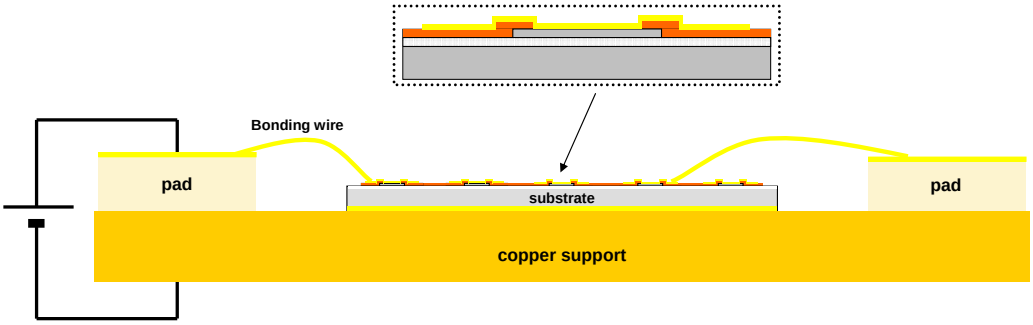

Figure B.3: Devices mounted on the holder and connected to the pads. The close-up shows one of the laser facets.

B.2 Electron beam lithography for metal patterning

In this work I developed a recipe based on the lectron beam lithography (EBL) to realize metallic nanometric gratings by the use of a Raith 150 electron-beam lithography system. The Raith 150 system is capable to define patterns with a resolution of 50 nm, resulting particularly suitable to obtain the metallic patterning of the couterpropagation device (see section 4.1.3), including the couplers and the first order DFB grating presented in Chap. 6. We first furnish a brief description of the EBL technique.

The EBL is a very precise and high-resolution technique, allowing to create extremely fine patterns with resolutions down to few nanometers. Electronic lithography started to be used between the '60s and '70s and is based on an instrument similar to the Scanning Electron Microscope (SEM). An EBL instrument schematic is shown in Fig. B.4. As in the SEM, an electron

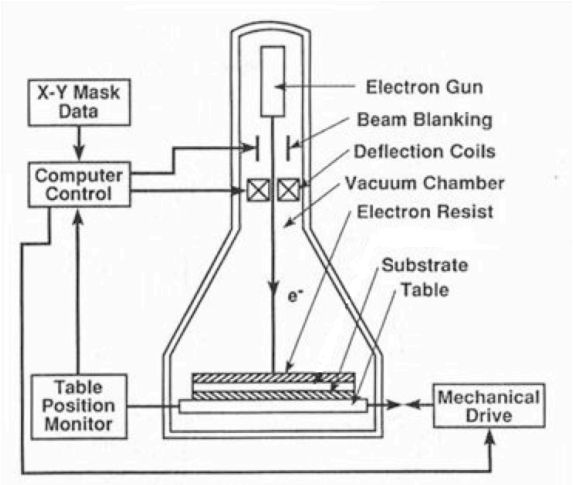

Figure B.4: Schematic of an EBL instrument [136].

gun emits an electron beam (e-beam) in a vacuum chamber. The electrons are produced in the uppermost section, which is called the electron source or gun. In the optical column the e-beam is directed toward the surface of the sample, which is mounted on a holder and clamped to the stage. Several additional stages permit to control the beam current and the beam shape on the sample surface. The collimated high energy e-beam (in recent systems

up to 100 keV) exposes the resist layer impinging on the sample surface. In order to expose any possible pattern it is necessary to switch the e-beam on and off with a beam blanker, that diverts it. The e-beam is moved on the sample surface through magnetic deflectors. Indeed, the Raith 150 system utilizes a vector-scanning approach where the substrate is kept stationary while the e-beam is deflected over the areas to be exposed. The maximum widths of one write field is around 800 μm, however for large writing fields the precision is lower than for the small ones. As we are dealing with sub-micron contact features, a small writing area is desirable so that the e-beam can cover it with good precision. For this reason we chose the write field size of 100 x 100 μm^2. To expose more writing fields the stage, consequently the sample, can be moved with piezo-electric motors. The position is controlled by an interferometric system, bringing under the e-beam a new area of the sample surface. The whole process is regulated by a computer that guides the e-beam along the desired pattern and control the stage position.

Recipe

- Cleaning in BOE for 40"
- Coating with polymethyl methacrylate (PMMA A3). PMMA is a transparent polymer, which is sensitive to the e-beam. When exposed to the electron beam, these complex macromolecules get broken down into simpler compounds, which can be easily dissolved in a chemical developer. A spinning at 4000 rpm, for 60 seconds gives a layer thickness of $\approx$ 150 nm
- Bake at 180°C for 20'. It allows to evaporate the resist solvent
- Scratch on the sample corner. The dust coming from the scratch is used in the focus procedure
- EBL exposure. The parameters are specified in Fig. B.5
- Development 50" in a solution of 3 parts IPA and 1 part methyl-isobutyl ketone (MIBK) by volume.

To determine the optimal exposure parameters we used a method based on dose modulation. The method consists in writing a large number of identical patterns and progressively increasing the dose in each one of them. The initial dose is estimated from the resist datasheet provided by the manufacturer. The dose for the first pattern is deliberately set below the expected optimal value and the step by which the dose is increased for subsequent

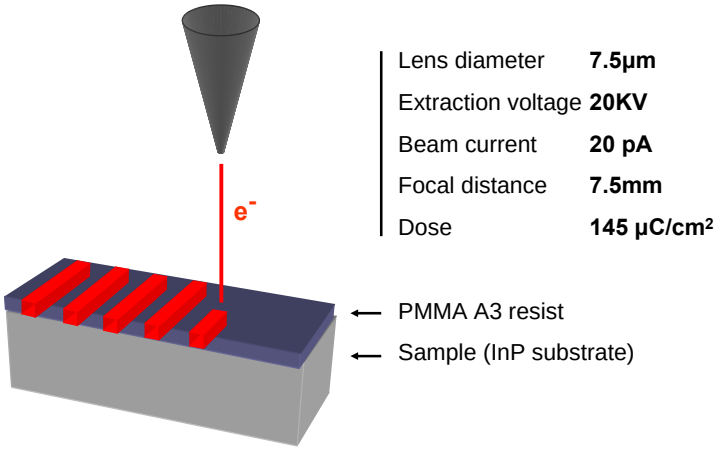

Figure B.5: Schematic of the exposure with the used parameters.

patterns is chosen small enough to determine the optimal value with a high precision. SEM observation after metallization and lift-off allows one to find the optimal dose.

We show in Fig. B.6 a schematic of the device after the EBL and the lift-off . Typically a sample has about ten ridges of length 7 mm, requiring an over-night lithography of several hours. The inset is an SEM image of a grating of width 7.8 μm.

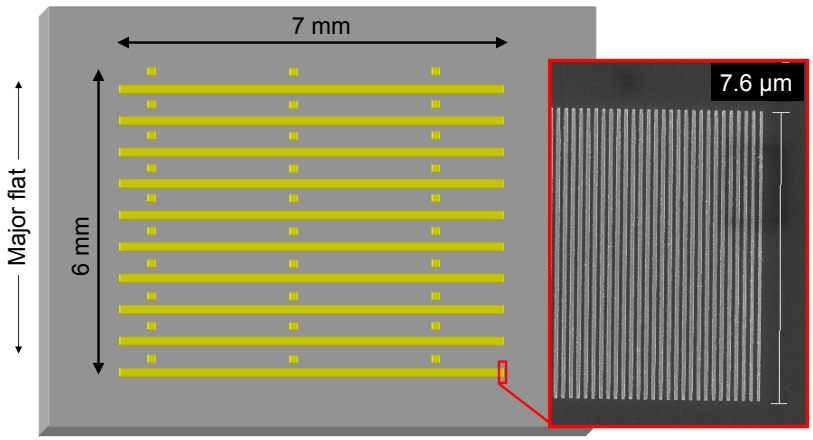

Figure B.6: Schematic of the sample after EBL step and the metal deposition. Typically about 10 ridges are fabricated with a length of 7 mm. The inset is an SEM image of the grating after the lift-off.

The close-up of Fig. B.7a shows a single period of the grating (nominal period 196 nm), exhibiting a duty cycle of about 50%. With our SEM it was not possible to precisely measure the period, but we can appreciate its increasing by averaging on several periods. An example of measurement is shown in Fig. B.7b, where the nominal value of the period in the EBL mask is written in white.

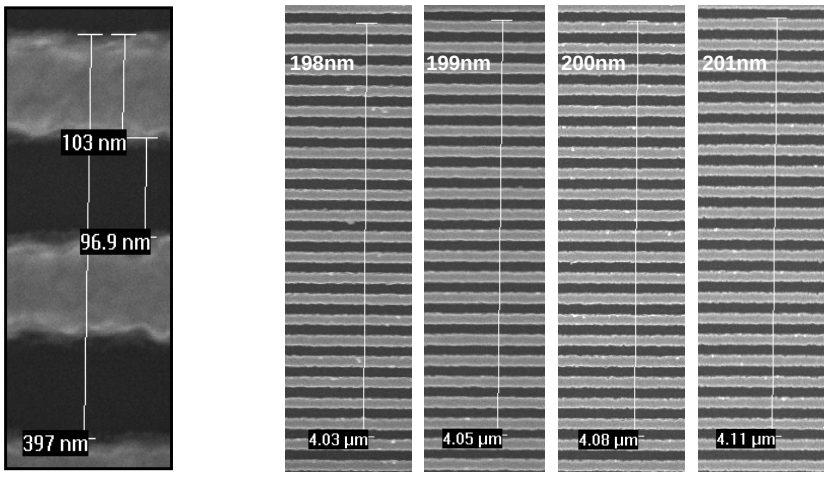

(a) (b)

Figure B.7: The period can be measured with the SEM microscope, for instance in (a) a nominal period of p = 196 nm. A more precise measurement can be obtained by averaging on several periods. The value does not correspond to the nominal one (written in white), but the relative trend is clear.

Proximity effects

When electrons penetrate into the resist film and into the substrate, they lose energy via elastic and inelastic scatterings. Electrons undergo both small-angle (inelastic or forward scatter) and large-angle (elastic or backscatter) scattering events, once they reach the resist and substrate (see Fig. B.8). The scattering process leads to a e-beam broadening that leads to the well known *pear shape* of the e-beam into the substrate. As a consequence, the energy is deposited within the resist layer, in a region which is more extended than the e-beam waist. These scattering processes have important consequences on the writing process. In particular, for adjacent patterns,

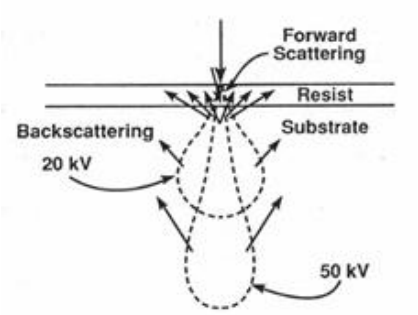

Figure B.8: Electron scattering in the resist and in the substrate [137]. By increasing the energy of the impinging electrons the e-beam waist can be reduced and the precision increased.

the exposure of one pattern contributes to the exposure of the other located within the scattering range of electrons. This is known as *proximity effect*. Such phenomena impose certain restrictions of the size and shape of the relief structures that can be written in the resist, in particular the sub-μm patterns. We highlight that the total amount of energy deposited in a pattern feature depends on its size and the distance of neighbouring features. As size and space pattern features change, proximity effects become more or less influential.

In our case the proximity effects play a big role. The points in the middle of the grating feel the contribution of the neighbors exposure. Not only the contribution of the points belonging to the same grating finger, but also of the points belonging to the precedent and the successive fingers. This is the situation for the point a) in the schematic in Fig. B.9a. The dose in the bright small red dot depends also from the contribution of the surrounding exposed dots included in the light red circle. The situation is different for points close to the finger edges. As shown in the schematic the point b) includes only two times less exposed points in its light red circle. In this case the proximity effects play for one half times compared to the point a).

A good result cannot be obtained with a unique value of dose for the whole grating. The fingers edge require a higher dose compared to the central finger section. The used EBL software provides a tool to take into account the proximity effect. However this tool requires a long computation time and is not easily applicable. To solve the problem I empirically dived the

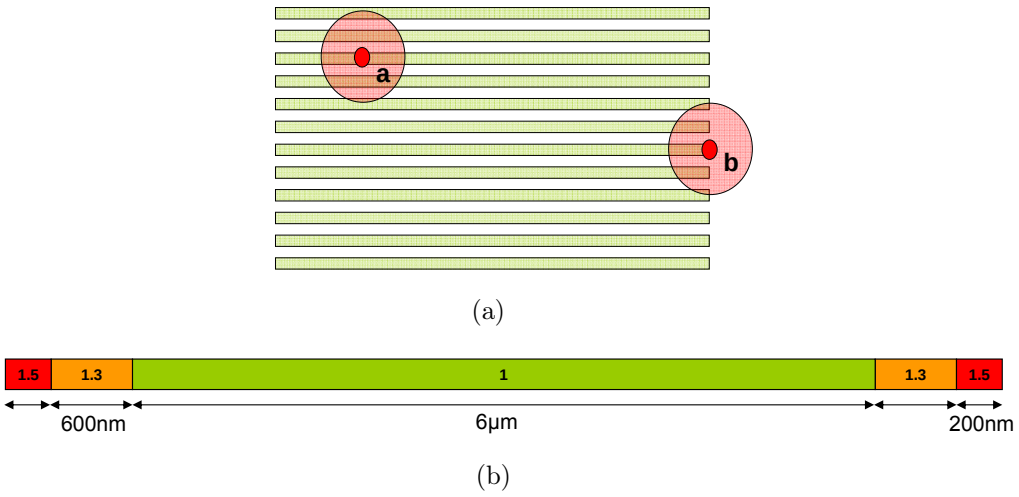

(a)

(b)

Figure B.9: (a) Schematic of the grating with two red points (bright dots) and their surrounding area (transparent red) that contributes to the point dose. (b) Schematic of the finger mask with sizes of the internal areas and realative dose of each area. The relative dose is a coefficient that multiplies the dose reported in Fig. B.5.

the finger into five rectangular areas as in Fig. B.9b. The two areas on the finger edge have a relative dose of 1.5 compared to the central dose.

EBL issues

The mastering of the recipe to fabricate reproducible grating needed some persistence. I report some of the issues experimented during the recipe trials.

Choice of the resist The resist PMMA A6 gives a layer of about 400 nm of thickness, that is four times compared to the finger width. This high aspect ratio makes the lithography not possible. The proximity effects dominates the lithography and the resist in the grating center un-sticks from the sample. The results of the attempts are shown in Fig. B.10.

Field stitching The required resolution limits the writing field to 100 x 100 μm^2, therefore the whole mask must be divided in several writing fields. The fields are written by moving the desired zone under the column. If the coordinate axes of the writing fields are not perfectly aligned with the stage

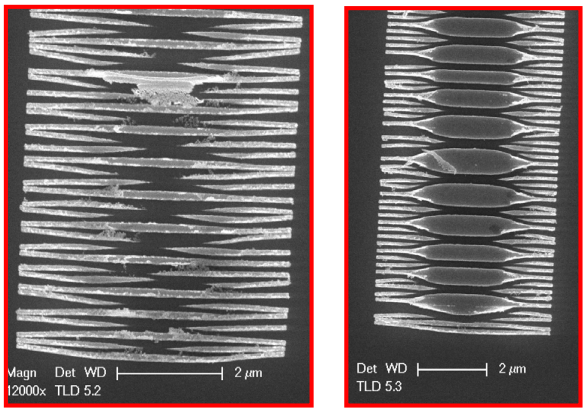

Figure B.10: A good resist choice is essential for a patterning with high resolution. A thicker resist is more sensitive to the proximity effects.

coordinate axes it is easy to have a field stitching problem, as in the cases illustrated in Fig. B.11. Stitching problems can also arise from the stage thermal drifting. It is necessary to wait about five hours between the sample loading in the EBL system and the exposure.

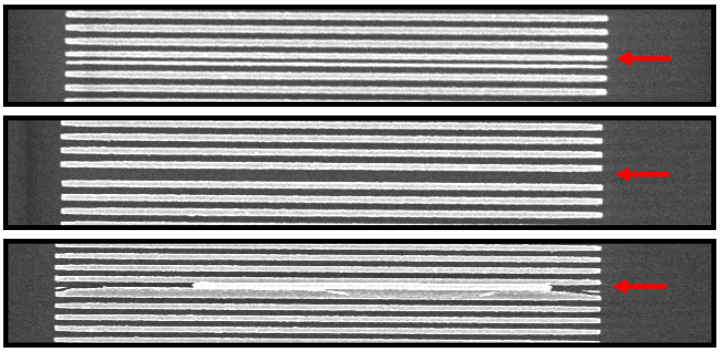

Figure B.11: Three different cases of field stitching. Stitching field errors happen if the coordinate reference of the writing field is not well aligned with the one of the stage.

Tilted sample If the e-beam is not well focused on the sample the effective dose can change, modifying the pattern duty cycle. For instance, if the

sample is not flat on the stage, the e-beam focus can be not optimized on a sample edge, as shown in Fig. B.12.

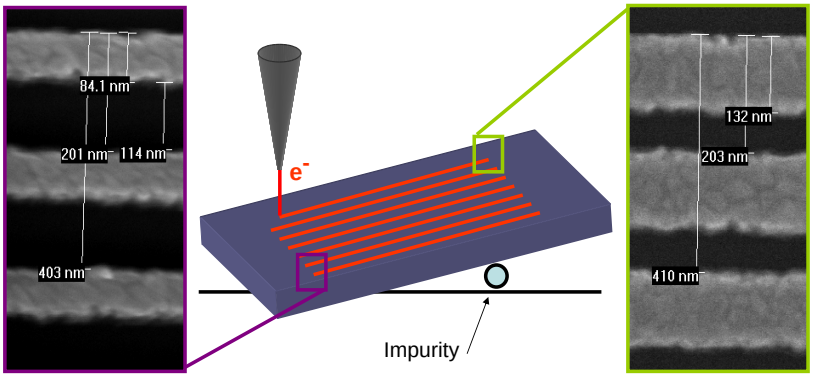

Figure B.12: Schematic of the tilted device with two SEM close-ups of the grating in different positions. A completely flat sample is required unless the effective dose changes according to the position on the sample.

Sample not cleaned The sample surface must be perfectly clean to avoid fabrication issues in the further steps. The sample can keep the "memory" of a previous unsuccessful EBL step. In the case shown in Fig. B.13 we hypothesize that a thin layer of PMMA resist remained on the sample surface. After the second lithography, this layer masked the etching, revealing the previous pattern.

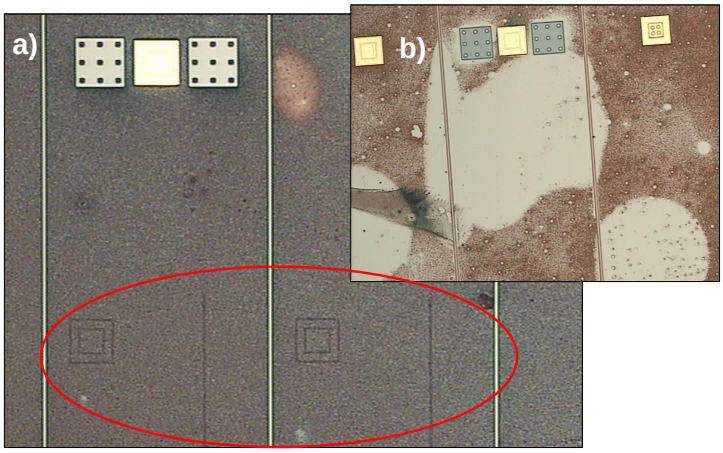

Figure B.13: A bad substrate cleaning after a unsuccessful EBL step can leave the "memory" of the previous step (a) and successively affect the etching creating an masking layer.

B.3 End-fire device fabrication

The devices are processed on the *thick cladding* structure.

ICP ridge etching

The necessity of a vertical facet in the middle of the device imposes the use of a dry ICP etching. We performed some attempts with a wet etching technique, shown at the end of the section, but with no success.

Generally the masks for wet etchings are achieved with a resist layer, but the resist can not hold a deep dry etching. Therefore, we used an SiO_2 layer mask of 800 nm of thickness, prepared as follows:

- Deposition of an homogeneous layer 800 nm-thick by PECVD
- Lithography with positive resist (S1818)
- 3' of O_2 light plasma to clean the surface from traces of undeveloped resist
- SiO_2 etch with RIE

The obtained SiO_2 mask is shown in Fig. B.14a and is also represented in the schematic of the fabrication steps (Fig. B.15a). The ICP etch is performed in the LPN laboratory and an SEM image of result is shown in B.14b. Finally the SiO_2 mask is removed with an HF attack of 20".

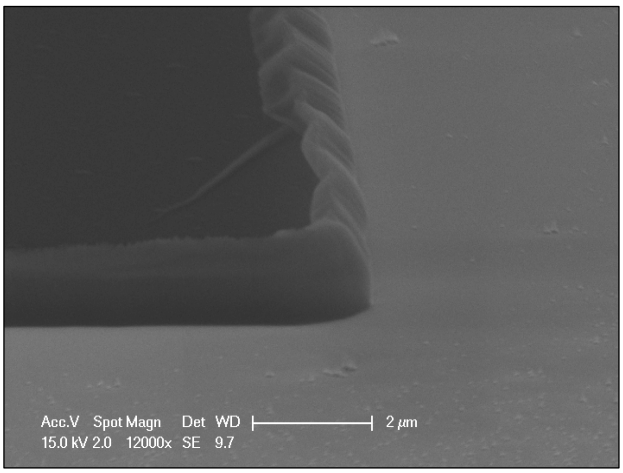

(a)

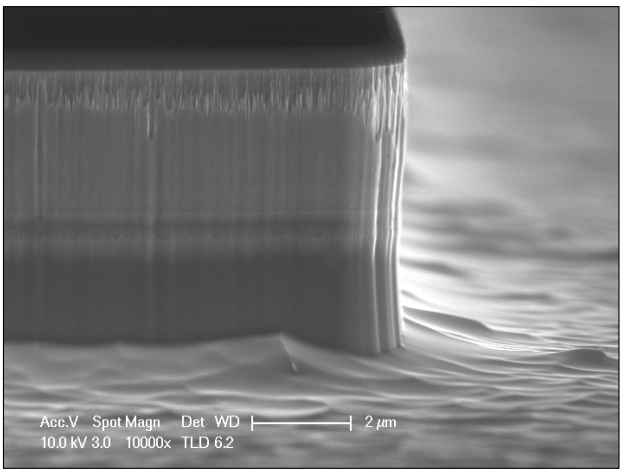

(b)

Figure B.14: (a) SiO_2 mask of thickness 800 nm and width 22 μm, obtained by optical lithography and RIE etching. (b) Sample after the ICP etching. The SiO_2 mask is removed with HF after the ICP etching.

Insulator deposition

As in the fabrication presented in section B.1, an insulating layer is needed to allow a correct injection in the ridge top. Furthermore, the same insulating layer is used to achieve the second order gratings, which probe the SPP field along the plasmonic waveguide.

The insulating layer of 300 nm of SiO_2 is etched by RIE after two different lithographic steps (see Fig. B.15c). A first electron-beam lithography is used to create the mask to define the second order gratings. The gratings are etched in the SiO_2 layer in front of the laser ridge, as shown in Fig. B.15d. The EBL is necessary due to desired the sub-micron resolution. The other lithography is optical and is used to create the mask for the etching that opens the SiO_2 layer on the ridge top, as shown in Fig. B.15e.

SPP passive waveguide deposition

The SPP passive waveguide is obtained by lift-off with an optical lithography. A negative resist is more appropriate for this purpose permitting an under-cut of the developed resist. Furthermore we want to protect the ridge borders from unwanted metal depositions. We chose a very thick negative resist called TI35 ES, following the recipe:

- Sticking layer (HMDS) and the negative resist TI35 ES (thickness 3,5 μm) are applied with a coating spinner
- Bake at 110°C for 3 min
- Borders removal (the borders of the resist mask are thicker and would prevent a good contact between the chrome mask and the resist on the sample surface)
- Exposure 20" in soft contact
- Bake at 40°C for 10 min
- Bake at 130°C for 2 min
- Flood exposure 60"
- Development 25"

The metal of the SPP waveguide is deposited by electron beam physical vapor deposition (EBPVD) with the *Plassys* machine:

- 5 nm of Ti (evaporation speed 0.1 nm/s)
- 200 nm of Au (evaporation speed 0.3 nm/s)

The device situation at this point is summarized in the schematic in Fig. B.15f. The metal of the SPP passive waveguide covers the grating etched in the SiO_2. The periodicity of the grating is reported on the SPP waveguide.

Top metal deposition

Also for the top metal deposition, since the ridge are extremely thick, we chose the resist TI35 ES. The recipe is the same as in the previous paragraph. Before the evaporation the sample is cleaned with a light O_2 plasma and deoxided for 40" in a solution of HCl:H_2O 1:4. This step is important to get rid of the layer of natural oxidation of the InGaAs that could affect the electric injection and increase the mode optical losses. The metal is deposited by electron beam physical vapor deposition (EBPVD) with the *Plassys* machine.

- 5 nm of Ti (evaporation speed 0.1 nm/s)
- 100 nm of Au (evaporation speed 0.3 nm/s)
- 200 nm of Au with a sample holder tilted at 45°and rotating (evaporation speed 0.3 nm/s)

This is the last step of the device fabrication (see Fig. B.15g), then as detailed in the last part of section B.1, we realize the back contact, the sample is cleaved and mounted on the copper support.

Trials of wet etching

The use of the ICP is necessary since no vertical facet is achievable with a wet etching. In this paragraph we report two attempts to realize a vertical facet with a wet etching technique. In both cases the control of the etching depth is excellent but, either in the direction along the major or in the direction along the minor flat, the ridge profile is irregular.

Each wet etching recipe is composed by four steps, to selectively etch, in the order, the contact layer, the InP cladding, the AR and the initial part of the InP substrate. The first recipe is based on the following wet etchings:

- H_2SO_4:H_2O_2:H_2O (1:8:10)
- HCl:H_3PO_4 (1:4)
- H_2SO_4:H_2O_2:H_2O (1:8:10)
- HCl:H_3PO_4 (1:4)

The result is shown in Fig. B.16. The profile in the direction along the minor flat is better than the one in the direction of the major flat, that results really tilted. However the large under-etch prevents a good coupling of the laser with the passive SPP waveguide.

The second recipe is based on four wet etching steps:

- HBr:HNO_3:H_2O (1:1:18)

– $HCl:H_3PO_4$ (1:4)
– $HBr:HNO_3:H_2O$ (1:1:10)
– $HCl:H_3PO_4$ (1:5)

At the end we observe, see Fig. B.17, a large step around the ridge, that, also in this case, prevents an optimal coupling between the ridge and the SPP passive waveguides.

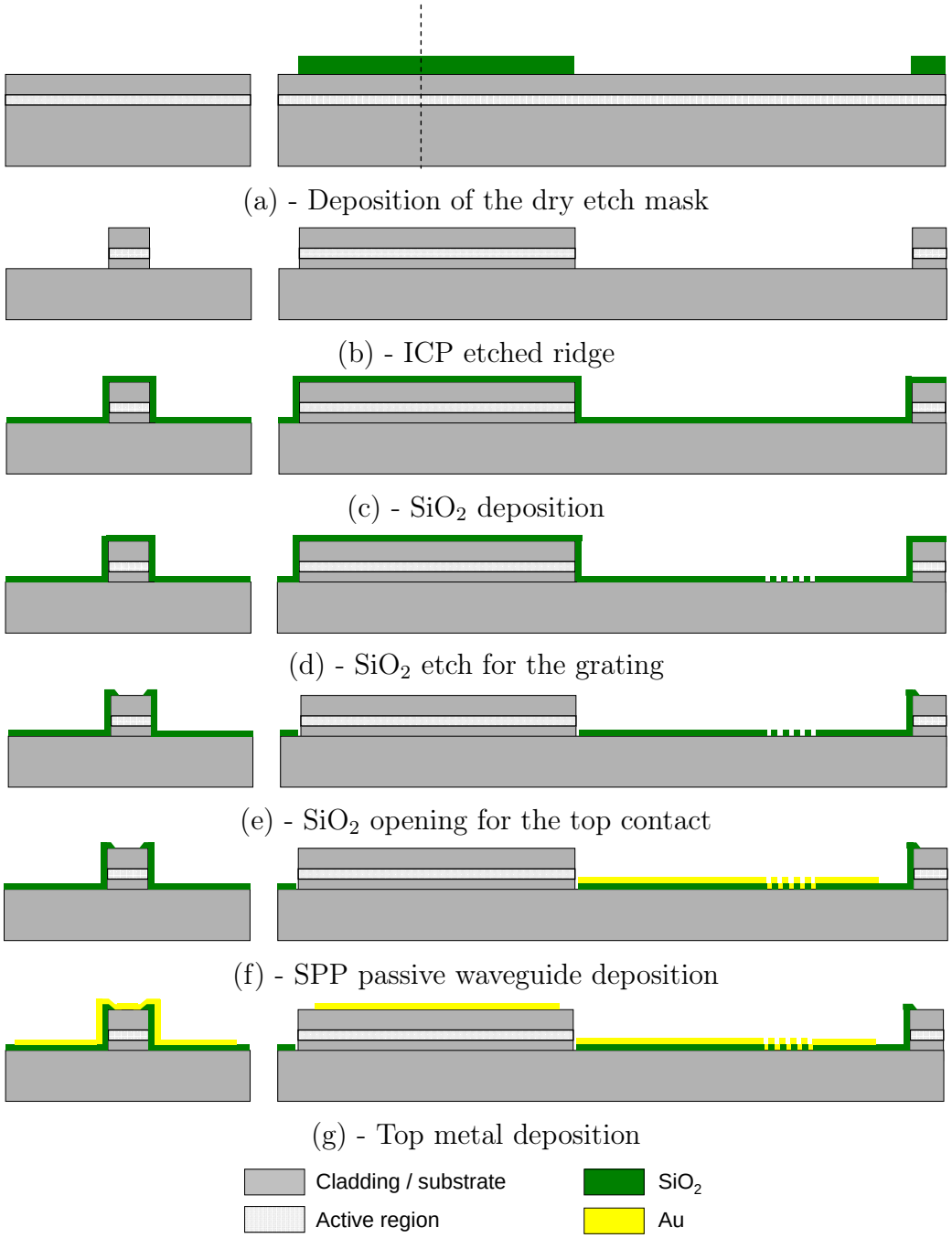

Figure B.15: Fabrication steps for the end-fire device. On the right part of the figure the lateral section of the ridge, while on the left part the transverse section in correspondence of the dotted line in (a).

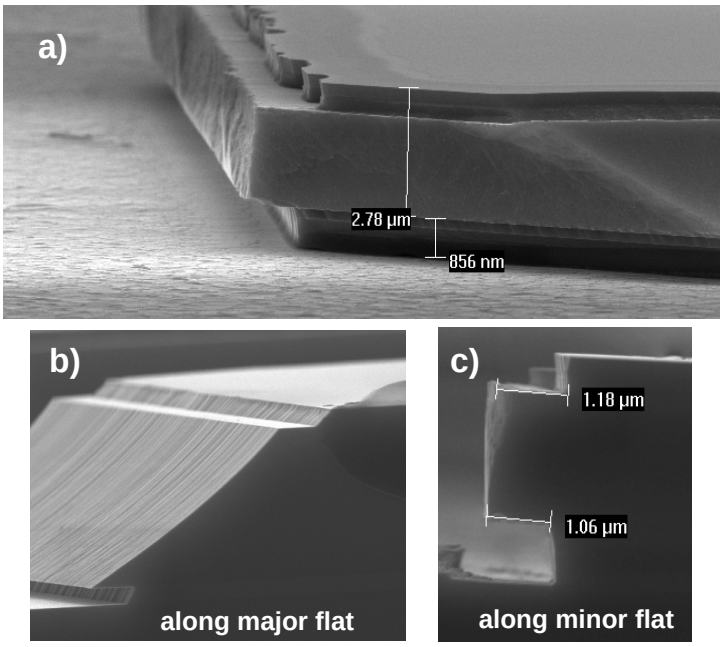

Figure B.16: Wet etch test for the end-fire device. Four different etching steps are performed, using H_2SO_4:H_2O_2:H_2O and HCl:H_3PO_4. (a) View of the ridge cornerm. Ridge profile along the direction of the (b) major flat and (c) the minor flat.

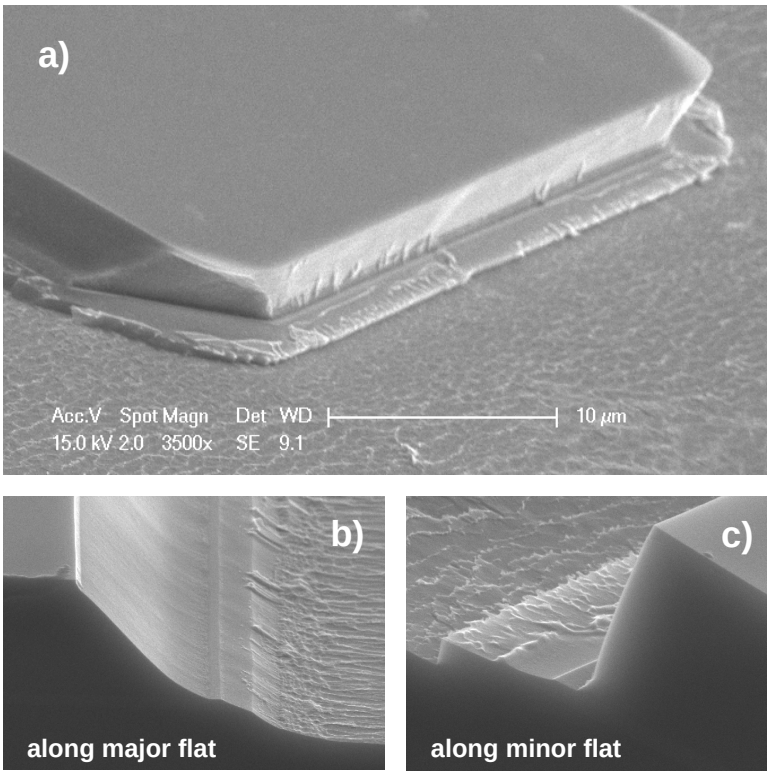

Figure B.17: Wet etch test for the end-fire device. Four different etching steps are performed, using HBr:HNO_3:H_2O and HCl:H_3PO_4. (a) View of the ridge cornerm. Ridge profile along the direction of the (b) major flat and (c) the minor flat.

Appendix C

Measurement setups

C.1 Passive measurements

Passive measurements are performed to characterize the absorption in the waveguide. The device is not electrically pumped, and an external light source is used as probe. The signal coming out from the cavity is detected and spectrally analyzed. The measurements were performed on the setup realized by M. Fevrier, in the team of B. Dagens, in our same department (Photonique - IEF) [138].

The setup is schematized in Fig. C.1. The optical signal is injected with a tunable laser (SANTEC TSL 210VF) ranging from 1260 nm and 1630 nm with a resolution in the order of the picometer. This source is composed by 4 diode lasers (covering the ranges 1260-1350 nm, 1350-1430 nm, 1430-1500 nm and 1500-1630 nm) and the output is fibered. The output power can reach 15 mW, but a constant power for all the spectral range is guaranteed for a maximum of 5 mW. The laser light is injected in the waveguide through a mirco-lensed tapered fiber. The sample is fixed on an extremely stable stage (ELLIOT-MARTOCK), which permits a micrometer control of the position in all three directions. The signal is collected in free space on the other device facet and sent to a power-meter Newport (2935C). The sample holder, with the tapered fiber and the collecting objective, is shown in Fig. C.1b. The polarization is controlled before the injection with a polarizer (THORLABS). Another polarization filter is performed through a polarizer in free space before the detection. A LabView routine controls the data acquisition.

A vertical imaging can be performed with an infrared CCD camera (NAVITAR) to facilitate the alignment procedure and also to detect light emitted in far-field. The system for the vertical imaging is shown in Fig. C.1a. Furthermore, a CCD camera can be used in place of the power-meter to image the device facet.

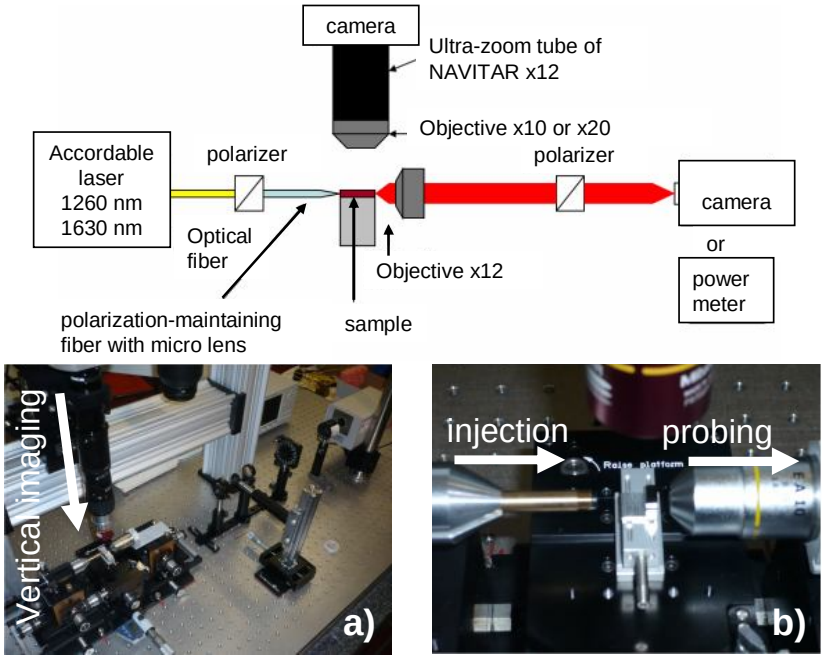

Figure C.1: Schematics of the setup for the passive measurements. a) Picture of the setup with a white arrow highlighting the infrared CCD camera. b) Closeup of the device holder.

C.1.1 Fiber injection in the SPP mode

This setup allowed us also to perform the passive measurements of the waveguides presented in Chap. 3. Moreover, it allowed us to directly inject SPPs into a single interface plasmonic waveguides. Using the EBL and gold deposition, I fabricated gold strips with different radii of curvature (R = 0 - 50 - 100 μm) and different width (W = 3 - 6 - 12 μm). The SEM images of the waveguides with W = 6 μm are represented in Fig. C.2. The goal is to verify the SPP propagation along the waveguide, in order to eventually

implement this passive element on the active devices. These passive elements would provide an indirect demonstration of the SPP propagation without the need of near-field imaging.

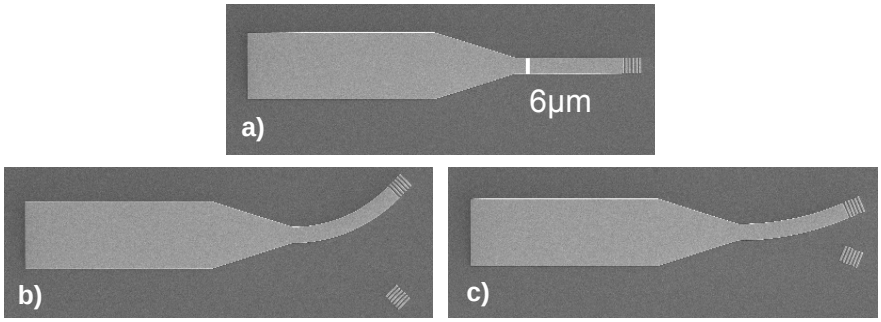

Figure C.2: SEM images of the passive plasmonic waveguides of width 6 μm with different radii of curvature: a) R = 0 μm b) R = 50 μm c) R = 100 μm. A second order grating is built at the end of the waveguide to vertically diffract the propagating SPP. The picture is taken before the cleave.

To experimentally demonstrate the SPP propagation I designed a second order grating at the waveguide end. The SPP light is diffracted on the grating in the vertical direction (as discussed in section 4.2.1) and can be measured in far field. The end-fire coupling between the microlensed injection fiber and the waveguide is more delicate than for the Fabry-Perot cavities. The SPP mode is well confined on the waveguide and the coupling is extremely sensitive to the relative height. A reference grating is realized close to the real one, but not connected with the metallic strip. This reference is extremely useful to verify if the light is really propagating in the SPP mode, and not only in the substrate or in the air.

In Fig. C.3 we show an infrared image of the coupling between the microlensed fiber and a straight SPP waveguide. In the first column of pictures the injected light is TM polarized, while is TE polarized for pictures in the second one. The big spot is due to the diffusion at the fiber extremity and the small spot is due to the diffracted light coming from the grating. In the case of an optimal coupling we observe that the grating emits only for an injected light which is TM polarized (a). For an injected light which is TE polarized no emission coming from the grating is observed. This is what expected for the SPP propagation, permitted only in TM polarization. However, if the

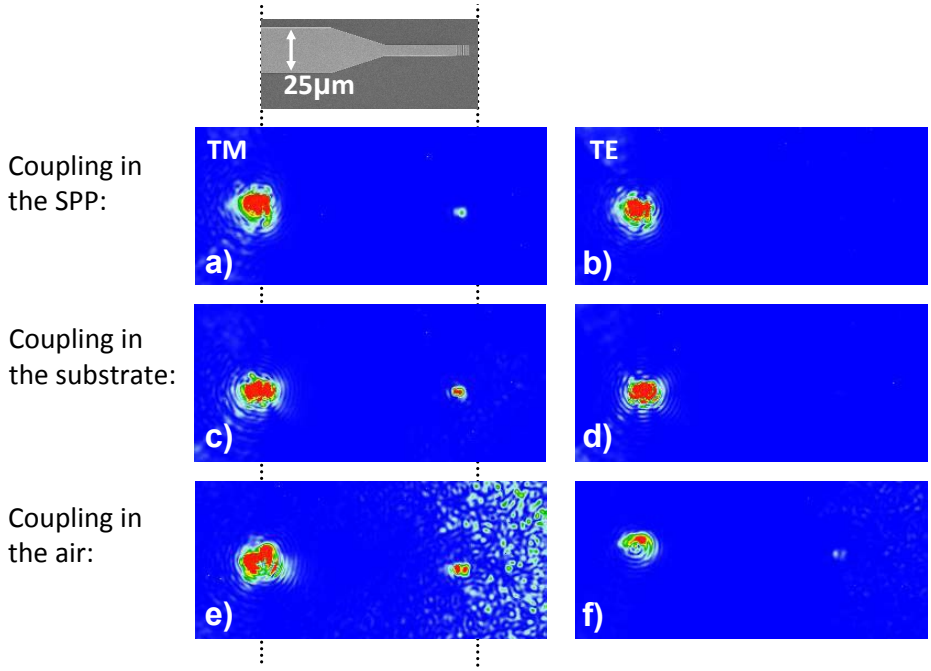

Figure C.3: The SEM image of the straight passive plasmonic waveguides (W = 6 μm) permits the interpretation of the infrared measurements. We show the infrared images of the top surface for both injected light polarizations, TM the first column and TE the second one. Furthermore we distinguish three couplings regimes, the desired one with the SPP mode and the couplings with radiating modes in substrate and in the air.

fiber is moved in the vertical direction, in the substrate, (c) and (d), or in the air, (e) and (f), we still observe a diffracted light coming from the grating. A clear demonstration requires curved SPP waveguides.

Figure C.4 reports the infrared pictures of an optimal coupling with a curved SPP waveguide of W = 6 μm and R = 100 μm. In the case of TM polarization the SEM image is put under the measurement to clearly identify the grating signal. The diffracted light is coming only from the grating connected by the SPP waveguide demonstrating the SPP propagation. No signal is coming from the grating for the TE polarization.

The SPP can follow a smaller radius of curvature if a layer of PMMA is deposited on the sample surface. The SPP in this case propagates at the interface between the gold strip and the PMMA and, due to a larger confine-

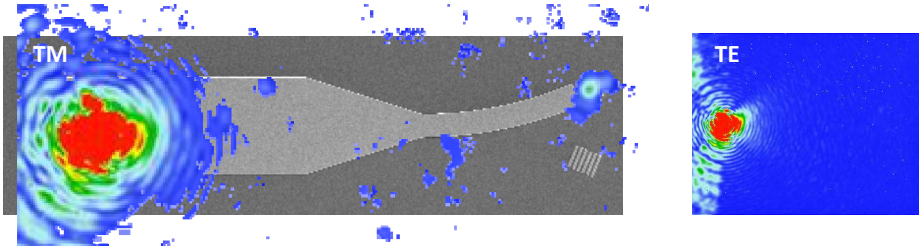

Figure C.4: Infrared measurement for TM polarized light superposed to the SEM image of the SPP waveguide with W = 6 μm and R = 100 μm. No light coming from the diffraction grating is visible for the TE polarization.

ment, it follows more curved paths. Figure C.5 shows the SPP propagation in a waveguide with W = 6 μm and R = 50 μm.

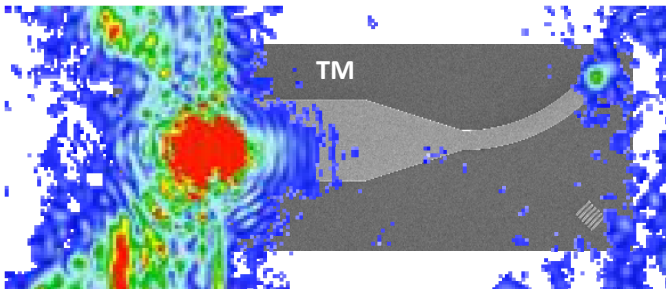

Figure C.5: Infrared measurement for TM polarized light superposed to the SEM image of the SPP waveguide with W = 6 μm and R = 50 μm. A layer of PMMA A 6 was deposited on the surface.

C.2 Active measurements

Fiber end-fire

The setup for active measurements at telecom wavelength is schematized in Fig. C.6. This setup allows one to inject a known current into the device and to measure the voltage difference. The device can operate in continuous wave (CW) if connected to the Agilent DC power supply (E3645A) Otherwise it can be operated in pulsed regime with an Agilent pulse generator (8114A).

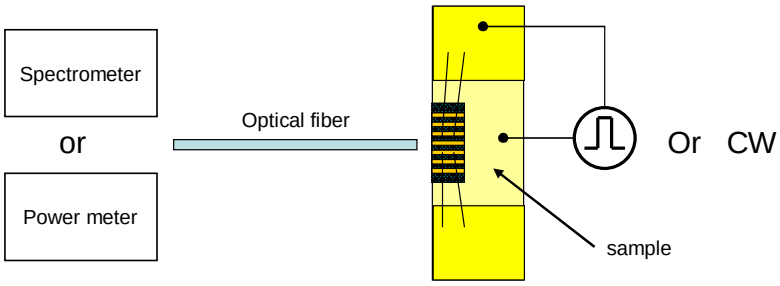

Figure C.6: Schematic of the setup for the active measurements.

In this case the current is read on a oscilloscope (Tektronix, TDS 2014) thanks to a current probe placed along the coaxial cable. The voltage is read on a different channel of the same oscilloscope. The current and the voltage signals are triggered with a reference signal coming from the pulse generator.

The device output is coupled with a cleaved multimode optical fiber. The position of the fiber in front of the device facet can be controlled with a micrometer screw. The signal is analyzed with an InGaAs power-meter (Anritsu, MTD9810A). A *Labview* routine permits to acquire automatically the LIV characteristic of the device. Alternatively the laser output can be sent to a fibered spectrometer (Anritsu MS9710C) to collect the spectrum. Even in this case I realized a routine to directly acquire the spectra on the computer.

The setup, realized thanks to the help of the group, is shown in Fig. C.7.

Far field

As though in the passive measurement setups, during active measurements it is possible to image the device top in far field with the NAVITAR infrared camera. Fig. 4.12 represents an example of the top device picture of a electrically pumped *counter-propagation* device.

I also could measure the device facet in far field. This measurement allowed to rapidly check the number of lobes of the lasing mode. The laser light is collected in-plane through a X10 microscope objective and then focused with another objective in a CCD camera connected to a monitor. We report the example of the facet imaging of a fully-metallic waveguide (one of the firsts fabricated and not optimized). This device is realized on the *thin*

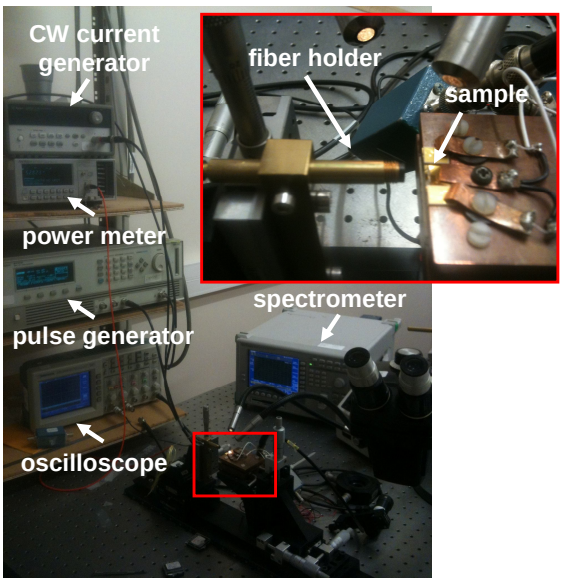

Figure C.7: Picture of the setup for the active measurements.

cladding structure and has a ridge with of 9 μm. The microscope image of the device top (Fig. C.8a) shows that the insulator is opened only on the ridge center for a width of 4 μm. Therefore the insulator on each ridge side is $\approx$ 2.5 μm large, permitting the existence of a low-loss mode on the sides, practically with no overlap with the metal. The luminescence light is equally distributed along the facet (see Fig. C.8b), but the lasing mode clearly exhibits two lobes (see Fig. C.8c). A mode with single lobe, well located at the ridge center, requires an insulator opened almost as the ridge width.

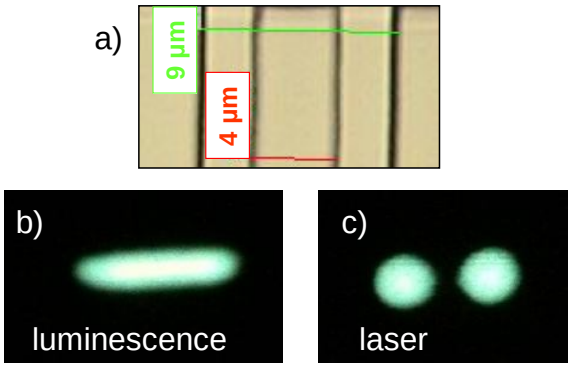

Figure C.8: (a) Microscope image of a ridge detail. Saturated far-field measurement of the laser facet in (b) luminescence and (c) laser regime.

C.3 Near field optic microscopes

We present the NSOM techniques used to characterize the devices in this work. The main results at telecom wavelengths are obtained with the transmission NSOM setup (the pyramidal tip is shown in Fig. C.9d), which permitted the measurements of the counter-propagating SPPs on the device top and of the near-field measurements on the device facets. The other NSOM techniques were used to obtain preliminary results, constituting very useful benchmark measurements. We used a NSOM setup with a tapered fiber (Fig. C.9a) and a polymer tip coated with metal (Fig. C.9b). The a-NSOM based on a metallic diffusive tip (Fig. C.9c) was used for the excellent measurements at $\lambda = 7.5$ μm and also for preliminary measurements at $\lambda = 1.3$ μm. All the presented NSOMs can simultaneously record the topographic and optical images.

C.3.1 Fiber probed NSOM

The NSOM setup based on the tapered fiber was made available from the group of S. Callard at the INL in Lyon.

The NSOM experimental set up is shown in Fig. C.10. It uses a stand alone commercial head (NT-MDT SMENA), positioned at the top of an inverted microscope. Two different kinds of probes were used: home-made bare silica tips (see Fig. C.11a) [139] and polymer metallized tips (see Fig.

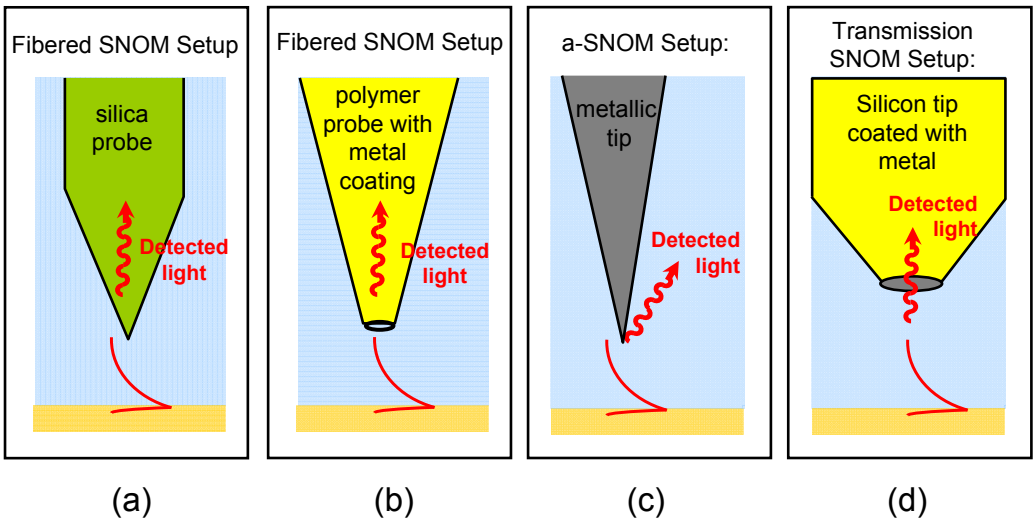

Figure C.9: The four tips used to measure the near-field of our devices.

C.11b) [140]. Both probes were made out of single mode optical fiber at $\lambda = 1.55$ μm with a core diameter of 9 μm. The NSOM is working in collection mode: the optical signal is collected in the near-field by the probe and sent to a monochromator (1 nm resolution). The detection is made by a thermo-electrically cooled InGaAs photodetector. The structure can be investigated over the spectral range $1350 < \lambda < 1650$ nm [141]. A lock-in amplifier is used to demodulate the signal and enhance the signal to noise ratio. For the topography imaging, the fiber is attached to a piezoelectric tuning fork setup which allows a shear-force feedback loop to regulate the distance between tip and sample surface (typically between 5 and 15 nm). Besides, the inverted microscope presents several output allowing the sample observation in far-field in the visible range (Si CCD camera), as shown in the monitor in Fig. C.10b.

C.3.2 a-NSOM

This setup was realized by the team of Y. De Wilde at the Institut Langevin (ESPCI, Paris) [142]. The best measurements of the plasmonic field at $\lambda = 7.5$ μm were performed with this a-NSOM setup.

The home-built setup is shown in Fig. C.12 and a schematic of the setup is presented in Fig. C.13. The a-NSOM uses a tungsten tip, which is glued

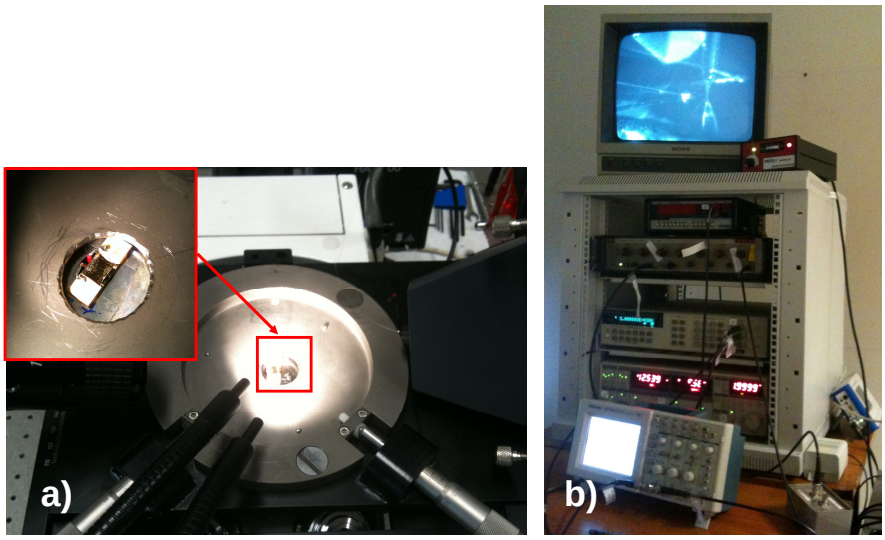

Figure C.10: (a) Sample mounted on the NSOM base, which is covered with the structure containing the tip. The tip is controlled by piezoelectric motors and it scans the sample. (b) Instruments of the setup, including a CCD camera, which allows the sample localization before the tip descent.

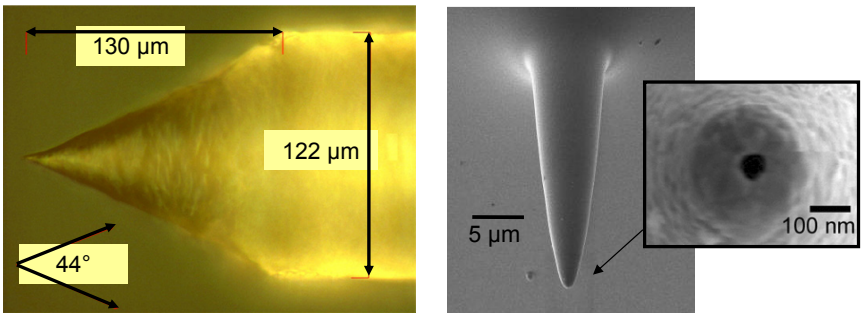

(a) (b)

Figure C.11: (a) Pulled fiber that constitute a silica probe with a tip diameter typically of ≈ 300 nm. (b) Polymer probe coated with Al. The hole diameter is typically of ≈ 200 nm.

on the extremity of a quartz tuning fork. The tip oscillates perpendicularly to the metallic grating on the laser top surface with an amplitude ≈100 nm at a frequency Ω_{tip} which is typically ≈ 32 kHz, while the mid-IR laser

is operated with 50 ns pulses at a $\approx$ 84 kHz repetition rate. Piezoelectric elements are used to scan the device laterally under the tip, and to control the separation between the tip and the laser surface. The a-NSOM is operated with RHK electronics (RHK Technology model SPM 100). This electronics includes a feed-back loop control which acts in order to maintain the average distance between the tip and the laser top surface at a preset value. The recording of the feed-back voltage, as a function of the tip position during the lateral scans of the laser, provides topographical (AFM) images of the scanned area. The tip acts as a scattering centre that radiates in the far field a signal linearly related to the near-field. The scattered field is collected with a large numerical aperture Cassegrain microscope objective and focused on a HgCdTe nitrogen cooled mid-IR detector or an InGaAs NIR detector. The near-field optical images are obtained simultaneously with the AFM images by demodulating the optical signal at frequency Ω_{tip} or at a higher harmonic using standard lock-in detection techniques, while the injection current in the device is above laser threshold.

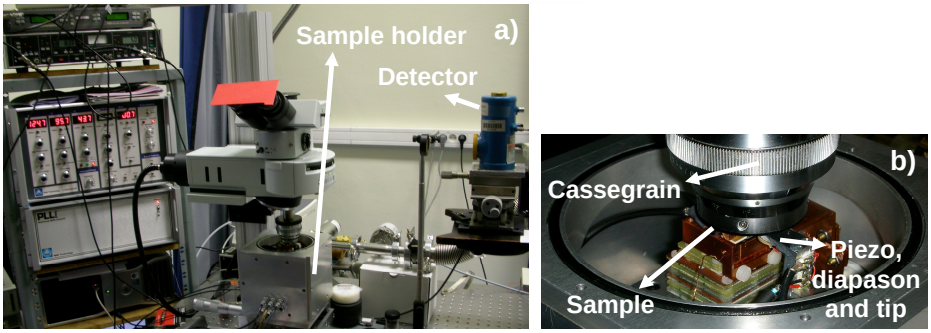

Figure C.12: (a) a-NSOM setup with the HgCdTe detector for the mid-IR wavelengths. (b) Close-up of the sample holder.

C.3.3 Transmission NSOM

This setup was realized by the team of Y. De Wilde at the Institut Langevin (ESPCI, Paris). With this NSOM setup were performed the best measurements of the plasmonic field, and of the near-field on the devices facets, at $\lambda = 1.3$ μm.

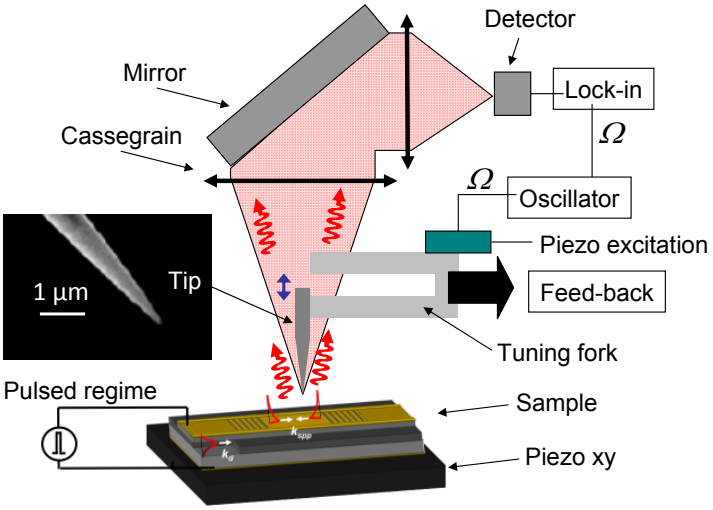

Figure C.13: Schematic of the a-NSOM setup, mainly used in the mid-IR range. A close-up of the tungsten tip is shown in the inset.

The setup is a commercial cantilever-based NSOM (WITec GmbH alpha 300S), a schematic is illustrated in Fig. C.14. The device is mounted under the microscope objective. In the case of a facet imaging the device is mounted vertically. The objective collects the near-field transmitted through the nano-aperture (diameter smaller than 100 nm) of an aluminum hollow pyramid mounted on a cantilever. The latter is optically conjugated with an optical fiber which acts as a confocal pinhole, and is then guided to a thermoelectrically-cooled InGaAs detector (Hamamatsu). The devices that operate in pulsed regime, generally with a 100-ns-wide pulses at a frequency of 1 MHz, are over-modulated with a pulse at 1 kHz. The near-field signal is acquired by scanning the device facet under the apex of the hollow pyramid and demodulating the signal at 1 kHz. The pyramid is kept in contact with the surface. The control of the probe-sample distance, relies on a beam-deflection laser ($\lambda = 980$ nm) which is sent onto the cantilever top through the same objective used to collect the transmitted near-field. The reflected beam goes back through the objective (Fig. C.15). A dichroic mirror allows then to separate the two beams, sending the beam-deflection laser towards a 4 quadrant photodiode. The measured signal is sent into a feedback loop which maintains a constant deflection of the cantilever. This feed-back mechanism

allows to simultaneously acquire the near-field distribution on the sample surface and its topography.

To our knowledge, this is the first time that a NSOM with hollow pyramid is employed at telecom wavelengths. Note that a similar setup has been used to investigate the propagation of SPPs at short, visible wavelengths.

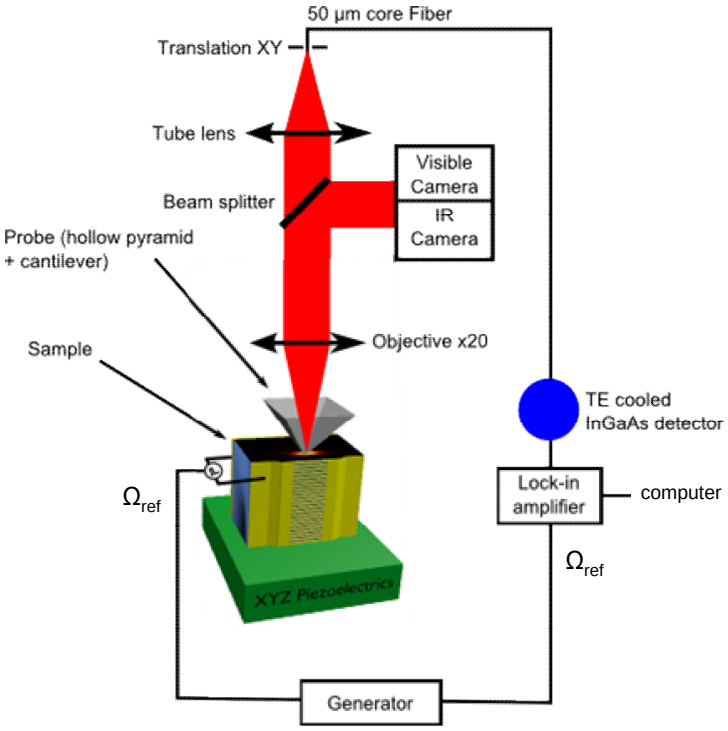

Figure C.14: Schematic of the NSOM setup used to measure the plasmonic field. In this case the facet of a DFB is scanned.

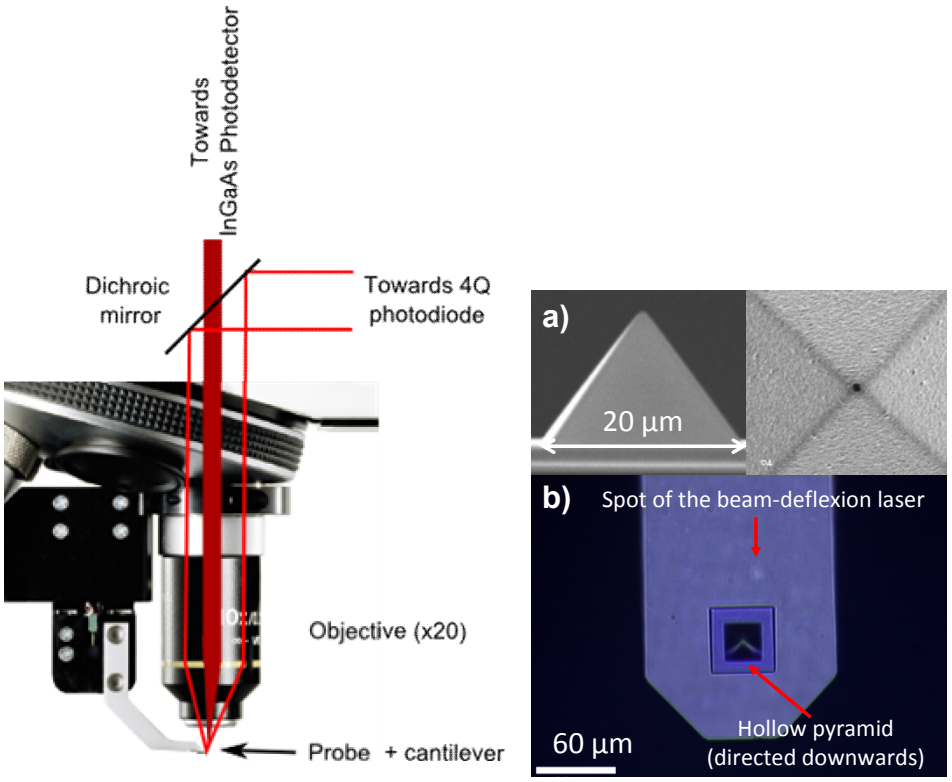

(a) Optical column (b) Pyramid details

Figure C.15: On the left: picture of the probe and the cantilever inserted in the system (courtesy of WITec GmbH). The optical paths are schematically represented on the picture. The thinner red lines correspond to the beam-deflection laser and the thick red line corresponds to the near-field signal transmitted through the nano-aperture of the pyramid. On the right: (a) SEM picture of the silica pyramid coated with metal (b) Optical image of the cantilever.

Appendix D

Grating coupler: numerical calculation details

We report the formula for a slab waveguide used in the simulations in paragraph 4.1.2 and we calculate the analytical expression of the power flux. The same is done for the power flux of the SPP. The ratio between the power fluxes gives the coupling efficiency $\eta = P_{SPP}/P_d$ (see Eq. 4.6).

The TM_0 mode of the asymmetric dielectric slab waveguide is fully characterized by its magnetic vector field $\mathbf{H}(\mathbf{r},t) = H_y(x,z)e^{i\omega t}\mathbf{e}_y$ [68]. The spatial distribution $H_y(x,z)$ can be written as follows:

$$H_y(x,z) = H^d_{max} e^{-ik_d x} \begin{cases} cos(\phi)e^{-\alpha_a z} & \text{for } z > 0, \\ cos(k_z + \phi) & \text{for } -t_c < z < 0, \\ cos(-k_z d + \phi)e^{-\alpha_s(z+t_c)} & \text{for } z < t_c \end{cases} \quad \text{(D.1)}$$

where the constants k_d, α_a, α_s and k_z must satisfy the relations:

$$\begin{cases} k_z d = tan^{-1}(\frac{\varepsilon_c \alpha_a}{\varepsilon_a k_z}) + tan^{-1}(\frac{\varepsilon_c \alpha_s}{\varepsilon_s k_z}) \\ \varepsilon_a k_0^2 = k_d^2 - \alpha_a^2 \\ \varepsilon_c k_0^2 = k_d^2 - k_z^2 \\ \varepsilon_s k_0^2 = k_d^2 - \alpha_s^2 \end{cases} \quad \text{(D.2)}$$

with $\phi = \frac{\varepsilon_c \alpha_a}{\varepsilon_a k_z}$ and $\varepsilon_i = n_i^2$ are the dielectric constants.

We used Eq. D.1 to impose the boundary condition for the slab waveguide. For instance in Fig. 4.3 the magnetic field function is imposed on the

left waveguide boundary. In a finite element simulation this is equivalent to inject the waveguided mode into the structure.

The power flux can be obtained by taking the real part of the complex Poynting vector and integrating over z:

$$P_d = \int dz \frac{1}{2} \mathrm{Re}\{(\mathbf{E} \times \mathbf{H}^*) \cdot \mathbf{e}_x\} = \tag{D.3}$$

$$|H^d_{max}|^2 \frac{k_d}{4\omega\varepsilon_0} \{ \frac{\cos^2(\phi)}{\varepsilon_a \alpha_a} + \frac{d}{\varepsilon_c} + \frac{\sin(2\phi) - \sin(-2k_z d + 2\phi)}{2\varepsilon_c k_z} + \frac{\cos^2(-k_z d + \phi)}{\varepsilon_s \alpha_s} \}$$

Likewise, the SPP mode at the metal-air interface is fully characterized by its magnetic vector field $\mathbf{H}(\mathbf{r},\mathrm{t}) = \mathrm{H}_y(\mathrm{x},\mathrm{z})\mathrm{e}^{i\omega t}\mathbf{e}_y$. The spatial distribution $\mathrm{H}_y(\mathrm{x},\mathrm{z})$ can be written as follows:

$$H_y(x,z) = H^{SPP}_{max} e^{-ik_{SPP}x} \begin{cases} e^{-\alpha_a^{'}(z-t_m)} & \text{for } z > t_m, \\ e^{-\alpha_m(z-t_m)} & \text{for } z < t_m, \end{cases} \tag{D.4}$$

where the constants k_{SPP}, $\alpha_a^{'}$ and α_m must satisfy the relations:

$$\begin{cases} k_{SPP} = k_0 \frac{\varepsilon_a \varepsilon_m}{\varepsilon_a \varepsilon_m} \\ \varepsilon_a k_0^2 = k_{SPP}^2 - \alpha_a^{'2} \\ \varepsilon_m k_0^2 = k_{SPP}^2 - \alpha_m^{'2} \end{cases} \tag{D.5}$$

The power flux is then related to H^{SPP}_{max} via the following formula:

$$P_{SPP} = \int dz \frac{1}{2} \mathrm{Re}\{(\mathbf{E} \times \mathbf{H}^*) \cdot \mathbf{e}_x\} = \tag{D.6}$$

$$|H^{SPP}_{max}|^2 \mathrm{Re}\{ \frac{k_{SPP}}{4\omega\varepsilon_0} [\frac{1}{\varepsilon_a \mathrm{Re}\alpha_a^{'}} + \frac{1}{\varepsilon_m \mathrm{Re}\alpha_m}] \}$$

To calculate P_{SPP} we extract the H^{SPP}_{max} from the simulation.

Appendix E

Other cladding structures

In paragraph 3.2.2 we presented the three claddings used to obtain the main results. Here we present other two claddings, that were not used in operating devices, but allowed us to better understand the system limits.

cladding n°63519: not enough doping

This structure helped us to understand the importance of the total doping and of the InGaAs layer. The cladding n°63519, presented in Tab. E.1, has a total thickness of ≈ 400 nm and is very similar to the *thin cladding*. However the total p-doping is lower because:

- The InGaAsP layer is 30 nm thick (instead of 80 nm).
- The doping of the InP layer is $8 \cdot 10^{17}$ (instead of $1.4 \cdot 10^{18}$ cm^{-3}).

Cladding 63519	Thickness (nm)	p-doping (cm^{-3})
InGaAs	15	$3 \cdot 10^{19}$
InGaAsP	30	$2 \cdot 10^{19}$
InP	295	$8 \cdot 10^{17}$
Active region		

Table E.1: Cladding (n°63519) is very similar to the *thin cladding*, Tab. 3.3. It only differs for the thinner thickness of the InGaAsP layer and the lower doping of the InP layer. It has a total thickness ≈ 400 nm (considering also the 50 nm thin layer of n.i.d InP grown on the AR top).

Firstly the cladding n°63519 had no top InGaAs layer. The fabricated devices exhibit a tendency to easily break and a very bad injection. The diode opens at more than 3 V and the voltage is not stable as shown in Fig. E.1. We conclude that the an high doped InGaAs layer, even of only 15 nm, is necessary for the injection.

A regrowth of 15 nm of InGaAs was performed in order to obtain the cladding n°63519 as presented in Tab. E.1. The VI characteristic is improved and the device is more robust. However, the diode opens at $\approx$ 2 V, which is the double of the value for a normal device (cfr reference device shown in green in Fig. E.1).

We attribute this anomalous behavior to a not sufficient total doping. An InGaAsP layer of 30 nm is not enough. For this reason we used a fixed contact layer (15 nm of InGaAs and 80 nm of InGaAsP) for the *thick*, *thin* and *ultra-thin cladding* and we only varied the InP thickness.

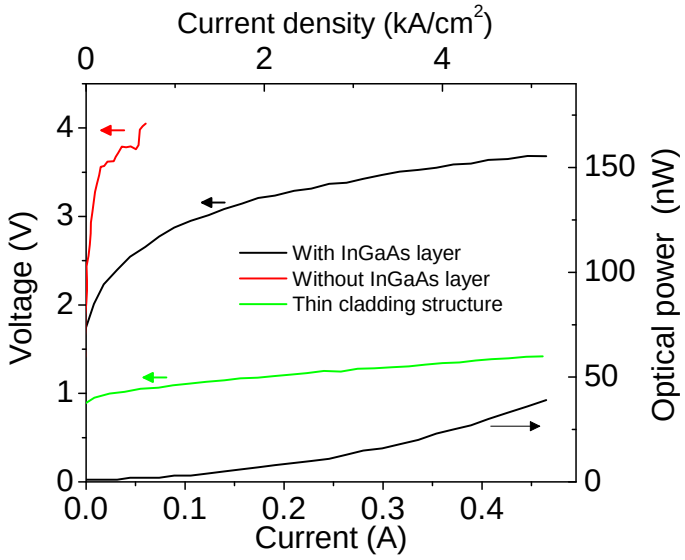

Figure E.1: Room-temperature VI characteristic of ridge devices with the n°63519 cladding, with and without the 15 nm InGaAs layer. Without the InGaAs layer the diode opens at more than 3 V and the device quickly breaks. The InGaAs layer improves the device robustness and the injection, but the diode opens at $\approx$ 2 V. Only a weak electro-luminescence signal is observed at RT. The reference VI of an operating device (*thin cladding* structure) is shown in green.

Cladding 63519	Thickness (nm)	p-doping (cm^{-3})
InGaAs	15	$3 \cdot 10^{19}$
InGaAsP	30	$2 \cdot 10^{19}$
Active region		

Table E.2: Cladding (n°63517) has no InP p-doped layer. It has a total thickness 80 nm (considering also the 50 nm thin layer of n.i.d InP grown on the AR top).

cladding n°63517: bad injection

This structure helped us to understand the risk of not correctly inject into the QWs. An excessively thin cladding permits to the electron to tunnel, avoiding the recombination in the QWs. The diode opens before the expected value and the electro-luminescence is only visible at low-temperature.

The cladding n°63517 is presented in Tab. E.2. It has a thickness of 80 nm. The VI characteristic in Fig. E.2 shows the diode opening at ≈ 0.7 V which is less than expected (cfr reference device shown in green).

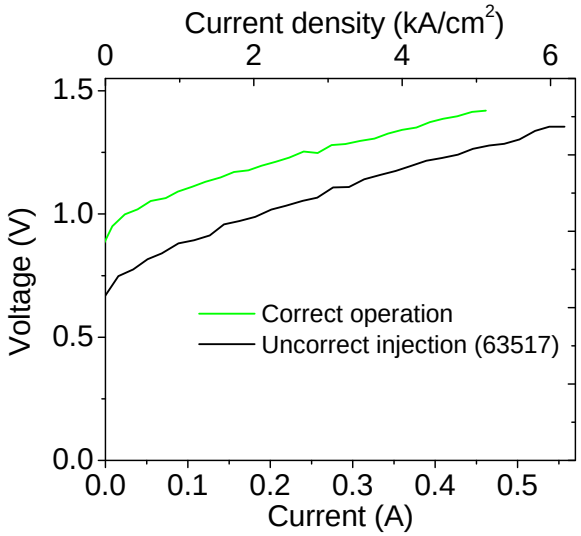

Figure E.2: Room-temperature VI characteristic of a device based on the cladding n°63517. The diode opens at a lower voltage (≈ 0.7 V) than the reference device shown in green.

Even if the injection is not correct it was possible to observe an electro-luminescence signal at low-temperature. The spectra collected with a Fourier Transform infrared (FTIR) pectrum analyzer are shown in Fig. E.3. Increasing the temperature the spectra correctly red shifts, but dramatically decrease in intensity. No signal could be detected at RT.

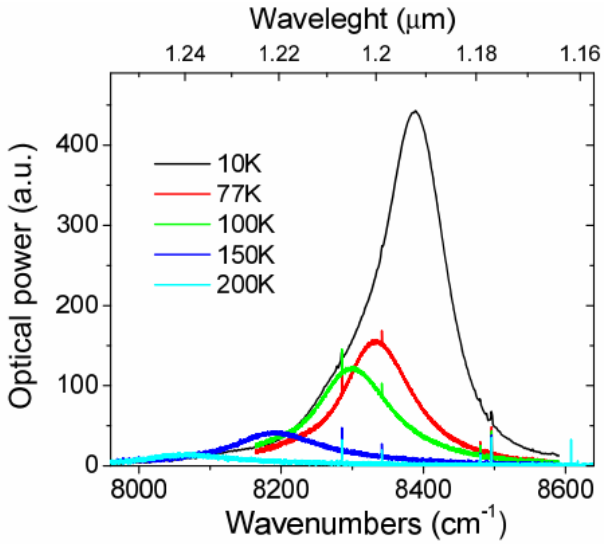

Figure E.3: Electro-luminescence spectra of a device based on a cladding n°63517 collected at different low-temperatures with FTIR spectrum analyzer. The device is operated at frequency 1MHz (duty cycle 10%) and injected current 800mA.

We attribute the bad injection to the excessively thin thickness of the cladding, which allows other channels for the electron-hole recombination. These channels prevail on the desired recombination in the QWs.

Bibliography

[1] T. Holmgaard, Z. Chen, S. I. Bozhevolnyi, L. Markey and A. Dereux, *Dielectric-loaded plasmonic waveguide-ring resonators*, Opt. Express **17**, 2968 (2009).

[2] R. Bachelot, P. Gleyzes and A. C. Boccara, *Near-field optical microscope based on local perturbation of a diffraction spot*, Opt. Lett. **20**, 1924 (1995).

[3] W. L. Barnes, *Surface plasmon-polariton length scales: a route to subwavelength optics*, Journal of Optics A: Pure and Applied Optics **8**, S87 (2006).

[4] D. J. Bergman and M. I. Stockman, *Surface Plasmon Amplification by Stimulated Emission of Radiation: Quantum Generation of Coherent Surface Plasmons in Nanosystems*, Phys. Rev. Lett. **90**, 027402 (2003).

[5] Editor, *Surface plasmon resurrection*, Nature Photonics **6**, 707 (2012).

[6] S. Nie and S. R. Emory, *Probing Single Molecules and Single Nanoparticles by Surface-Enhanced Raman Scattering*, Science **275**, 1102 (1997).

[7] K. Kneipp, Y. Wang, H. Kneipp, L. T. Perelman, I. Itzkan, R. R. Dasari and M. S. Feld, *Single Molecule Detection Using Surface-Enhanced Raman Scattering (SERS)*, Phys. Rev. Lett. **78**, 1667 (1997).

[8] *Biacore - GE Healthcare*, http://www.biacore.com.

[9] A. Polman and H. Atwater, *Photonic design principles for ultrahigh-efficiency photovoltaics*, Nature Materials **11**, 174 (2012).

[10] J.-Y. Laluet, E. Devaux, C. Genet, T. W. Ebbesen, J.-C. Weeber and A. Dereux, *Optimization of surface plasmons launching from subwavelength hole arrays: modelling and experiments*, Opt. Express **15**, 3488 (2007).

[11] T. W. Ebbesen, C. Genet and S. I. Bozhevolnyi, *Surface-plasmon circuitry*, Physics Today **61**, 44 (2008).

[12] B. Hecht, H. Bielefeldt, L. Novotny, Y. Inouye and D. W. Pohl, *Local Excitation, Scattering, and Interference of Surface Plasmons*, Phys. Rev. Lett. **77**, 1889 (1996).

[13] J. Renger, R. Quidant, N. van Hulst, S. Palomba and L. Novotny, *Free-Space Excitation of Propagating Surface Plasmon Polaritons by Nonlinear Four-Wave Mixing*, Phys. Rev. Lett. **103**, 266802 (2009).

[14] J. Seidel, S. Grafström and L. Eng, *Stimulated Emission of Surface Plasmons at the Interface between a Silver Film and an Optically Pumped Dye Solution*, Phys. Rev. Lett. **94**, 177401 (2005).

[15] D. M. Koller, A. Hohenau, H. Ditlbacher, N. Galler, F. Reil, F. R. Aussenegg, A. Leitner, E. J. W. List and J. R. Krenn, *Organic plasmon-emitting diode*, Nature Photonics **2**, 684 (2008).

[16] R. J. Walters, R. V. A. van Loon, I. Brunets, J. Schmitz and A. Polman, *A silicon-based electrical source of surface plasmon polaritons*, Nature Materials **9**, 21 (2009).

[17] P. Neutens, L. Lagae, G. Borghs and P. Van Dorpe, *Electrical Excitation of Confined Surface Plasmon Polaritons in Metallic Slot Waveguides*, Nano Letters **10**, 1429 (2010), pMID: 20334350.

[18] P. Fan, C. Colombo, K. C. Y. Huang, P. Krogstrup, J. Nygard, A. Fontcuberta i Morral and M. L. Brongersma, *An Electrically-Driven GaAs Nanowire Surface Plasmon Source*, Nano Letters **12**, 4943 (2012).

[19] H. Raether, *Surface Plasmons on Smooth and Rough Surfaces and on Gratings*, Springer, Berlin (1988).

[20] A. Sommerfeld, *Ueber die Fortpflanzung electrodynamischer Wellen laengs eines Drahtes.*, Ann. Phys. und Chemie **67**, 233 (1899).

[21] J. Zenneck, *Ueber die Fortpflanzung ebener elektromagnetischer Wellen laengs einer ebenen Leiterflaeche und ihre Beziehung zur drahtlosen Telegraphie*, Ann. d. Phys. **23**, 846 (1907).

[22] R. W. Wood, *On a remarkable case of uneven distribution of light in a diffraction grating spectrum*, Proc. Phys. Soc. London, **18**, 269 (1902).

[23] U. Fano, *The theory of anomalous diffraction gratings and of quasi-stationary waves on metallic surfaces (Sommerfeld's waves).*, J. Opt. Soc. Am. **31**, 213 (1941).

[24] R. H. Ritchie, *Plasma losses by fast electrons in thin films*, Phys. Rev. **106**, 874 (1957).

[25] E. Kretschmann and H. Raether, *Radiative decay of non-radiative surface plasmons excited by light*, Z. Naturforschung **23A**, 2135 (1968).

[26] S. A. Maier, *Plasmonics: Fundamental and applications*, Springer (2007).

[27] G. Mie, *Beiträge zur Optik trüber Medien, speaiell kolloidaler Metallösungen*, Ann. Phys. **25**, 377 (1908).

[28] S. A. Maier and H. A. Atwater, *Plasmonics: Localization and guiding of electromagnetic energy in metal/dielectric structures*, J. App. Phys (2005).

[29] A. Archambault, T. V. Teperik, F. Marquier and J. J. Greffet, *Surface plasmon Fourier optics*, Phys. Rev. B **79**, 195414 (2009).

[30] J.-P. Tetienne, *Generation de plasmons de surface par injection electrique*, Master's thesis, ENS de Cachan (2008-2009).

[31] D. R. Smith, J. B. Pendry and M. C. K. Wiltshire, *Metamaterials and Negative Refractive Index*, Science **305**, 788 (2004).

[32] G. Grosso and G. P. Parravicini, *Solid State Physics*, Accademic Press (2003).

[33] P. Design, *Fimmwave*, http://www.photond.com/products/fimmwave.htm.

[34] M. A. Ordal, R. J. Bell, R. W. Alexander, L. L. Long and M. R. Querry, *Optical properties of fourteen metals in the infrared and far infrared : Al, Co, Cu, Au, Fe, Pb, Mo, Ni, Pd, Pt, Ag, Ti, V, and W*, Appl. Opt. **24**, 4493 (1985).

[35] E. D.Palik, *Handbook of Optical Constants of Solids*, Academic Press edition (1998).

[36] E. T. Arakawa, M. W. Williams, R. N. Hamm and R. H. Ritchie, *Effect of Damping on Surface Plasmon Dispersion*, Phys. Rev. Lett. **31**, 1127 (1973).

[37] V. A. Fedotov, T. Uchino and J. Y. Ou, *Low-loss plasmonic metamaterial based on epitaxial gold monocrystal film*, Opt. Express **20**, 9545 (2012).

[38] P. Berini, *Figures of merit for surface plasmon waveguides*, Opt. Express **14**, 13030 (2006).

[39] A. Boltasseva and H. A. Atwater, *Low-Loss Plasmonic Metamaterials*, Science **331**, 290 (2011).

[40] G. V. Naik, J. L. Schroeder, X. Ni, A. V. Kildishev, T. D. Sands and A. Boltasseva, *Titanium nitride as a plasmonic material for visible and near-infrared wavelengths*, Opt. Mater. Express **2**, 478 (2012).

[41] J. B. Khurgin and G. Sun, *In search of the elusive lossless metal*, Appl. Phys. Lett. **96**, 181102 (2010).

[42] C. J. Powell and J. B. Swan, *Effect of Oxidation on the Characteristic Loss Spectra of Aluminum and Magnesium*, Phys. Rev. **118**, 640 (1960).

[43] J. T. van Wijngaarden, E. Verhagen, A. Polman, C. E. Ross, H. J. Lezec and H. A. Atwater, *Direct imaging of propagation and damping of near-resonance surface plasmon polaritons using cathodoluminescence spectroscopy*, Applied Physics Letters **88**, 221111 (2006).

[44] M. V. Bashevoy, F. Jonsson, A. V. Krasavin, N. I. Zheludev, Y. Chen and M. I. Stockman, *Generation of Traveling Surface Plasmon Waves by Free-Electron Impact*, Nano Letters **6**, 1113 (2006).

[45] T. Wang, E. Boer-Duchemin, Y. Zhang, G. Comtet and G. Dujardin, *Excitation of propagating surface plasmons with a scanning tunnelling microscope*, Nanotechnology **22**, 175201 (2011).

[46] P. Bharadwaj, A. Bouhelier and L. Novotny, *Electrical Excitation of Surface Plasmons*, Phys. Rev. Lett. **106**, 226802 (2011).

[47] E. Kretschmann and H. Raether, *Radiative decay of non-radiative surface plas- mons excited by light*, Z. Naturforschun **23**, 2135 (1968).

[48] A. Otto, *Excitation of nonradiative surface plasma waves in silver by the method of frustrated total reflection*, Z. Physik **216**, 398 (1968).

[49] J. Homola, S. S. Yee and G. Gauglitz, *Surface plasmon resonance sensors: review*, Sensors and Actuators B: Chemical **54**, 3 (1999).

[50] S. Herminjard, L. Sirigu, H. P. Herzig, E. Studemann, A. Crottini, J.-P. Pellaux, T. Gresch, M. Fischer and J. Faist, *Surface Plasmon Resonance sensor showing enhanced sensitivity for CO_2 detection in the mid-infrared range*, Opt. Express **17**, 293 (2009).

[51] T. Ebbesen, H. Lezec, H. Ghaemi, T. Thio and P. Wolff, *Extraordinary optical transmission through sub-wavelength hole arrays*, Nature **391**, 667 (1998).

[52] R. Zia, J. A. Schuller, A. Chandran and M. L. Brongersma, *Plasmonics: the next chip-scale technology*, Materials Today **9**, 20 (2006).

[53] D. A. B. Miller, *Are optical transistors the logical next step?*, Nat Photon **4**, 3 (2010).

[54] J. Faist, F. Capasso, D. L. Sivco, C. Sirtori, A. L. Hutchinson and A. Y. Cho, *Quantum Cascade Laser*, Science **264**, 553 (1994).

[55] F. Capasso, *High-performance midinfrared quantum cascade lasers*, Optical Engineering **49**, 111102 (2010).

[56] R. Colombelli, K. Srinivasan, M. Troccoli, O. Painter, C. F. Gmachl, D. M. Tennant, A. M. Sergent, D. L. Sivco, A. Y. Cho and F. Capasso, *Quantum Cascade Surface-Emitting Photonic Crystal Laser*, Science **302**, 1374 (2003).

[57] M. Belkin, Q. J. Wang, C. Pflugl, A. Belyanin, S. Khanna, A. Davies, E. Linfield and F. Capasso, *High-Temperature Operation of Terahertz Quantum Cascade Laser Sources*, Selected Topics in Quantum Electronics, IEEE Journal of **15**, 952 (2009).

[58] M. Beck, D. Hofstetter, T. Aellen, J. Faist, U. Oesterle, M. Ilegems, E. Gini and H. Melchior, *Continuous Wave Operation*

of a Mid-Infrared Semiconductor Laser at Room Temperature, Science **295**, 301 (2002).

[59] A. Evans, J. S. Yu, S. Slivken and M. Razeghi, *Continuous-wave operation of lambda ≈ 4.8 μm quantum-cascade lasers at room temperature*, Applied Physics Letters **85**, 2166 (2004).

[60] M. Bahriz, V. Moreau, J. Palomo, R. Colombelli, D. A. Austin, J. W. Cockburn, L. R. Wilson, A. B. Krysa and J. S. Roberts, *Room-temperature operation of lambda ≈ 7.5 μm surface-plasmon quantum cascade lasers*, Applied Physics Letters **88**, 181103 (2006).

[61] A. Bousseksou, V. Moreau, R. Colombelli, C. Sirtori, G. Patriarche, O. Mauguin, L. Largeau, G. Beaudoin and I. Sagnes, *Surface-plasmon distributed-feedback mid-infrared quantum cascade lasers based on hybrid plasmon/air-guided modes*, Electronics Letters **44**, 807 (2008).

[62] A. Babuty, A. Bousseksou, J.-P. Tetienne, I. M. Doyen, C. Sirtori, G. Beaudoin, I. Sagnes, Y. De Wilde and R. Colombelli, *Semiconductor Surface Plasmon Sources*, Phys. Rev. Lett. **104**, 226806 (2010).

[63] A. Bousseksou, R. Colombelli, A. Babuty, Y. D. Wilde, Y. Chassagneux, C. Sirtori, G. Patriarche, G. Beaudoin and I. Sagnes, *A semiconductor laser device for the generation of surface-plasmons uponelectrical injection*, Opt. Express **17**, 9391 (2009).

[64] P. Lalanne, J. Hugonin, H. Liu and B. Wang, *A microscopic view of the electromagnetic properties of sub-λ metallic surfaces*, Surface Science Reports **64**, 453 (2009).

[65] Y. D. Wilde, F. Formanek, R. Carminati, B. Gralak, P. A. Lemoine, K. Joulain, J. P. Mulet, Y. Chen and J. J. Greffet, *Thermal radiation scanning tunnelling microscopy*, Nature (London) 444, 740 (2006).

[66] J.-P. Tetienne, A. Bousseksou, D. Costantini, R. Colombelli, A. Babuty, I. Moldovan-Doyen, Y. D. Wilde, C. Sirtori, G. Beaudoin, L. Largeau, O. Mauguin and I. Sagnes, *Injection of midinfrared surface plasmon polaritons with an integrated device*, Applied Physics Letters **97**, 211110 (2010).

[67] A. Bousseksou, Y. Chassagneux, J. R. Coudevylle, R. Colombelli, C. Sirtori, G. Patriarche, G. Beaudoin and I. Sagnes, *Surface-plasmon distributed-feedback quantum cascade lasers operating pulsed, room temperature*, Applied Physics Letters **95**, 091105 (2009).

[68] S. L. Chuang, *Physics of optoelectronics devices*, Wiley Inter-Science (1995).

[69] R. N. Hall, G. E. Fenner, J. D. Kingsley, T. J. Soltys and R. O. Carlson, *Coherent Light Emission From GaAs Junctions*, Phys. Rev. Lett. **9**, 366 (1962).

[70] Z. I. Alferov, V. M. Andreev, E. L. Portnoi and M. K. Trukan, *AlAs - GaAs heterojunction injection lasers with a low room-temperature threshold*, Sov. Phys. Semicond. **3**, 1107 (1969).

[71] Z. I. Alferov, *The history and the future of semiconductor heterostructures*, Semiconductors **32** (1998).

[72] W. T. Tsang, *A graded-index waveguide separate-confinement laser with very low threshold and a narrow Gaussian beam*, Applied Physics Letters **39**, 134 (1981).

[73] E. Yablonovitch and E. O. Kane, *Reduction of lasing threshold current density by the lowering of valence band effective mass*, J. Lightwave Technol. 504–506 (1986).

[74] H. K. Choi and C. A. Wang, *InGaAs/AlGaAs strained single quantum well diode lasers with extremely low threshold current density and high efficiency*, Applied Physics Letters **57**, 321 (1990).

[75] J. Singh, *Seminconductor optoelectronics*, Mc Graw-Hill (1995).

[76] V. Parys, *Optimization of an Integrated Optical Isolator Based on a Semiconductor Amplifier with a Ferromagnetic Metal Contact*, Ph.D. thesis, University of Gent (2009).

[77] P. Thiis, L. Tiemeijer, J. Binsma and T. Van Dongen, *Progress in long-wavelength strained-layer InGaAs(P) quantum-well semiconductor lasers and amplifiers*, Quantum Electronics, IEEE Journal of **30**, 477 (1994).

[78] T. DeTemple and C. Herzinger, *On the semiconductor laser logarithmic gain-current density relation*, Quantum Electronics, IEEE Journal of **29**, 1246 (1993).

[79] M. Vanwolleghem, *Een geintegreerde InP-gebaseerde optische golfgeleiderisolator op basis van ferromagnetische CoFe-contacten, An integrated InP-based Optical Waveguide Isolator Using Ferromagnetic CoFe Contacts*, Ph.D. thesis, Ghent University, Belgium (2005).

[80] C.-E. Zah, R. Bhat, B. Pathak, F. Favire, W. Lin, M. Wang, N. Andreadakis, D. Hwang, M. Koza, T.-P. Lee, Z. Wang, D. Darby, D. Flanders and J. Heieh, *High-performance uncooled 1.3 – μm $Al_xGa_yIn_{1-x-y}As/InP$ strained-layer quantum-well lasers for subscriber loop applications*, Quantum Electronics, IEEE Journal of **30**, 511 (1994).

[81] J. Decobert, N. Lagay, C. Cuisin, B. Dagens, B. Thedrez and F. Laruelle, *MOVPE growth of AlGaInAs-InP highly tensile-strained MQWs for 1.3um low-threshold lasers*, Journal of Crystal Growth **272**, 543 (2004).

[82] G. Stareev, H. Kunzel and G. Dortmann, *A controllable mechanism of forming extremely low-resistance nonalloyed ohmic contacts to group III-V compound semiconductors*, Journal of Applied Physics **74**, 7344 (1993).

[83] D. Costantini, A. Bousseksou, M. Fevrier, B. Dagens and R. Colombelli, *Loss and gain measurements of tensile-strained quantum well diode lasers for plasmonic devices at telecom wavelengths*, IEEE, Journal of Quantum Electronics **48**, 73 (2012).

[84] V. Moreau, M. Bahriz, R. Colombelli, R. Perahia, O. Painter, L. R. Wilson and A. B. Krysa, *Demonstration of air-guided quantum cascade lasers without top claddings*, Opt. Express **15**, 14861 (2007).

[85] T. Feuchter and C. Thirstrup, *High precision planar waveguide propagation loss measurement technique using a Fabry-Perot cavity*, I E E E Photonics Technology Letters **6**, 1244 (1994).

[86] H. C. Casey and M. B. Panish, *Heterostructured Lasers, Part A.*, p. 80, New York: Academic (1978).

[87] *COMSOL: Multiphysics Finite Element Analysis Simulation Software*, [Online]. Available: http://www.comsol.com/products/multiphysics/.

[88] J. H. C. Casey and P. L. Carter, *Variation of intervalence band absorption with hole concentration in p-type InP*, Applied Physics Letters **44**, 82 (1984).

[89] S. Adachi, *Physical Properties of III–V Semiconductor Compounds.*, New York, Wiley (1992).

[90] P. B. Johnson and R. W. Christy, *Optical constants of transition metals: Ti, V, Cr, Mn, Fe, Co, Ni, and Pd*, Phys. Rev. B **9**, 5056 (1974).

[91] B. W. Hakki and T. L. Paoli, *Gain spectra in GaAs double - heterostructure injection lasers*, Journal of Applied Physics **46**, 1299 (1975).

[92] J.-P. Tetienne, A. Bousseksou, D. Costantini, Y. D. Wilde and R. Colombelli, *Design of an integrated coupler for the electrical generation of surface plasmon polaritons*, Opt. Express **19**, 18155 (2011).

[93] S.-Y. Park, J. T. Kim, J.-S. Shin and S.-Y. Shin, *Hybrid vertical directional coupling between a long range surface plasmon polariton waveguide and a dielectric waveguide*, Optics Communications **282**, 4513 (2009).

[94] H. Ditlbacher, N. Galler, D. M. Koller, A. Hohenau, A. Leitner, F. R. Aussenegg and J. R. Krenn, *Coupling dielectric waveguide modes to surface plasmon polaritons*, Opt. Express **16**, 10455 (2008).

[95] D. Costantini, L. Greusard, A. Bousseksou, R. Rungsawang, T. P. Zhang, S. Callard, J. Decobert, F. Lelarge, G.-H. Duan, Y. De Wilde and R. Colombelli, *In Situ Generation of Surface Plasmon Polaritons Using a Near-Infrared Laser Diode*, Nano Letters **12**, 4693 (2012).

[96] L. Aigouy, P. Lalanne, J. P. Hugonin, G. Julié, V. Mathet and M. Mortier, *Near-Field Analysis of Surface Waves Launched at Nanoslit Apertures*, Phys. Rev. Lett. **98**, 153902 (2007).

[97] S. Ravets, J. C. Rodier, B. E. Kim, J. P. Hugonin, L. Jacubowiez and P. Lalanne, *Surface plasmons in the Young slit doublet experiment*, J. Opt. Soc. Am. B **26**, B28 (2009).

[98] A. Bousseksou, V. Moreau, R. Colombelli, C. Sirtori, G. Patriarche, O. Mauguin, L. Largeau, G. Beaudoin and I. Sagnes, *Surface-plasmon distributed-feedback mid-infrared quantum cascade lasers based on hybrid plasmon/air-guided modes*, Electronics Letters **44**, 807 (2008).

[99] C. S. Kim, I. Vurgaftman, R. A. Flynn, M. Kim, J. R. Lindle, W. W. Bewley, K. Bussmann, J. R. Meyer and J. P. Long, *An integrated surface-plasmon source*, Opt. Express **18**, 10609 (2010).

[100] *Lumerical FDTD*, http://www.lumerical.com.

[101] P. Berini and I. De Leon, *Surface plasmon–polariton amplifiers and lasers*, Nature Photonics **6**, 16 (2011).

[102] G. A. Plotz, H. J. Simon and J. M. Tucciarone, *Enhanced total reflection with surface plasmons*, J. Opt. Soc. Am. **69**, 419 (1979).

[103] A. Tredicucci, C. Gmachl, F. Capasso, A. L. Hutchinson, D. L. Sivco and A. Y. Cho, *Single-mode surface-plasmon laser*, Applied Physics Letters **76**, 2164 (2000).

[104] M. A. Noginov, V. A. Podolskiy, G. Zhu, M. Mayy, M. Bahoura, J. A. Adegoke, B. A. Ritzo and K. Reynolds, *Compensation of loss in propagating surface plasmon polariton by gain in adjacent dielectric medium*, Opt. Express **16**, 1385 (2008).

[105] P. Bolger, W. Dickson, A. Krasavin, L. Liebscher, S. Hickey, D. Skryabin and A. Zayats, *Amplified spontaneous emission of surface plasmon polaritons and limitations on the increase of their propagation length*, Opt. Lett. **35**, 1197 (2010).

[106] M. Ambati, S. H. Nam, E. Ulin-Avila, D. A. Genov, G. Bartal and X. Zhang, *Observation of Stimulated Emission of Surface Plasmon Polaritons*, Nano Letters **8**, 3998 (2008), pMID: 18837543.

[107] I. De Leon and P. Berini, *Amplification of long-range surface plasmons by a dipolar gain medium*, Nat Photon **4**, 382 (2010).

[108] R. A. Flynn, C. S. Kim, I. Vurgaftman, M. Kim, J. R. Meyer, A. J. Mäkinen, K. Bussmann, L. Cheng, F.-S. Choa and J. P. Long, *A room-temperature semiconductor spaser operating near 1.5 μm*, Opt. Express **19**, 8954 (2011).

[109] I. De Leon and P. Berini, *Theory of surface plasmon-polariton amplification in planar structures incorporating dipolar gain media*, Phys. Rev. B **78**, 161401 (2008).

[110] J. Grandidier, G. C. des Francs, S. Massenot, A. Bouhelier, L. Markey, J.-C. Weeber, C. Finot and A. Dereux, *Gain-Assisted Propagation in a Plasmonic Waveguide at Telecom Wavelength*, Nano Letters **9**, 2935 (2009), pMID: 19719111.

[111] R. F. Oulton, V. J. Sorger, T. Zentgraf, R.-M. Ma, C. Gladden, L. Dai, G. Bartal and X. Zhang, *Plasmon lasers at deep subwavelength scale*, Nature **461**, 629 (2009).

[112] R. F. Oulton, V. J. Sorger, D. A. Genov, D. F. P. Pile and X. Zhang, *A hybrid plasmonic waveguide for subwavelength confinement and long-range propagation*, Nature Photonics **2**, 496 (2008).

[113] M. T. Hill, M. Marell, E. S. P. Leong, B. Smalbrugge, Y. Zhu, M. Sun, P. J. van Veldhoven, E. J. Geluk, F. Karouta, Y.-S. Oei, R. Nötzel, C.-Z. Ning and M. K. Smit, *Lasing in metal-insulator-metal sub-wavelength plasmonic waveguides*, Opt. Express **17**, 11107 (2009).

[114] D. Y. Fedyanin, *Toward an electrically pumped spaser*, Opt. Lett. **37**, 404 (2012).

[115] D. Y. Fedyanin, A. V. Krasavin, A. V. Arsenin and A. V. Zayats, *Surface Plasmon Polariton Amplification upon Electrical Injection in Highly Integrated Plasmonic Circuits*, Nano Letters **12**, 2459 (2012).

[116] M. Pelton, J. Aizpurua and G. Bryant, *Metal-nanoparticle plasmonics*, Laser & Photonics Reviews **2**, 136 (2008).

[117] M. I. Stockman, *Spasers explained*, Nature Photonics **2**, 327 (2008).

[118] M. A. Noginov, G. Zhu, A. M. Belgrave, R. Bakker, V. M. Shalaev, E. E. Narimanov, S. Stout, E. Herz, T. Suteewong and U. Wiesner, *Demonstration of a spaser-based nanolaser.*, Nature **460**, 1110 (2009).

[119] M. C. Gather, *A rocky road to plasmonic lasers*, Nature Photonics **6**, 708 (2012).

[120] K. Ding, Z. C. Liu, L. J. Yin, M. T. Hill, M. J. H. Marell, P. J. van Veldhoven, R. Nöetzel and C. Z. Ning, *Room-temperature*

continuous wave lasing in deep-subwavelength metallic cavities under electrical injection, Phys. Rev. B **85**, 041301 (2012).

[121] M. Khajavikhan, A. Simic, M. Katz, J. H. Lee, B. Slutsky, A. Mizrahi, V. Lomakin and Y. Fainman, *Thresholdless nanoscale coaxial lasers*, Nature **482**, 204 (2012).

[122] Y.-J. Lu, J. Kim, H.-Y. Chen, C. Wu, N. Dabidian, C. E. Sanders, C.-Y. Wang, M.-Y. Lu, B.-H. Li, X. Qiu, W.-H. Chang, L.-J. Chen, G. Shvets, C.-K. Shih and S. Gwo, *Plasmonic Nanolaser Using Epitaxially Grown Silver Film*, Science **337**, 450 (2012).

[123] J. B. Khurgin and G. Sun, *How small can "Nano" be in a "Nanolaser"?*, Nanophotonics **1** (2012).

[124] D. Costantini, L. Greusard, A.Bousseksou, B. Habert, F. Marquier, J.-J. Greffet, A.Accard, J. Decobert, G.-H. Duan, Y. D. Wilde and R.Colombelli, *A hybrid plasmonic semiconductor laser*, Submitted to App. Phys. Lett. (2013).

[125] A. Christ, S. G. Tikhodeev, N. A. Gippius, J. Kuhl and H. Giessen, *Waveguide-Plasmon Polaritons: Strong Coupling of Photonic and Electronic Resonances in a Metallic Photonic Crystal Slab*, Phys. Rev. Lett. **91**, 183901 (2003).

[126] A. Degiron, S.-Y. Cho, T. Tyler, N. M. Jokerst and D. R. Smith, *Directional coupling between dielectric and long-range plasmon waveguides*, New Journal of Physics **11**, 015002 (2009).

[127] J. Boucart, C. Starck, F. Gaborit, A. Plais, N. Bouche, E. Derouin, L. Goldstein, C. Fortin, D. Carpentier, P. Salet, F. Brillouet and J. Jacquet, *1-mW CW–RT Monolithic VCSEL at 1.55 μm*, IEEE PHOTONICS TECHNOLOGY LETTERS (1999).

[128] J. Boucart, C. Starck, F. Gaborit, A. Plais, N. Bouche, E. Derouin, J. C. Remy, J. Bonnet-Gamard, L. Goldstein, C. Fortin, D. Carpentier, P. Salet, F. Brillouet and J. Jacquet, *Metamorphic DBR and Tunnel-Junction Injection: A CW RT Monolithic Long-Wavelength VCSEL*, IEEE JOURNAL OF SELECTED TOPICS IN QUANTUM ELECTRONICS **5** (1999).

[129] L. A. Coldren, S. W. Corzine and M. L. Masanovic, *Diode lasers and photonic integrated circuits*, Wiley (2012).

[130] J. J. Coleman, A. C. Bryce and C. Jagadish, *Advances in semiconductor lasers*, Elsevier (2012).

[131] Y. Suematsu and K. Iga, *Semiconductor Lasers in Photonics*, Lightwave Technology, Journal of **26**, 1132 (2008).

[132] J. E. Carroll, J. E. Whiteaway and D. Plumb, *Distributed Feedback Semiconductor Lasers*, IEEE (1998).

[133] W. Zeller, L. Naehle, P. Fuchs, F. Gerschuetz, L. Hildebrandt and J. Koeth, *DFB Lasers Between 760 nm and 16 μm for Sensing Applications*, Sensors **10**, 2492 (2010).

[134] M. Carras and A. De Rossi, *Photonic modes of metallodielectric periodic waveguides in the midinfrared spectral range*, Phys. Rev. B **74**, 235120 (2006).

[135] L.Greusard, D. Costantini, A. Bousseksou, J. Decobert, F. Lelarge, G.-H. Duan, Y. D. Wilde and R. Colombelli, *Near-field analysis of metallic DFB lasers at telecom wavelengths*, Submitted to SMALL (2013).

[136] D. Costantini, *Analysis of transport properties and photoconductive response of single InAs nanowires*, Master's thesis, University of Pisa (2009).

[137] *Introduction on electron beam lithography*, http://henderson.chbe.gatech.edu/Introductions/intro

[138] M. Fevrier, *Couplage entre un guide d'onde diélectrique et un guide á plasmon de surface localisé : conception, fabrication et caractérisation*, Ph.D. thesis, Universié Paris Sud (2012).

[139] R. Stöckle, C. Fokas, V. Deckert, R. Zenobi, B. Sick, B. Hecht and U. P. Wild, *High-quality near-field optical probes by tube etching*, Applied Physics Letters **75**, 160 (1999).

[140] R. Bachelot, C. Ecoffet, D. Deloeil, P. Royer and D.-J. Lougnot, *Integration of Micrometer-Sized Polymer Elements at the End of Optical Fibers by Free-Radical Photopolymerization*, Appl. Opt. **40**, 5860 (2001).

[141] T.-P. Vo, A. Rahmani, A. Belarouci, C. Seassal, D. Nedeljkovic and S. Callard, *Near-field and far-field analysis of an azimuthally polarized slow Bloch mode microlaser*, Opt. Express **18**, 26879 (2010).

[142] Y. D. Wilde, F. Formanek and L. Aigouy, *Apertureless near-field scanning optical microscope based on a quartz tuning fork*, Review of Scientific Instruments **74**, 3889 (2003).

Publications related to this Thesis

Papers published in peer-reviewed journals

J.-P. Tetienne, A. Bousseksou, **D. Costantini**, R. Colombelli, A. Babuty, I. Moldovan-Doyen, Y. D. Wilde, C. Sirtori, G. Beaudoin, L. Largeau, O. Mauguin and I. Sagnes, *Injection of midinfrared surface plasmon polaritons with an integrated device*, Applied Physics Letters **97**, 211110 (2010).

J.-P. Tetienne, A. Bousseksou, **D. Costantini**, Y. D. Wilde and R. Colombelli, *Design of an integrated coupler for the electrical generation of surface plasmon polaritons*, Opt. Express **19**, 18155 (2011).

D. Costantini, A. Bousseksou, M. Fevrier, B. Dagens and R. Colombelli, *Loss and gain measurements of tensile-strained quantum well diode lasers for plasmonic devices at telecom wavelengths*, IEEE, Journal of Quantum Electronics **48**, 73 (2012).

D. Costantini, L. Greusard, A. Bousseksou, R. Rungsawang, T. P. Zhang, S. Callard, J. Decobert, F. Lelarge, G.-H. Duan, Y. De Wilde and R. Colombelli, *In Situ Generation of Surface Plasmon Polaritons Using a Near-Infrared Laser Diode*, Nano Letters **12**, 4693 (2012).

D. Costantini, L. Greusard, A.Bousseksou, B. Habert, F. Marquier, J.-J. Greffet, A.Accard, J. Decobert, G.-H. Duan, Y. D. Wilde and R.Colombelli, *A hybrid plasmonic semiconductor laser*, App. Phys. Lett. **102** 101106 (2013).

L.Greusard, **D. Costantini**, A. Bousseksou, J. Decobert, F. Lelarge, G.-H. Duan, Y. D. Wilde and R. Colombelli, *Near-field analysis of metallic DFB lasers at telecom wavelengths*, Opt. Express **21**, 10422 (2013).

Conference proceedings & workshops

- April 2012, ECIO 16th European Conference on Integrated Optics, Sitges, Spain. INVITED TALK
  D. Costantini,
  "Towards surface-plasmon generation by electrical injection at telecom wavelengths with a semiconductor device"
- April 2012, META2012 3rd International conference on Metamaterials, Photonics Crystals and Plasmonics, Paris, France
  D. Costantini, R. Colombelli, A. Bousseksou, M. Fevrier, B. Dagens, A. Accard, J. De Cobert, G Duan, L. Greusard, R. Rungsawang, Y. De Wilde, S. Callard, T. Zhang,
  "Towards SP generation/amplification at telecom wavelengths using transverse-magnetic polarized semiconductor diode lasers"
- May 2011, Conference on Lasers and Electro-Optics 2011: Applications and Technology (CLEO: A and T), Baltimore, Maryland, Joint Symposium on Hybrid Quantum Nanoplasmonic Systems
  D. Costantini, A. Bousseksou, A. Babuty, L. Greusard, Y. De Wilde, C. Sirtori, A. Accard, G. Duan, and R. Colombelli
  "Plasmonic waveguides for active semiconductor devices at telecom wavelengths using transverse-magnetic-polarized diode lasers"
- August 2010, International Quantum Cascade Laser Workshop and School 2010 (IQCL)
  D. Costantini, A. Bousseksou, A. Babuty, I Doyen, Y. De Wilde, C. Sirtori, A. Accard, G-H. Duan, I. Sagnes, R. Colombelli,
  "Generation of surface plasmon polaritons by electrical injection at telecom wavelengths"

Participation at schools

- May 2012, NATO and SFO Workshop on Plasmonic, Amphitheater Pierre Faurre Ecole Polytechnique, 91128 Palaiseau Cedex, France
  D. Costantini, A. Bousseksou, M. Fevrier, B. Dagens, A. Accard, J. Decobert, G Duan, L. Greusard, R. Rungsawang, Y. De Wilde, S. Callard, T. Zhang, R. Colombelli,
  "Towards SP generation/amplification at telecom wavelengths using

transverse-magnetic polarized semiconductor diode lasers"

– October 2011, Summer School On Plasmonics 2 (SSOP2), Porquerolles, France
D. Costantini, A. Bousseksou, M. Fevrier, B. Dagens, L. Greusard, R. Rungsawang, Y. De Wilde, T. Zhang, S. Callard, A. Accard, J. Decobert, G-H. Duan, I. Sagnes, R. Colombelli,
"Generation of surface plasmon polaritons by electrical injection at telecom wavelengths"

– June 2010, Journées Nationales du Réseau Doctoral de Microélectronique (JNRDM) 2010
D. Costantini, A. Bousseksou, J-P. Tetienne, A. Babuty, I. Doyen, Y. De, C. Sirtori, A. Accard, G-H. Duan, I. Sagnes, R. Colombelli,
"Génération de plasmon de surface par injection électrique"

Acknowledgments

Grazie grazie grazie! [1]

Tout d'abord je remercie de coeur mon directeur Raffaele qui m'a permis d'intégrer son groupe de recherche et de développer une recherche extrêmement intéressante. Pendant ces trois années je n'ai jamais arrêté de me former et d'apprendre. Raffaele, grâce à ta direction scientifique j'ai obtenu des beaux résultats dont je suis très satisfait et fier. Tu as toujours été présent, en m'orientant vers la bonne direction et en me montrant que tout problème a une solution. J'apprécie énormément ta grande compétence scientifique, ton optimisme, l'énergie que tu as (malgré l'RER quotidien) et la passion pour la Physique et la Science. "Dulcis in fundo" ... merci pour les viennoiseries de Serge et pour la mitica Colomba, nomen omen!

Un grand merci à Adel de m'avoir suivi pendant tout ce parcours. Tu m'as appris les technique de fabrication en salle et tu as toujours été présent en cas de nécessité, même plus: aussi tard le soir avant la deadline d'une conf pour relire mon abstract. Toujours compétent, motivé et efficient. Un remerciement à François qui dirige le groupe Photis avec la bonne humeur et avec la blague sur la pointe de la langue. Grâce à toi j'ai appris l'art de la contrepèterie qui est utile en toute situation: ah quel bel métier professeur! Merci pour la bonne musique jazz et pour le repa convivial de groupe organisé dans ton beau jardin. Merci d'avoir toujours été disponible, d'avoir pris le soin de relire mon manuscrit et pour tes compliments.

Merci à tous les commissaires qui ont accepté de participer au jury de thèse. Merci pour l'intérêt que vous avez montré pour mon travail et votre appréciation.

Merci à Yannick et Leo pour les belles images de champ proche indispensables à compléter mon travail. C'était un plaisir de travailler avec vous

1. Merci merci merci!

et d'arriver ensemble aux résultats! Grazie également de m'avoir fait découvrir Golosino, j'avoue j'y suis retourné! A tous les autres partenaires qui ont travaillé au projet GOSPEL: Benjamin, François, Jean-Jacques, G-H Duan, F. Lelarge, A. Accard, J. Decobert. A S. Callard qui nous a aidé pour les premières mesures SNOM.

Pendant ces trois ans j'ai pu découvrir à l'IEF un environnent riche du point de vue humain et des compétences. En commençant par le groupe Photis et tout ceux qui sont passés par la! Elodie et moi avons debuté nos thèses au même temps et dès le début nous avons construit une sincère amitié, renforcée avec le temps. Merci Elo pour ton soutien pendant les moments difficiles, c'était toujours inspirant de parler avec toi. Je n'oublie pas ta patience dans l'écoute de mes répètes, les bonnes questions et l'encouragement notamment à Baltimore et pour la thèse même. C'est toujours très intéressant de discuter avec toi de science et de tout autre sujet. Cresus is not dead! Thank you Gangyi for your generosity and your openness to discuss. Merci Gwenolé - Guenolino - qui m'a fait découvrir la fête de l'Huma. Salam - Salamino - toujours actif dans l'organisation des diners de groupe. Andrés - Cocca - pas possible d'oublier ton guacamole, les longs moments en salle blanche en essayant de résoudre les problèmes de chargement du Raith! Lorenzo, pour ta veine poétique et les excellentes "leccornie" que tu as ramené de Bologna. Grégoire, qui m'a introduit à l'art de la dactylographie. Maria, qui m'impressionne avec son efficacité russe. Yacine, merci pour m'avoir appris plus sur l'intégration III-V et désolé de t'avoir si bien visé avec les boules de neiges, eheh. Jean-Michel sûrement tu as ramené un peu de soleil de la Grèce, merci pour ta bonne humeur et bon courage pour le couplage critique. Merci Souad de ne jamais oublier de m'appeler pour aller manger et pour l'enthousiasme que tu as montré pour mon mini-moteur électrique, j'étais ravis. Daniel, mon homonyme, mon successeur, tu m'as fait repenser à quand j'ai commencé ma thèse, bon j'étais un peu moins rasta. Rappelles toi, c'est dans les bonbons aux fruits qu'il y a les bonnes vitamines! Merci à Patrick! Bruno, indispensable car tu as apporté une saine touche du Sud! Toujours enthousiaste, de discuter de science, politique et "buon Cibo". L'Italia m'a un peu manqué, mais grâce à Bruno, Davide e Simone j'ai bien pu supporter la distance. Grazie Davide per le chiacchierate e le "grassanate" varie! Grazie a Simone che sa un sacco di cose su tutto e dal quale non si smette di imparare, in particolar modo di treni (cmq ti ripeto che l'Orlybus

costa di meno dell'Orlyval, che è sempre "in panna" tra l'altro). Merci aussi à Sirona qui est passée pour une courte période, mais qui a porté une bonne dose d'énergie espagnole!

Et maintenant un paragraphe pour les "copains" de bureau! Un grand merci à Jean-Philippe avec qui j'ai eu le plaisir de travailler au début de la thèse, j'ai beaucoup appris et avec toi j'ai pu commencer mon doctorat du bon pied. Très compétent, précis et modeste, je te souhaite le meilleur! Pierre, c'était vraiment bien de t'avoir à ma droite. Merci de m'avoir aidé, "juste un petit peu", quand j'étais en roller en revenant de la piscine; nous sommes arrivés avant à la cantine. Aujourd'hui je suis en train d'écrire les remerciements avec le Tshirt de notre triathlon. A propos de Maki Maki, merci Charlotte de avoir couru les 5 Km ... W les blondes! Jean-René qui n'est formellement pas dans notre bureau, mais ce n'est pas important. Merci de ton aide en salle blanche, toujours disponible et avec la bonne solution (piranha par ex.)! Et merci pour le sucre. Pour bien conclure cette partie, un immense merci a Nathalie avec laquelle j'ai partagé le bureau pendant trois ans. Tu as toujours ce qu'il faut, stylos, bonbons, tournevis, fils d'or!!! Tout ce qu'il faut au bon moment. Merci pour ta générosité qui a été vraiment indispensable souvent et elle a toujours rendu la vie au labo bien meilleure. L'arbre de Noël, le gâteau à la broche, les chansons, les bonbons et "mine de rien, air de tout" toutes les belles expressions françaises les plus authentiques (que je garde dans mon cahier). Et je n'oublie pas Maquette que j'ai vu grandir et devenir une charmante demoiselle ! N'arrêtes quand même pas de jongler!!!

Merci Arnaud de m'avoir aidé dès le début, pour le CV par exemple à l'occasion de la demande de monitorat! Et pour tout le reste, JNRDM, les papiers envoyés ... Toujours présent, même tard le soir, et toujours dispo. Merci à Delphine, Guillaume, Philippe et Navy de avoir accompagné dans ma première expérience d'enseignement. Et encore, merci Béatrice pour la collaboration, merci Mickael qui a *la classe à Dallas*, ou mieux au Texas maintenant. Gracias à Robert, tout le temps de bonne humeur et avec mille propositions culturellement stimulantes. Philippe qui m'a prouvé pour de vrai l'existence des plasmons (avant j'étais un peu sceptique!). Merci à David de la CTU et à tous les autres de la CTU. Merci à tous les organisateurs du JNRDM 11!

Grazie ai miei amici di Pisa e "dintorni", Dario, Stefano, Alessandra, Alice, Angelo, Davide, Monica, Irene, AlexTM, Chiara, Giacomo, Federica

che son venuti a festeggiare a Parigi il we della discussione! E' stato stupendo avervi tutti qui assieme, uscire a fare due passi per la "villa luce" con voi al Jardin de Luxembourg, crêpes, sushi ... sono davvero felice che siate venuti tutti quanti :) Grazie anche a tutti gli altri, ogni volta che torno a Pisa sembra quasi di non essere partito, e mi sento nuovamente a casa! Un grand merci à Laurent avec lequel j'ai a partagé une grande partie de la durée de ma thèse dans le mythique Pink Palace. C'était "trop bien", merci de m'avoir fait connaitre plein de gens sympas, pour les brunches, la fête européenne, les discussions enrichissantes et pour le bananier, c'est vraimeint un coup de génie! Je l'adore! Grazie Giulietta! Grazie à tous les autres "parisien", Pietro, Giovanni, Lucia, Giulia, Marta, Marco, Elia, Massimiliano, Giuseppe, Luna, Caroline, Alienor, Fabien, Kostia, Matthew, Samantha, Boris, Jas, Ruxandra, Anne-Lies, Gloria, Thomas avec lesquels j'ai passé des très beaux moments!

Merci de coeur à ma famille, Alessandro, Stefania et Flavio, qui m'ont soutenu, comme toujours d'autre part, dans cette aventure. Vous avez su me donner force lorsqu'il le fallait et vous étiez la pour applaudir mes conquêtes. Merci pour me faire toujours sentir à la maison quand je rentre à Pisa. Merci de m'aider quand je suis ici à Paris, grâce à la bonne bouffe "nostrana"! C'est étonnant, mais, même après 28 ans, je continue à beaucoup apprendre grâce à vous!

Ho incrociato il tuo sguardo due anni fa ed ora, ogni giorno cha passa, non posso più farne a meno. Pour l'amour, la force, la joie, l'élégance que chaque jour tu m'offres: Grazie Natalia!

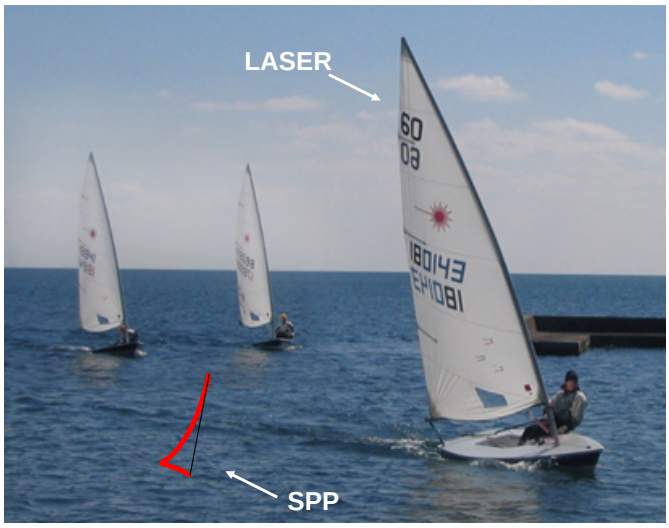

Figure E.4: An SPP which is *lasing*...a SPASER?!